APPLICATION OF THE PYROELECTRIC EFFECT FOR X-RAY GENERATION

Emily Wern Jien Yap

A thesis in fulfilment of the requirements for the degree of

Doctor of Philosophy

School of Materials Science and Engineering

Faculty of Science

August 2019

Thesis/Dissertation Sheet

Surname/Family Name	:	Yap
Given Name/s	:	Emily Wern Jien
Abbreviation for degree as give in the University calendar	:	PhD
Faculty	:	Science
School	:	Materials Science and Engineering
Thesis Title	:	Application of the Pyroelectric Effect for X-ray Generation

Abstract 350 words maximum: (PLEASE TYPE)

Over the 100 years of their use, X-ray generators have proven to be indispensable in a wide array of applications. However, the methods for generating X-rays have not developed significantly, and the inherent size and power draw of existing X-ray generators limit the manufacture of more portable X-ray systems. The first demonstration of applying the pyroelectric effect for X-ray generation in 1992 made it a promising candidate for in-field and on-line analyses. This method of thermally cycling a pyroelectric material in a high vacuum exhibits advantages of being lightweight, compact and battery operated.

In this thesis, an X-ray generator that utilises the pyroelectric effect was developed and optimised to maximise its performance, in terms of X-ray flux and end-point energy. The generation of X-rays relied on the emission of electrons which was dependent on the electric field created between the pyroelectric crystal and the target placed at a gap distance. Evaluation of the material figures-of-merit and utilisation of electrostatics simulations to estimate the electric field in the gap determined a theoretical optimal combination of material properties, crystal thickness and gap distance.

An experimental system was built to simultaneously control the temperature of the pyroelectric crystal in a high vacuum chamber and collect time and energy-resolved X-ray emissions. The effects of various parametric combinations were then investigated and found to deviate from the theoretical findings. Thus, the most optimal combination of parameters was using the pyroelectric crystal, lithium tantalate, at a gap distance of 5 mm and pressure of 0.33 Pa. This produced an X-ray flux of 1.22×10^5 cm^2/s and an end-point energy of 40 keV.

The enhancement of the electric field at the crystal edges was exploited in an attempt to improve the X-ray generator's performance by dicing the crystal to introduce more edges per unit area. Using lithium tantalate, a range of dicing combinations were assessed and found to underperform compared to its uniform counterpart.

Finally, the X-ray generator was operated over 200 cumulative hours and its output monitored. The X-ray flux and end-point energy fluctuated over this time and was found to correlate with the gradual surface degradation observed on the pyroelectric crystal.

INCLUSION OF PUBLICATIONS STATEMENT

UNSW is supportive of candidates publishing their research results during their candidature as detailed in the UNSW Thesis Examination Procedure.

Publications can be used in their thesis in lieu of a Chapter if:

- The student contributed greater than 50% of the content in the publication and is the "primary author", i.e. the student was responsible primarily for the planning, execution and preparation of the work for publication
- The student has approval to include the publication in their thesis in lieu of a Chapter from their supervisor and Postgraduate Coordinator.
- The publication is not subject to any obligations or contractual agreements with a third party that would constrain its inclusion in the thesis

Please indicate whether this thesis contains published material or not.

☒ *This thesis contains no publications, either published or submitted for publication (if this box is checked, you may delete all the material on page 2)*

☐ *Some of the work described in this thesis has been published and it has been documented in the relevant Chapters with acknowledgement (if this box is checked, you may delete all the material on page 2)*

☐ *This thesis has publications (either published or submitted for publication) incorporated into it in lieu of a chapter and the details are presented below*

CANDIDATE'S DECLARATION

I declare that:

- I have complied with the Thesis Examination Procedure
- where I have used a publication in lieu of a Chapter, the listed publication(s) below meet(s) the requirements to be included in the thesis.

Name	Signature	Date (dd/mm/yy)

Postgraduate Coordinator's Declaration (to be filled in where publications are used in lieu of Chapters)

I declare that:

- the information below is accurate
- where listed publication(s) have been used in lieu of Chapter(s), their use complies with the Thesis Examination Procedure
- the minimum requirements for the format of the thesis have been met.

PGC's Name	PGC's Signature	Date (dd/mm/yy)

ORIGINALITY STATEMENT

'I hereby declare that this submission is my own work and to the best of my knowledge it contains no materials previously published or written by another person, or substantial proportions of material which have been accepted for the award of any other degree or diploma at UNSW or other educational institution, except where due acknowledgement is made in the thesis. Any contribution made to the research by others, with whom I have worked at UNSW or elsewhere, is explicitly acknowledged in the thesis. I also declare that the intellectual content of this thesis is the product of my own work, except to the extent that assistance from others in the project's design and conception or in style, presentation and linguistic expression is acknowledged.'

Signed: .....

Date: .....

COPYRIGHT STATEMENT

Signed: .....

Date: .....

AUTHENTICITY STATEMENT

'I certify that the Library deposit digital copy is a direct equivalent of the final officially approved version of my thesis.'

Signed: .....

Date: .....

Acknowledgements

Embarking on this journey of undertaking a PhD project has given me the opportunity to work with many individuals and groups of different expertise. With that, I have an immense amount of gratitude and appreciation for the breadth of support provided.

Firstly, I would like to acknowledge the advice and guidance provided by my two supervisors, Dr. Rhys M. Preston and Assoc. Prof. John E. Daniels. This project proved to have many hurdles to overcome and I believe I learned more about the skills and attributes that make a good researcher than the many questions posed by the project.

The collaborative involvement between UNSW Sydney and CSIRO of this project has allowed me to access several labs and receive financial and technical support. This project would not have progressed without the help of the technical lab staff and Dr. Nitish Kumar from the School of Materials Science and Engineering, as well as the scientists and engineers at the Sensing and Sorting Group of CSIRO Mineral Resources. Sincerest thanks to Dr. Nick Cutmore for creating a space for students to grow and ensuring we have sufficient funds to purchase lab equipment. Furthermore, I am very thankful for being given the chance to conduct a part of my research overseas as well as the conferences and courses I have attended.

Many thanks to Prof. Dragan Damjanovic for allowing me to visit your laboratory at EPFL, Switzerland. You and your research group made me feel very welcomed and your knowledge of pyroelectrics and ferroelectrics was tremendously helpful.

I would like to thank Brianna Ganly for constantly sparking curiosity and excitement in my project, helping me with my data and having confidence in my capabilities. I really would have been at a roadblock for a long time if it weren't for you.

The computer simulations work was performed in part of the New South Wales Node of the Australian National Fabrication Facility, a company established under the National Collaborative Research Infrastructure Strategy to provide nano and micro-fabrication facilities for Australia's researchers. In particular, thank you Dr. Jeffrey Cheung for helping me with my COMSOL-related issues.

Thank you to JEDI and PGSOC for making me feel inclusive within the group and at uni even though I was technically an off-campus student. I still enjoyed being able to learn about ferroelectrics and the other projects going on in our research group (plus the pranks and lunches). And I'm glad that I was able to make a positive impact within the postgraduate community.

Special thanks to Thai Ly, Maggie Zhou, Patrick Tung, Kara Poon and Vivian Huynh for lending an ear when times got tough and putting up with me when I was on my emotional rollercoaster ride. To my many friends I made along the way, thank you for making sure my life is consistently filled with fun and joy and being incredibly understanding. And finally, to my family, you may not have completely understood what I was working on, but you had faith in my ability to complete this arduous task, and that is what matters.

Abstract

Over the 100 years of their use, X-ray generators have proven to be indispensable in a wide array of applications. However, the methods for generating X-rays have not developed significantly, and the inherent size and power draw of existing X-ray generators limit the manufacture of more portable X-ray systems. The first demonstration of applying the pyroelectric effect for X-ray generation in 1992 made it a promising candidate for in-field and on-line analyses. This method of thermally cycling a pyroelectric material in a high vacuum exhibits advantages of being lightweight, compact and battery-operated.

In this thesis, an X-ray generator that utilises the pyroelectric effect was developed and optimised to maximise its performance, in terms of X-ray flux and end-point energy. The generation of X-rays relied on the emission of electrons which was dependent on the electric field created between the pyroelectric crystal and the target placed at a gap distance. Evaluation of the material figures-of-merit and utilisation of electrostatics simulations to estimate the electric field in the gap determined a theoretical optimal combination of material properties, crystal thickness and gap distance.

An experimental system was built to simultaneously control the temperature of the pyroelectric crystal in a high vacuum chamber and collect time and energy-resolved X-ray emissions. The effects of various parametric combinations were then investigated and found to deviate from the theoretical findings. Thus, the most optimal combination of parameters was using the pyroelectric crystal, lithium tantalate, at a gap distance of 5 mm and pressure of 0.33 Pa. This produced an X-ray flux of 1.22×10^5 cm^2/s and an end-point energy of 40 keV.

The enhancement of the electric field at the crystal edges was exploited in an attempt to improve the X-ray generator's performance by dicing the crystal to introduce more edges per unit area. Using lithium tantalate, a range of dicing combinations were assessed and found to underperform compared to its uniform counterpart.

Finally, the X-ray generator was operated over 200 cumulative hours and its output monitored. The X-ray flux and end-point energy fluctuated over this time and was found to correlate with the gradual surface degradation observed on the pyroelectric crystal.

Table of Contents

Acknowledgements ix

Abstract xi

List of Figures xvii

List of Tables xxix

1 INTRODUCTION 1-1

2 LITERATURE REVIEW 2-1

2.1 Overview 2-1

2.2 X-ray Generation Technologies 2-2

2.2.1 X-ray production 2-2

2.2.2 Conventional X-ray generation 2-4

2.2.3 X-ray tubes 2-6

2.2.4 Photoelectric probability 2-7

2.3 Ferroelectric Materials 2-9

2.3.1 Classes of dielectric materials 2-9

2.3.2 Crystal structure 2-10

2.3.3 Domains 2-15

2.4 Alternate Methods to Generate X-rays 2-16

2.4.1 X-ray generation from ferroelectric materials 2-16

2.4.2 X-ray generation via triboelectricity 2-20

2.4.3 X-ray generation via field electron emission using carbon nanotubes 2-22

2.5 Pyroelectric X-ray Generators 2-23

2.5.1 Single-crystal configuration 2-23

2.5.2 Multi-crystal configuration 2-25

2.5.3 Combination of pyroelectric crystal with other materials 2-26

2.5.4 Other modifications 2-28

2.6 Summary 2-29

3 CHARACTERISATION OF PYROELECTRIC MATERIALS ___ 3-1

3.1 Overview ___ 3-1

3.2 Literature ___ 3-2

3.2.1 Dielectric and pyroelectric material properties, and its limitations ___ 3-2

3.2.2 Theory of measuring pyroelectric coefficient ___ 3-4

3.2.3 Figure-of-merit ___ 3-6

3.2.4 Potential materials ___ 3-11

3.3 Experimental Methodology ___ 3-14

3.3.1 Sample preparation ___ 3-14

3.3.2 Pyroelectric coefficient ___ 3-16

3.3.3 DC conductivity ___ 3-17

3.4 Results and Discussion ___ 3-19

3.4.1 Optical micrographs ___ 3-19

3.4.2 Quality of electrodes on samples ___ 3-21

3.4.3 Pyroelectric coefficient ___ 3-23

3.4.4 DC conductivity ___ 3-32

3.4.5 Figure-of-merit ___ 3-34

4 ELECTROSTATICS SIMULATIONS ___ 4-1

4.1 Overview ___ 4-1

4.2 Simulation Model Setup ___ 4-2

4.3 Results and Discussion ___ 4-5

4.3.1 Electric field around the pyroelectric crystal ___ 4-5

4.3.2 Effect of crystal thickness ___ 4-9

4.3.3 Effect of crystal composition ___ 4-17

4.3.4 Effect of gap distance ___ 4-23

5 X-RAY GENERATOR APPARATUS ___ 5-1

5.1 Overview ___ 5-1

5.2 Vacuum System ___ 5-2

5.3 Temperature Control System ___ 5-5

5.4 Data Acquisition System 5-8
5.4.1 Temperature control 5-8
5.4.2 X-ray detection 5-8
5.4.3 Ion current measurement 5-10
5.5 Generator Setup 5-11
5.6 Vacuum setup 5-14
6 CHARACTERISATION AND OPTIMISATION OF THE X-RAY GENERATOR 6-1
6.1 Overview 6-1
6.2 Experimental Methodology 6-2
6.3 X-ray Spectra 6-4
6.3.1 Characteristics of the X-ray spectra 6-4
6.3.2 End-point energy evaluation 6-9
6.3.3 Variation of count rate and end-point energy with temperature and time 6-10
6.4 X-ray Spectra Correction 6-13
6.5 X-ray Generation as a Function of Various Parameters 6-15
6.5.1 Effect of crystal thickness 6-15
6.5.2 Effect of crystal composition 6-20
6.5.3 Effect of pressure and gap distance 6-26
6.5.4 Combination of crystal composition, pressure and gap distance 6-35
7 EDGE EFFECT OF THE PYROELECTRIC CRYSTAL 7-1
7.1 Overview 7-1
7.2 X-Ray Generation with Insulated Edges 7-2
7.2.1 X-ray generation experimental methodology 7-2
7.2.2 Insulated edge measurement results and discussion 7-3
7.2.3 Electrostatics simulation model 7-12
7.2.4 Simulation results and discussion 7-14

7.3 X-ray Generation using a Diced Crystal 7-22
7.3.1 X-ray generation experimental methodology 7-22
7.3.2 Diced pyroelectric crystal results and discussion 7-22
7.3.3 Electrostatics simulation model 7-29
7.3.4 Effect of number of kerfs and kerf widths 7-30

8 FATIGUE TEST OF THE X-RAY GENERATOR 8-1

8.1 Overview 8-1

8.2 Experimental Methodology 8-2

8.3 Results and Discussion 8-4
8.3.1 X-ray intensity 8-4
8.3.2 Optical micrographs of the crystal surface 8-9
8.3.3 Confocal laser scanning micrographs of the surface 8-15

9 CONCLUSIONS 9-1

10 FUTURE WORK 10-1

References 1

Appendix A DC conductivity A-1

Appendix B Electric potential distributions of $LiTaO_3$ of varying thickness B-1

Appendix C Arduino program code: Generator8 C-1

Appendix D End-point energy evaluation for various parametric variations D-1

Appendix E Electric potential distribution of $LiTaO_3$ with insulated edges E-1

Appendix F Updated Arduino program code: Generator12 F-1

Appendix G IGOR Pro operation program code G-1

List of Figures

Figure 2-1 Production of different X-rays from the collision of electrons with the atomic structure. Adapted with permission by the Society of Nuclear Medicine and Molecular Imaging from [22]. 2-3

Figure 2-2 Example of X-ray energy spectra consisting of bremsstrahlung and characteristic X-rays being filtered at different sections within and outside a conventional X-ray tube. The X-ray spectrum after leaving the tube is reduced due to inherent filtration from glass window and housing. Reproduced with permission by John Wiley and Sons from [23]..... 2-4

Figure 2-3 Schematic diagram of a conventional X-ray tube. Adapted with permission by Openstax under the Creative Commons Attribution Licence 4.0 (CC BY) from [36]..... 2-6

Figure 2-4 Effect of peak voltage (kVp) and tube current (mA) on the output of an X-ray tube with a tungsten target. The tube current is fixed in (a) and the applied voltage is fixed in (b). A filter is assumed to be added. 2-7

Figure 2-5 Mass attenuation coefficient (μ/ϱ) as a function of incident photon energy. Data taken from [37-39]..... 2-8

Figure 2-6 Perovskite structure ABO_3 as a cubic unit cell. 2-10

Figure 2-7 Surface charges become apparent when the A and B ions are displaced relative to the oxygen ions, creating a spontaneous polarisation, P_S. The green coloured plane indicates a positively charged surface while the red coloured plane indicates a negatively charged surface. 2-11

Figure 2-8 Three structures of unit cell. The top row represents the possible directions the polar axis can take while the bottom row illustrates the distortion of the unit cell in the direction of the black arrow. 2-12

Figure 2-9 Relationship between the rhombohedral (blue solid line), hexagonal (black solid and dotted lines) and cubic unit cells (red dotted line). (a) shows the rhombohedral lattice inside the hexagonal lattice while (b) includes the cubic lattice with the same solid black lattice section of (a). Reproduced and adapted with permission by the University of Oklahoma and Elsevier from [44-46]..... 2-12

Figure 2-10 Lattice parameters of $BaTiO_3$ as a function of temperature. Reproduced with permission by Elsevier from [40]. 2-13

Figure 2-11 Phase diagram of the PMN-PT binary system. Reproduced with permission by IOP Publishing under the Creative Commons Attribution Licence (CC BY) from [47]. 2-14

Figure 2-12 Energy band diagram illustrating the overbarrier (thermionic and photoemission) and tunnelling (field emission) mechanisms at the emitter to vacuum interface. 2-17

Figure 2-13 Typical experimental setups for "weak" (a) and "strong" (b) electron emission from ferroelectric materials. Depending on the experiment, the collector can be an electron detector or replaced with a target and an X-ray detector placed in line with the target and ferroelectric crystal. 2-18

Figure 2-14 Photographs of the commercialised COOL-X pyroelectric (a) and in-development piezoelectric (b) X-ray generators. Reproduced with permission by AMPTEK, Inc. and Rob Hill courtesy of MIZZOU alumni magazine from [14, 83]. 2-20

Figure 2-15 The capsule-like X-ray emitter (a) and the Watson M1 X-ray handheld analyser (b) developed by Tribogenics, Inc. Reproduced with permission by SPIE Publication from [85, 91]. 2-21

Figure 3-1 Temperature dependence of spontaneous polarisation, P_S, and the pyroelectric coefficient, p. Reproduced with permission by Springer Nature from [135]. 3-2

Figure 3-2 Spontaneous polarisation as a function of temperature of barium titanate single crystal. Reproduced with permission by John Wiley and Sons from [51]. 3-3

Figure 3-3 Temperature dependence of spontaneous polarisation and relative permittivity of an ideal ferroelectric material. T_C represents the Curie Point. Reproduced with permission by Elsevier from [53]. 3-4

Figure 3-4 Schematic model of a pyroelectric crystal connected in a circuit to measure pyroelectric current. (a) In an open circuit, the pyroelectric crystal will attract charged ions to compensate the surface charges. (b) When the crystal connected in a short circuit with electrodes on its polar surfaces and is at equilibrium, no current flows through the ammeter. (c) During heating, the spontaneous polarisation, P_S, decreases causing the respective charged ions to flow away from the electrodes. (d) During cooling, P_S increases and respective charged ions flow towards the electrodes to accommodate for the change. The cyclic thermal gradient will generate an oscillating current. Reproduced with permission by Taylor and Francis Group, LLC, a division of Informa plc from [141]. 3-5

Figure 3-5 Schematic of the generator (a) and its corresponding electric schematic diagram (b) where the two capacitors are the crystal and the gap. 3-6

Figure 3-6 In-house pyroelectric measurement equipment built by the Group of Ferroelectrics and Functional Oxides, EPFL, Lausanne, Switzerland 3-16

Figure 3-7 Surface defects can be seen on the surface of the lithium niobate single crystal. 3-19

Figure 3-8 Cleaned surface of lithium tantalate with visible surface defects. 3-20

Figure 3-9 Barium titanate single crystal viewed under an optical microscope with a polarising filter applied. The single domain can be seen breaking into small domains. 3-20

Figure 3-10 Lithium niobate with area of 25 mm^2 and thickness 0.5 mm with affected areas of gold coating removed (a) and recoated with silver paint (b). 3-21

Figure 3-11 Closer inspection of the affected areas on the gold electrode during removal of the nail polish applied after sputtering. 3-22

Figure 3-12 Optical micrograph of the gold electrode on a lithium niobate crystal with minor damage from cleaning the sample edge and areas of the gold electrode shrivelling due to heat. The damaged areas were repaired by silver paint. 3-22

Figure 3-13 Gold coating on the single crystals before and after re-application of silver paint. (a) and (b) are of the three thicknesses of lithium niobate before and after respectively. Similarly, (c) and (d) are of lithium tantalate. 3-23

Figure 3-14 Pyroelectric current response measured at temperatures from 10°C to 60°C on lithium niobate with thickness of 0.5 mm. 3-24

Figure 3-15 Mean pyroelectric coefficient of lithium niobate measured over a range of temperatures. Error bars represent a standard deviation over three repeated measurements. 3-25

Figure 3-16 Mean pyroelectric coefficient of lithium tantalate measured over a range of temperatures. Error bars represent a standard deviation over three repeated measurements. 3-26

Figure 3-17 Mean pyroelectric coefficient as a function of temperature of lead zirconate titanate (PIC151), prepared by pulse poling and high temperature field poling. Error bars represent a standard deviation over three repeated measurements. 3-27

Figure 3-18 Mean pyroelectric coefficient as a function of temperature of selected barium titanate single crystals with single domains. Error bars represent a standard deviation over three repeated measurements. 3-29

Figure 3-19 Mean pyroelectric coefficient as a function of temperature of the single crystals, PMN-33PT and PMN-28PT prepared in the [001] and [111] directions. Error bars represent a standard deviation over three repeated measurements. 3-30

Figure 3-20 Mean pyroelectric coefficient of various compositions as a function of temperature. Error bars represent a standard deviation over three repeated measurements. 3-31

Figure 3-21 Variation of ln(DC conductivity) with inverse temperature of $LiNbO_3$, $LiTaO_3$, PZT and PMN-30PT. 3-33

Figure 3-22 Charge density on the exposed surface of the crystal and the electric field attainable in the gap evaluated at a gap distance of 3.7 mm. 3-35

Figure 3-23 Figure-of-merit, F_ε, as a function of crystal thickness, calculated at a gap distance of 3.7 mm. 3-36

Figure 3-24 Figure-of-merit, F_ε, as a function of gap distance, evaluated with a crystal thickness of 2.0 mm. 3-37

Figure 3-25 Figure-of-merit, F_σ, as a function of crystal thickness, calculated at a gap distance of 3.7 mm. 3-38

Figure 3-26 Figure-of-merit, F_σ, as a function of gap distance, calculated with a crystal thickness of 2.0 mm. 3-38

Figure 4-1 Geometry of the X-ray generator model. 4-2

Figure 4-2 Electric field produced by $LiTaO_3$ with a negative surface charge density on its emitting surface, simulating the heating phase. The resultant field intensity is shown where the colour scale represents the magnitude and the vectors show the direction of electrons. The three views displayed are an orthographic 3D projection (a), cross-section of the X-axis (b) and top view of the top surface of the pyroelectric crystal (c). 4-7

Figure 4-3 Electric field produced by $LiTaO_3$ with a positive surface charge density on its emitting surface, simulating the cooling phase. The resultant field intensity is shown where the colour scale represents the magnitude and the vectors show the direction of the electrons. The three views displayed are an orthographic 3D projection (a), cross-section of the X-axis (b) and top view of the top surface of the pyroelectric crystal (c). 4-8

Figure 4-4 Series of electric field distributions produced from $LiTaO_3$ with thicknesses of 0.5 mm (a-c), 1.0 mm (d-f), 2.0 mm (g-i) (next page) and 5.0 mm (j-l) (next page). The threshold electric field applied to all distributions is 13.38×10^8 V/m. 4-10

Figure 4-5 Series of electric field distributions produced from $LiTaO_3$ with 0.5 mm (a-c) (previous page), 1.0 mm (d-f) (previous page), 2.0 mm (g-i) and 5.0 mm (j-l) thicknesses. The threshold electric field applied to all distributions is 13.38×10^8 V/m. 4-11

Figure 4-6 Histogram of the electric field distribution produced by $LiTaO_3$ of four different thicknesses, which are 0.5, 1.0, 2.0 and 5.0 mm. Histogram (a) is of the top crystal surface with histogram bin width is 1×10^8 V/m, and histogram (b) is of the target with histogram bin width of 0.5×10^8 V/m. 4-13

Figure 4-7 Histogram of the electric potential distribution produced by $LiTaO_3$ of four crystal thicknesses at the top crystal surface (top) and at the target (bottom). The bin widths for the top and bottom histograms are 10 kV and 0.1 kV, respectively. 4-14

Figure 4-8 The electric field covering the greatest surface area at the top crystal surface and target, obtained from their respective histograms in Figure 4-6. 4-15

Figure 4-9 Potential difference between the electrical potential mode at the top crystal surface of $LiTaO_3$ and the target, with increasing crystal thickness. 4-15

Figure 4-10 Electric field distributions produced by $LiNbO_3$ (a – c) and PMN-30PT (d – f). The top pair are orthographic 3D projections (a, d), the middle pair are cross-sections normal to the X-axis (b, e) and the bottom pair is a top view of the top crystal surface (c, f). The threshold electric field magnitude of $LiNbO_3$ and PMN-30PT are 5.75×10^8 V/m and 9.363×10^6 V/m, respectively. The electric field distributions produced by $LiTaO_3$ can be seen in Figure 4-5(g – i). 4-18

Figure 4-11 Combined histogram of the electric field distribution produced by $LiTaO_3$, $LiNbO_3$ and PMN-30PT. The thickness of the simulated crystals is 2.0 mm. The histogram bin width is 1×10^8 V/m. 4-19

Figure 4-12 Histogram of the electric field distribution produced by PMN-30PT at the top crystal surface. The histogram bin width is 1×10^6 V/m. 4-20

Figure 4-13 Electric field distributions produced by $LiTaO_3$ at gap distance of 3.7 mm (a – c, left vertical series), 5.0 mm (d – f, right vertical series) and 10.0 mm (g – i, next page). The crystal thickness is 2.0 mm. The top figures are orthographic 3D projections (a, d, g), the middle pair are cross-sections normal to the X-axis (b, e, h) and the bottom pair is a top view of the top crystal surface (c, f, i). The threshold electric field applied to all distributions are 11.5×10^8 V/m. 4-24

Figure 4-14 Electric field distributions produced by $LiTaO_3$ at gap distance of 3.7 mm (a – c, previous page), 5.0 mm (d – f, previous page) and 10.0 mm (g – i). The crystal thickness is 2.0 mm. The top figures are orthographic 3D projections (a, d, g), the middle pair are cross-sections normal to the X-axis (b, e, h) and the bottom pair is a top view of the top crystal surface (c, f, i). The threshold electric field applied to all distributions are 11.5×10^8 V/m. 4-25

Figure 4-15 Histogram of the electric field distributions at the top crystal surface (top) and the target (bottom) produced by $LiTaO_3$, when arranged at gap distances of 3.7, 5.0 and 10.0 mm. The bin width for the top and bottom histograms are 1×10^8 V/m and 0.5×10^8 V/m, respectively. 4-26

Figure 4-16 Histogram of the electric potential produced at the top crystal surface (top) and the target (bottom), arranged at three gap distances of 3.7, 5.0 and 10.0 mm. The bin widths for the top and bottom histogram are 1 kV and 200 V, respectively. 4-27

Figure 5-1 Components of the vacuum system. 5-3

Figure 5-2 Schematic diagram of the vacuum system and the experimental setup inside the vacuum chamber. 5-4

Figure 5-3 Electrical components of the temperature control system that sit outside the vacuum chamber. 5-6

Figure 5-4 Electrical circuit schematic of the temperature control system. 5-7

Figure 5-5 Total X-ray counts collected from the multi-channel analyser (MCA) and single-channel analyser (SCA). 5-10

Figure 5-6 Front view of the experimental setup. 5-11

Figure 5-7 Side view of the experimental setup. 5-12

Figure 5-8 Front view of the complete experimental apparatus that sits inside the vacuum chamber. 5-13

Figure 5-9 Top view of the experimental apparatus sitting inside the vacuum chamber, and the pyroelectric crystal and the metal target in line with the X-ray detector. 5-13

Figure 6-1 An X-ray spectrum of the X-rays produced from the pyroelectric X-ray generator. The collection time was over 1 h or 3 heating-cooling cycles. The inset shows characteristic X-ray emission lines predominantly from nickel and tantalum. The bremsstrahlung reaches to energies of approximately 55 keV. 6-4

Figure 6-2 X-ray spectrum collected during heating phase and fitted with elemental characteristic peaks. 6-5

Figure 6-3 X-ray spectrum collected during the cooling phase. 6-7

Figure 6-4 Recorded temperature, current density, time-resolved counts and energy-resolved spectrum (bottom) measured for 2 min. The X-ray counts detected per second follows the same profile as the temperature cycle where it increases as the temperature approaches 100°C and decreases upon cooling. 6-8

Figure 6-5 Fitting of the bremsstrahlung continuum in a normalised X-ray spectrum. 6-9

Figure 6-6 Two-minute interval time-resolved and energy-resolved measurements of the heating phase. The end-point energy of each measurement is indicated in the top right corner of the spectrum. 6-11

Figure 6-7 Two-minute interval time-resolved and energy-resolved measurements of the cooling phase, following from Figure 6-6. The end-point energy of each measurement is in the top right corner of the spectrum, unless left indeterminable. 6-12

Figure 6-8 Intrinsic efficiency over photon energy of the Amptek X-123 silicon drift detector with a 12.7 μm beryllium window and 500 μm silicon detector. 6-14

Figure 6-9 Comparison of the original energy spectrum collected from $LiTaO_3$ and its corrected version. 6-14

Figure 6-10 Comparison of the total X-ray counts and end-point energy produced by $LiTaO_3$ single crystal of two thicknesses, 0.5 mm and 2.0 mm, at a gap distance of 5.0 mm. Error bars represent a standard deviation over three repeated measurements. 6-17

Figure 6-11 Comparison of the energy spectra (a) and its normalisation (b) produced by $LiTaO_3$ of two crystal thickness at a pressure of 0.33 Pa and gap distance of 5.0 mm. 6-18

Figure 6-12 X-ray spectrum produced by $LiNbO_3$ crystal with a thickness of 2.0 mm. It was collected for 1 h at a gap distance of 3.7 mm and a pressure of 0.24 Pa. The inset shows a magnified view of characteristic peaks. 6-20

Figure 6-13 Spectrum of X-rays produced by PMN-30PT with a crystal thickness of 2.0 mm. It is collected at a gap distance of 3.7 mm and pressure of 0.24 Pa. 6-21

Figure 6-14 Comparison of the total X-ray counts and end-point energies produced over a range of pressures and collected from three different compositions at a gap distance of 3.7 mm. The end-point energy of PMN-30PT is not included. Error bars represent a standard deviation over three to four repeated measurements. 6-24

Figure 6-15 Total X-ray counts and end-point energy as a function of pressure measured at three different gap distances from $LiTaO_3$ with a thickness of 2.0 mm. Error bars represent a standard deviation over three repeated measurements. 6-27

Figure 6-16 Total X-ray counts and end-point energy as a function of pressure measured at three different gap distances from $LiNbO_3$ with a thickness of 2.0 mm. Error bars represent a standard deviation over three to four repeated measurements. 6-28

Figure 6-17 Total X-ray counts as a function of pressure measured at two gap distances from PMN-30PT with a thickness of 2.0 mm. Error bars represent a standard deviation over three repeated measurements. 6-29

Figure 6-18 A sharp change in the current density is quickly followed by a sudden halt in X-ray production. The X-ray generator system will then need to rebuild enough charges to continue producing X-rays. 6-30

Figure 6-19 A typical Paschen curve of air showing the breakdown voltage between two parallel electrodes as a function of the product of pressure, p, and distance between the electrodes, d. Image reproduced from [213]..... 6-31

Figure 6-20 Spectra (top) collected from $LiTaO_3$ over five pressures at a gap distance of 5.0 mm. The bottom plot is of the same spectra normalised to each spectrum's total X-ray counts..... 6-33

Figure 6-21 Count rate and temperature measured from $LiTaO_3$ at pressure of <5.32 mPa and gap distance of 5.0 mm. It corresponds to the black energy spectrum in Figure 6-20..... 6-34

Figure 6-22 Total X-ray counts and end-point energy produced by $LiTaO_3$ at all combinations of gap distance and pressure with the least electrical breakdowns, compared to the figure-of-merit, F_e. The crystal thickness is 2.0 mm. 6-36

Figure 6-23 Total X-ray counts and end-point energy produced by $LiNbO_3$ at all combinations of gap distance and pressure with the least electrical breakdowns, compared to the figure-of-merit, F_e. The crystal thickness is 2.0 mm. 6-38

Figure 6-24 Total X-ray counts and end-point energy produced by $LiTaO_3$, with a crystal thickness of 0.5 mm, at all combinations of gap distance and pressure with the least electrical breakdowns, compared to the figure-of-merit, F_e. 6-39

Figure 6-25 Three repeated measurements of time-resolved counts generated from $LiTaO_3$ (2.0 mm thickness) at gap distance of 3.7 mm and pressure of 0.33 Pa. The dotted lines separate the heating (H) and cooling (C) phases. 6-40

Figure 7-1 Process of sample preparation: (a) Sample is mounted and encapsulated with silicone potting compound, (b) Result of cured silicone surrounding the sample, (c) Cured silicone is cut to width of approximately 2.0 mm around the edge of the crystal, (d) Silver paint is applied only on the +Z polar face of the crystal. 7-3

Figure 7-2 Before (a) and after (b) cleaning silicone on $LiTaO_3$ polar surfaces..... 7-3

Figure 7-3 Spectra collected from the measurement variations with and without silicone insulation, and with and without a metal target. The bottom figure plots the spectra normalised to each spectrum's total X-ray counts..... 7-5

Figure 7-4 Analogy of the electric field created by the pyroelectric crystal alike to magnetic field lines between two unlike poles and around individual bar magnets. 7-7

Figure 7-5 Spectral fitting of X-rays produced from a non-insulated $LiTaO_3$ crystal with a nickel target, normalised to the total X-ray counts. 7-10

Figure 7-6 Spectral fitting of X-rays produced from $LiTaO_3$ with silicone insulation around the crystal edge faces and a nickel target, normalised to the total X-ray counts. 7-10

Figure 7-7 Spectral fitting of X-rays produced from $LiTaO_3$ with no insulation and no target. 7-11

Figure 7-8 Spectral fitting of X-rays produced from $LiTaO_3$ with silicone insulation around the crystal edge faces and no target. 7-11

Figure 7-9 Geometry of the pyroelectric crystal with insulation around its edge faces. 7-12

Figure 7-10 X-ray generator model using a non-insulated crystal with the beryllium window of the spectrometer replacing the metal target. 7-13

Figure 7-11 X-ray generator model with insulated crystal and beryllium window. ... 7-14

Figure 7-12 Comparison of the electric field distribution of a non-insulated crystal (left vertical series) and silicone insulated crystal (right vertical series) during the heating phase. The vectors represent electrons, which are travelling towards the target. The bottom pair is a top view of the top crystal surface (c, f). The threshold electric field of the non-insulated and insulated crystals are 11.5×10^8 V/m and 12.7×10^7 V/m, respectively. 7-16

Figure 7-13 Comparison of the electric field distribution of a non-insulated crystal (left vertical series) and silicone insulated crystal (right vertical series) during the cooling phase. The vectors represent electrons, which are travelling towards the top crystal surface. The bottom pair is a top view of the top crystal surface (c, f). The threshold electric field of the non-insulated and insulated crystals are 14.0×10^7 V/m and 12.7×10^7 V/m, respectively. 7-17

Figure 7-14 Histograms of the electric field produced by non-insulated (top) and insulated (bottom) crystals at the top crystal surface. Their bin widths are 0.5×10^8 V/m and 1×10^7 V/m, respectively. 7-18

Figure 7-15 Comparison of the electric field distribution of a non-insulated crystal (left vertical series) and silicone insulated crystal (right vertical series) with no metal target. The beryllium detector window is replaced instead. The bottom pair is a top view of the top crystal surface (c, f). The threshold electric field of both models is 10.8×10^7 V/m. 7-20

Figure 7-16 Blended micrographs of the diced $LiTaO_3$. Damage occurred during the machining and cleaning process where a pillar and a half was broken off. 7-23

Figure 7-17 Blended micrograph of a side view of the diced $LiTaO_3$ crystal with a kerf depth of approximately 0.13 mm. 7-23

Figure 7-18 Total X-ray counts produced by the diced $LiTaO_3$ crystal presented as a function of pressure over a range of gap distances. Error bars represent a standard deviation over three repeated measurements. 7-25

Figure 7-19 A comparison of the total X-ray counts and end-point energies produced by the original and diced $LiTaO_3$ crystal. Error bars represent a standard deviation over three repeated measurements. 7-26

Figure 7-20 Spectra from the original non-diced crystal and the diced crystal, collected at pressure of 0.33 Pa and gap distance of 10.0 mm. The bottom figure plots the spectra normalised to each spectrum's total X-ray counts..... 7-27

Figure 7-21 Geometry of the model of the diced pyroelectric crystal. 7-29

Figure 7-22 Electric field distribution of the top crystal surface with varying number of kerfs and kerf widths. The top and bottom horizontal series show kerf widths of 50 μm and 100 μm, respectively. The figure continues onto Figure 7-23. 7-34

Figure 7-23 Electric field distribution of the top crystal surface with the number of kerfs and kerf width parameterised. This figure is a continuation from Figure 7-22. The top and bottom horizontal series show kerf widths of 150 μm and 200 μm, respectively. 7-35

Figure 7-24 Histogram of the electric field distribution at the top crystal surface. (a) correlates to Figure 7-22 (a – e) series and (b) correlates to Figure 7-22 (f– j) series. 7-36

Figure 7-25 Histogram of the electric field distribution produced at the top crystal surface. (c) correlates to Figure 7-23 (k – o) series and (d) correlates to Figure 7-23 (p – t) series..... 7-37

Figure 8-1 Total X-ray counts and end-point energy collected for each individual hourly experimental run indicated by the marker. The dotted lines represent the break between each fatigue measurement. 8-5

Figure 8-2 Energy spectra of the experimental run corresponding to the highest (A-4) and lowest (C-16) total X-ray counts. 8-6

Figure 8-3 Counts produced per minute over one 24 h measurement. It correlates to the third measurement labelled C in Figure 8-1. The dotted vertical lines represent the break between each hourly X-ray spectrum acquisition. The thermal cycle always starts with a heating phase and each hourly measurement goes through three thermal cycles. 8-8

Figure 8-4 Optical micrographs of the electron emitting crystal surface collected after each fatigue measurement. Each labelled image correlates to Figure 8-1 and is a blend of smaller micrograph sections. 8-10

Figure 8-5 Degradation marks on the -Z surface of the crystal. 8-11

Figure 8-6 Degradation marks on the -Z surface of the crystal with fern-like lines. 8-11

Figure 8-7 Degradation marks on the -Z surface of the crystal with dark defect spots around the degradation lines. 8-12

Figure 8-8 Crack propagating from a chipped corner and travelling at an angle through the thickness of the crystal. 8-12

Figure 8-9 Spherical projection of points normal to crystal faces. Reproduced with permission by John Wiley and Sons from [224]. 8-14

Figure 8-10 Stereographic projection of hkl planes for a cubic crystal perpendicular to the (111) face with the $<\bar{1}10>$ family of planes highlighted. Reproduced with permission by Springer Nature from [225]. 8-14

Figure 8-11 CLS micrograph of a fresh $LiTaO_3$ crystal. 8-16

Figure 8-12 CLS micrograph A with two lined profiles. 8-16

Figure 8-13 Profile measurement corresponding to Profile 1 drawn in red in Figure 8-12. The blue cross is the deepest part from the surface (dotted line). 8-17

Figure 8-14 Profile measurement corresponding to Profile 2 drawn in magenta in Figure 8-12. The left green cross lies over the stem of the tracking. The green cross on the right lies on the deepest part of the profile from the surface (dotted line). 8-17

Figure 8-15 CLS micrograph B taken in the same area as Figure 8-7. 8-18

Figure 8-16 Profile measurement of Profile 1 in CLS micrograph B. The yellow cross is the deepest part of the feature from the surface (dotted line). 8-18

Figure 8-17 CLS micrograph C with a profile line crossing the deepest section of the crater. 8-19

Figure 8-18 Profile measurement corresponding to micrograph C. 8-19

Figure 8-19 $LiTaO_3$ crystal taken with a mobile phone camera at the conclusion of the fatigue measurements. 8-20

List of Tables

Table 2-1 Summary of the X-ray generator parameters and output from the most optimum configuration. The geometry is assumed to be single-crystal configuration unless otherwise stated in the *Additional Variation* column. Empty cells represent unprovided information. 2-30

Table 3-1 Properties of pyroelectric materials that contribute to the electron emission via pyroelectricity. The bulk conductivity and activation energy were measured at or near room temperature. The missing values represent the material property has not been studied. 3-11

Table 3-2 Dimensions and orientation of samples obtained for measurements. ... 3-14

Table 3-3 Capacitance and relative permittivity of barium titanate samples. 3-28

Table 3-4 Resistivity of macor measured at two temperatures and compared to literature values. 3-33

Table 3-5 Activation energy and conductivity of measured samples evaluated from the Arrhenius relationship between conductivity and temperature. 3-34

Table 3-6 Pyroelectric coefficient and DC conductivity of the samples taken as an average of the temperatures the materials. 3-34

Table 4-1 Variable parameters of the simple simulation model. 4-2

Table 4-2 Material properties of the modelled crystal compositions 4-3

Table 4-3 The minimum and maximum electric field on the top crystal surface and target, and potential difference across the gap obtained from the two crystal thicknesses. The potential difference is taken as the difference in the mode electric potential at the top crystal surface and the target. The gap distance is 3.7 mm. 4-16

Table 4-4 The minimum and maximum electric field at the top crystal surface, and potential difference across the gap achieved by the three crystal compositions with a crystal thickness of 2.0 mm and gap distance of 3.7 mm. The corresponding figures-of-merit from Chapter 3 are also included. 4-22

Table 4-5 The minimum and maximum electric field at the top crystal surface and potential difference across the gap. The corresponding figures-of-merit determined in Chapter 3 are included. The potential difference is taken as the difference in the mode electric potential at the top crystal surface and the target from Figure 4-16. 4-28

Table 6-1 Crystal compositions and their dimensions and orientations tested. 6-3

Table 6-2 The values of the parameters tested for each crystal. 6-3

Table 6-3 Summary of the total X-ray counts, count rate and end-point energy produced by $LiTaO_3$ of two crystal thicknesses at varying pressures and gap distance fixed at 5.0 mm. The figures-of-merit from Chapter 3, as well as the max electric field at the crystal surface, E_{max}, and potential difference, ΔV, from Chapter 4 are included. 6-19

Table 6-4 Summary of the total X-ray counts, count rate and end-point energy produced by each crystal composition at different pressures and gap distance of 3.7 mm. The corresponding figures-of-merit from Chapter 3, as well as the max electric field, E_{max}, at the top crystal surface and potential difference, ΔV, from Chapter 4 are included. 6-25

Table 6-5 A complete summary of the total X-ray counts, count rate, end-point energy and average number of electric breakdowns, N_B, over three repeated measurements produced from all measured configurations. The figures-of-merit from Chapter 3, and the max electric field at the top crystal surface, E_{max}, and potential difference, ΔV, from Chapter 4 are included. L_{gap} refers to gap distance. This table spans over two pages and is to be read portrait-wise. 6-42

Table 7-1 Total X-ray counts, count rate and end-point energy produced from each configuration, with and without silicone and target. 7-6

Table 7-2 The minimum and maximum electric field produced at the top crystal surface, and the target or detector window depending on the model. The count rate and end-point energy collected from the corresponding measurements are included. 7-21

Table 7-3 Summary of the X-ray generator output from the diced crystal, including the average number of electrical breakdowns over three repeated measurements. 7-28

Table 7-4 Variable parameters of the diced crystal simulation model. 7-29

1

INTRODUCTION

"Replace the fear of the unknown with curiosity."

– *Penelope Ward*

Since the discovery of X-rays by Wilhelm Röntgen in 1895, X-rays have become a ubiquitous and powerful analytical tool in all fields of science. Apart from their notable use in imaging, X-rays are also used for material analysis techniques such as X-ray fluorescence and X-ray diffraction. These techniques brought about new ways to analyse matter and phenomena, leading to achievements such as the deduction of the structure of DNA to quantitative elemental analysis of planetary surfaces in space exploration. Portable X-ray instruments allow for better monitoring, improved cost-efficiency and smaller footprint for real-time in-field and on-line analysis [1-3]. This has led to the transition away from laboratory-based measurements for a wide range of fields that includes but not limited to environmental sampling, mineral processing, archaeological exploration. [4-8].

Currently there exists three widely used types of X-ray generator: The X-ray tube, synchrotron and linear accelerator. Each type has its own advantages and limitations, and each find use in particular applications. In order to generate X-rays, they require high-energy electrons. For X-ray tubes, this is achieved by applying a high voltage across the tube using an external power supply. Synchrotrons and linear accelerators can produce even greater energies by accelerating charged particles at high speeds over long distances using varying electric fields. However, as technology continues to evolve, there is a greater interest in creating X-ray generators that have a small construction, consume less power and are portable for in-field and on-line analysis [9, 10]. Unfortunately, the size, weight, cost and power requirements of conventional X-ray generators have limited further technology advancements. Therefore, new methods that meet the same capabilities as conventional X-ray generators at a much smaller scale are being explored.

Functional materials that possess pyroelectricity have received attention as a potential candidate to generate X-rays. Pyroelectricity is an effect whereby an applied differential temperature induces an accumulation of charge on the material's polar surfaces. When placed in an electric circuit, a flowing current can be observed in response to the changing temperature. There are a range of materials that are pyroelectric such as single crystals, oxide ceramics and polymers. They have long been used in an array of applications such as infrared detectors, motion detectors and pollution monitoring. Since they are solid-state materials, they also do not pose the same risks as radioisotopes.

Another advantage of using pyroelectric materials in an X-ray generator is its ability to play two roles. The pyroelectric material can create an electric field between the material and the target and produce electrons via ferroelectric electron emission and field ionisation. Since such an intense electric field is developed, an external high-voltage power supply is not required to accelerate the electrons towards the target and produce X-rays. Instead, voltage is only necessary to operate the heating-cooling component, which tends to be below 10 V. This makes utilising the pyroelectric effect a promising technique to downsize conventional X-ray sources, where it has been demonstrated for X-ray fluorescence analysis [11-13].

Although there is one X-ray generator that uses the pyroelectric effect available in the commercial market, it has several limiting features [14]. The generation of X-rays relies on heating and cooling the pyroelectric material, and so, its X-ray output is not constant and follows the thermal cycle. Majority of the studies on developing this type of X-ray generator have tended to concentrate on improving its performance. That is, to increase the X-ray counts and energy, and producing X-rays in a more uniform and reproducible manner. The original configuration uses a single pyroelectric material and has since expanded to utilising additional pyroelectric materials or combining with other low work function materials. This will be discussed in more detail in the following chapter. Despite these iterations, the understanding behind the X-ray generation phenomenon still remains ambiguous. Several investigations have been undertaken to clarify the physical mechanism of electron emission and X-ray generation involved with using pyroelectric materials. However, there exists two main explanations of the mechanism; one being ferroelectric electron emission and the other field ionisation [15, 16]. While the basic working principle is widely accepted, there are contradicting discussions amongst literature based on these two possible mechanisms [17, 18]. This may be because two different X-ray energy spectra are produced during the thermal cycle and depends on how the pyroelectric material is arranged in the generator configuration [19]. Thus, a thorough understanding must be solidified before further improvements can be made.

As mentioned earlier, several variations of the X-ray generator have been reported. These variations include applying different combinations of system parameters, such as the pressure of the vacuum chamber and gap distance between the pyroelectric material and target. This has also led to a variation of results, with some studies noting a lack of reproducibility [20]. On the contrary, there is little variation in the pyroelectric material used in the X-ray generator, mainly being lithium tantalate and lithium niobate. Since pyroelectric materials are thermally stimulated, its material properties such as the pyroelectric coefficient and spontaneous polarisation also changes with temperature. It is a dynamic process that has not been well explored in terms of its contribution to the application. Therefore, potential pyroelectric materials should be characterised in accordance with the functioning of the X-ray generator. This should then be integrated with characterisation of the system as a means to consolidate a comprehensive

understanding of the X-ray generation phenomenon. Thereafter, different approaches can be tested to improve the X-ray output.

As a prospective device to expand X-ray analytical technologies, an investigation that is lacking in literature is the X-ray generator's performance under extended usage. There is known for there to only be one study that reported the X-ray output over repeated cycles [21]. However, there is no mention if each measurement is immediately continuing from the previous cycle or if the system is allowed to relax between measurements. Additionally, it has been mentioned previously in some studies that the X-ray output is not consistent. Not only is it important to know the lifetime of the X-ray generator system but investigating the behaviour of the system under intense prolonged use may give insight into the cause of this inconsistency and irreproducibility.

The development of an X-ray generator by applying the pyroelectric effect and reinforcement of the mechanisms involved in this device will consist of several objectives, which are as follows:

1. Characterisation of pyroelectric materials by measuring its material properties as a function of temperature
2. Construction of the X-ray generator experimental apparatus
3. Analysis of the X-ray output produced during the heating and cooling phases of the thermal cycle as a function of energy and time
4. Characterisation and optimisation of the X-ray generator by exploring the effects of various system parameters, including testing different pyroelectric materials
5. Simulation of the X-ray generator using finite element modelling to determine the electric field intensity and distribution produced by the pyroelectric material
6. Demonstration of an approach to improve the X-ray generator performance
7. Investigation of the fatigue behaviour of the X-ray generator

This thesis will then conclude with a summary of the critical results found from the above objectives and provide a recommendation of the future work that can be undertaken to improve the performance and function of the X-ray generator.

2

LITERATURE REVIEW

"You don't have to see the whole staircase. Just take the first step."

- *Martin Luther King Jr.*

2.1 Overview

This chapter consists of three parts to introduce the reader to the field of X-ray generation and ferroelectricity. The first part presents the science and technology behind X-ray generation, as well as some fundamentals on ferroelectric materials to understand the experiments and discussions in the follow chapters. The second part explores new methods of X-ray generation, with the focus mainly on employing ferroelectric materials. Finally, the chapter will close with a review on previous studies to understand the different approaches that have been undertaken and some of the key observations made.

2.2 X-ray Generation Technologies

2.2.1 X-ray production

X-rays are a form of electromagnetic radiation produced from the conversion of the kinetic energy of fast-moving electrons due to their collision with the atomic structure of the target material. There are two main types of radiation produced from this interaction being bremsstrahlung and characteristic X-rays. When fast incoming electrons collide with the material, not all its kinetic energy is completely converted. Depending on the vicinity of the interaction, X-rays with a continuum of energies are produced, which is the bremsstrahlung. Going from Event 1 to 3 in Figure 2-1, as the interaction between the incoming electron nears the nucleus of the atom, the X-ray energy released increases.

Characteristic X-rays comes from incoming electrons knocking out an orbital electron, as illustrated in Event 4 in Figure 2-1. This excitation event causes the atom to be unstable and an electron from the higher electron shell must transition to fill the vacancy. Since the binding energies of electron shells decreases the further away from the nucleus they are, transitioning from say the L-shell to K-shell will result in the emission of the extra energy. This is the emission of characteristic X-ray with discrete energy.

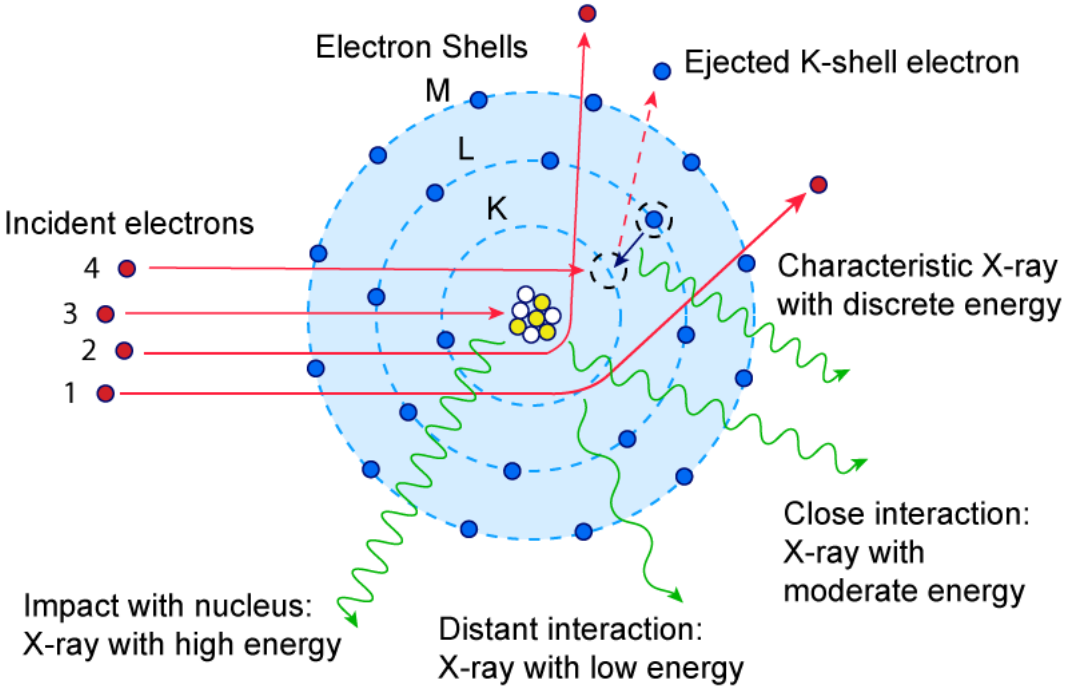

Figure 2-1 Production of different X-rays from the collision of electrons with the atomic structure. Adapted with permission by the Society of Nuclear Medicine and Molecular Imaging from [22].

The resulting energy spectrum of the emitted X-rays is a superimposition of the bremsstrahlung continuum and characteristic emission lines. The unfiltered bremsstrahlung would look like the black line in Figure 2-2. To ensure the X-rays emitted are not dominated by low-energy photons, they are filtered or preferentially removed through the use of absorbers. Low energy X-rays attenuate easily when they travel through atoms of a material and reduces their intensity. So, the process of producing X-rays at the target material would also filter out the low energy X-rays, as depicted in the difference between the black and red line of Figure 2-2.

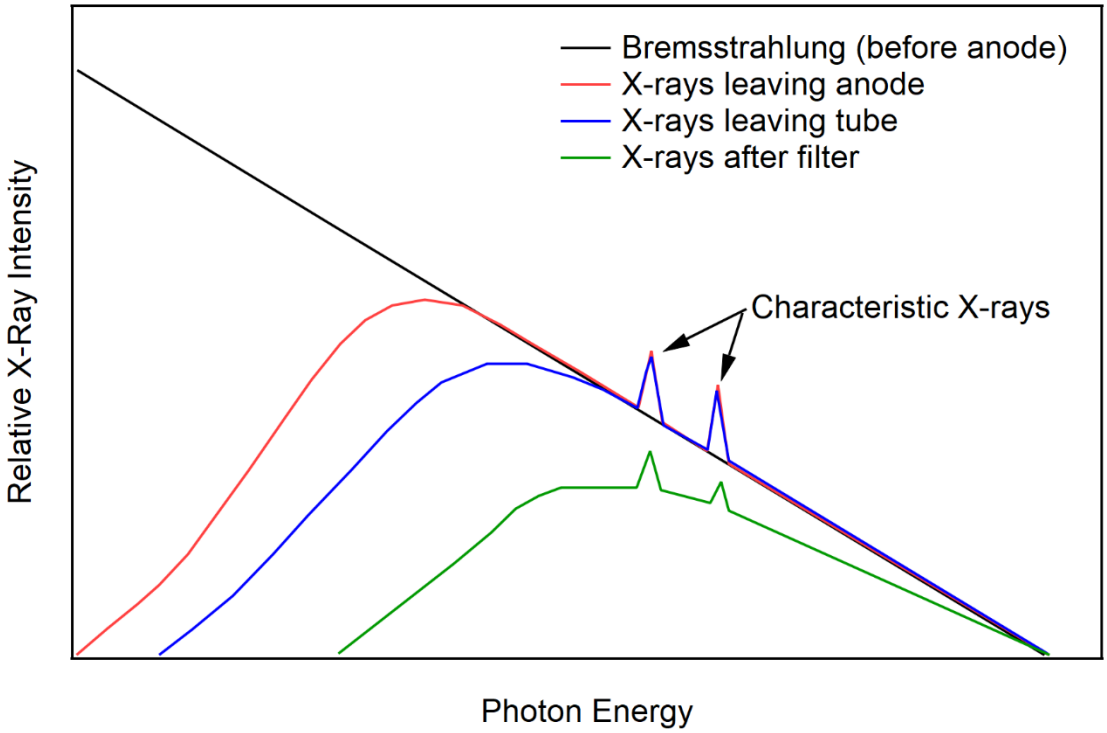

Figure 2-2 Example of X-ray energy spectra consisting of bremsstrahlung and characteristic X-rays being filtered at different sections within and outside a conventional X-ray tube. The X-ray spectrum after leaving the tube is reduced due to inherent filtration from glass window and housing. Reproduced with permission by John Wiley and Sons from [23].

2.2.2 Conventional X-ray generation

Now it is known that electrons with high energy are key to generating X-rays, the technologies available to produce the X-rays will be briefly introduced. Perhaps the most common technology is the X-ray tube. Electrons are produced via thermionic emission and are accelerated to higher energies through the application of a high voltage. Since the early days of the Coolidge tube, as it was known, the design of current X-ray tubes has changed to accommodate higher voltages and tube current, as well as include safety features. A palm-sized compact X-ray tube such as MOXTEK Inc.'s MAGPRO™ can produce X-ray energies up to 70 keV [24]. Generating X-rays to even greater energies can be achieved by accelerating the electrons in higher electromagnetic fields and for longer distances. Examples of this technique are synchrotrons and linear accelerators where photon energies can reach the giga- and mega-electron volts range, respectively [25-27]. While synchrotrons and linear accelerators have allowed more complex experiments, their dimensions are very large and does not allow for in-field or on-line analyses. In these

technologies, they contain the same fundamental components of an electron source and a target in an evacuated envelope or containment, and a high-voltage power source.

The energy and intensity of the X-ray output are also limited by the material used as the target. Generating X-rays by accelerating electrons at a metal target is an inherently inefficient process, with 1% of the kinetic energy of the incident electrons is converted to X-rays [28, 29]. The remaining 99% is lost as heat at the target. Heat is an issue as it can melt the target material at the region of electron impact from the high-power electron beam. The material selected as the target must therefore not only have a high atomic number to maximise the X-ray energy and intensity output but also have a high melting point, thermal conductivity and thermal diffusivity to dissipate heat away quickly. In addition to the optimised material selection, there are two widely used X-ray tube designs to further dissipate heat away, which are the stationary anode and rotating anode [28, 30-32].

Depending on the application, the focal spot size and power (product of the high voltage and tube current) of the X-ray beam are important characteristics. Heat will not only reduce X-ray emission but cause blurring of the focal spot. On the other hand, restricting the spot size also limits the power of the X-ray beam. With the demand for higher power X-ray tubes with smaller defined spot sizes, applications have opted for liquid-metal jet X-ray tubes that is still costly [29, 33-35].

2.2.3 X-ray tubes

Taking a closer look at hot-cathode X-ray tubes, the electron source is a cathode and the target is an anode, as indicated in Figure 2-3. It uses two voltages for different purposes. A voltage of about 10 V is driven into the cathodic filament to release electrons via thermionic emission [28]. This process is where the filament is heated up and when supplied with sufficient thermal energy, electrons are expelled from its surface. A higher voltage, typically in kilovolts, is applied across the tube to drive the emitted electrons to higher energies as they approach the anode [28, 32].

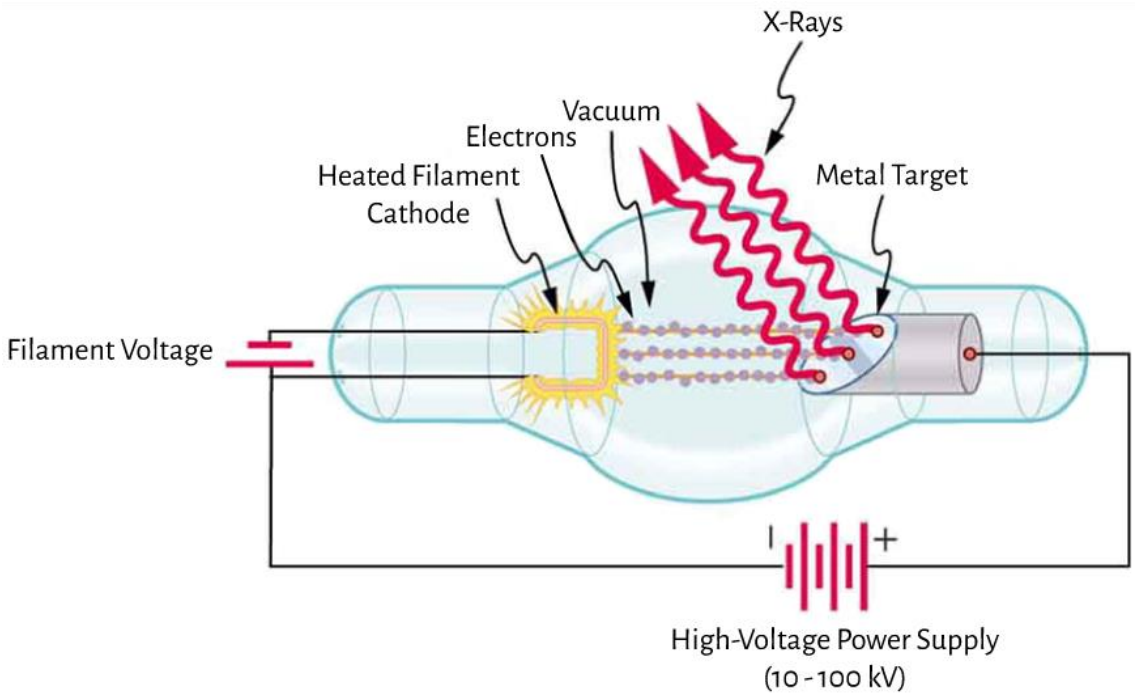

Figure 2-3 Schematic diagram of a conventional X-ray tube. Adapted with permission by Openstax under the Creative Commons Attribution Licence 4.0 (CC BY) from [36].

There are several factors that determine the output and functionality of the X-ray tube. Two of these that control the X-ray energy and intensity are the high voltage and the current applied across the tube. The intensity is dependent on the high voltage and tube current, as exemplified in Figure 2-4. However, when the high voltage increases so does the end-point energy, or maximum energy.

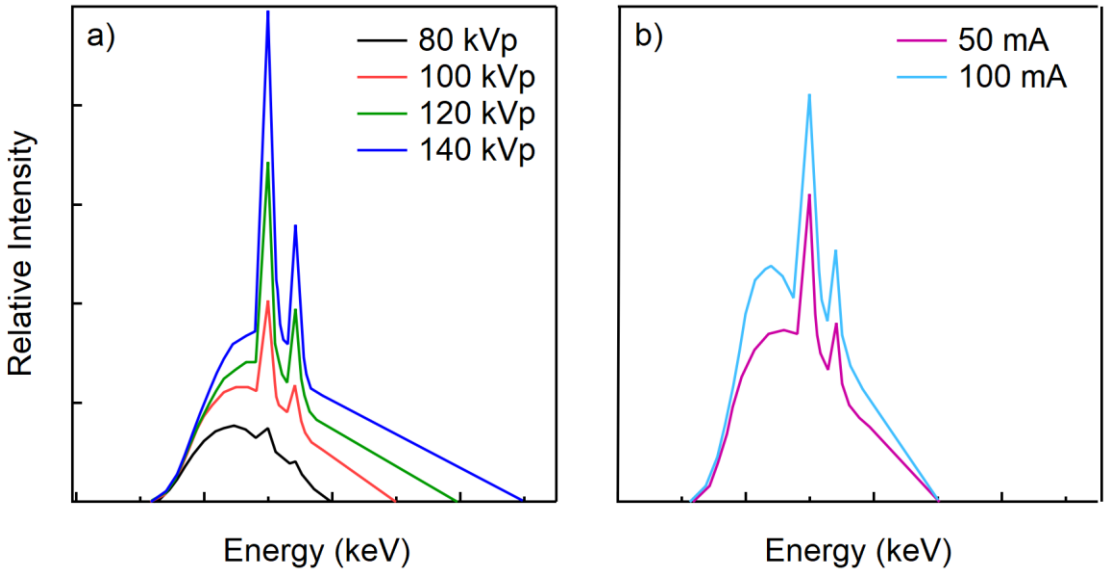

Figure 2-4 Effect of peak voltage (kVp) and tube current (mA) on the output of an X-ray tube with a tungsten target. The tube current is fixed in (a) and the applied voltage is fixed in (b). A filter is assumed to be added.

The miniaturisation of the X-ray sources has also been of high interest for portable and remote diagnosis and analysis in the fields such as health, security, environmental and space exploration. With these in mind, it is desirable for the next X-ray generators to have a small footprint but also meet and exceed existing conventional X-ray generators.

2.2.4 Photoelectric probability

For fluorescence emission or characteristic X-ray emission to occur, the incident photon energy must exceed the electron shell binding energy. This emission is a probability event dictated by the photoelectric effect. All elements and compositions have an atomic cross section and corresponding mass attenuation coefficient that exhibits a sawtooth-like decay with increasing incident photon energy, as illustrated in Figure 2-5. The sharp discontinuities in the mass attenuation coefficient are known as absorption edges and relate to each electron shell as indicated in the figure. For photon energies just above the absorption edge, the probability of fluorescence emission assumes its greatest value. However, at the absorption edges, it is unlikely to occur unless the photon energy is much greater than the absorption edge energy. This can affect the X-ray fluorescence yield because a variation in the average energy of the incoming electrons can result in inconsistent quantitative analysis between measurements.

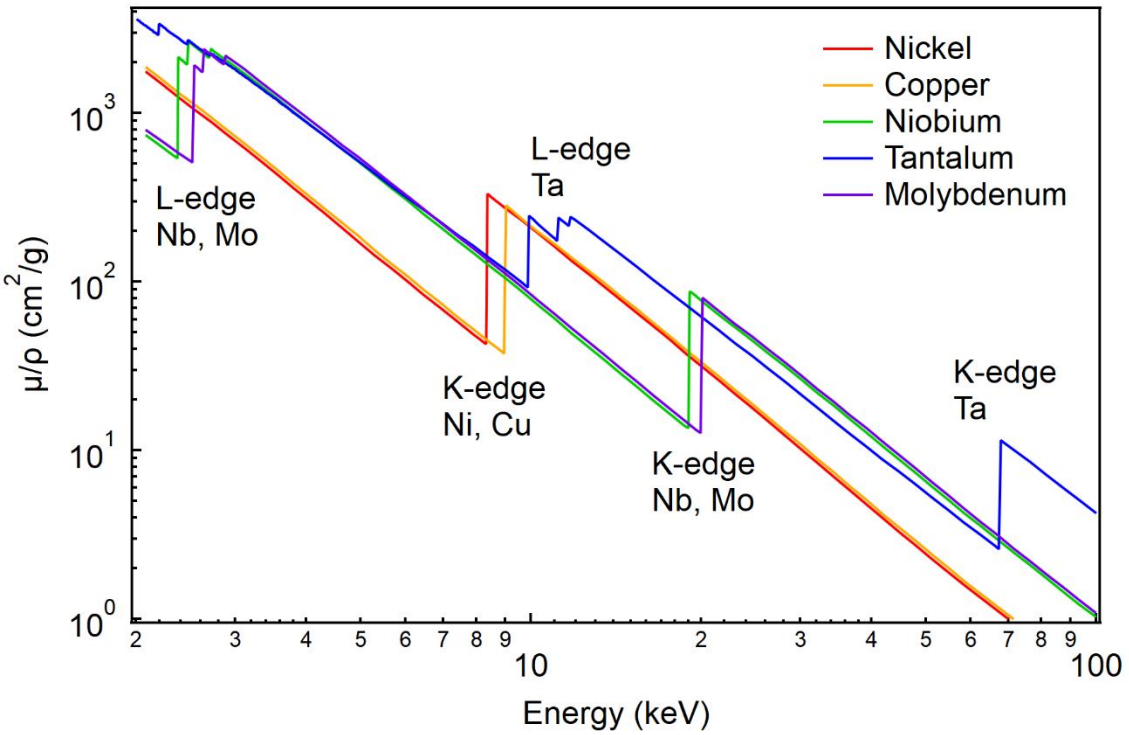

Figure 2-5 Mass attenuation coefficient (μ/ϱ) as a function of incident photon energy. Data taken from [37-39].

2.3 Ferroelectric Materials

2.3.1 Classes of dielectric materials

Dielectric materials can be thought of as analogous to capacitors, "electrical insulators" that have the ability to hold electrical charge under an applied voltage. When an electric field is applied to dielectric materials, there is a displacement of positive and negative charges from their equilibrium positions creating a net dipole moment. The dielectric material is said to be polarised [40, 41]. This dipole moment can be measured as the bound charges apparent on material's surface.

In certain dielectrics, a change in polarisation can be achieved by stressing the material. This is the direct piezoelectric effect. Conversely, applying an electric field can cause the material to strain, where its dimensions change. Of the 32 crystal classes that exist for crystalline materials, 21 of them are considered piezoelectric due to their non-centrosymmetry [42]. A subset of piezoelectric materials are pyroelectric materials that make up 10 crystal classes. These materials already possess an internal dipole moment and exhibit a spontaneous polarisation [40, 43]. Upon a thermal change, the magnitude of the polarisation will change. Within the 10 crystal classes that are pyroelectric is a smaller subset known as ferroelectric materials. Like pyroelectric materials, ferroelectric materials already have a spontaneous polarisation, but its direction can be reversed upon application of an external electric field.

Since ferroelectric materials belong to the smallest subset, it means that all ferroelectric materials also possess the properties of piezoelectricity and pyroelectricity. Therefore, ferroelectric materials become a versatile material in many practical applications because they can harness the direct and converse piezoelectric effect, as well as the pyroelectric effect. Some of the applications that ferroelectric materials have been utilised in are capacitors, transducers, non-volatile memory and infra-red detectors.

2.3.2 Crystal structure

A common structure that ferroelectric materials possess is the perovskite structure. This oxygen-octahedral structure can be portrayed as a cubic unit cell, as illustrated in Figure 2-6. The general formula of a perovskite is ABO_3. So, if a composition is $BaTiO_3$, the barium atoms would lie on the corners of the cube and the titanium atom would lie in the centre of the unit cell.

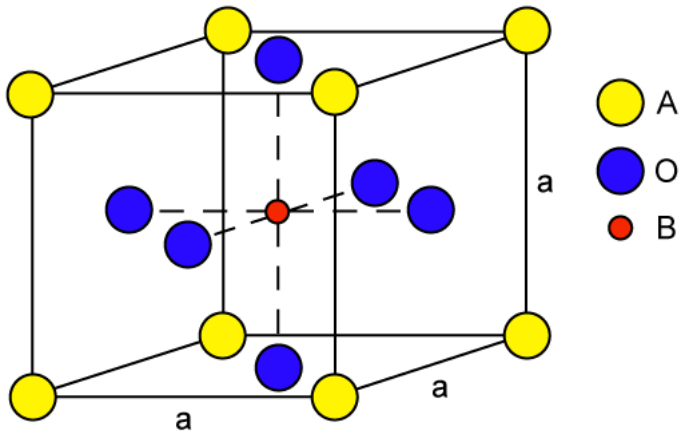

Figure 2-6 Perovskite structure ABO_3 as a cubic unit cell.

A material becomes polarised or acquires a spontaneous polarisation when the A and B ions are displaced relative to the oxygen ions from their cubic positions, leading to a net dipole moment. This is exemplified in Figure 2-7. If the material is cut along the planes perpendicular to the direction of polarisation, polar charges will be apparent on these surfaces. They are otherwise known as polar surfaces. This displacement will also cause a distortion of the unit cell from its original dimensions. It is this non-centrosymmetry that gives rise to piezoelectricity, pyroelectricity and ferroelectricity.

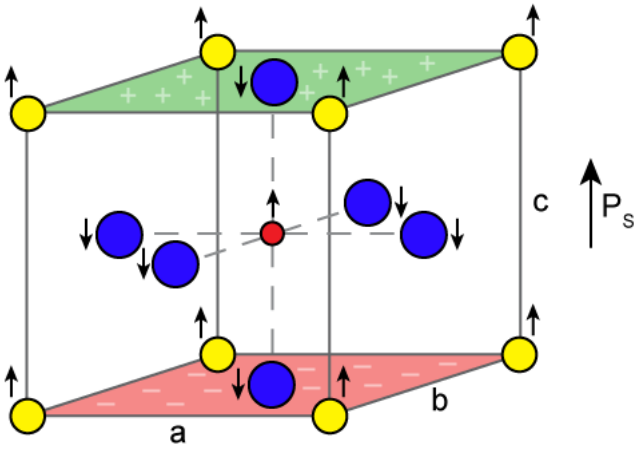

Figure 2-7 Surface charges become apparent when the A and B ions are displaced relative to the oxygen ions, creating a spontaneous polarisation, P_S. The green coloured plane indicates a positively charged surface while the red coloured plane indicates a negatively charged surface.

Ferroelectric materials can take different polymorphic forms of the perovskite structure depending on the temperature and chemistry of the ferroelectric material. These forms are based on the seven basic crystal systems but only five of them will be explored here. The cubic phase has already been introduced and it is usually paraelectric and non-polar. Its lattice parameters a, b and c are also equal to each other. Three of the other unit cell structures are shown in Figure 2-8. The possible directions of the polar axis, or spontaneous polarisation, are indicated in the angle brackets and are equivalent to the directions of the cubic phase. They can sometimes be described as the pseudo-cubic directions.

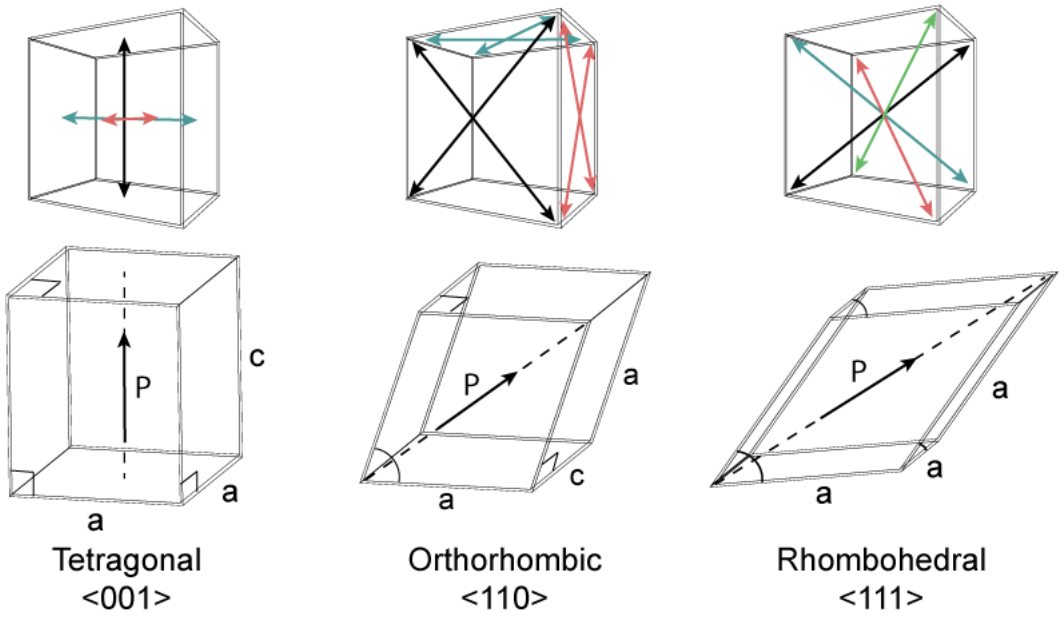

Figure 2-8 Three structures of unit cell. The top row represents the possible directions the polar axis can take while the bottom row illustrates the distortion of the unit cell in the direction of the black arrow.

The fifth unit cell is the hexagonal structure which the rhombohedral structure shares under the trigonal crystal system. Looking at Figure 2-9, the rhombohedral unit cell can be described within a hexagonal lattice or a cubic lattice, both with orthogonal (x, y, z) axes. Therefore, if the polar axis of the rhombohedral phase has a pseudo-cubic [111] direction, the equivalent direction of the polar axis in the hexagonal lattice is [001].

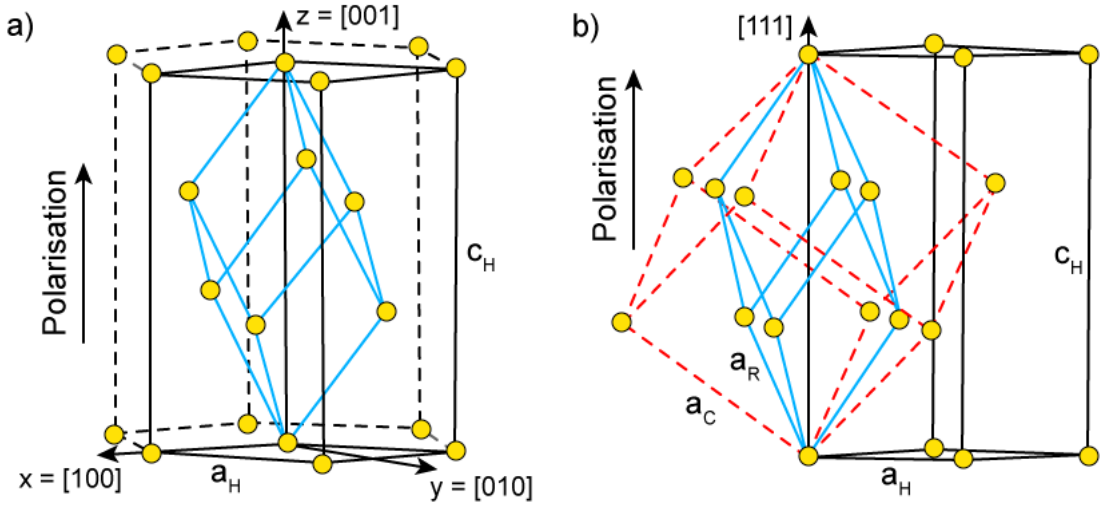

Figure 2-9 Relationship between the rhombohedral (blue solid line), hexagonal (black solid and dotted lines) and cubic unit cells (red dotted line). (a) shows the rhombohedral lattice inside the hexagonal lattice while (b) includes the cubic lattice with the same solid black lattice section of (a). Reproduced and adapted with permission by the University of Oklahoma and Elsevier from [44-46].

The temperature dependence of the phases in a ferroelectric material can be exemplified by the composition, barium titanate ($BaTiO_3$). Referring to Figure 2-10, it can undergo several crystallographic phase transformations in different temperature regimes where different unit cell structures, or phases, are stable. Since the cubic phase is paraelectric, the temperature at which the material becomes polar is known as the Curie Point, T_C. Therefore, for materials to possess their functional properties, they must be below this temperature.

The chemical composition of the ferroelectric material is also an important criteria as different phases are stable in different compositional ranges. The phase diagram of the ferroelectric material, lead magnesium niobate – lead titanate ($(1-x)Pb(Mg, Nb)O_3–xPbTiO_3$, or further abbreviated to PMN-PT) is shown in Figure 2-11. An interesting feature that can be extracted from phase diagrams is the morphotropic phase boundary. As the name suggests, two phases can exist at this morphotropic phase boundary, such as the line between the rhombohedral and orthorhombic phases. Any compositions near or at the morphotropic phase boundary is of interest because of the enhancement of its properties [47-49].

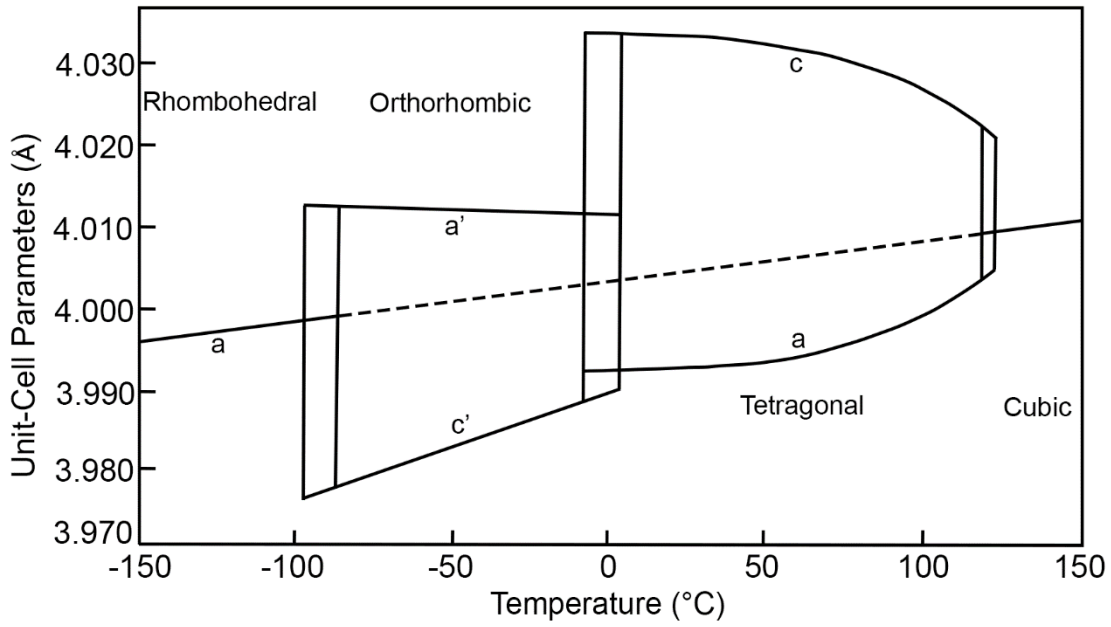

Figure 2-10 Lattice parameters of $BaTiO_3$ as a function of temperature. Reproduced with permission by Elsevier from [40].

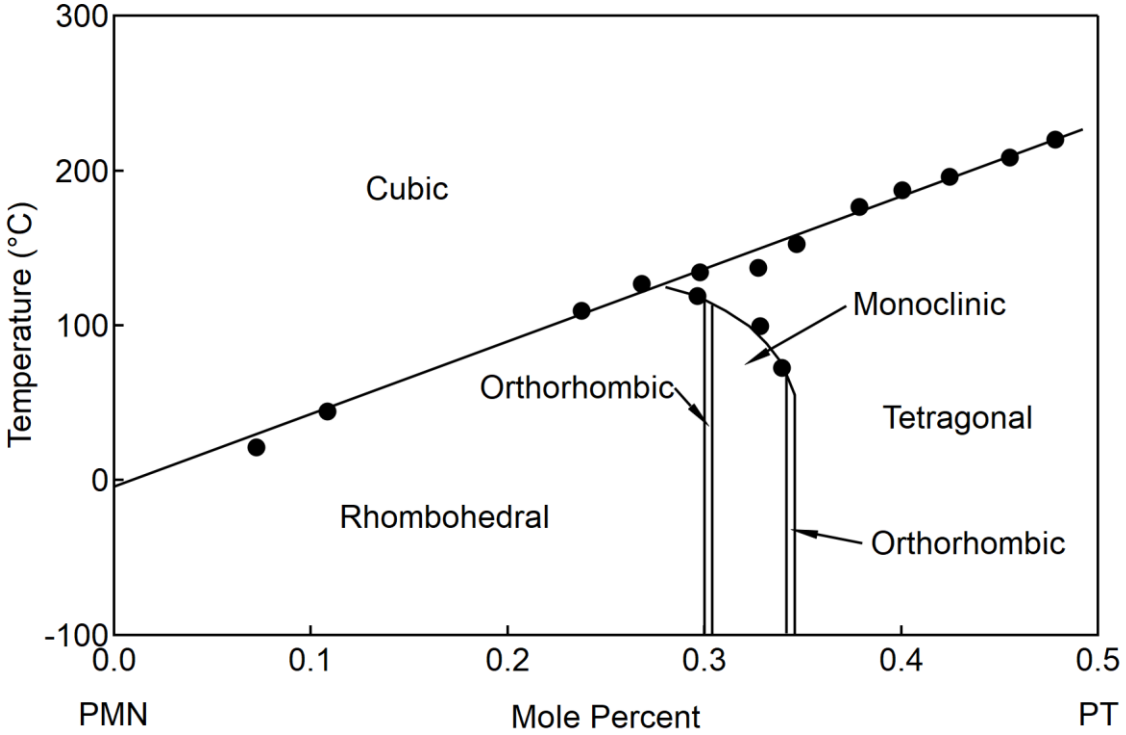

Figure 2-11 Phase diagram of the PMN-PT binary system. Reproduced with permission by IOP Publishing under the Creative Commons Attribution Licence (CC BY) from [47].

2.3.3 Domains

Until now, it has been assumed that the ferroelectric material is a single crystal with a single domain. However, single crystals with multiple domains and polycrystals with multiple domains are most common. If a single crystal can have a single domain, a polycrystalline material will naturally have multi-domains within each crystal. Domains in ferroelectric materials are regions which have a uniform polar axis. Since single domains have opposing charges on opposite ends of the polar axis, multi-domains form to minimise the electrostatic energy and nullify the charges on the surfaces [40, 50, 51]. That is, the orientation of the domains in a polycrystalline material will be arranged randomly such that the charges cancel out each other and the intergranular stresses are reduced.

For a multi-domain material to have a near-common polar axis, or a net dipole moment, the material undergoes a process called poling [50, 51]. This is where a large electric field is applied to align the domains with the direction of the electric field. When the electric field is removed, the domains will mostly maintain its new poled orientation. A single or common polar axis for this X-ray generator application is important to ensure its pyroelectric and ferroelectric properties are maintained and maximise the surface charge available on its polar surfaces.

2.4 Alternate Methods to Generate X-rays

Apart from the thermionic emission and acceleration of electrons still in use today in many X-ray tubes, there exists many other methods to generate X-rays, or more correctly to emit and accelerate electrons at a target. The other mechanisms include photoemission, secondary electron emission, field electron emission and ferroelectric electron emission [52, 53]. It is the emission of electrons that has brought about an array of technologies such as MOSFETs, electron microscopy and energy converters. The miniaturisation of X-ray sources and desire to overcome the disadvantages of conventional X-ray tubes have driven the development of X-ray generators via other methods [9]. For this sub-chapter, the focus will be on the techniques that have been applied to the generation of X-rays and categorised into ferroelectric, triboelectric and carbon nanotube-based field emission X-ray generation.

2.4.1 X-ray generation from ferroelectric materials

As introduced earlier in Chapter 2.3, ferroelectric materials are the smallest subset within the classification of dielectric materials. The term ferroelectric materials used here will encompass those that also possess pyroelectric and piezoelectric properties. The generation of X-rays involves several electron emission mechanisms, being ferroelectric electron emission and field ionisation [15, 19, 54].

Electron emission can occur in two ways, namely overbarrier and tunnelling emission [52, 55]. The overbarrier emission is where the energy supplied must overcome the surface potential barrier and have energy greater than the material's work function. Thermionic and photoelectron emissions follow this mechanism, with energy provided in the form of heat and light respectively. Tunnelling emission is quite different as the surface potential is bent via the application of an electric field to allow electrons to "tunnel" through. Both mechanisms are illustrated in Figure 2-12. Field electron emission uses this mechanism and the typical electric field required is in the order of 10^8 - 10^9 V/m, and depends highly on the work function of the material [56, 57].

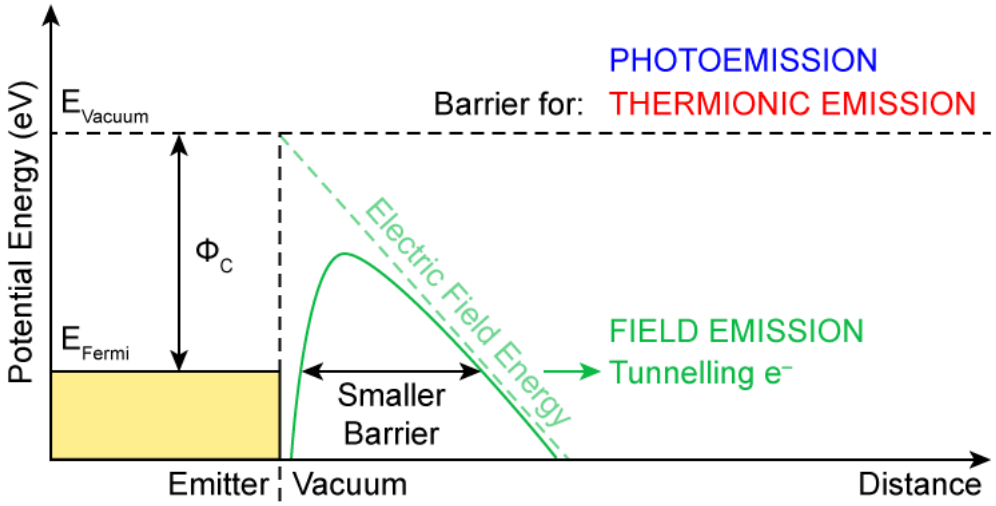

Figure 2-12 Energy band diagram illustrating the overbarrier (thermionic and photoemission) and tunnelling (field emission) mechanisms at the emitter to vacuum interface.

One of the electron emission mechanisms involved in the generation of X-rays using ferroelectric materials is ferroelectric electron emission. It can be thought of as being very similar to field electron emission as it also utilises tunnelling mechanism. However, the characteristic difference is that the ferroelectric material can create a high electric field, and therefore, does not require the external application of an electric field. Studies into this phenomenon reports that electron emission can occur from the pyroelectric effect, piezoelectric effect or by polarisation switching [15, 53, 58, 59]. The method of polarisation switching works by applying a switching AC electric field of about 10^4 V/m to quickly reorientate the direction of the polar axis [59]. Any excitation or perturbation applied on the ferroelectric material will cause its spontaneous polarisation to change from its equilibrium state. This brings about uncompensated charges on its polar surfaces and creates an intense electric field in the order of 10^8 V/m [54, 60]. Electrons are then emitted as one of the pathways to balance the surface charges and return to equilibrium. However, this mechanism involves the emission of electrons from the material's surface.

Another mechanism for electron emission was suspected by Brownridge and Shafroth [16] when they investigated the phenomenon behind the generation of X-rays using the pyroelectric effect. They believed that the source of electrons originated from the ionisation of residual gas molecules near the exposed surface of the pyroelectric crystal. Rather than being a different mechanism in the X-ray generation process, it may be possible that it is a supplementary mechanism instead.

This mechanism is known as field ionisation and can be thought of as the reverse of field electron emission. The ionisation of gas molecules requires much higher electric fields compared to field and ferroelectric electron emission, being in the order of 10^9 - 10^{10} V/m [56, 61]. It is not exclusive to methods involving only the pyroelectric effect as it has been observed with polarisation switching methods [62]. However, it is more commonly observed when using the pyroelectric effect because it is the simplest method to create a sufficiently intense electric field.

The electron emission from ferroelectric materials can be thought of as one current pathway for the non-compensated surface charges to be neutralised. There exist two types of emissions from ferroelectrics; "weak" emission and "strong" emission. For the "weak" electron emission, a thermally or mechanically stimulated ferroelectric material is able to produce a current density in the range of 10^{-12}-10^{-7} A/cm^2 range [15]. It is only the magnitude of the spontaneous polarisation that changes with the applied stimulus. Depending on the material selected, higher current densities in the range of 10 - 10^2 A/cm^2 can been observed [59]. The geometry for such emission is where one polar surface of the ferroelectric material is facing parallel to an electron detector or a metal target, illustrated in Figure 2-13(a).

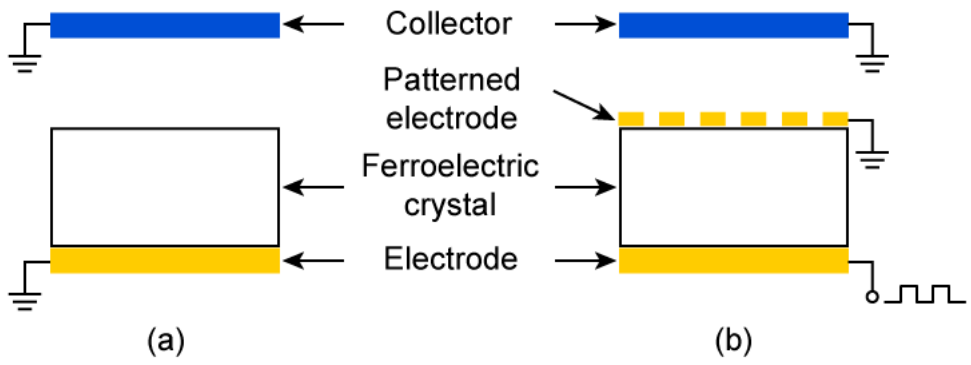

Figure 2-13 Typical experimental setups for "weak" (a) and "strong" (b) electron emission from ferroelectric materials. Depending on the experiment, the collector can be an electron detector or replaced with a target and an X-ray detector placed in line with the target and ferroelectric crystal.

The "strong" electron emission is very different as it has a different geometry and uses an external electric field. The distinction between the two geometries depicted in Figure 2-13(b) is the use of a metallic patterned electrode of various shapes such as a

lattice or ring [63, 64], which enables the creation of plasma over the ferroelectric surface. Such plasma-assisted emission was found to achieve current densities in the range of 10^2 - 10^5 A/cm^2 when the material is excited by very fast switching pulses [15, 53, 65-71]. The high voltage trigger pulse of 75 V to 1 kV are able to control the polarisation switching mechanism to produce the high current densities [68, 69, 72]. The current density produced is important because it determines the electron current emitted into the vacuum space between the emitting polar surface of the ferroelectric and the electron detector or metal target. However, this project will be focused on utilising the "weak" electron emission, particularly by using the pyroelectric effect, to eliminate the dependency of an external power supply.

Employing the pyroelectric and piezoelectric effect for X-ray generation provides several advantages. Firstly, an advantage over radioisotopes is that these materials are solid-state, allowing it to be safely handled when not in use. The second advantage of these X-ray generators is that they can operate using low voltages and with small power draws, suitable for battery operation. One typical example draws 1.4 mW and runs using a 12 V battery [14, 73-75]. Additionally, it has been demonstrated that these X-ray generators can achieve end-point energies of about 170 keV in its simplest configuration [75-78]. The dimensions of the materials tested for pyroelectric X-ray generators typically range from 2 mm to 10 mm in thickness and surface area of 4 to 25 mm^2 [79-82]. The research group that developed the piezoelectric X-ray generator used rectangular pieces with dimensions of 100×10×1.5 mm^3 [74, 75]. The small sizes of the commercialised pyroelectric X-ray generator and in-development piezoelectric X-ray generator pictured in Figure 2-14 prove these methods of X-ray generation as a potential device that is low-powered with a small footprint.

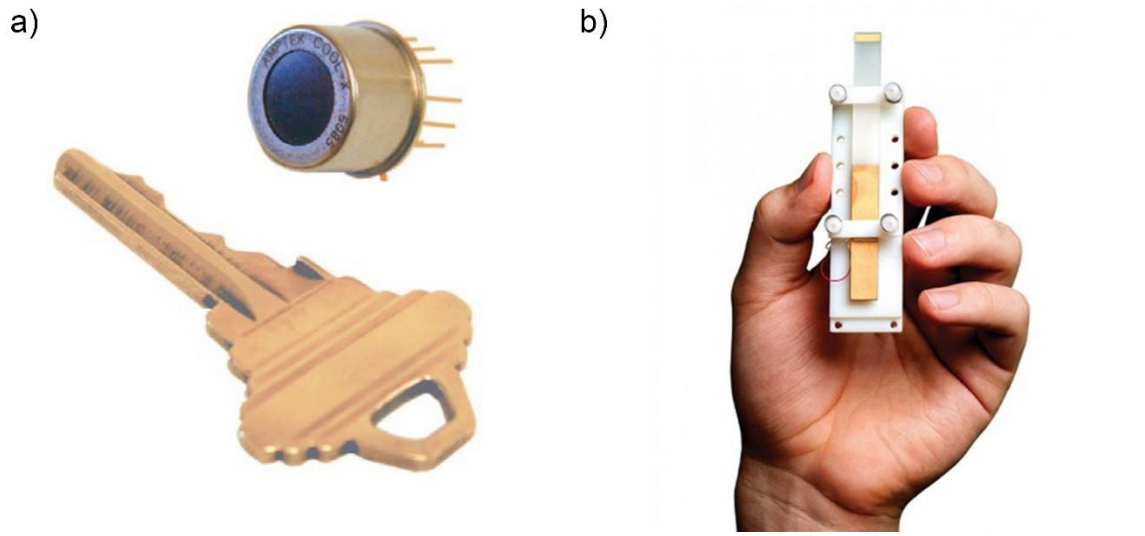

Figure 2-14 Photographs of the commercialised COOL-X pyroelectric (a) and in-development piezoelectric (b) X-ray generators. Reproduced with permission by AMPTEK, Inc. and Rob Hill courtesy of MIZZOU alumni magazine from [14, 83].

Despite its advantages, this method of generation also suffers from its disadvantages. The duration of X-ray production from both pyroelectric and piezoelectric X-ray generators is limited to only a few minutes [75]. For pyroelectric X-ray generators, this is because the count rate follows the thermal cycle and produces a non-continuous and non-uniform X-ray flux [73]. Another disadvantage is if the generator is stopped in the middle of a heating or cooling cycle, it is highly likely to continue producing X-rays because of its long relaxation time [75]. On the other hand, the generator can also suddenly stop producing X-rays where some have attributed this event caused by an electrical discharge.

2.4.2 X-ray generation via triboelectricity

The triboelectric effect is another method that has been harnessed to generate X-rays. Like all X-ray generator systems, there must be electrons before X-rays are produced. The emission of electrons is achieved through a process called tribocharging whereby two materials are placed in contact and undergo a mechanical action such as sliding or tapping to create friction between the two contact surfaces. This friction is then converted to charge on the materials' surfaces via a phenomenon called triboelectrification [84]. There is an eventual release of electrons due to charge separation at the moment the two surfaces are out of contact [85]. The generation of X-rays then comes about from collision with nearby gaseous particles in the small gap between the

two surfaces and is observed as triboluminescence, which is the emission of visible and X-ray photons [86, 87].

The production of X-rays via triboelectricity was initially demonstrated by a simple peeling of adhesive tape. Like ferroelectric X-ray generation, X-rays were observed when the ambient pressure was dropped to the high vacuum range. Early investigations reported the charge density emitted was ~10^{12} electrons/cm^2 and are release in 2-5 ns pulses [86, 87]. At the optimised pressure, the X-ray energy emitted could be up to 65 keV [88].

Further investigations then moved to adding metallic elements to one of the materials. By doing so, characteristic X-rays of the added metallic elements could be observed. Several methods of metallising polymers have been presented and the maximum flux achieved was ~10^9 X-ray counts/s [88-90]. It is believed that the configuration that produced the highest X-ray flux was developed into a commercial product by Tribogenics, Inc. for X-ray fluorescence spectrometry purposes and the product was called Watson, pictured in Figure 2-15 [85]. It is interesting to note that triboelectric X-ray generators also suffer from energy variability as it has been reported there appears to be about a 20 keV drop from the first 100 ms to the last 100 ms of energy spectrum collection [89].

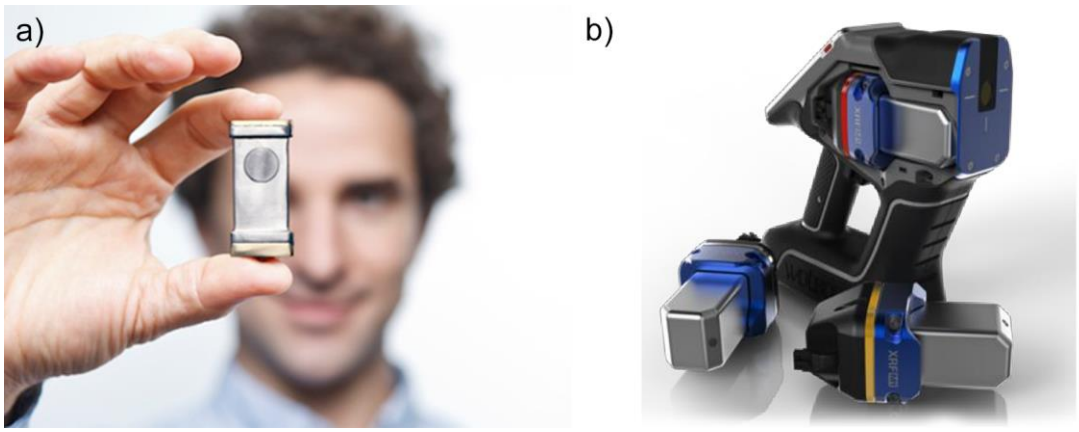

Figure 2-15 The capsule-like X-ray emitter (a) and the Watson M1 X-ray handheld analyser (b) developed by Tribogenics, Inc. Reproduced with permission by SPIE Publication from [85, 91].

2.4.3 X-ray generation via field electron emission using carbon nanotubes

An additional method that has garnered attention is the return of X-ray generators that employ field electron emission. Earlier, the mechanism of field electron emission was briefly introduced. This method brought about the first type of X-ray tubes, also known as the cold-cathode tube. These tubes require a strong electric field and a very stable ultra-high vacuum. Unfortunately, the technology available then meant that using thermionic emission X-ray tubes were more efficient and did not suffer from the same complications [2, 52, 92, 93].

However, the discovery of carbon nanotubes (CNT) has made it possible to use this method again. The electric field required for CNT to emit electrons is up to two orders lower than other electron emissive materials [94]. Advancement in fabrication techniques has made it possible to make fine tips or whiskers. By fabricating CNT into tips, the vacuum required is reduced and the electron emission current is more stable. This has led to developments that combine the field of nanomaterials with X-ray technology [2, 94-102].

2.5 Pyroelectric X-ray Generators

The demonstration of the X-ray generator using the pyroelectric effect was first shown by Brownridge [103] in 1992 using cesium nitrate, $CsNO_3$. Since then, several investigations have been performed to understand the mechanism behind the generation of X-rays as well as to present methods of overcoming the limitations of the X-ray generator and enhancing its output.

2.5.1 Single-crystal configuration

Several research studies were undertaken using a single-crystal configuration. That is, there is a single pyroelectric crystal attached to a thermal source and a metallic target placed some distance away from the exposed surface of the crystal. The purpose of simply testing the X-ray generator with such configuration was to establish any parametric dependencies and determine the mechanism of X-ray generation.

Early investigations into the generation of X-rays using the pyroelectric effect found that the X-ray counts and end-point energy had several dependencies. These dependencies were related to the operating conditions and configuration of the X-ray generator. Some of these include the pressure of the vacuum chamber, the gas species, the gap distance between the pyroelectric crystal and the target, as well as the dimensions of the pyroelectric crystal [77, 81, 82]. The different parameters applied in each research study are listed in Table 2-1.

It has been found amongst the early studies that the pressure of the chamber in which the X-ray generator sits in is one of primary dependencies. Earlier, it was introduced that the generation of X-rays relied on the development of uncompensated surface charges apparent on the polar surface of the pyroelectric crystal. One of the processes in which these surface charges can be neutralised or returned to equilibrium is by the adsorption of electrical charges from the surrounding ionised gas. While it should be taken into consideration with the gap distance, it has been reported that the level of the vacuum can affect the rate of charge compensation, the electron mean free path and the likelihood of an electrical breakdown [16, 77, 104, 105].

As listed in Table 2-1, many of the measurements were conducted in the medium and high vacuum ranges. The medium vacuum range covers from 0.1 Pa to 100 Pa, and the high vacuum range covers from 0.1 Pa to 10^{-5} Pa [106]. The gap distance used in several studies also varied highly from a few millimetres to 30 mm. A few studies have explicitly commented that further reducing the pressure of the vacuum chamber does not correlate to an increase in the X-ray performance in terms of X-ray counts and energy [77, 107]. Further studies on the type of gas fed into the vacuum chamber also added to the variation as the X-ray generator performance maximises at different pressures. However, this could be related to different energies required for ionisation as well as the mobility of the ions [57]. With different crystal dimensions, gap distances and other parameters used between research studies, it does incline one to think that an optimisation of the pressure is necessary regardless if similar parameters are selected.

Although the electron emission from a pyroelectric crystal relies on heating and cooling suggesting the effect of thermal change would affect the X-ray output, this was only reported once [82]. The brief discussion stated that a slow thermal cycling rate would allow time for the surface charges to be neutralised but using too fast of a rate would not allow the crystal to experience the full thermal cycle along its thickness. However, while this study used a thermoelectric cooler to control the thermal cycle in a triangular waveform, many of the early studies used a resistor as the heating element and allowed the crystal to cool naturally. This brings about many inconsistencies when wanting to compare the performance of one X-ray generator to another especially when many details were not reported. This is evident by the missing table cells in Table 2-1.

However, it is worth mentioning that there are more parameters that have not been studied such as the thermal cycling rate and the profile of the thermal cycle, which has not been consistent across the literature findings. The involvement of X-ray physics has also not been highly considered, in particular the selection of target element and its thickness.

2.5.2 Multi-crystal configuration

Using a single crystal configuration saw some limitations that were introduced earlier. To overcome or reduce these limitations, some investigations have been undertaken by employing multiple crystals in different arrangements.

Through understanding the electrostatics behind the generation of X-rays via the pyroelectric effect, it has been demonstrated that using a two-crystal system can approximately double the electric field in the gap, the measured X-ray counts and end-point energy [80, 82, 108, 109]. Under optimised conditions, the end-point energy increased from 107 keV as a single crystal configuration to 184 keV in a two-crystal configuration. The count rate during the cooling also increased from 261 cps to 518 cps.

Similarly, it was theorised that stacking pyroelectric crystals on top of one another will improve the end-point energy. As the X-ray generator system can be modelled as capacitors, stacking the pyroelectric crystals would be equivalent to having a set of capacitors in parallel, thereby reducing the combined capacitance [110]. It was predicted that the end-point energy alone should multiple with the number of pyroelectric crystals stacked. However, adding up to three of the same pyroelectric crystal only increased the end-point energy by 20 keV. This shows that the effect of stacking multiple crystals did not have a significant impact compared to the two-crystal system placed in line with each other.

One of the reasons used to explain the poor results from using a stacked crystal configuration was the low thermal conductivity of the crystal. Dielectric materials in general possess low thermal conductivity which in this application can be an inhibiting factor. This is because it has been shown that there is a positive linear correlation between the X-ray output and crystal thickness [82]. Many of the studies of this X-ray generator apply a thermal gradient on one polar face of the crystal. If a pyroelectric crystal with thickness of say 5 mm or 10 mm is used, it would not experience the full thermal cycle range across its crystal thickness.

A variation of the two-crystal system was also attempted but with a wedge-shaped target placed between the two crystals [111, 112]. The purpose of this configuration was to not only improve the X-ray counts but also the stability of the X-ray production. As mentioned previously, a limitation of using a single crystal configuration is the discontinuous non-uniform generation of X-rays. In the previously described two-crystal system, the two crystals were thermally cycled together under the same thermal gradient. In Guan *et al.*'s work [111, 112] however, they explore the effect of applying various thermal gradient combinations with the two pyroelectric crystals. That is, both crystals will be either heated and cooled at the same rate and temperature range, or one is heated while the other is cooled. It was reported that applying thermal gradients of opposing direction on each crystal increased the X-ray counts by 20 times compared to using an individual crystal. Additionally, the duration of X-ray production without disruption was twice as long. It is uncertain if the end-point energy also increased in this configuration as the analysis was restricted up to 20 keV.

As an extension to the idea of smoothening the continuity of X-ray generation, the same research group demonstrated the use of six pyroelectric crystals thermally cycled in out-of-phase periods [113]. The X-ray count rate was described as being ripple-like which increases with the count rate. It was also shown that the choice of surrounding material, a "case", affects the X-ray output. Aluminium achieved the highest count rate compared to copper and stainless steel, which corresponds to also having the lowest work function of the three materials. Although the intensity of this six-crystal system is not on par with the earlier two-crystal version, it could be a better solution for applications requiring a consistent X-ray output.

2.5.3 Combination of pyroelectric crystal with other materials

Another method to improve the X-ray yield of this type of X-ray generator is by placing an additional material in the setup to provide two different functions. Depending on the integration of the material, it can either act as a supplementary source of electrons or act to heighten the electric field in the gap. The choice of material tended to be one with a low work function such as tungsten and carbon nanotubes. In a cold-cathode X-ray tube that uses carbon nanotubes, an intense electric field of about 10^6 V/m is still required for field emission of electrons and an external high voltage needs to be applied [94]. The

incorporation of low work function materials in these X-ray generators where the pyroelectric crystal is able to create the same level of electric field is a promising technique to improve the device's performance.

By placing a small area of carbon nanotubes in the gap between the pyroelectric crystal and the target, an improvement in the X-ray yield can be seen. Though the effect of adding carbon nanotubes is not significant for fresh pyroelectric crystals, Fukao *et al.* [21] showed that carbon nanotubes can maintain a reasonable count rate after several thermal cycles, thereby extending the lifetime of the X-ray generator system. A fresh crystal was able to produce approximately 1000 cps, and after 80 thermal cycles, it dropped to a measly 4 cps. But when a 150 mm^2 area of carbon nanotubes was inserted into the setup, the count rate rose again to 200 cps.

In addition to utilising low work function materials, it is a well-known effect that materials with a geometry of small radius of curvature and high aspect ratio can provide electric field enhancement [56, 114]. New methods of material fabrication have made it possible to produce materials with a radius in the nanometre range and lengths in the micrometre range [2, 99]. Attaching a single tungsten tip can increase the X-ray yield and end-point energy significantly. Pauley demonstrated this on an opened COOL-X, a commercial pyroelectric X-ray generator where the end-point energy increased from about 30 keV to 80 keV [115]. Although the focus was towards neutron production, a few research groups have incorporated single tungsten tips into both single and two-crystal configurations. Naranjo *et al.* [116] reported that the electric field achieved with the tungsten tip was in the order of 10^9 V/m. For their single crystal system, the X-ray energy produced up to 120 keV. In a two-crystal configuration with a single tip on one of the crystals built by Geuther *et al.* [117], the X-ray counts peaked up to 4000 cps and achieved an end-point energy of 200 keV.

However, tungsten and carbon nanotubes also have their limitations: despite their mechanical strength, they can experience degradation such as from arcing, cathode sputtering and oxidation [93, 114, 118]. Alivov *et al.* [119] have shown that using titanium dioxide nanotubes as a substitute proves to be better for electron emission. With a cluster of nanotubes developed to reduce the electric field screening effects, the titanium dioxide

nanotube arrays were applied to the pyroelectric crystal [120, 121]. Compared to their setup of the single crystal configuration, the maximum end-point energy rose from 45 keV to 74 keV. Likewise, the total X-ray counts from the heating and cooling cycles doubled. This indicates that the electric field is the gap does intensify. Additionally, a further improvement to the output was made by using a crystal that was twice the originally tested crystal thickness. The maximum end-point energy achieved by the thicker crystal with nanotube arrays was 97 keV and the total X-ray counts increased by tenfold. Although the X-ray output collected using the titanium dioxide nanotube arrays is not as comparable to using a single tungsten tip, it may be a matter employing better temperature control, further optimising the system and possibly even using a two-crystal configuration.

2.5.4 Other modifications

Many of the studies discussed earlier heated the pyroelectric crystal, or crystals, with a resistor or thermoelectric cooler. An Osaka University-based research group heated the pyroelectric crystal using a laser light. The X-ray count rate and end-point energy is rather comparable to the single-crystal configuration heated by the resistor or thermoelectric cooler, however, the advantage lies in the short pulsing of the laser light. Nakahama *et al.* [122, 123] have shown high count rates at time intervals of 15 s up to 120 s. The control over the fast generation of X-rays can be very useful for on-field X-ray instruments which need quick analysis.

Rather than adding a single tip or an array of nanotubes, one research group has manufactured the pyroelectric crystal with a cone-shaped emitter with a radius of curvature of 1 μm [124]. In this way, the effect of field enhancement is still taken advantage of. By fabricating the cone-shaped emitters into an array, this UCLA-based group has shown a uniform production of X-rays with an end-point energy above 100 keV [125]. This has also allowed the research group to design the X-ray generator as a flat-panel source. The promising approach of this X-ray generator has led to a start-up for medical X-ray imaging [126-128].

2.6 Summary

Applying the pyroelectric effect for the generation of X-rays presents itself many challenges and complexities. Previous studies indicate that there are several system parameters that govern the X-ray generator performance in terms of counts and energy. These system parameters include both operation and configuration parameters. The dependencies on some of these parameters have been investigated however it appears that an in-depth study is still required to answer some unresolved issues.

However, the studies that look into the parametric dependencies are within individual investigations. Knowing the most optimal setting for each parameter becomes rather difficult when comparing across several studies. As seen in Table 2-1, each study applied a different parametric combination, with some having not reported certain parameters. An added difficulty is from the reporting of results. Although presenting the X-ray energy spectrum is critical, the performance of the X-ray generator should also be characterised by the X-ray count rate. This can be said similarly for the reporting of the end-point energy. Furthermore, the determination of the X-ray end-point energy has also not been consistent. Thus, a more comparable means of reporting the X-ray generator results should be implemented, such as by using a consistent calculation method.

While there are some basic considerations into the use of pyroelectric materials for this application, it is lacking in the correlation between the material properties with the system parameters and X-ray generator performance. Additionally, nearly all investigations often use only two crystal compositions, namely lithium tantalate ($LiTaO_3$) and lithium niobate ($LiNbO_3$). There are several other pyroelectric materials available that possess higher pyroelectric properties and have not been demonstrated in the X-ray generator setup.

Review of the literature suggests that the X-ray generator to be constructed must undergo its own characterisation and optimisation first to create a comprehensive understanding of the X-ray generation phenomenon. It is only then can new techniques to improve the performance of the X-ray generator be employed. Additionally, incorporating an application-focused characterisation of pyroelectric materials will be beneficial in laying down the foundations of this X-ray generator. Finally, the lifetime of the X-ray generator should be investigated under extended thermal cycling periods.

Table 2-1 Summary of the X-ray generator parameters and output from the most optimum configuration. The geometry is assumed to be single-crystal configuration unless otherwise stated in the *Additional Variation* column. Empty cells represent unprovided information.

Crystal	Crystal Dimensions		Gap Distance (mm)	Temperature Range (°C)	Pressure (Pa)	Gas	X-ray Output	End-point Energy (keV)	Additional Variation	Ref.
	Area (mm^2)	Thickness (mm)								
$LiTaO_3$				35 – 125			10^8 cps	35	COOL-X head size: Ø 15 mm x 10 mm	[14, 129]
$LiNbO_3$	19.63	5	22	RT – 115	<1.33	N_2		170		[76]
$LiTaO_3$	4	2		18 – 115				~40		[79, 81]
$LiNbO_3$	19.63	5	10 - 30	RT – 100	1.33×10^{-3}	N_2		135		[79]
$LiNbO_3$	12.57	10	<5	RT - 180	1.07×10^{-3} – 1.6	N_2, O_2, Ar, He		<160		[77]
$LiTaO_3$	100	0.5	~8	25 – 100	6.78			~9		[82]
	25	1			9.71			~10		
	25	2			7.05			~17		
	25	4			6.12			~18		
	25	10			4.79			~36		
$LiTaO_3$	100	0.5	4.5	RT – 120	10		10^5 counts	~21		[130]
					15		3×10^4 counts	~16		
					20		3×10^3 counts	~10		
					25		3×10^3 counts	~10		

Crystal	Crystal Dimensions		Gap Distance (mm)	Temperature Range (°C)	Pressure (Pa)	Gas	X-ray Output	End-point Energy (keV)	Additional Variation	Ref.
	Area (mm^2)	Thickness (mm)								
$LiTaO_3$	100	5	5.4	RT – 80	1		10^5 counts	~55		[107]
					2		4×10^4 counts	~65		
					3		10^5 counts	~70		
					4		4×10^4 counts	~50		
					5		5×10^3 counts	~25		
					6		5×10^3 counts	~25		
					7		5×10^2 counts	~10		
					8		5×10^2 counts	~10		
$LiNbO_3$	12.57	10						90.5	W/Bi target	[131]
$LiNbO_3$	12.57	5						65	Pt/Sn target	[131]
$LiTaO_3$	25	4		45 – 143	0.01			52	Single crystal	[110]
								60	Two-stacked	
								70	Three-stacked	
$LiTaO_3$	156	5	23	25 – 205	3 – 7			~100		[105]
$LiNbO_3$	100	5	27	5 – 70		N_2	$<10^6$ counts		Uses a “ case” around the crystal	[104]

Crystal	Crystal Dimensions		Gap Distance (mm)	Temperature Range (°C)	Pressure (Pa)	Gas	X-ray Output	End-point Energy (keV)	Additional Variation	Ref.
	Area (mm^2)	Thickness (mm)								
$LiTaO_3$	169	5	27	-5 – 70	3.5	O_2	220 cps		Crystal is placed at one end of a graphite cylinder	[132]
					3.7	Kr	180 cps			
					4.6	N_2	200 cps			
					4.9	Ar	170 cps			
					11.0	Ne	170 cps			
					27.2	He	200 cps			
$LiNbO_3$	78.54	5		10 – 90	10^{-4}	Air	~100 cps		Single crystal	[21, 112]
							~7000 cps		Two-crystal, Same thermal gradient	
							~2000 cps		Two-crystal, Opposite thermal gradient	
									With wedge-shaped target	
$LiTaO_3$	25	5			1.5×10^{-3}		220 cps	Cut at 40	Copper case	[113]
							680 cps		Stainless steel case	
							1100 cps		Aluminium case	
									Six crystals with cone-shaped target	

Crystal	Crystal Dimensions		Gap Distance (mm)	Temperature Range (°C)	Pressure (Pa)	Gas	X-ray Output	End-point Energy (keV)	Additional Variation	Ref.
	Area (mm^2)	Thickness (mm)								
$LiTaO_3$	14.52	2	6	RT – 105	0.1 – 1	N_2	–	35	Tested with Cu and Mo targets	[13]
		4					1.1×10^4 cps	58		
$LiTaO_3$	14.52	4	6	RT – 105	1	N_2	$\sim1\times10^4$ cps			[12]
					10^{-2}	Dry air	$\sim1.4\times10^4$ cps			
$LiTaO_3$	14.52	4		RT – 105	0.1	N_2	$\sim1.6\times10^4$ cps			[12]
	39.59				1		$\sim1.1\times10^4$ cps			
$LiTaO_3$	14.52	4	6	RT – 105			$\sim5\times10^3$ cps		Ø 10 mm target	[12]
	39.59		12				$\sim1.0\times10^4$ cps		Ø 10 mm target	
			12				$\sim1.4\times10^4$ cps		Ø 20 mm target	
			12				$\sim1.5\times10^4$ cps		Ø 30 mm target	
$LiTaO_3$	706.9	10		-33.15 – 6.85	0.7			120	W tip r = 100 nm, l = 2.3 mm	[116]
$LiNbO_3$	100	10	10					>100	Fabricated into a cone shape r = 100 nm	[125]

Crystal	Crystal Dimensions		Gap Distance (mm)	Temperature Range (°C)	Pressure (Pa)	Gas	X-ray Output	End-point Energy (keV)	Additional Variation	Ref.
	Area (mm^2)	Thickness (mm)								
$LiTaO_3$	314.2	10	15 Between two crystals	RT – 130	0.160		4000 cps	200	Two-crystal W tip on one crystal r = 70 nm, l = 3 mm	[117]
$LiNbO_3$	100	5	27	10 – 85	7×10^{-3}	Air	1000 cps*/ 4 cps†		No CNT	[21]
							~20 cps*, †		50 mm^2 of CNT	
							~200 cps*/ ~80 cps†		100 mm^2 of CNT	
							~200 cps†		150 mm^2 of CNT	
							~200 cps*		200 mm^2 of CNT	
$LiNbO_3$	100	10	20	20 – 150	0.40	Air	27097 counts	45	No nanotubes	[121]
							263981 counts	66		
		20	20				58255 counts	74	TiO_2 nanotubes	
							580719 counts		r = 40 nm, l = ~10 μm	

Crystal	Crystal Dimensions		Gap Distance (mm)	Temperature Range (°C)	Pressure (Pa)	Gas	X-ray Output	End-point Energy (keV)	Additional Variation	Ref.
	Area (mm^2)	Thickness (mm)								
$LiTaO_3$	78.54	4	5		0.3		3500 cps	38	Heated with Nd:YLF laser λ = 1047 nm P = 0.89 W 15 s exposure	[122]
$LiNbO_3$	78.54	4	6	RT – 85/90	0.3		~8.7×10^4 counts ~1.5×10^5 counts	47	Cu target Ø 15 mm Cu target Ø 30 mm Heated with Nd:YLF laser λ = 1047 nm P = 0.89 W 120 s exposure	[123, 133]
$LiTaO_3$	12.57	5			0.3			>50	Heated with fiber laser light λ = 1062 nm P = 5.0 W	[134]

* Non-deteriorated crystal

† Deteriorated crystal

This page is intentionally left blank.

3

CHARACTERISATION OF PYROELECTRIC MATERIALS

"Nothing in life is to be feared, it is only to be understood.
Now is the time to understand more, so that we may fear less."

– Marie Curie

3.1 Overview

The generation of X-rays via the pyroelectric effect provides an intense electric field for ferroelectric electron emission and field ionisation. There are several material properties that determine how well the pyroelectric material will create an electric field and produce electrons for X-ray generation. This chapter will cover the identification and measurement of these key material properties. The application of two figures-of-merit specifically for electron emission will also be demonstrated in order to determine the optimal materials for use in a pyroelectric X-ray generator.

3.2 Literature

3.2.1 Dielectric and pyroelectric material properties, and its limitations

Pyroelectric materials have a temperature-dependent spontaneous polarisation, with the relationship defined as

$$\Delta P_S = p\Delta T \tag{3-1}$$

Where ΔP_S is the change in spontaneous polarisation, p is the pyroelectric coefficient, and ΔT is the change in temperature.

The variation of spontaneous polarisation as a function of temperature is depicted in Figure 3-1. As the pyroelectric material reaches its Curie Point, T_C, its spontaneous polarisation drops towards zero. The pyroelectric coefficient represents the derivative of the change in spontaneous polarisation with temperature, increasing exponentially as the temperature approaches T_C before sharply descending to zero.

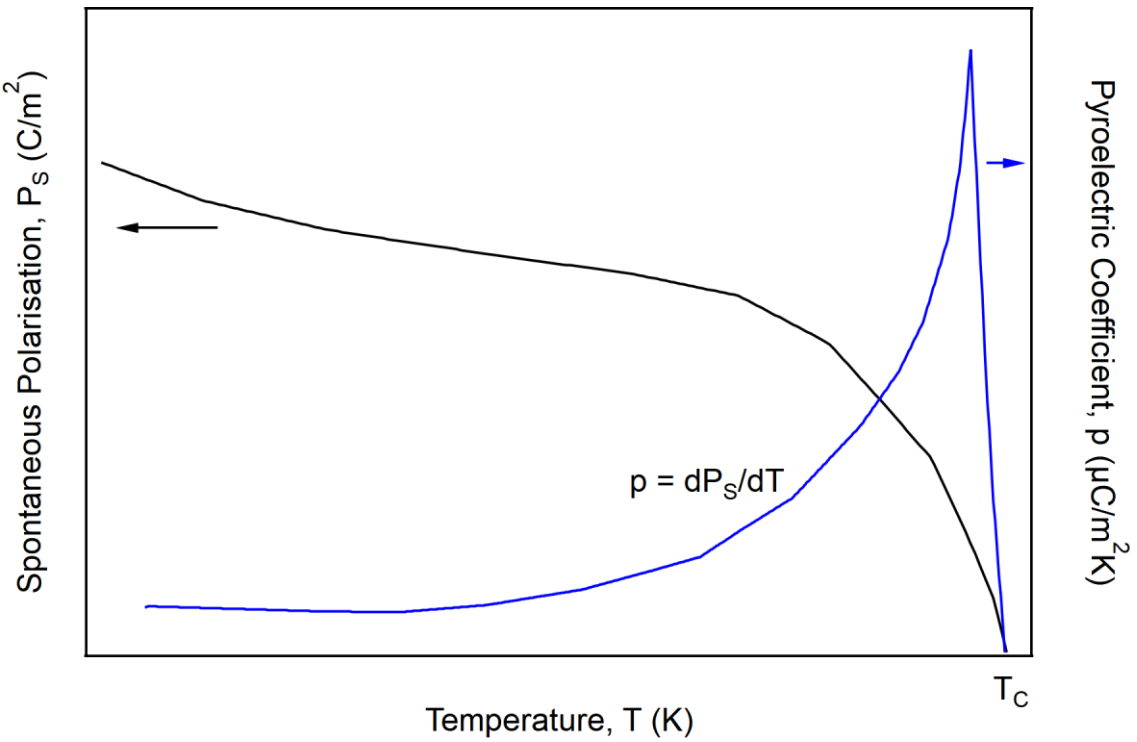

Figure 3-1 Temperature dependence of spontaneous polarisation, P_S, and the pyroelectric coefficient, p. Reproduced with permission by Springer Nature from [135].

In the application for X-ray generation, the crystal is typically cycled over a temperature range: from zero to 100°C, for example. There are few studies that have measured pyroelectric coefficients over such a wide temperature range, however this information is crucial for optimising the choice of material for an X-ray generator. While many reports focus on the magnitude of the pyroelectric coefficient for X-ray generation, there are also other key material properties that have a major impact [82, 117].

While searching for pyroelectric materials suitable for X-ray generation, there are some material properties that need to be considered. Any polymorphic phase transformation can restrict the usable temperature range. Taking single crystal, barium titanate ($BaTiO_3$) as an example, it undergoes several phase transitions, as illustrated in Figure 3-2. At temperatures above 120°C, $BaTiO_3$ is in its cubic paraelectric phase. This means its spontaneous polarisation is equal to zero and it is a normal dielectric. When transitioning between other ferroelectric phases, its material properties will change dramatically which will affect the efficiency and reproducibility of the electron emission process [15].

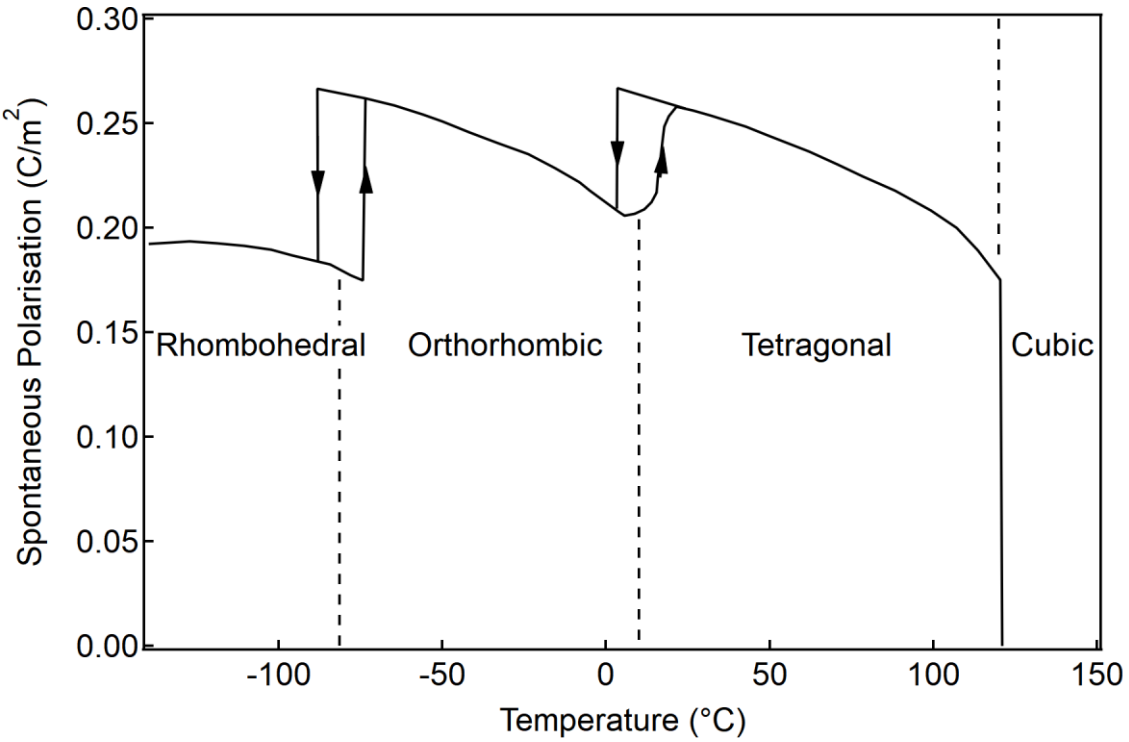

Figure 3-2 Spontaneous polarisation as a function of temperature of barium titanate single crystal. Reproduced with permission by John Wiley and Sons from [51].

Additionally, the usable temperature range within a ferroelectric phase must be selected with caution. Like the pyroelectric coefficient, the relative permittivity can vary dramatically with temperature as it approaches T_C, as illustrated in Figure 3-3. For a ferroelectric material with multiple phases, its relative permittivity can also change sharply as the temperature crosses a ferroelectric phase.

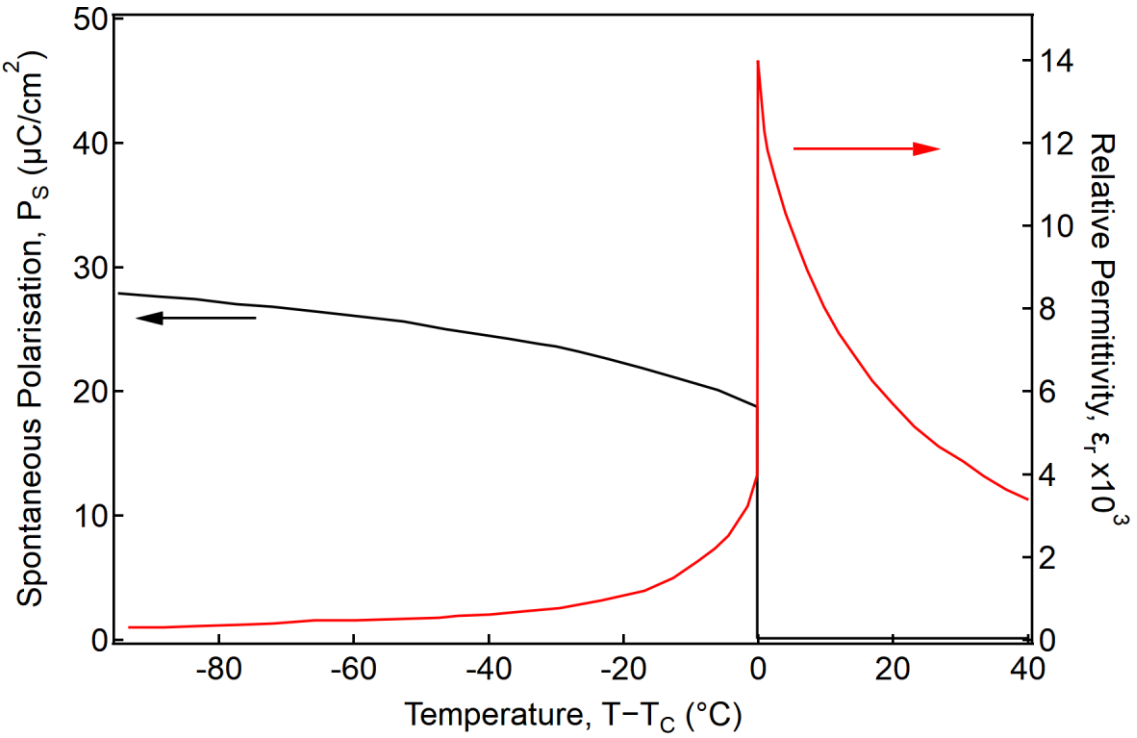

Figure 3-3 Temperature dependence of spontaneous polarisation and relative permittivity of an ideal ferroelectric material. T_C represents the Curie Point. Reproduced with permission by Elsevier from [53].

3.2.2 Theory of measuring pyroelectric coefficient

A dielectric material will exhibit pyroelectricity when it satisfies Equation 3-1. The change in spontaneous polarisation, ΔP_S, can be observed as net charge, σ_q, on the polar surfaces of the material:

$$\sigma_q = \frac{q}{A} = p\Delta T \qquad (3\text{-}2)$$

Where q is charge and A is the area of the electrode surface of the material.

A dynamic method, also known as the temperature oscillation method [136-139], can be applied to measure charge when the sample is subjected to a change in temperature. A schematic of the method is depicted in Figure 3-4. To further simplify the measurement, it is known that current is the rate of charge flowing through a circuit. Therefore, the pyroelectric coefficient can be determined using Equation 3-3:

$$i = pA\frac{\Delta T}{\Delta t} \tag{3-3}$$

Where i is the pyroelectric current measured from the electrodes of the samples when it is heated or cooled at a constant rate of 1°C/min [140], Δt is the change in time.

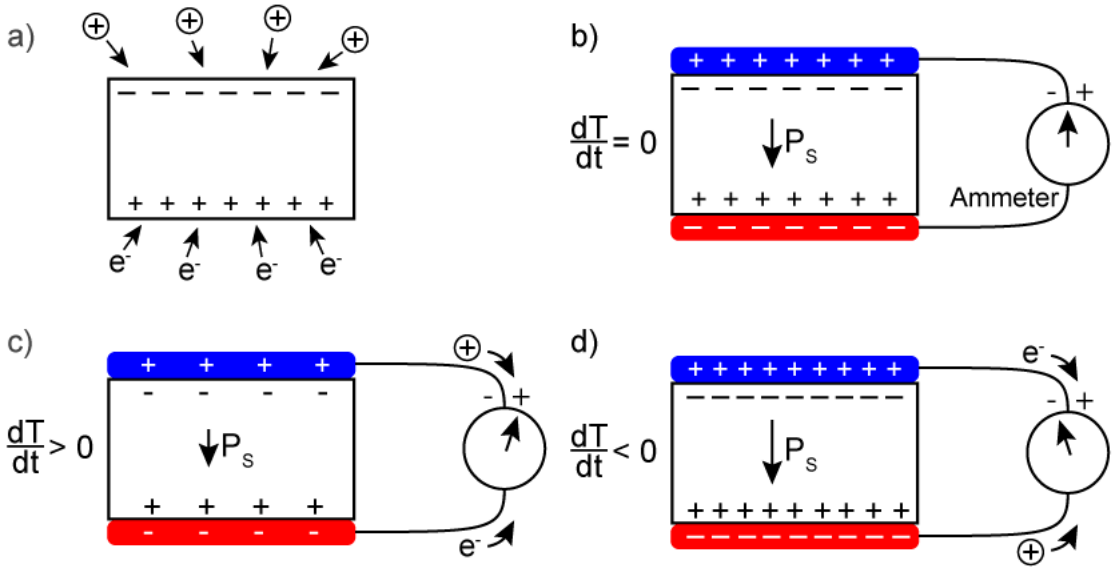

Figure 3-4 Schematic model of a pyroelectric crystal connected in a circuit to measure pyroelectric current. (a) In an open circuit, the pyroelectric crystal will attract charged ions to compensate the surface charges. (b) When the crystal connected in a short circuit with electrodes on its polar surfaces and is at equilibrium, no current flows through the ammeter. (c) During heating, the spontaneous polarisation, P_S, decreases causing the respective charged ions to flow away from the electrodes. (d) During cooling, P_S increases and respective charged ions flow towards the electrodes to accommodate for the change. The cyclic thermal gradient will generate an oscillating current. Reproduced with permission by Taylor and Francis Group, LLC, a division of Informa plc from [141].

3.2.3 Figure-of-merit

The generation of X-rays using ferroelectric materials is observed due to ferroelectric electron emission and field ionisation [16, 19]. The extraction of electrons in both mechanisms is highly dependent on the magnitude of the electric field created between the ferroelectric material and the target. While the mechanism of ferroelectric electron emission and field ionisation can be considered like field electron emission, it is influenced by different factors. For a conventional field emitter, the electric field is determined by high voltage applied externally. To increase the magnitude of the electric field, materials with high relative permittivity and high conductivity are chosen [142]. When using ferroelectric materials, the creation of the electric field is brought about by uncompensated surface charges on the polar surfaces induced by the pyroelectric or piezoelectric effect, though the focus here will be on applying the pyroelectric effect. As has been introduced in Chapter 2, one of the two electron emission mechanisms will be more dominant in either the heating or cooling phases of the thermal cycle. The term electron emission will refer to both ferroelectric electron emission and field ionisation in the remainder of this thesis, unless the specific mechanism is stated.

The arrangement of the X-ray generator can be thought of as having an electric circuit system analogous to a two-capacitor system, as depicted in Figure 3-5. Since, a ferroelectric crystal is a dielectric and the circuit can be idealised as two parallel-plate capacitors [109].

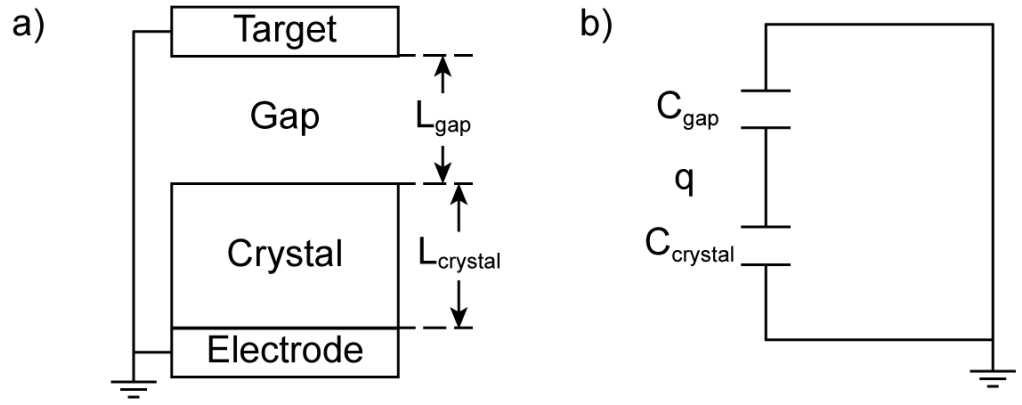

Figure 3-5 Schematic of the generator (a) and its corresponding electric schematic diagram (b) where the two capacitors are the crystal and the gap.

The capacitance of both the pyroelectric crystal and the gap are respectively given by:

$$C_{crystal} = \frac{\varepsilon_0 \varepsilon_{crystal} A}{L_{crystal}} \tag{3-4}$$

$$C_{gap} = \frac{\varepsilon_0 \varepsilon_{gap} A}{L_{gap}} \tag{3-5}$$

Where ε is the relative permittivity of the material or gap, and ε_0 is the free permittivity.

Therefore, the voltage generated across the two capacitors can be represented as,

$$V = \frac{q}{C_{crystal} + C_{gap}}$$

$$V = \frac{q}{\frac{\varepsilon_0 \varepsilon_{crystal} A}{L_{crystal}} + \frac{\varepsilon_0 \varepsilon_{gap} A}{L_{gap}}}$$

$$V = \frac{q}{\varepsilon_0 A \left(\frac{\varepsilon_{crystal}}{L_{crystal}} + \frac{\varepsilon_{gap}}{L_{gap}} \right)} \tag{3-6}$$

Combining Equation 3-2 and Equation 3-6, the electric field across the gap can be evaluated as,

$$E = \frac{V}{L}$$

$$E_{gap} = \frac{1}{L_{gap}} \left(\frac{pA\Delta T}{\varepsilon_0 A \left(\frac{\varepsilon_{crystal}}{L_{crystal}} + \frac{\varepsilon_{gap}}{L_{gap}} \right)} \right)$$

$$E_{gap} = \frac{p\Delta T}{\varepsilon_0 \left(\varepsilon_{crystal} \frac{L_{gap}}{L_{crystal}} + \varepsilon_{gap} \right)}$$

$$E_{gap} = \frac{\sigma_q}{\varepsilon_0 \left(\varepsilon_{crystal} \frac{L_{gap}}{L_{crystal}} + \varepsilon_{gap} \right)} \tag{3-7}$$

Similarly, the electric field across the crystal is,

$$E_{crystal} = \frac{1}{L_{crystal}}\left(\frac{pA\Delta T}{\varepsilon_0 A\left(\frac{\varepsilon_{crystal}}{L_{crystal}}+\frac{\varepsilon_{gap}}{L_{gap}}\right)}\right)$$

$$E_{crystal} = \frac{p\Delta T}{\varepsilon_0\varepsilon_{crystal}+\varepsilon_0\varepsilon_{gap}\frac{L_{crystal}}{L_{gap}}}$$

$$E_{crystal} = \frac{\sigma_q}{\varepsilon_0\left(\varepsilon_{crystal}+\varepsilon_{gap}\frac{L_{crystal}}{L_{gap}}\right)} \quad (3\text{-}8)$$

The current density, j, from the crystal

$$j_{crystal} = \sigma_c E_{crystal} \quad (3\text{-}9)$$

Where σ_c is the bulk conductivity of the crystal.

The observed surface charge density is a result of charges occurring from three different events. The change in temperature causes a deviation of the spontaneous polarisation, ΔP_S, which generates uncompensated charge at the crystal polar surfaces. This charge is then compensated by two screening currents; one from the electron emission phenomena, j_{EE}, and the other from the bulk conductivity current, $j_{crystal}$. The electron emission phenomena cover both ferroelectric electron emission and field ionisation. Mathematically, it is expressed as:

$$\sigma_q = p\Delta T - \int_0^t j_{EE}\,dt - \int_0^t j_{crystal}\,dt \quad (3\text{-}10)$$

As,

$$d(\partial q) = j(\partial A)\,dt$$

$$d\left(\frac{\partial q}{\partial A}\right) = j\,dt$$

$$d\sigma = j\,dt$$

Shur and Rosenman [142] found that the charge density from ΔP_S measured over a range of materials is significantly larger than the charge density from the emitted electron current. This then simplifies Equation 3-10 into

$$\sigma_q = p\Delta T - \int_0^t j_{crystal}\, dt \tag{3-11}$$

By solving for the electric field in the gap using Equation 3-7 and Equation 3-11, the resulting equation is

$$E_{gap} = \frac{p}{\sigma_{c,crystal}} \frac{\Delta T}{\Delta t} \frac{L_{crystal}}{L_{gap}} \left(1 - \exp\left(-\frac{t}{\tau}\right)\right) \tag{3-12}$$

Where τ is the charge relaxation time.

At steady state, $t \gg \tau$, Equation 3-12 is simplified into Equation 3-13. Rosenman *et al.* [15, 60, 143, 144] observed the electric field to induce ferroelectric electron emission via the pyroelectric effect was 10^8 V/m. Field ionisation typically occurs in electric fields of 10^9 V/m [61, 145]. Depending on the phase of the thermal cycle, these values can then become a threshold that must be overcome in order to observe electron emission. Equation 3-13 can be considered a figure-of-merit, F_σ, as it is dependent on the bulk conductivity of the pyroelectric crystal.

$$F_\sigma = E_{gap} = \frac{p}{\sigma_{c,crystal}} \frac{\Delta T}{\Delta t} \frac{L_{crystal}}{L_{gap}} \tag{3-13}$$

This is critical because in order to generate X-rays, electrons must be produced first.

It is also worth mentioning that when field ionisation is occurring, field electron emission from the metallic target is also possible because it can occur in electric fields of 10^9 - 10^{10} V/m [146].

A second figure-of-merit, F_ε, can be established from Equation 3-7 by taking the condition of $t \ll \tau$, where all materials with low-conductivity will satisfy. Thus, the equation can be adapted into Equation 3-14, given ε_{gap} is assumed as 1 and ΔT is a constant.

$$F_\varepsilon = \frac{p}{\varepsilon} \frac{L_{crystal}}{L_{gap}} \tag{3-15}$$

Although it was shown in Chapter 3.2.1 that ε varies with temperature its value will be assumed a constant provided that the maximum temperature is below a phase transition temperature or T_C.

3.2.4 Potential materials

Table 3-1 Properties of pyroelectric materials that contribute to the electron emission via pyroelectricity. The bulk conductivity and activation energy were measured at or near room temperature. The missing values represent the material property has not been studied.

Material	Type	p ($\mu C/m^2K$)	T_C (K)	ε_r	E_a (eV)	σ_c $(\Omega^{-1}cm^{-1})$	Ref.
Lithium niobate ($LiNbO_3$)	Single crystal	67 – 103.9	1413.15	28 – 31.4	0.50 – 1.0	10^{-17}-~10^{-8}	[43, 147-158]
Lithium tantalate ($LiTaO_3$)	Single crystal	176 – 230	883.15	47	0.27 – 1.0	~10^{-34}	[147, 148, 155, 157, 159, 160]
Lead magnesium niobate – lead titanate (PMN-0.25PT)	Polycrystalline ceramic	746					[147]
PMN-0.25PT <111>	Single crystal	1300 – 1790					[147]
PMN-0.33PT <001>	Single crystal	560		5810			[137]
PMN-0.33PT <011>	Single crystal	854		2710			[137]
PMN-0.33PT <111>	Single crystal	654		1390			[137]
PMN-0.28PT <001>	Single crystal	377		3160			[137]
PMN-0.28PT <011>	Single crystal	888		2510			[137]
PMN-0.28PT <111>	Single crystal	803		1260			[137]
PMN-30PT	Single crystal				0.24 ($<T_E$) 1.24 ($>T_E$)	~10^{-24}	[161]

Material	Type	p ($\mu C/m^2K$)	T_C (K)	ε_r	E_a (eV)	σ_c ($\Omega^{-1}cm^{-1}$)	Ref.
Lead zinc niobate – lead titanate (PZN-0.08PT) <001>	Single crystal	490		3920			[137, 162]
PZN-0.08PT <011>	Single crystal	650		1530			[137]
PZN-0.08PT <111>	Single crystal	650		6170			[137, 162]
Poly(vinylidene difluoride) (PVDF)	Polymer	25 – 30	332.15 – 353.15	9 – 12			[147, 150, 159, 160,
Poly(vinylidene difluoride-co-trifluoroethylene) (P(VDF-TrFE) 80/20)	Polymer	31	408.15	7			[147, 150, 164]
P(VDF-TrFE) 50/50	Polymer	40	322.15	18			[147, 150, 163, 165]
Commercial PZT (PIC151) $Pb_{0.99}[Zr_{0.45}Ti_{0.47}(Nb_{0.33}Sb_{0.67})_{0.88}]O_3$	Polycrystalline ceramic	533	523.15	2400			[166]
Lead zirconate titanate (PZT-5A)	Polycrystalline ceramic	746			1.55 1.4 1.4	$\sim 10^{-13}$ 10^{-22}	[167-170]
Barium calcium zirconium titanate (BCT-50BZT) (Pulse poling)	Polycrystalline ceramic	480	430				[171]
BCT-50BZT (DC poling)	Polycrystalline ceramic	584					[171]

Material	Type	p ($\mu C/m^2K$)	T_C (K)	ε_r	E_a (eV)	σ_c ($\Omega^{-1}cm^{-1}$)	Ref.
Strontium barium niobate ($Sr_{0.5}Ba_{0.5}NbO3$)	Single crystal	550	398.15	400			[147, 159, 172, 173]
Triglycine sulfate (NH_2CH_2COOH) (TGS)	Single crystal	160 – 450	322.15	20 – 100		10^{-10}	[148, 150, 160]
Mn:BNT-BT <111>	Single crystal	588		279			[147]
Mn:BNT-BT <110>	Single crystal	513					[147]
Mn:BNT-BT <001>	Single crystal	380		835			[147]
$Bi_{0.5}Na_{0.5}TiO_3 – Bi_{0.5}K_{0.5}TiO3 – Bi_{0.5}Li_{0.5}TiO_3 – BaTiO_3$ (BNLKBT)	Polycrystalline ceramic	360		858			[147, 150, 174]
$(Bi_{0.5}Na_{0.5})TiO_3 – (Bi_{0.5}K_{0.5})TiO_3 – BaTiO_3$ (BNKBT)	Polycrystalline ceramic	325		853			[147]
Barium titanate (BT) (Tetragonal)	Polycrystalline ceramic	200	395.15 – 408.15	1200			[40, 147, 148, 160]
Potassium sodium niobate $(K_{0.5}Na_{0.5})NbO_3$ (KNN)	Polycrystalline ceramic			420			[40, 75]
$((K_{0.5}Na_{0.5})_{0.96}Li_{0.04})(Nb_{0.8}Ta_{0.2})O_3$ (KNN-LT)	Polycrystalline ceramic	165		1230			[147, 150]
$((K_{0.5}Na_{0.5})_{0.96}Li_{0.04})(Nb_{0.84}Ta_{0.1}Sb_{0.06})O_3$ (KNN-LTS)	Polycrystalline ceramic	190		1520		10^{-12}	[147, 150]

3.3 Experimental Methodology

3.3.1 Sample preparation

A range of materials were obtained for the series of pyroelectric measurements to be performed. The materials are lithium niobate ($LiNbO_3$), lithium tantalate ($LiTaO_3$), barium titanate ($BaTiO_3$), commercial modified lead zirconate titanate (PZT), and two compositions of lead magnesium niobate – lead titanate (PMN-33PT and PMN-28PT). The samples acquired are listed in Table 3-2, along with their dimensions and crystal orientations.

Table 3-2 Dimensions and orientation of samples obtained for measurements.

Sample	Area (mm^2)	Thickness (mm)	Orientation	Manufacturer
$LiNbO_3$ single crystal	5.00×5.00	0.5, 1.0, 2.0	Z-cut	HeFei Crystal Technical Material Co., Ltd., HeFei, China
$LiTaO_3$ single crystal	5.00×5.00	0.5, 1.0, 2.0	Z-cut	HeFei Crystal Technical Material Co., Ltd., HeFei, China
$BaTiO_3$ single crystal	5.00×5.00	0.5, 1.0	[001]	HeFei Crystal Technical Material Co., Ltd., HeFei, China
PZT (PIC151)	3.55×3.78	0.48	Poly-crystalline	PI Ceramic GmbH, Lederhose, Germany
PMN-33PT single crystal	4.21×5.34	0.46	[001]	H.C. Materials Corp., Urbana, IL, U.S.A.
PMN-33PT single crystal	4.95×5.04	0.52	[111]	H.C. Materials Corp., Urbana, IL, U.S.A.
PMN-28PT single crystal	4.92×4.78	0.53	[001]	H.C. Materials Corp., Urbana, IL, U.S.A.
PMN-28PT single crystal	5.10×4.85	0.52	[111]	H.C. Materials Corp., Urbana, IL, U.S.A.

As various samples were obtained from different suppliers, they underwent different early sample preparation procedures.

The single crystals obtained from HeFei Crystal Technical Material Co., Ltd. were inspected for any surface defects under an optical/polarising microscope (Leitz

Orthoplan, Ernst Leitz GmbH, Wetzlar, Germany coupled with Leica DFC420 Camera, Leica Microsystems Ltd., Wetzlar, Germany). As there were no defects, the single crystals were cleaned with cotton swabs and acetone. Cleaning in an ultrasonic bath was avoided as the vibrations could cause domain formation. The average piezoelectric constant, d_{33}, of $LiNbO_3$ and $LiTaO_3$ across all thicknesses were 8.9 pC/N and 7.9 pC/N. They are in good agreement with the range of measured values from [149, 175-177].

PZT was cut from a rectangular block using a diamond wire (Diamond Wire Saw Model STX-202A, MTI Corporation, CA, U.S.A.) to the final area size. The surfaces of the two parallel larger areas were then polished using silicon carbide paper with grit size moving from 320 to 1200. The polished surfaces of the ceramic were inspected under an optical microscope (Nikon Eclipse ME600L, Nikon Instruments Inc., Melville, NY, U.S.A.).

The lead-based single crystals from H.C. Materials Corp. were provided by Professor Dragan Damjanovic from the Group of Ferroelectrics and Functional Oxides, EPFL. The sample preparation steps are outlined in the journal article by Davis et al.[137].

Two different steps were undertaken prior to sputter coating the samples. For the samples with a thickness of approximately 0.5 mm, nail polish was applied carefully on the edges. As for the samples with thicknesses of 1.0 mm and 2.0 mm, the edges were wrapped tightly with masking tape.

After the edges of all the samples were covered, the samples were sputter coated with gold (Model EMS575, Electron Microscopy Sciences, Hatfield, PA, U.S.A.). The sputter coating was performed at a current of 40 mA for 4 min and repeated three times for each side.

For the samples with nail polish applied on the edges, the nail polish was gently removed with acetone and cotton bud. Because the cleaning was not very precise, the acetone did remove small areas of the gold coating near the edge of the crystal's faces.

Out of the samples in the list, only PZT required poling, as other crystals were provided in the poled state. Two different methods of poling were undertaken, which were pulse poling and high-temperature field poling. The poling procedures were performed on

in-house laboratory equipment. For pulse poling, a triangular wave is applied at an incremental electric field from 0.5 kV/mm to 2 kV/mm in steps of 0.5 kV/mm. For high-temperature DC field poling, the sample was placed in a silicone oil bath that was heated to 100°C and an electric field of 2 kV/mm. After the electric field was applied for 30 min, the electric field was removed and the silicone oil bath was naturally cooled to room temperature before removal.

3.3.2 Pyroelectric coefficient

The pyroelectric current and coefficient were measured using an in-house equipment developed by the Group of Ferroelectrics and Functional Oxides, EPFL, Switzerland. The equipment works by changing the temperature of a sample at a set frequency and measuring the current generated at the sample's surface. The components of the equipment include a Peltier element where the sample sits on with two needle manipulators, one to connect the bottom face of the sample to electrical ground and the other to collect current from the exposed top face of the sample. The equipment with a sample placed on it is pictured in Figure 3-6. The Peltier element is connected to a function generator that changes the temperature at a set frequency in a triangular waveform.

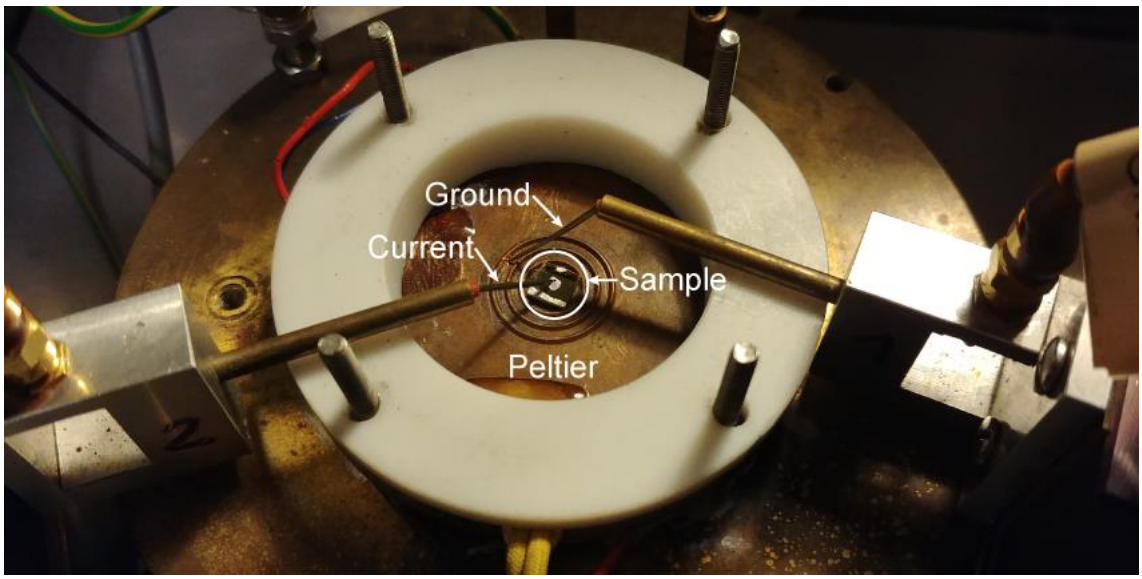

Figure 3-6 In-house pyroelectric measurement equipment built by the Group of Ferroelectrics and Functional Oxides, EPFL, Lausanne, Switzerland

The key settings to be input for each measurement are the base temperature at which the temperature straddles around, the change in temperature, frequency of the change in temperature and the surface area of the sample connected to the current-measuring manipulator. The only variable setting was the base temperature. The change in temperature and frequency were kept at constant values of 1 K and 10 mHz respectively. The frequency of 10 mHz was selected because it was suitable for all thicknesses of the crystals to be measured, giving enough time for the sample bulk to cycle between the high and low temperatures.

Each sample began the temperature dependent pyroelectric measurements at room temperature to determine the polarity of each face. Then each sample underwent the same measurement beginning from the base temperature of 10℃ to 60℃ at incremental steps of 10℃. Each sample was measured six times at each base temperature. The first three measurements are disregarded as the sample may be adjusting to the new base temperature and the Peltier may not have reached the intended new base temperature.

3.3.3 DC conductivity

The experimental apparatus to measure the DC conductivity of the samples was adapted in accordance with the standard test method D257 developed by ASTM International [178]. The experimental apparatus was set up by coupling a picoammeter (Model 6487; Keithley Instruments, Inc., Cleveland, OH, U.S.A.) with a Probostat (Probostat™ Version A-6; NorECs Norwegian Electro Ceramics AS, Oslo, Norway) to measure resistance at high temperatures. The connections were made according to the diagram specific for DC resistance measurements found in the picoammeter manual [179]. The Probostat was also connected to a display unit (Model 34972A LXI Data Acquisition/Data Logger Switch Unit; Keysight Technologies, Santa Rosa, CA, U.S.A.) to show the temperature measured by the thermocouple near the sample.

The picoammeter acted as a voltage source when the "ohms function" was enabled to measure resistance. As the Probostat was not equipped to handle high voltages, direct measurements of resistance by applying 500 V DC cannot be made. Instead, the experiments will use an extrapolation method by applying a low voltage at high temperatures because resistance decreases at higher temperatures allowing the

picoammeter to take a measurement without tripping over the current limit. The measurement will start from 373.15 K and increasing in steps of 30 K to 673.15 K, if possible. The starting temperature was chosen as it was within the range at which the picoammeter can measure. A 20 V DC will be applied for 60 s, according to Procedure 12.2 in the ASTM D257, after which the resistance value will be recorded.

The samples must be prepared with metallic electrodes on the two parallel surfaces that will be in contact with the platinum electrodes of the Probostat. The samples were sputter coated (EM ACE600 high vacuum sputter coater; Leica Microsystems Pty. Ltd., Vienna, Austria) with 60 nm of platinum to avoid contamination with the Probostat electrodes. The remaining four surfaces perpendicular to the sputter-coated surfaces were ensured to have no coating.

The experimental apparatus and procedure were verified with a reference material of known DC volume resistivity. The material chosen was an insulative ceramic, macor (RS Components Pty. Ltd., NSW, Australia) and the measurements were referenced with temperature-dependent DC resistivity values collected by Corning SAS [180]. The samples that were tested, as listed in Table 3-2, were $LiNbO_3$, $LiTaO_3$ and PZT. Additionally, the composition, PMN-30PT prepared in the [111] orientation (Innovia Materials Co., Ltd., Shanghai, China), was measured. All samples had a thickness of approximately 0.5 mm.

3.4 Results and Discussion

3.4.1 Optical micrographs

The surfaces on the crystals from Hefei Crystal Technical Material Co., Ltd. were inspected under an optical microscope. As can be seen in Figure 3-7, Figure 3-8, Figure 3-9, the surfaces contain several surface defects and point scratches. However, this should not be an issue when measuring its pyroelectric properties as the parallel polar surfaces were sputter coated with gold. Unfortunately for the barium titanate samples, domains started forming in differing densities across all the barium titanate single crystals rendering them multi-domain single crystals.

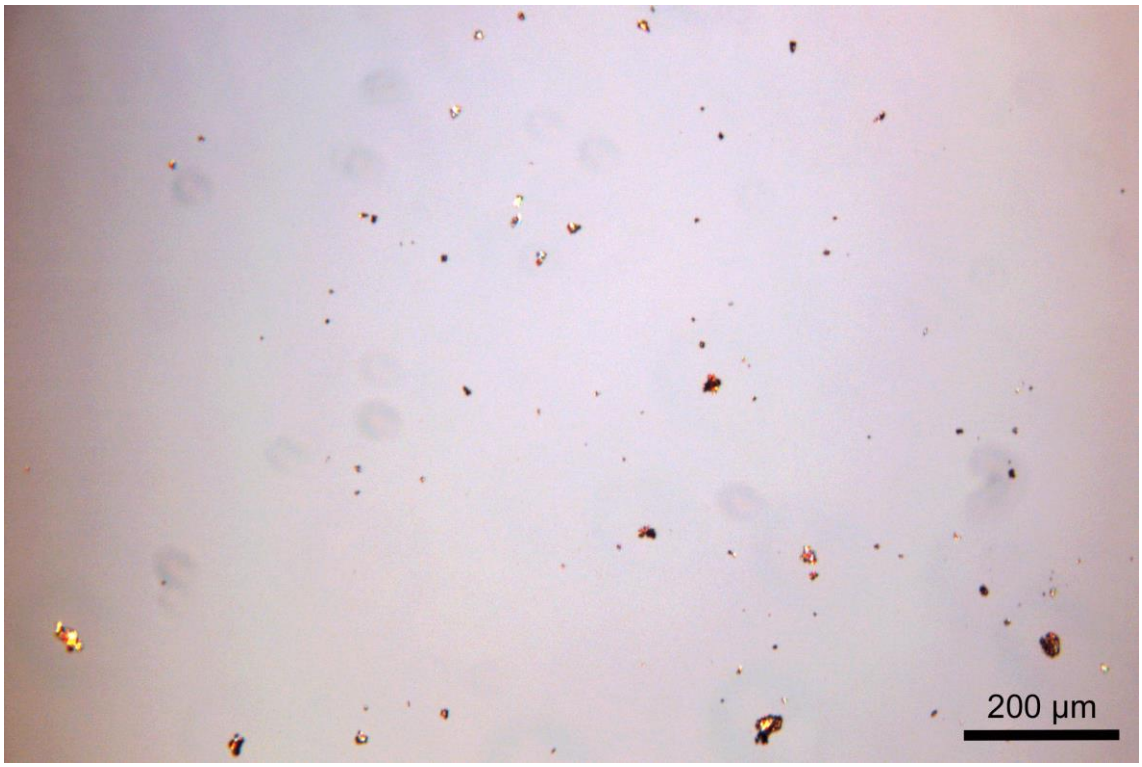

Figure 3-7 Surface defects can be seen on the surface of the lithium niobate single crystal.

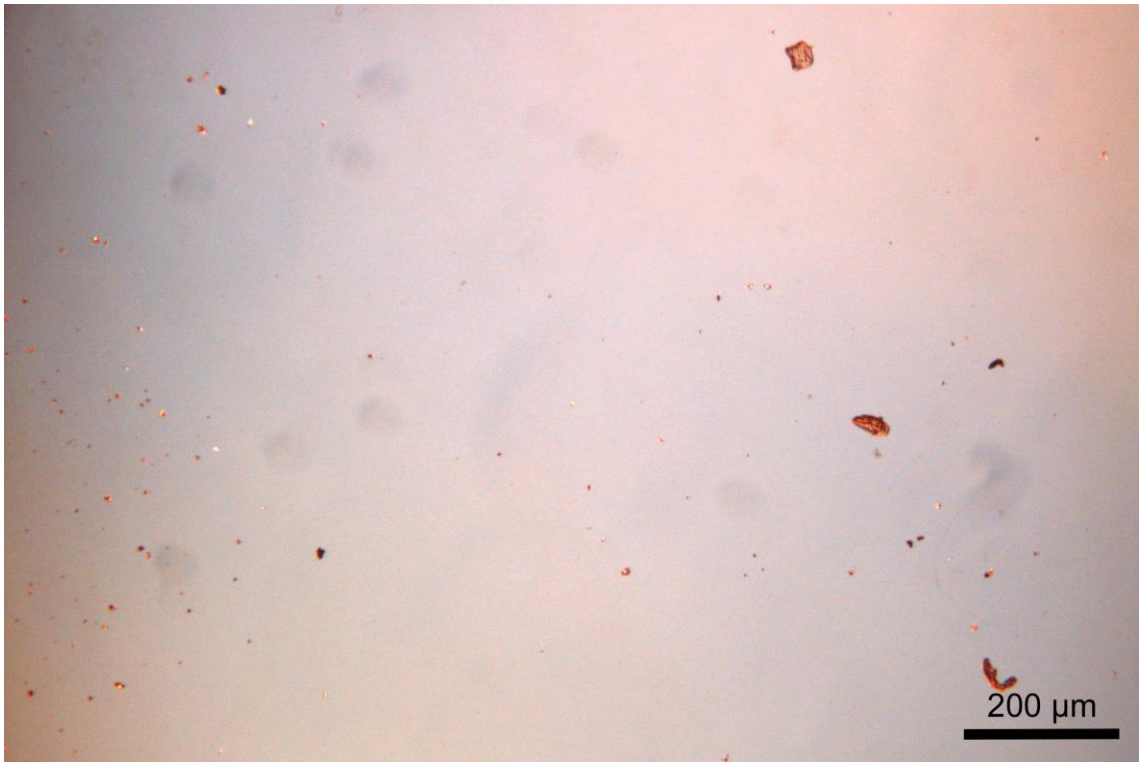

Figure 3-8 Cleaned surface of lithium tantalate with visible surface defects.

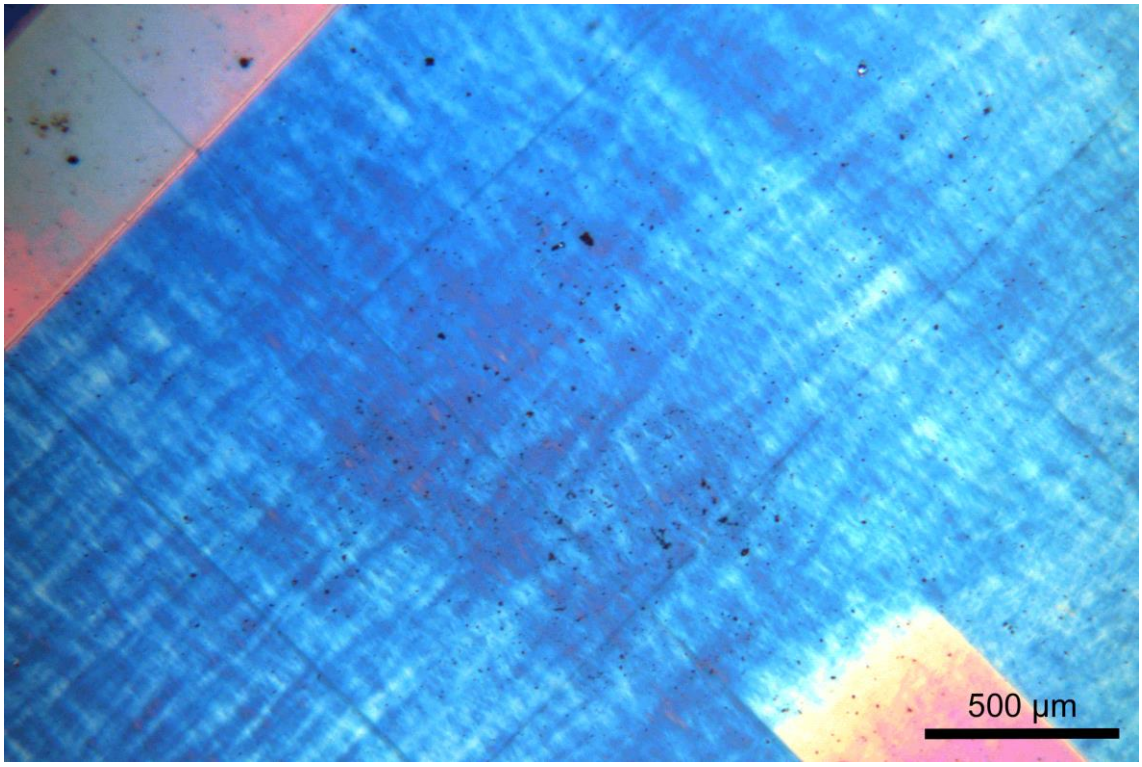

Figure 3-9 Barium titanate single crystal viewed under an optical microscope with a polarising filter applied. The single domain can be seen breaking into small domains.

3.4.2 Quality of electrodes on samples

First of all, the samples with a thickness of 0.5 mm proved difficult to shield the sides from being coated with masking tape. Therefore, another solution was to apply nail polish carefully on the edges. However, after cleaning the nail polish off the edge of 0.5 mm thick samples, small areas of the gold coating were accidentally removed. This can be seen in Figure 3-10 where the small cleaned areas were manually reapplied with silver paint. Upon closer inspection under the optical microscope (Figure 3-11), there were small minor areas close to the edges that were missed during the reapplication of silver paint.

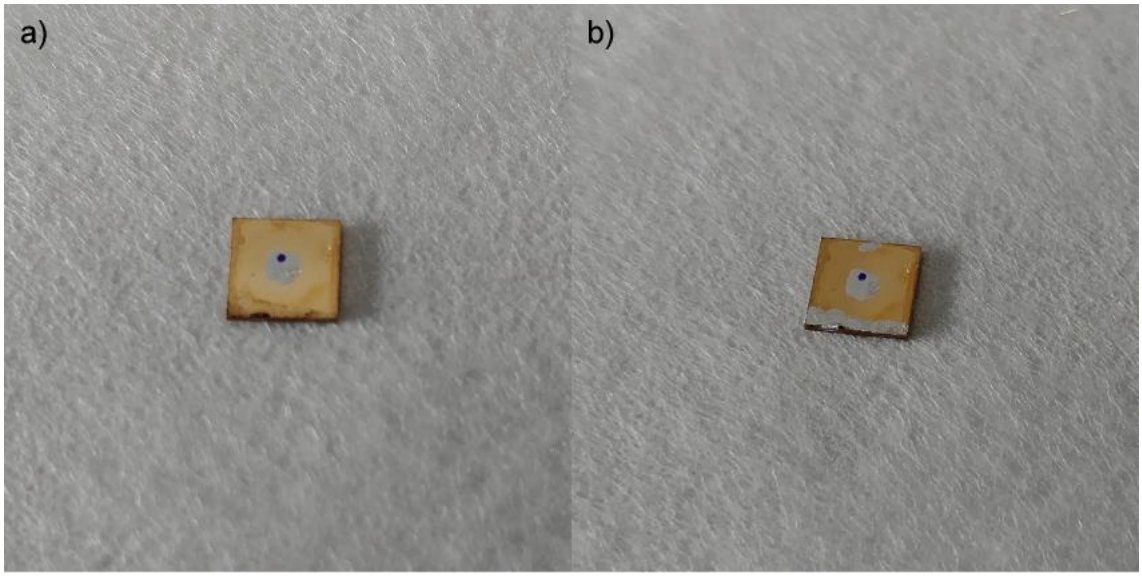

Figure 3-10 Lithium niobate with area of 25 mm^2 and thickness 0.5 mm with affected areas of gold coating removed (a) and recoated with silver paint (b).

During early measurements of the crystals, it was noticed that the sputter-coated gold coating began to debond. Figure 3-12 shows the coating of the crystal viewed under the optical microscope and Figure 3-13 shows the overall appearance of the crystals captured using a mobile phone camera. It was suspected that this was due to the repeated slow thermal cycling. As the pyroelectric coefficient is dependent on the surface area, the debonding of the coating could lead to miscalculation of the pyroelectric coefficient. To avoid this, silver paint was gently applied over affected areas using a small width flat paint brush.

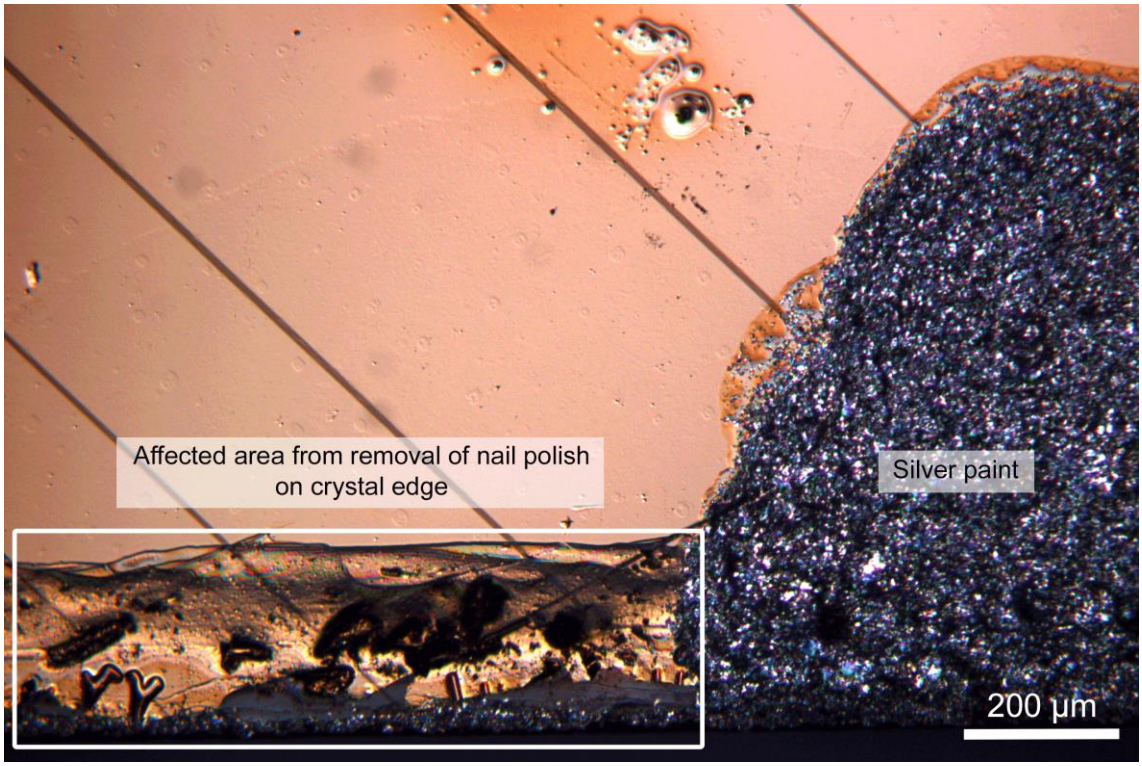

Figure 3-11 Closer inspection of the affected areas on the gold electrode during removal of the nail polish applied after sputtering.

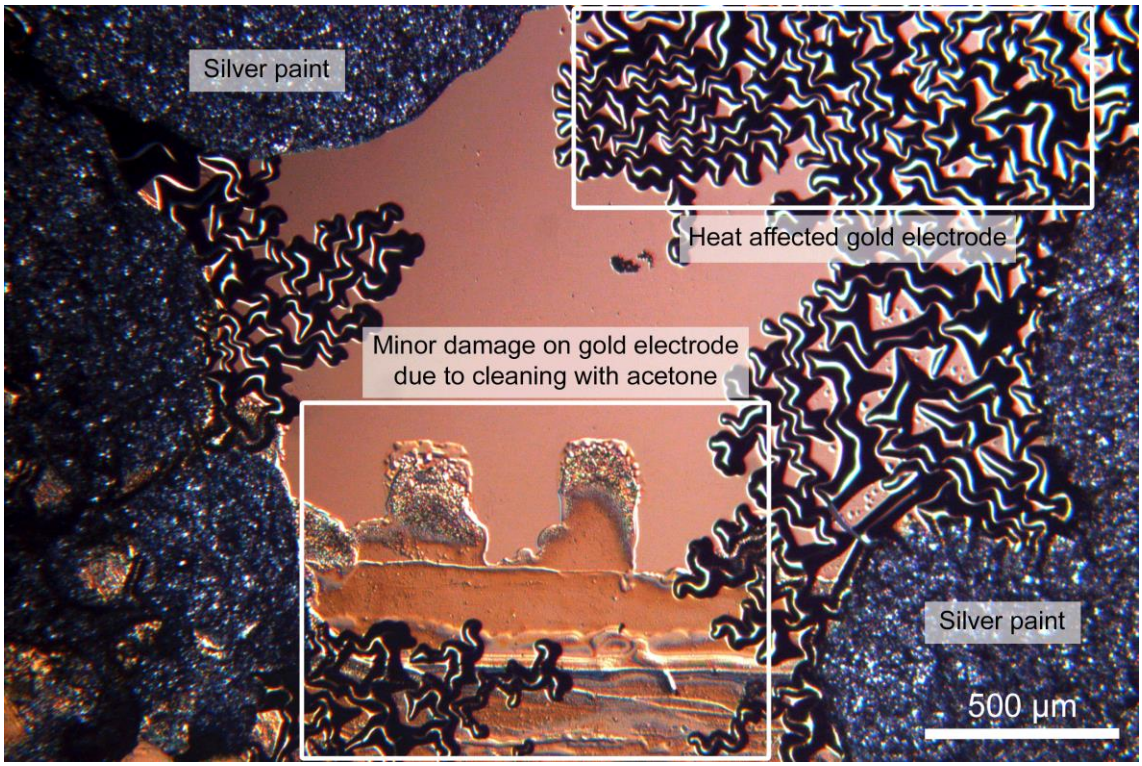

Figure 3-12 Optical micrograph of the gold electrode on a lithium niobate crystal with minor damage from cleaning the sample edge and areas of the gold electrode shrivelling due to heat. The damaged areas were repaired by silver paint.

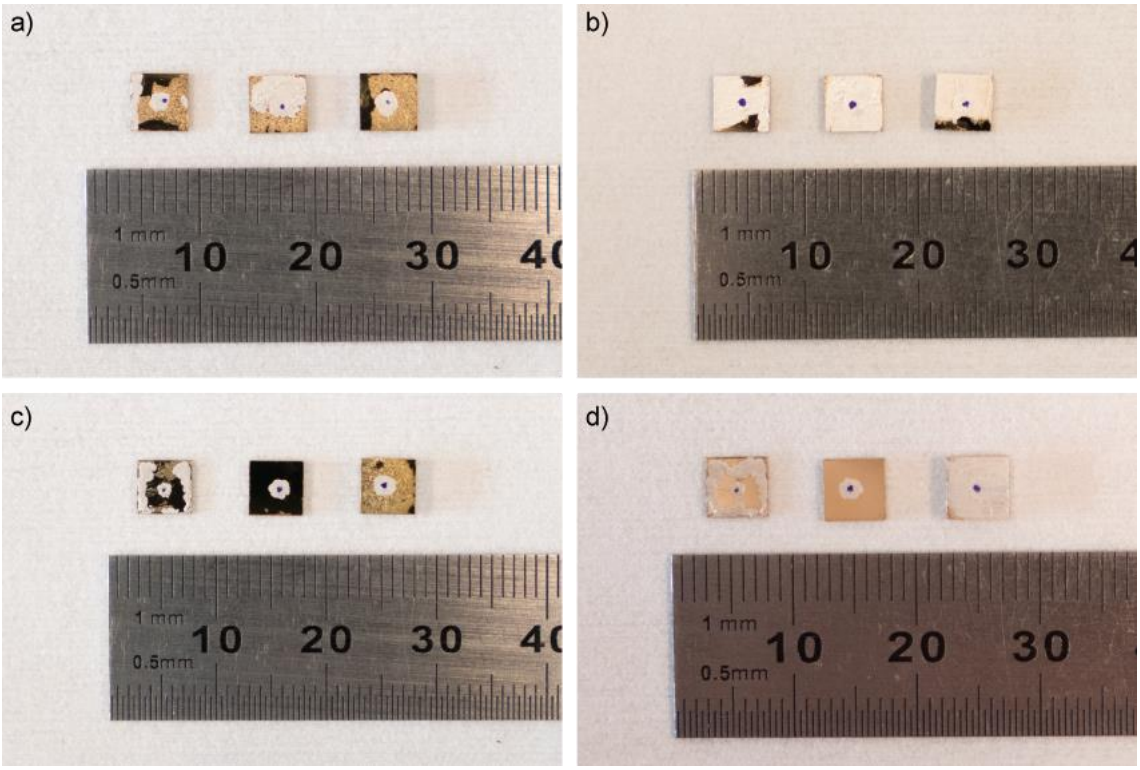

Figure 3-13 Gold coating on the single crystals before and after re-application of silver paint. (a) and (b) are of the three thicknesses of lithium niobate before and after respectively. Similarly, (c) and (d) are of lithium tantalate.

3.4.3 Pyroelectric coefficient

Using the dynamic method described in Chapter 3.2.2, Figure 3-14 presents the pyroelectric current measured as a function of time during ΔT of 1 K. The square waveform of the measurements is very similar across all samples measured. As the T_C of $LiNbO_3$ is 1140°C, the pyroelectric coefficient does not vary greatly between 10°C and 60°C. Therefore, the range of the current recorded at each set temperature will be relatively similar.

Figure 3-15 shows the evaluated pyroelectric coefficient measured at each set temperature. For lithium niobate single crystals, the pyroelectric coefficient increases marginally with temperature. However, there is no recognisable trend when comparing between the samples with thickness of 0.5 mm, 1.0 mm and 2.0 mm. As the pyroelectric coefficients of these three samples lie close to or within standard deviation of each other indicate that the thickness of the sample does not affect the pyroelectric performance of the sample. This agrees with Equation 3-3 where it does not include the thickness of the pyroelectric crystal as a factor. Such trend is also observed in the pyroelectric

measurement of lithium tantalate across the three thicknesses as illustrated in Figure 3-16. The pyroelectric coefficient of $LiNbO_3$ measured at room temperature also sits within the range of other reported pyroelectric coefficient values, listed in Table 3-1, acquired at room temperature via other methods.

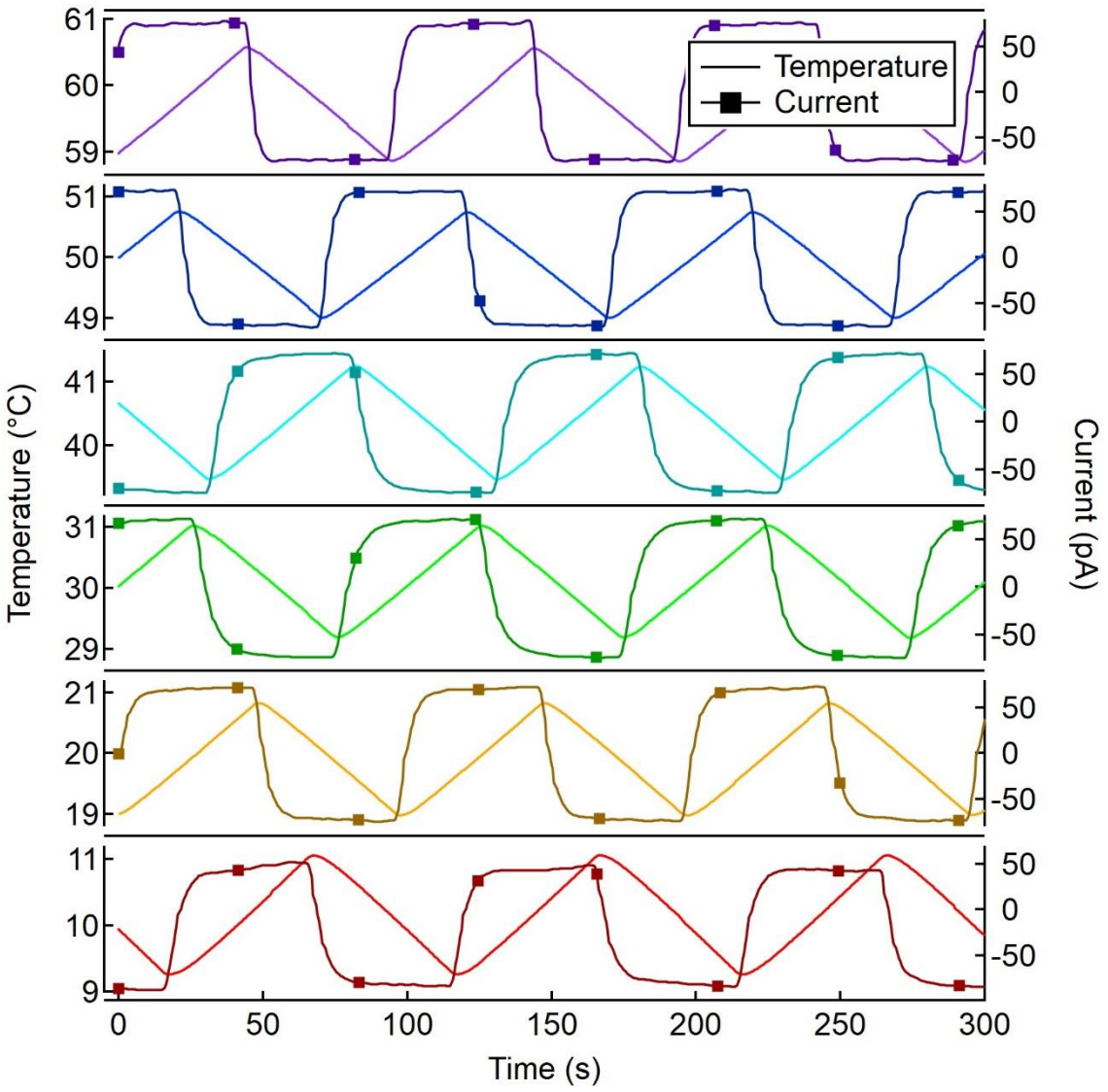

Figure 3-14 Pyroelectric current response measured at temperatures from 10°C to 60°C on lithium niobate with thickness of 0.5 mm.

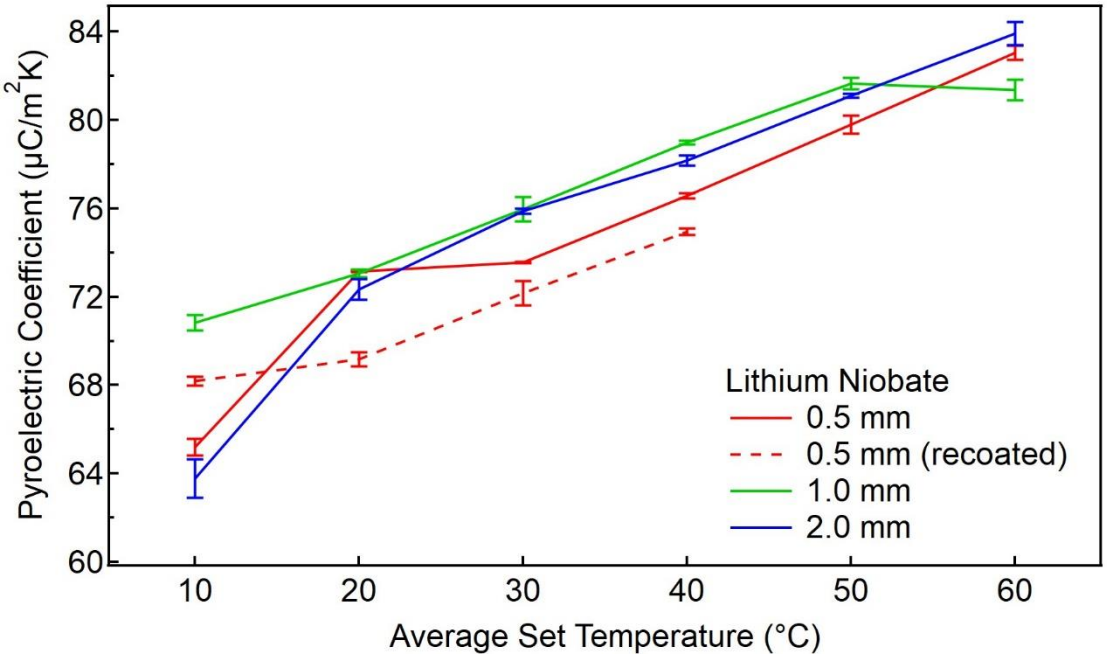

Figure 3-15 Mean pyroelectric coefficient of lithium niobate measured over a range of temperatures. Error bars represent a standard deviation over three repeated measurements.

Due to the debonding of the gold coating on the crystal surface and retouching of the affected areas with silver paint, the lithium niobate single crystal with thickness of 0.5 mm is measured again to determine if it may have caused incorrect measurement of the pyroelectric coefficient due to a reduction in coated surface area. The data in Figure 3-15 and Figure 3-16 show that while there is a reduction in the pyroelectric coefficient, the difference is marginal and may have been due to a thicker uneven organic electrode. This also confirms that the measurement before the sample is retouched can be used for further calculations.

The pyroelectric coefficient of $LiTaO_3$ at 25°C averaged at about 157 $\mu C/m^2K$ across the three crystal thicknesses. This sits within a reasonable range with reported values acquired in Table 3-1 where the pyroelectric properties were measured at room temperature (25-27°C).

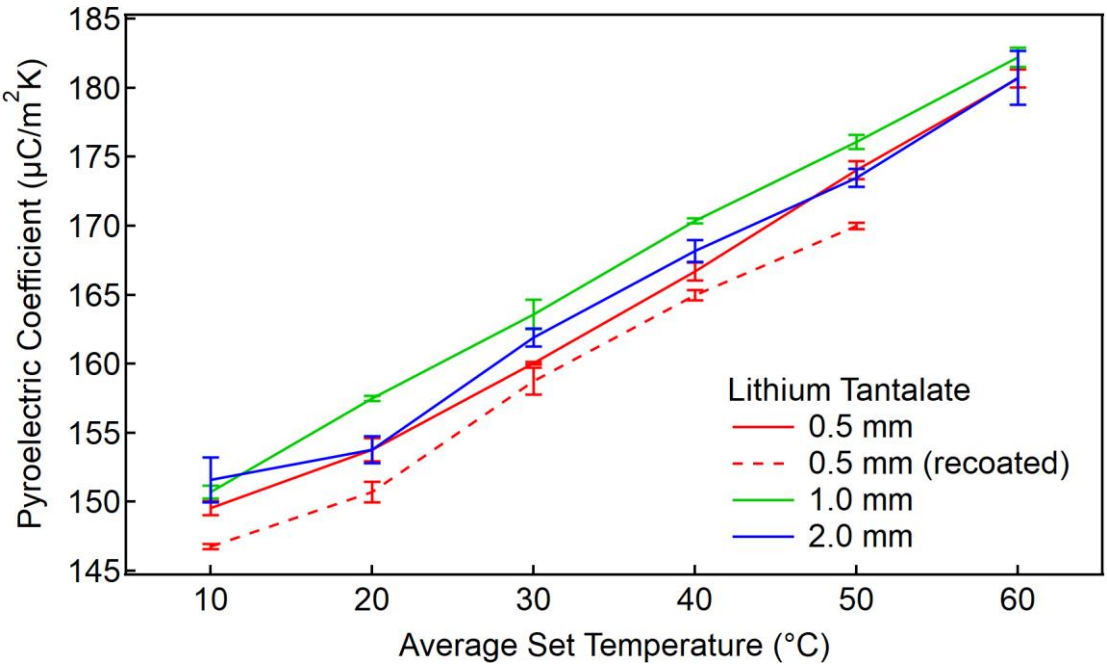

Figure 3-16 Mean pyroelectric coefficient of lithium tantalate measured over a range of temperatures. Error bars represent a standard deviation over three repeated measurements.

The pyroelectric coefficient of PZT displays the same increasing trend with applied temperature as with $LiNbO_3$ and $LiTaO_3$. The rising gradient on the pyroelectric coefficient was also observed by Cook *et al.* [181]. Furthermore, it is evident in Figure 3-17 that when PZT is poled via high temperature field poling, it produces a greater pyroelectric coefficient than when it is poled via pulse poling. An extended period of poling at elevated temperatures is able to overcome any interdomain stresses and reorient most domains, thus maintaining the alignment of majority of the dipoles after removal of the poling field [40].

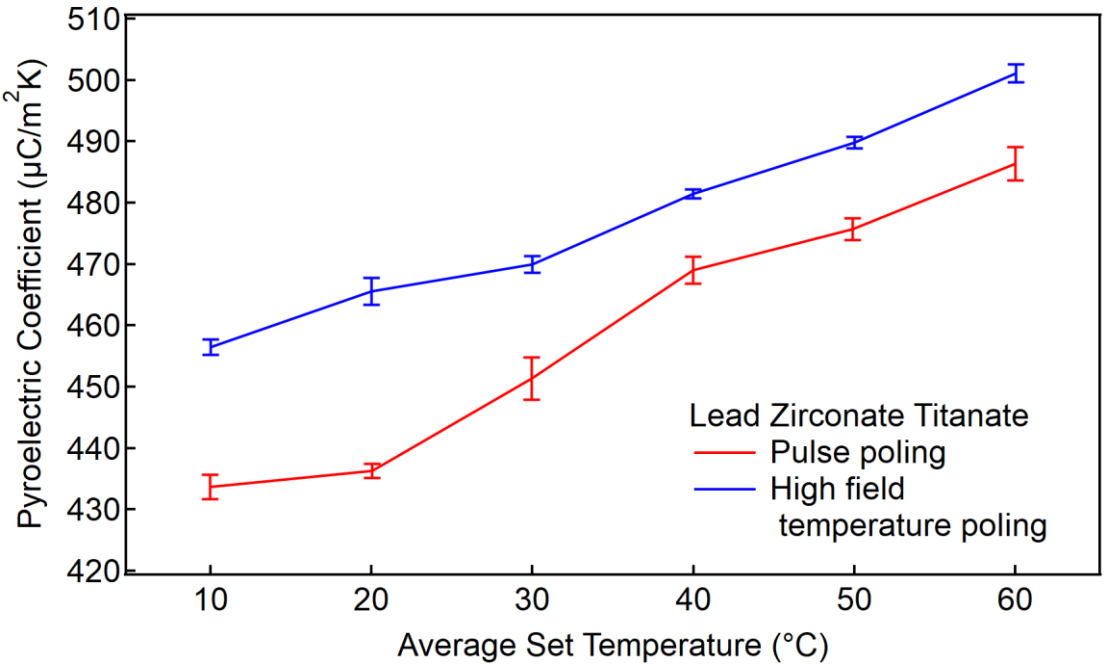

Figure 3-17 Mean pyroelectric coefficient as a function of temperature of lead zirconate titanate (PIC151), prepared by pulse poling and high temperature field poling. Error bars represent a standard deviation over three repeated measurements.

The single crystal $BaTiO_3$ presents a mix of results due to a combination of temperature and stress the single crystals had been exposed to. To use $BaTiO_3$ as an X-ray generator source, it must have a unipolar axis aligned perpendicular to the target. This means that $BaTiO_3$ must be in its tetragonal crystal system with the polar surfaces perpendicular to the [001] direction. Because of this condition, the usable temperature range is limited between 5°C and 120°C. It is possible during its transit from the manufacturer to the lab that the single crystals may have been stressed causing the single domain to break into smaller domains, as observed in Figure 3-9. As a result, each $BaTiO_3$ single crystal is tested to confirm its poled state by measuring its capacitance and comparing with literature values, prior to undertaking pyroelectric coefficient measurements.

Table 3-3 Capacitance and relative permittivity of barium titanate samples.

Sample	Capacitance, C (pF)	Relative Permittivity, ε_r
BaTiO3, crystal thickness of 0.5 mm		
1	55	140
2	55	140
3	99	252
4	0.001	N/A
5	61	154
BaTiO3, crystal thickness of 1.0 mm		
1	39	180
2	25	115
3	78	355
4	61	279
5	26	117

Based on the capacitance values, sample 3 and sample 4 of both thicknesses of $BaTiO_3$ have formed multiple domains and causing depoling of the samples. Therefore, only samples 1, 2 and 5 can be measured. The surface area of the samples was consistent amongst all the samples. Due to the large variation in capacitance, all three samples of both thicknesses were measured. While all pyroelectric current curves in Figure 3-18 look very similar, the pyroelectric coefficient displayed some differences. The coefficients measured seems to agree with single crystal and ceramic $BaTiO_3$ measured via other methods after the temperature has surpassed further from the orthorhombic-tetragonal phase transition temperature [181, 182].

Although the effect of multi-domains in ferroelectric materials for X-ray generation has not been studied, the use of polycrystalline ferroelectric ceramics has been previously demonstrated [183, 184]. However, the multi-domains inherent to polycrystalline ceramics would have been poled such that it obtains a net polarisation direction. In the case of samples 3 and 4 of both thicknesses, the multi-domain formation and depoling events occur to nullify the surface charge density on the polar surfaces. This leads to a reduction of its net polarisation from its initial single domain polarisation state. As a result, it lowers the ferroelectric material's ability to create a sufficiently intense electric field within the gap and reduces its overall efficiency.

While the multi-domain formation and depoling is unfavourable for this application and may have been due to transportation of the samples, the two events occurring together is not exclusive to $BaTiO_3$ and applies to all ferroelectric materials. Thus, it is preferable to maintain a single domain state to maximise the surface charge density apparent on the polar surfaces to attain maximal X-ray generation.

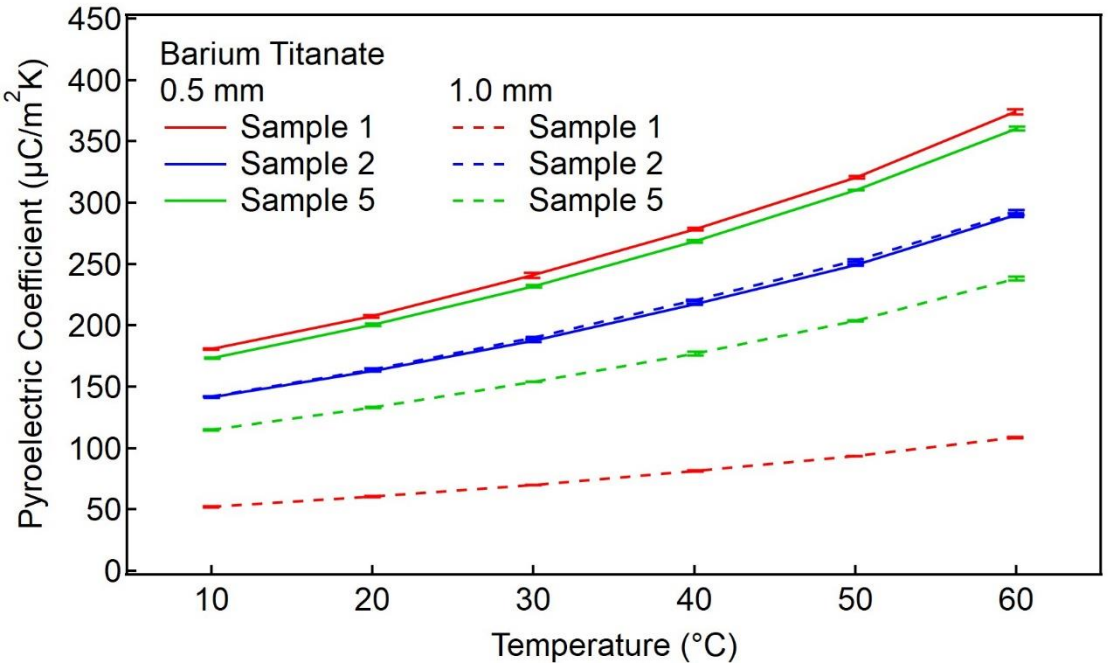

Figure 3-18 Mean pyroelectric coefficient as a function of temperature of selected barium titanate single crystals with single domains. Error bars represent a standard deviation over three repeated measurements.

The PMN-33PT and PMN-28PT single crystals with orientations in the [111] direction have higher pyroelectric coefficients than the single crystals with the [001] orientation, as seen in Figure 3-19. The pyroelectric coefficient values measured at room temperature are slightly lower than the published results of the same materials by Davis *et al.* [137] as the materials may have depoled after several years however the measurements do not differ significantly. The difference between PMN-28PT and PMN-33PT can be attributed to the phase the composition lies in. PMN-28PT sits in the rhombohedral phase while PMN-33PT lies in the narrow monoclinic morphotropic phase boundary. It has been reported previously that compositions of the rhombohedral phase near the morphotropic phase boundary possess superior piezoelectric properties [47, 137, 185-187]. However, the superior piezoelectric properties are not necessarily correlated with superior pyroelectric properties, as the two mechanisms are not directly linked.

Particularly in morphotropic phase boundary regions, electric field induced variations to the polar vector can be very different to temperature induced changes.

Additionally, according to the aforementioned study [137], the poling conditions applied on PMN-33PT is such that its monoclinic phase can be assumed to share the same symmetry as a rhombohedral phase. Due to crystal anisotropy, when a multi-domain composition is poled along its unique spontaneous polarisation direction or polar axis, it is able to match more closely to a monodomain state and its pyroelectric behaviour is maximised. Thus, poling the material off-axis will result in a lower pyroelectric coefficient.

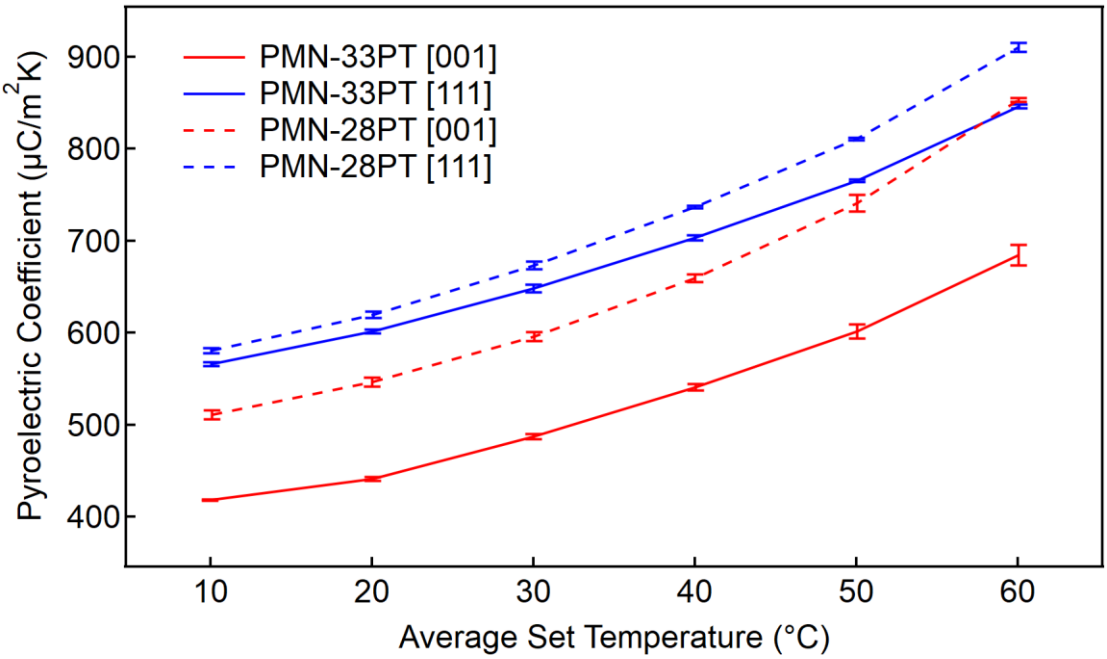

Figure 3-19 Mean pyroelectric coefficient as a function of temperature of the single crystals, PMN-33PT and PMN-28PT prepared in the [001] and [111] directions. Error bars represent a standard deviation over three repeated measurements.

Figure 3-20 combines the pyroelectric coefficient for all the measured samples as a function of temperature. All the lead-based samples possessed greater pyroelectric coefficients than $BaTiO_3$, $LiTaO_3$ and $LiNbO_3$. The average of the three samples for each crystal thickness is taken as the pyroelectric coefficient of $BaTiO_3$. Little variation is observed for the range of crystal thicknesses measured in $LiTaO_3$ and $LiNbO_3$. The reason for the difference in the gradients is due to the magnitude of the samples' Curie point or phase transition temperature. The lead-based PMN-PT and PZT samples are

limited by their phase transition temperature of ~100℃ and T_C of 250℃, respectively, whereas the T_C of $LiTaO_3$ and $LiNbO_3$ are 610℃ and 1140℃, respectively. In terms of employing materials for pyroelectric X-ray generators, it is beneficial to thermally cycle a composition near T_C because its pyroelectric coefficient and ΔP_S increases dramatically. Therefore, a large surface charge can be harnessed to emit more electronic charge and increase the X-ray count. This has been exemplified by Riege [53] who demonstrated a heightened spectrum of electrons when a TGS crystal is heated near T_C.

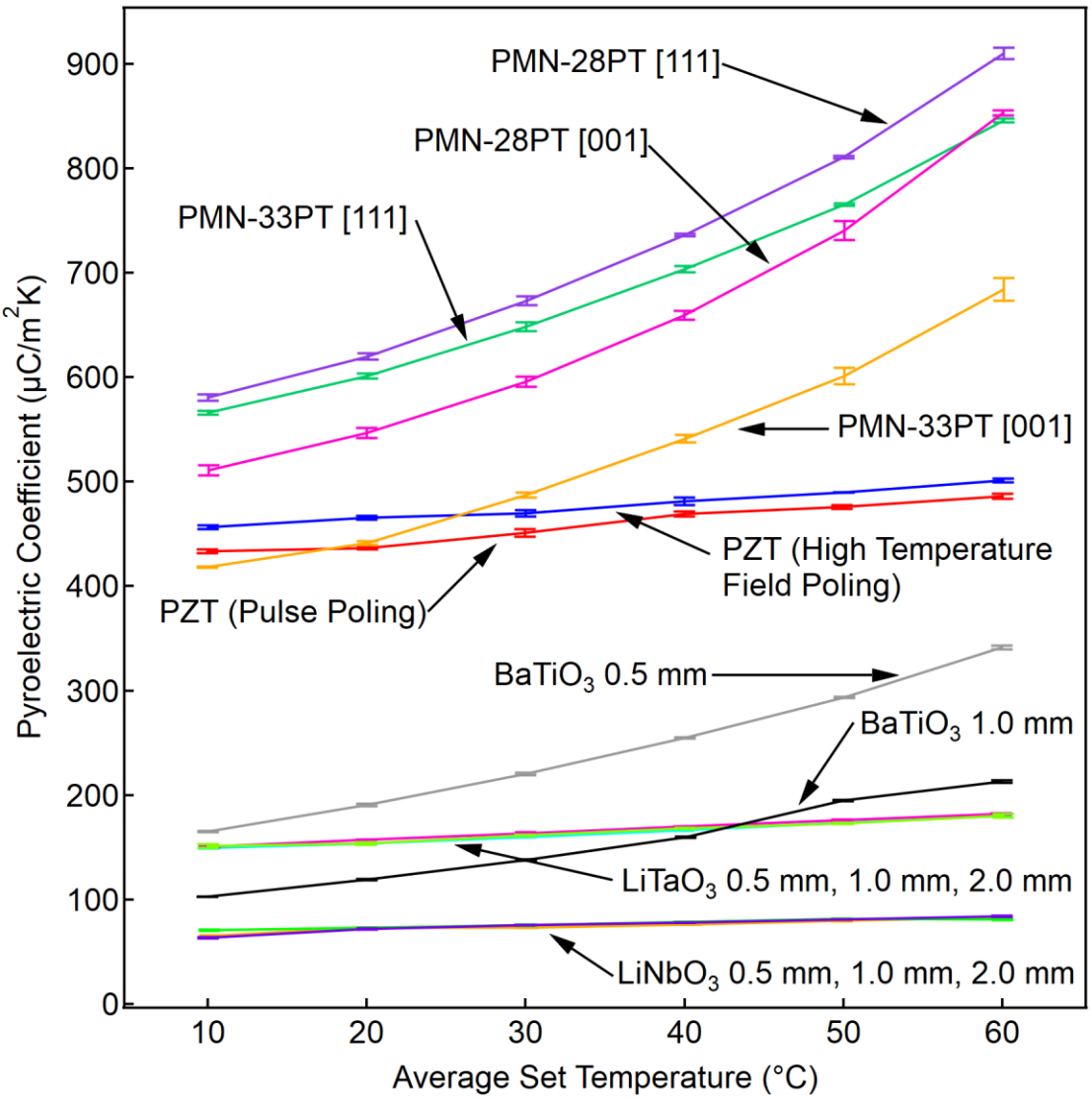

Figure 3-20 Mean pyroelectric coefficient of various compositions as a function of temperature. Error bars represent a standard deviation over three repeated measurements.

3.4.4 DC conductivity

According to Table 1 in the ASTM D257 Standard Test Method [178], the DC volume resistivity for square planed samples can be calculated using:

$$\varrho = \frac{A}{t} R \tag{3-16}$$

where ϱ is the volume resistivity, A is the area of the electrodes, t is the thickness of the sample or the distance separating the electrodes, and R is the measured resistance.

The DC conductivity at room temperature can be extrapolated from DC resistance measurements at high temperatures by using the Arrhenius relationship of conductivity as a function of absolute temperature.

$$\sigma_c = \sigma_0 e^{-\frac{E_a}{kT}} \tag{3-17}$$

where σ_c is the DC conductivity of the sample, σ_0 is the pre-exponential factor, T is the absolute temperature, E_a is the activation energy (eV) and k is the Boltzmann constant (8.6173303×10^{-5} eV/K).

Equation 3-17 can be rearranged,

$$\ln(\sigma_c) = \ln(\sigma_0) - \frac{E_a}{kT} \tag{3-18}$$

By plotting the log conductivity measurements against the inverse temperatures, the activation energy can be determined from the slope of the linear fit line.

The modified experimental apparatus and procedure is verified by testing an insulative ceramic, macor, at higher temperatures. The measured resistivity displayed in Table 3-4 showed good agreement with the literature values indicating that the adapted experimental apparatus can be trusted to measure other samples.

Table 3-4 Resistivity of macor measured at two temperatures and compared to literature values.

Temperature (°C)	Measured Resistivity (Ω·cm)	Literature log(Resistivity) (Ω·cm)
186.7	1.435×10^{11}	11
295.0	1.382×10^{9}	9

The conductivities of the selected samples are plotted in Figure 3-21. For $LiTaO_3$ and PZT, there appears to be two linear regions of different activation energies. The region at higher temperatures was used, as the resistance measured at lower temperatures was not reliable due to the current limit on the picoammeter. Similarly, in $LiNbO_3$, three regions can be seen. These different regions suggest that there is a change in the conduction process.

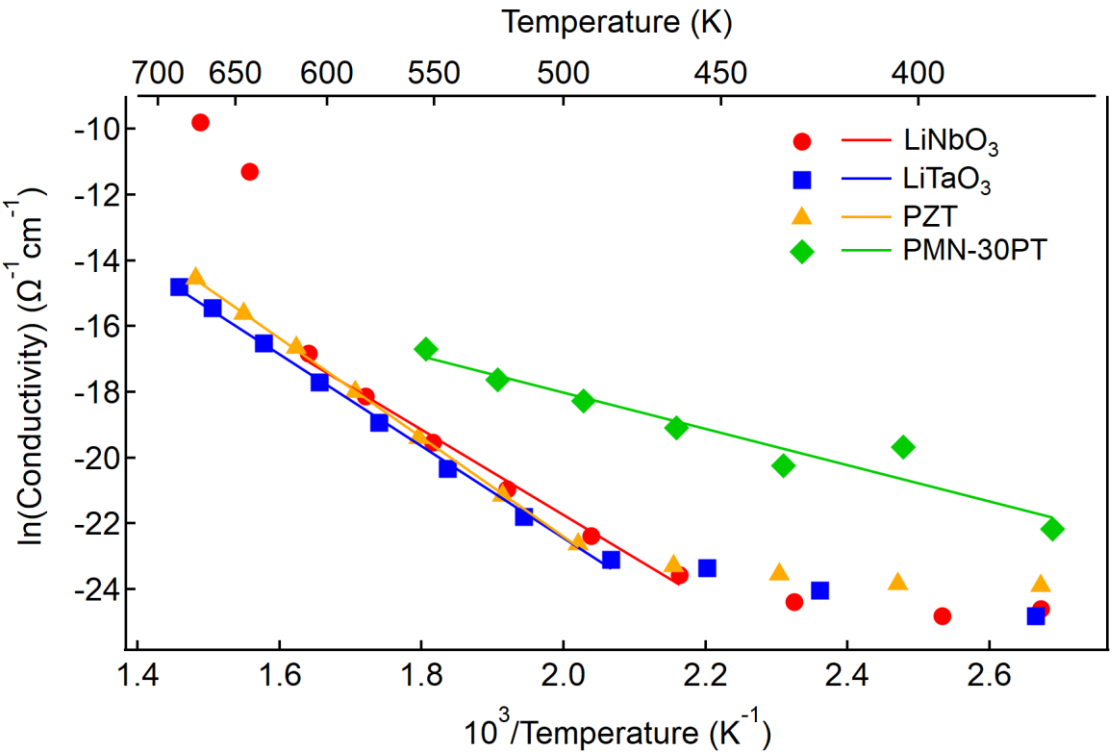

Figure 3-21 Variation of ln(DC conductivity) with inverse temperature of $LiNbO_3$, $LiTaO_3$, PZT and PMN-30PT.

The evaluated activation energies and extrapolated conductivity at temperatures 0°C and 100°C are presented in Table 3-5. These evaluated activation energies are consistent with the findings in other reports [155, 156, 188, 189]. However, there is some variation in the

bulk conductivity of the samples. $LiNbO_3$, $LiTaO_3$ and PZT displays similar activation energies while PMN-30PT is half in magnitude.

Table 3-5 Activation energy and conductivity of measured samples evaluated from the Arrhenius relationship between conductivity and temperature.

Composition	E_a (eV)	σ_c $(\Omega^{-1}cm^{-1})$ at		
		T = 273.15 K	T = 293.15 K	T = 373.15 K
$LiNbO_3$	1.1164	1.622×10^{-19}	4.123×10^{-18}	5.367×10^{-14}
$LiTaO_3$	1.2032	1.508×10^{-20}	4.933×10^{-19}	1.343×10^{-14}
PZT	1.3004	2.438×10^{-21}	1.057×10^{-19}	6.562×10^{-15}
PMN-30PT	0.4753	1.558×10^{-12}	6.179×10^{-12}	3.489×10^{-10}

3.4.5 Figure-of-merit

The series of values, charge density on the polar surface, electric field in the gap and the two figure-of-merits, are evaluated using equations presented in Chapter 3.2.3 and the pyroelectric coefficient and conductivity determined in Chapters 3.4.3 and 3.4.4. The pyroelectric coefficient and DC conductivity used in the calculations were taken as an average over the measure temperature range.

Table 3-6 Pyroelectric coefficient and DC conductivity of the samples taken as an average of the temperatures the materials.

Composition	p ($\mu C/m^2K$)	σ_c $(\Omega^{-1}cm^{-1})$
$LiNbO_3$	75.2206, 76.9833, 75.8739	7.78253×10^{-15}
$LiTaO_3$	164.139, 166.739, 164.933	1.86763×10^{-15}
$BaTiO_3$	257.65, 154.716, 206.183	–
PZT	377.395	8.76304×10^{-16}
PMN-28PT [001]	651.383	–
PMN-28PT [111]	721.906	–
PMN-33PT [001]	528.966	–
PMN-33PT [111]	688.422	–
$BiFeO_3$	32	–
PMN-30PT [111]	–	8.77689×10^{-11}

In Figure 3-22, the charge density on the exposed surface of the crystal and the electric field in the gap was calculated for the three thicknesses measured in the set of pyroelectric measurements. The distance of the gap was fixed at 3.7 mm for simplicity. The ΔT is selected based on the phase of the crystal. That is, for $BaTiO_3$ and PMN-PT, the ΔT is set at 90°C instead of 100°C to ensure it is below the phase transition temperature. The rate of temperature change is maintained at 10°C/min. Focusing on the range of PMN-PT compositions, their pyroelectric coefficients had greater pyroelectric coefficients than the other samples. As the charge density relies only on the pyroelectric coefficient, all PMN-PT compositions will also have higher charge densities over the other samples. However, the PMN-PT compositions produced lower electric fields in the gap than the $LiNbO_3$ and $LiTaO_3$ samples. This is because the electric field in the gap (Equation 3-8) relies on both the material's pyroelectric coefficient and relative permittivity. In essence, the ratio of the material's pyroelectric coefficient to its relative permittivity determines the magnitude of the electric field in the gap.

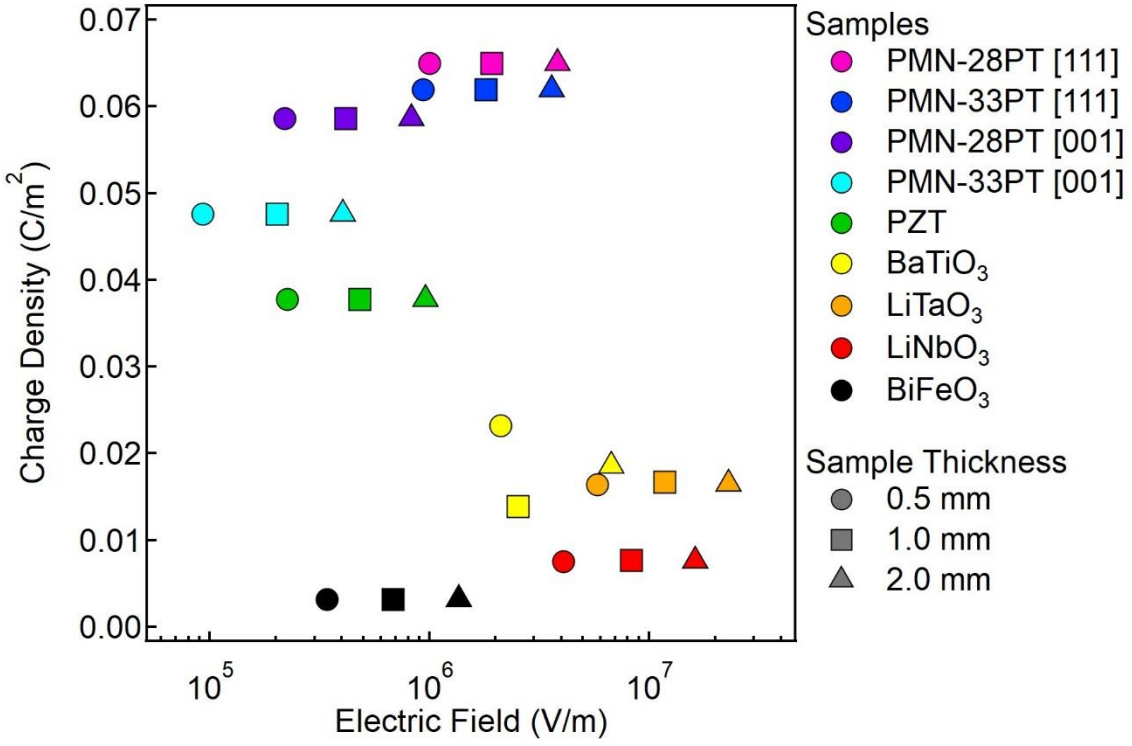

Figure 3-22 Charge density on the exposed surface of the crystal and the electric field attainable in the gap evaluated at a gap distance of 3.7 mm.

As explained in Chapter 3.2.3, Shur and Rosenman [142] determined two figures-of-merit for the electron emission phenomena. The results using the figure of merit, F_ε, will be discussed first. When applying Equation 3-15, it can be seen in Figure 3-23 and Figure 3-24, $LiTaO_3$ has the highest ratio of pyroelectric coefficient to relative permittivity followed by $LiNbO_3$. These two compositions sit above the PMN-PT compositions, and the order follows the same order of electric field magnitude as Figure 3-22. Furthermore, F_ε increases with increasing crystal thickness and smaller gap distances. Therefore, a combination of a pyroelectric material with high pyroelectric coefficient and small relative permittivity, as well as a large crystal thickness and small gap distance are preferable in order to obtain a high F_ε.

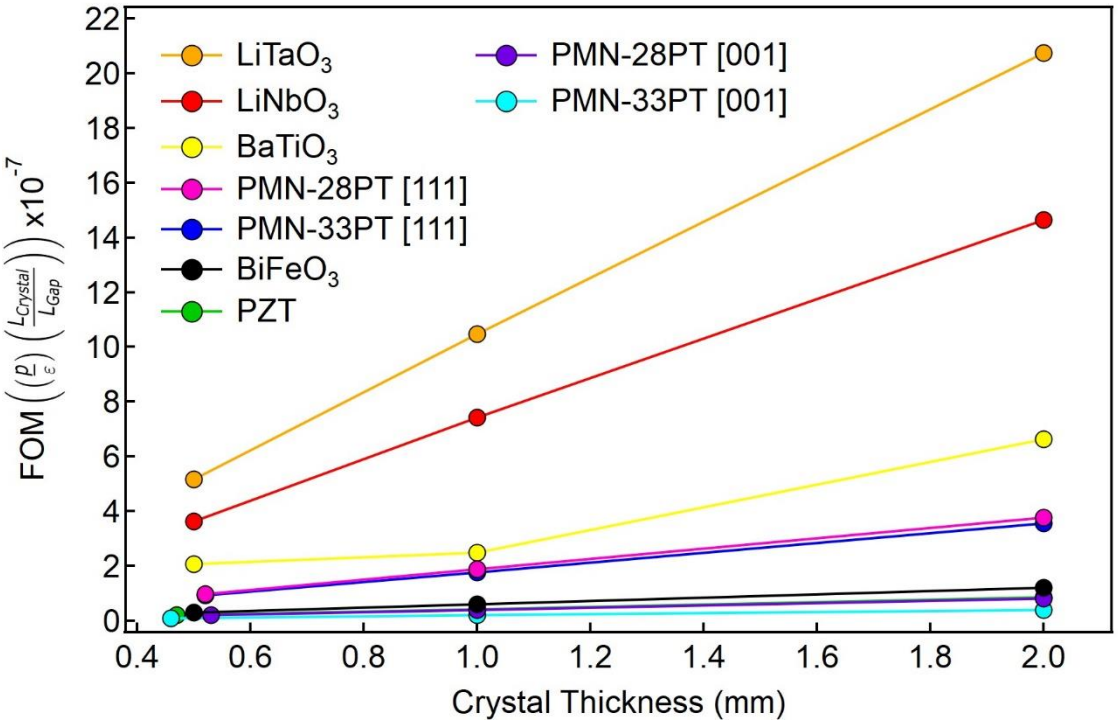

Figure 3-23 Figure-of-merit, F_ε, as a function of crystal thickness, calculated at a gap distance of 3.7 mm.

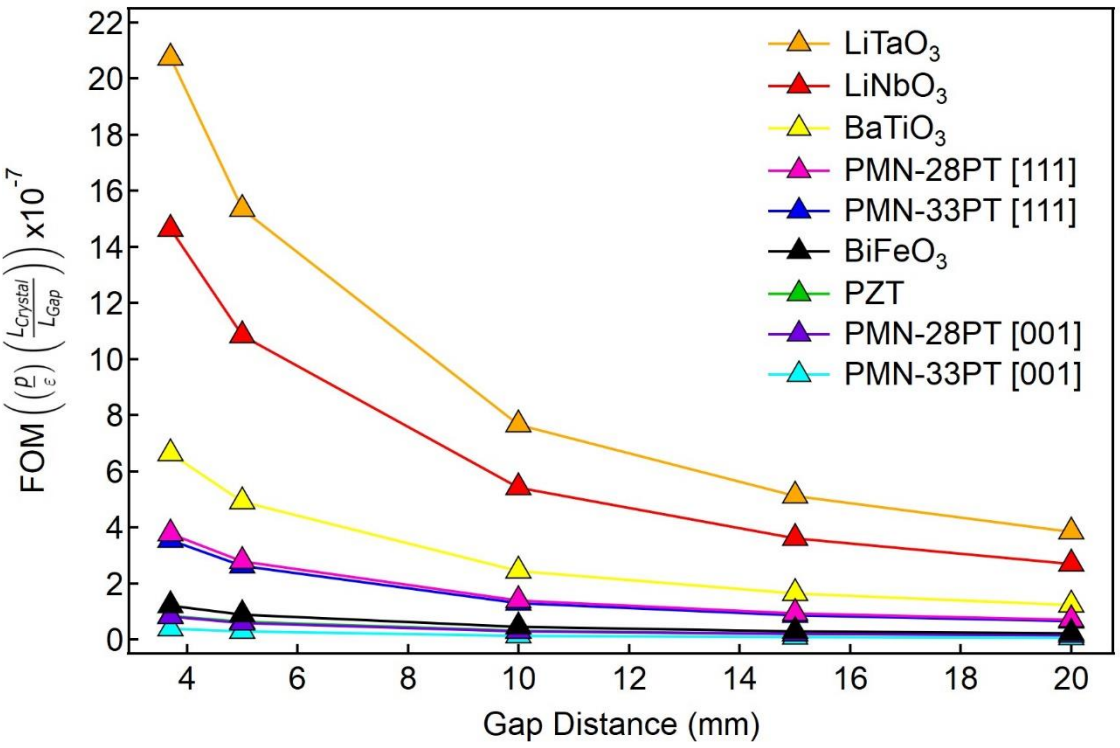

Figure 3-24 Figure-of-merit, F_ε, as a function of gap distance, evaluated with a crystal thickness of 2.0 mm.

The results calculating from F_σ with the condition that it must exceed at least 10^7 V/m to observe X-rays is now presented. As the DC conductivity of PMN-28PT, PMN-33PT and $BiFeO_3$ were not measured, F_σ is not evaluated for those compositions. The figure-of-merit for PMN-30PT presented here will be compared to PMN-28PT in the earlier figure-of-merit as PMN-28PT and PMN-30PT lie in the rhombohedral phase.

Unlike the earlier results presented in Figure 3-22, Figure 3-23 and Figure 3-24, the commercial PZT exhibited a higher F_σ than $LiTaO_3$ and $LiNbO_3$. This is predominantly due to its bulk conductivity being the smallest amongst all the compositions measured. However, a comparison study of the X-ray output from $LiNbO_3$ and PZT-19 demonstrated that F_ε was the more applicable criterion as $LiNbO_3$ produced better results [184].

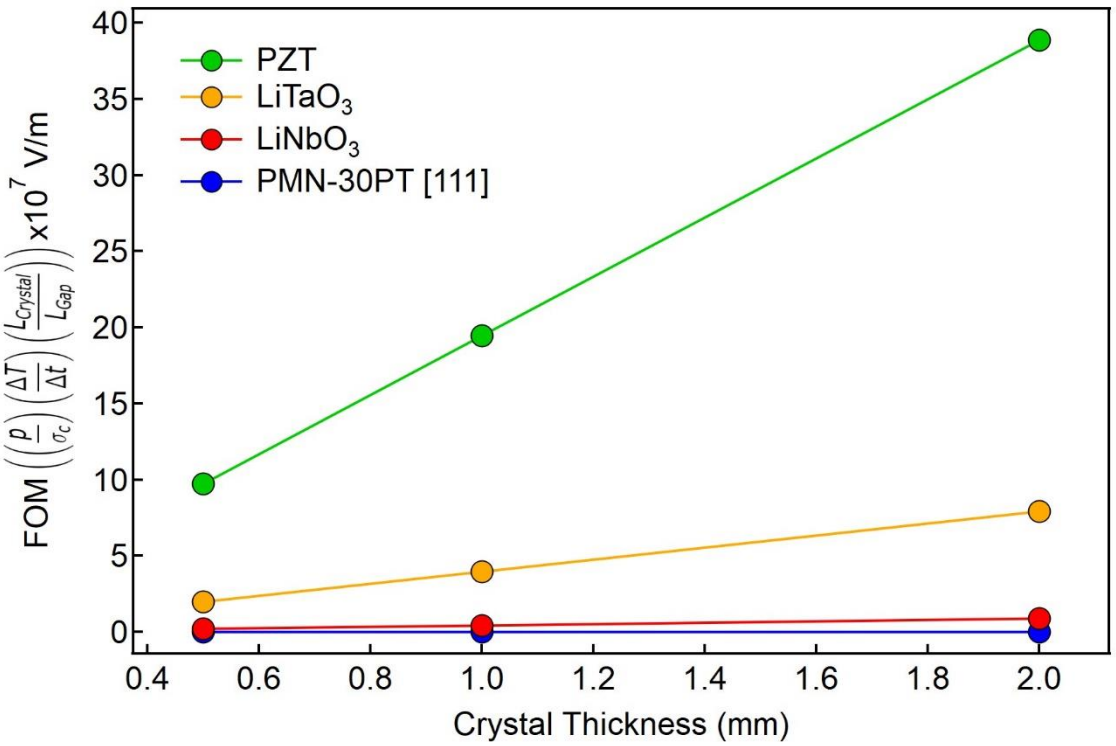

Figure 3-25 Figure-of-merit, F_σ, as a function of crystal thickness, calculated at a gap distance of 3.7 mm.

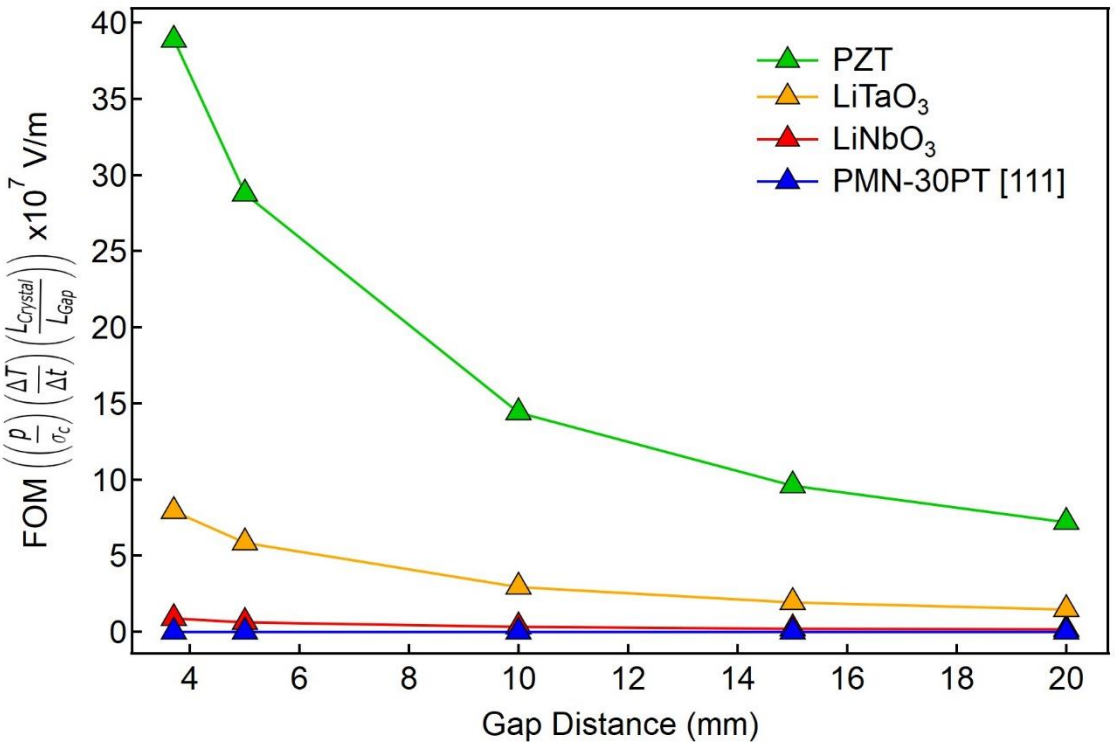

Figure 3-26 Figure-of-merit, F_σ, as a function of gap distance, calculated with a crystal thickness of 2.0 mm.

On the other hand, if considering the electric field at which the electron emission phenomena occurs, the resulting F_σ calculated for most of the materials suggest that the electric field in the gap is not intense enough. The difference in electric field magnitude compared to literature could be due to variation in material property values or experimental parameters. In Rosenblum *et al.*'s [54] study where the electric field was determined, the thermal cycling rate was double that of the rate used in the above calculations. In Rosenman *et al.*'s [60, 142, 143] few studies using $LiNbO_3$, the pyroelectric coefficient was larger and the bulk conductivity was smaller. This leads to the electric field being one magnitude larger than the values deduced here.

The trends exhibited from the two figures-of-merit reinforce a few important concepts. The chosen material should have a high p/ε ratio and high p/σ_c ratio. A thicker crystal placed at a shorter gap distance as well as a fast temperature change rate will also create a larger electric field in the gap However, there are a few limiting features. Finding a pyroelectric material with a good combination of p/ε and p/σ_c is difficult. Furthermore, the temperature range the material can be cycled in is dependent on its phase and as these materials have low thermal conductivity, it is impractical to have uniform heating across the thickness of the material when the thermoelectric cooler is only placed on one face. Tornow *et al.* [190] mentions the same difficulty with using thicker crystals due to a larger mass leading to non-uniform heating and cooling.

It must be reinforced that these figures-of-merit employed are specific only to the electric field in the gap. There are other factors that can influence the emission of electrons such as the work function of the pyroelectric material and metal target, and the ionisation energy of the gas in the vacuum chamber. Subsequently, these factors can also affect the generation of X-rays and need to be optimised. Therefore, the compositions measured in this chapter must be tested in the X-ray generator to validate of the applicability of the figures-of-merit and to optimise one parameter of the X-ray generator.

This page is intentionally left blank.

4

ELECTROSTATICS SIMULATIONS

"Every puzzle has an answer."

– *Professor Layton*

4.1 Overview

This chapter explores the pyroelectric generation of X-rays via finite element modelling. The software employed was COMSOL Multiphysics® and its electrostatics module. Very few computer modelling studies have been reported in literature with most using Monte Carlo to predict the best materials and geometry in the X-ray generator configuration. By undertaking an electrostatics simulation study, it serves as an extension of the two-capacitor model presented in Chapter 3 and to provide a more accurate representation of the electric field and potential produced around the pyroelectric crystal and the target.

4.2 Simulation Model Setup

The simulation model was drawn such that it resembled a simplified version of the experimental setup. The pyroelectric crystal was set a gap distance away from a metal target, with both parts inside a volume of dry air, as shown in Figure 4-1. As the simulation package was an electrostatics module, the parameters that were not included were pressure of the dry air volume and temperature of the pyroelectric crystal. The main components of the pyroelectric X-ray generator were modelled to simulate the electric field and electric potential produced under different combinations of parameters. It should be established that the pyroelectric crystal is free-standing in order to see how the electric field distributes around the crystal.

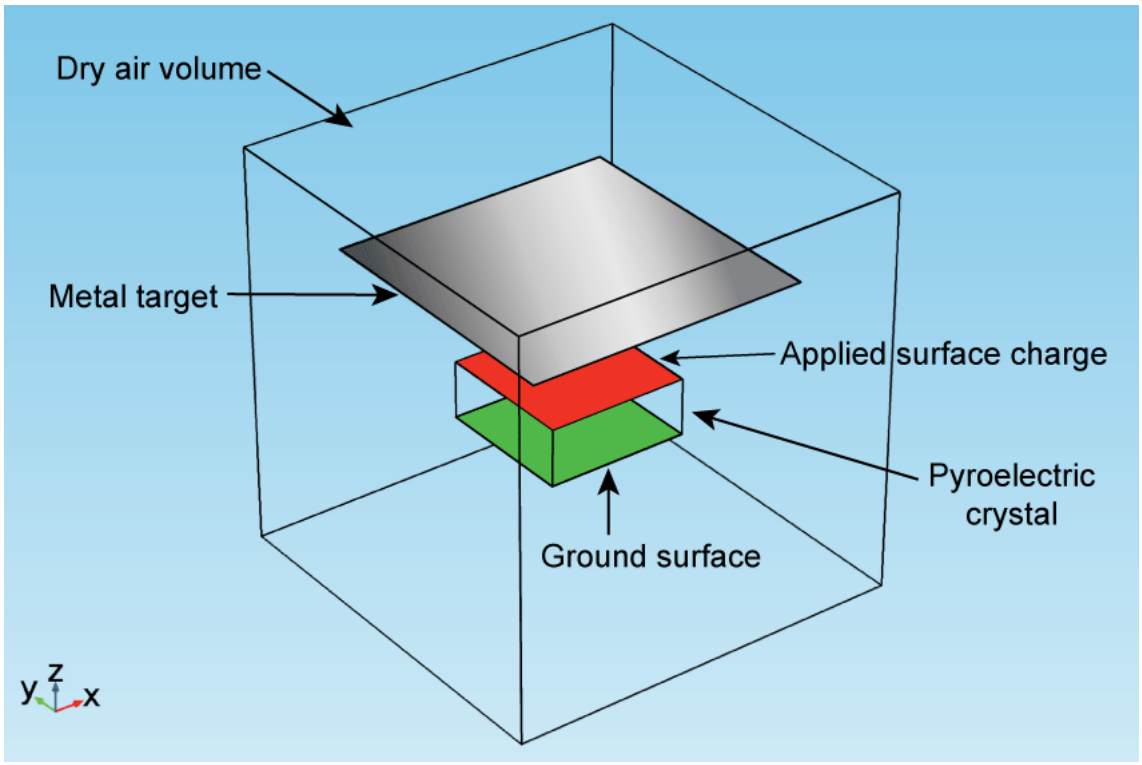

Figure 4-1 Geometry of the X-ray generator model.

Table 4-1 Variable parameters of the simple simulation model.

Variable Parameter	Value
Crystal Composition	$LiTaO_3$, $LiNbO_3$, PMN-30PT
Crystal Thickness (mm)	0.5, 1.0, 2.0, 5.0
Gap Distance (mm)	3.7, 5.0, 10.0

Although the properties of the pyroelectric crystal can be selected from the library of materials, the surface charge density, σ_q, of the surface facing the metal target (indicated in red) was assigned using the pyroelectric coefficient of the respective material, measured in Chapter 3.4.3. This surface will be further referred to as the top crystal surface. A cubic spline interpolation was performed on the pyroelectric coefficient of each material as a function of temperature, collected in Chapter 3, and the average value was taken. The σ_q was then calculated using Equation 3-1 where ΔT was 100°C for $LiTaO_3$ and $LiNbO_3$, and 80°C for PMN-30PT. The ΔT selected here matched the same ΔT used in the experiments.

The pyroelectric coefficient of PMN-30PT was taken from the pyroelectric measurements of PMN-28PT [111] as both compositions lie in the same ferroelectric polymorphic phase. As PMN-30PT was not available in the material library, its piezoelectric properties input were based off PMN-30PT poled in the [001] direction [191]. Isotropy will be assumed.

The surface charge density and relative permittivity values for each crystal composition applied were listed in Table 4-2. Like the experimental setup, all the surfaces of the metal target and the bottom surface of the pyroelectric crystal, indicated in green in Figure 4-1 were electrically grounded.

Table 4-2 Material properties of the modelled crystal compositions

Crystal Composition	Pyroelectric Coefficient ($\mu C/m^2K$)	Surface Charge Density, σ_q (C/m^2)	Relative Permittivity, ε_r
LiTaO3	163.906	16.3906×10^{-3}	40.9
LiNbO3	75.5156	7.55156×10^{-3}	43.6
PMN-30PT	716.34	57.3072×10^{-3}	1434

The parameters kept constant were:

- Surface area of the pyroelectric crystal, set at 25 mm^2
- Gas surrounding the pyroelectric crystal and metal target, using dry air
- Material and thickness of the metal target, using 7.5 μm thick nickel
- Area of the metal target, set at 100 mm^2

The simulation was additionally performed with the polarity of the surface charge density reversed. When the polarity of the surface charge density was positive, it simulated the heating phase of the X-ray generation phenomenon. Conversely, switching the polarity of the surface charge density simulates the cooling phase. All other variable and constant parameters were maintained.

4.3 Results and Discussion

4.3.1 Electric field around the pyroelectric crystal

The distribution of the electric field around the pyroelectric crystal will be explained using 2.0 mm thick $LiTaO_3$ crystal with a positive and negative surface charge density to simulate the heating and cooling phases of the thermal cycle. The vectors in the electric field distribution figures will represent the direction of electrons, rather than of positive charges which is the usual convention. A negative applied surface charge density represents the heating phase, as displayed in Figure 4-2. The electrons in the central region of the crystal surface move upwards but near the edges, the electrons bend outwards as they move in the upward direction. This field near the edges is known as the fringing field [192]. When the polarity of the applied surface charge density is positive, electrons are attracted to the pyroelectric crystal simulating the cooling phase, as shown in Figure 4-3. The magnitude of electric field around the crystal during both heating and cooling phases remains the same but the direction of the electrons is in reverse. The threshold of the all subsequent 3D electric field distribution figures is set at 85% of the maximum electric field.

Both Figure 4-2 and Figure 4-3 also show the electric field concentrates at the edges of the crystal's top surface. This would indicate that during the heating phase, more of the electrons would be emitted from the edges compared to the inner surface. While during the cooling phase, most of the electrons would be travelling towards the edge when compensating for the increase in positive charges. The higher electric field at the edges is not unexpected since charges concentrate at higher density at surfaces of higher radius of curvature in order to reduce their repulsive forces against each other [193, 194].

The distribution of the electric field agrees well with the ring charge that has been observed along the edge of the crystal [142]. However, it has also been demonstrated that there is a charge focusing phenomenon that occurs [195-197]. That is, at an optimised distance the electrons emitted from the crystal will converge at a focal point. A similar finite element modelling study was performed that suggests the charge focusing phenomenon occurs due to a non-uniform surface charge distribution [197]. In these series of electrostatics simulations, the surface charge is uniformly distributed.

It is also worth mentioning that the electric field distribution across the gap is not uniform as one would imagine between two infinite parallel charged plates. Due to the setting of the boundary conditions, the electric field appears non-uniform and the fringing field effect can be seen [198, 199]. The simulation results will be assessed by the electric field at the top crystal surface because, while the electric field in the gap is equally important, the top crystal surface is the location that determines the likelihood of electron emission. It will be assumed that the "tapering" of the electric field across the gap will follow proportionally across all models, unless otherwise stated. That is, if the average electric field at the top crystal surface is greater in one model than another, it is assumed that the average electric field across the gap will also be greater in the former model.

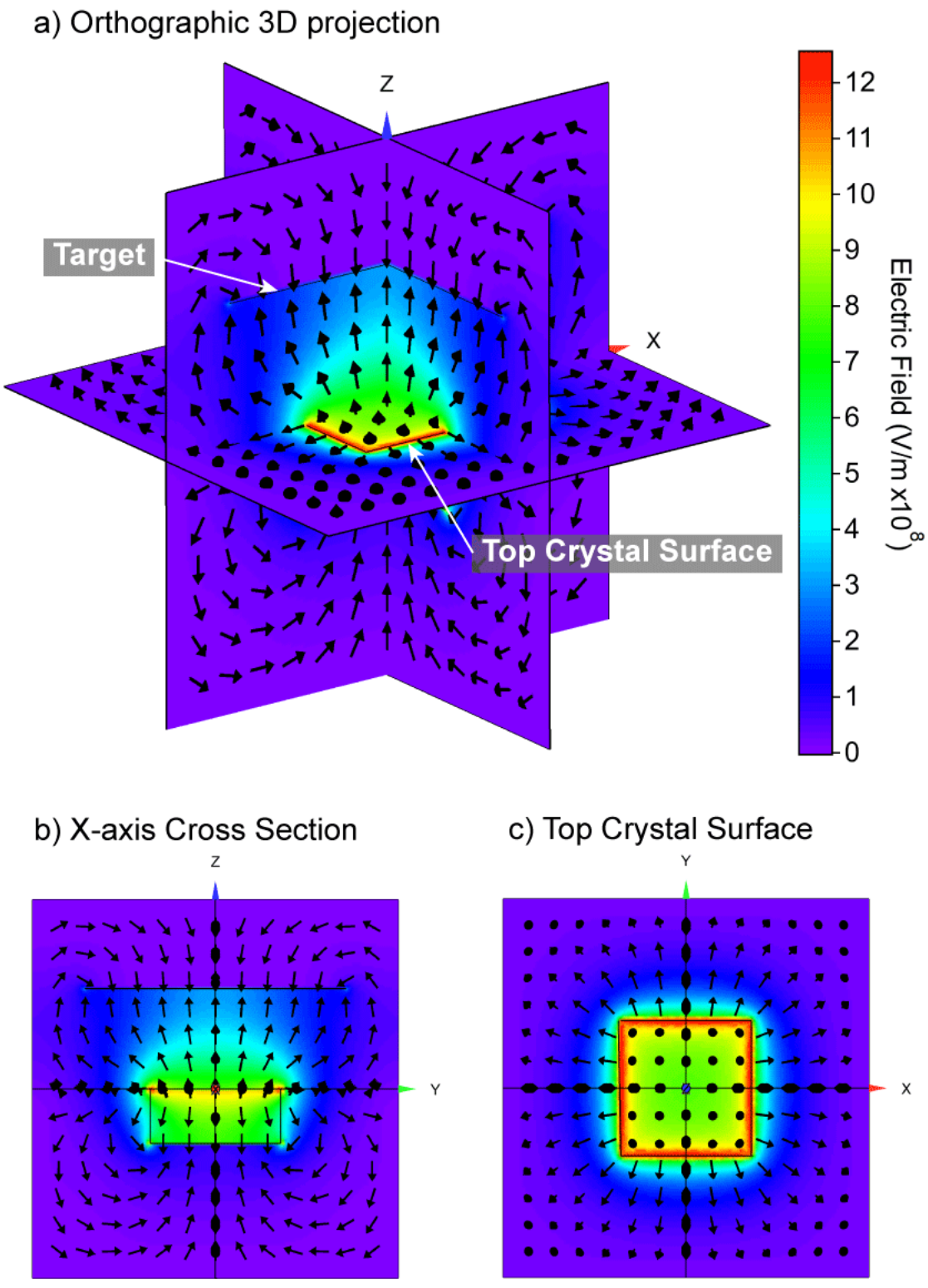

Figure 4-2 Electric field produced by $LiTaO_3$ with a negative surface charge density on its emitting surface, simulating the heating phase. The resultant field intensity is shown where the colour scale represents the magnitude and the vectors show the direction of electrons. The three views displayed are an orthographic 3D projection (a), cross-section of the X-axis (b) and top view of the top surface of the pyroelectric crystal (c).

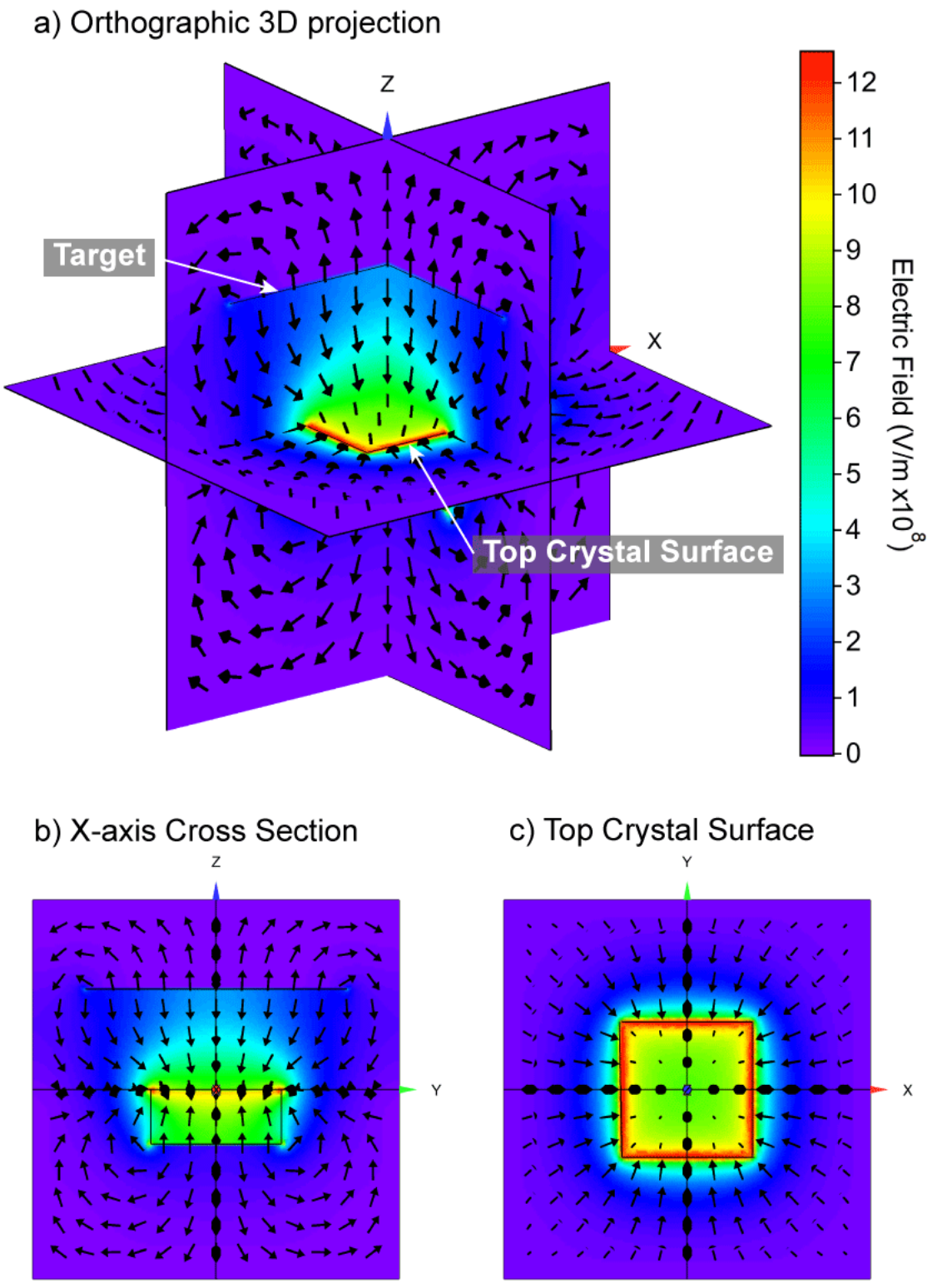

Figure 4-3 Electric field produced by $LiTaO_3$ with a positive surface charge density on its emitting surface, simulating the cooling phase. The resultant field intensity is shown where the colour scale represents the magnitude and the vectors show the direction of the electrons. The three views displayed are an orthographic 3D projection (a), cross-section of the X-axis (b) and top view of the top surface of the pyroelectric crystal (c).

4.3.2 Effect of crystal thickness

A sweep of increasing crystal thickness was simulated and the electric field on the top surface of the crystals were extracted. Here, only the data from $LiTaO_3$ will be discussed.

The electric field distribution produced from each crystal thickness is presented in Figure 4-4 and Figure 4-5. Looking at the top views of the top surface (Figure 4-4(c, f), Figure 4-5(i, l)), the overall electric field progressively increases with increasing crystal thickness. To better see this trend, a histogram is made by extracting the electric field from the top crystal surface and dividing over the area of the crystal. As the volume of the dry air box is drawn to $14\times14\times14$ mm^3, the exported electric field and electric potential has a volume of $141\times141\times141$ data points. Similarly, the area of the pyroelectric crystal has 51×51 data points while the target has 101×101 data points. The histograms in Figure 4-6 show portions of the top crystal surface area and target area from each crystal thickness binned into increasing electric field magnitudes. The bin widths for the histogram of the top crystal surface is 1×10^8 V/m, unless specified in the figure captions.

The electric field in the gap of the setup is of interest as it is the region at which the electrons are emitted close to the crystal surface, during both heating and cooling, and then accelerates as they travel towards the target. Viewing at the cross-sections normal to the X-axis (Figure 4-4(b, e), Figure 4-5(h, k)), with the gap distance remaining at a constant, it is evident that the electric field increases in the gap as the crystal thickness increases. The histogram of each crystal thickness in Figure 4-6(a) shows the same distribution that is skewed to the right with smaller peaks appearing at the tail end. As the crystal thickness increases, the histogram shifts right to higher electric fields. The electric field in the gap created by a crystal with thickness of 0.5 mm ranges about 3.0×10^8 V/m between the top crystal surface and the target. This is very different to the electric field created by a crystal with thickness of 5.0 mm where there is a greater volume in the gap that ranges from about 2.0×10^8 V/m near the target to about 10.0×10^8 V/m near the top crystal surface. Due to this difference in ranges, the likelihood of electron emission increases with thicker crystals. It is then expected that the X-ray counts should also increase.

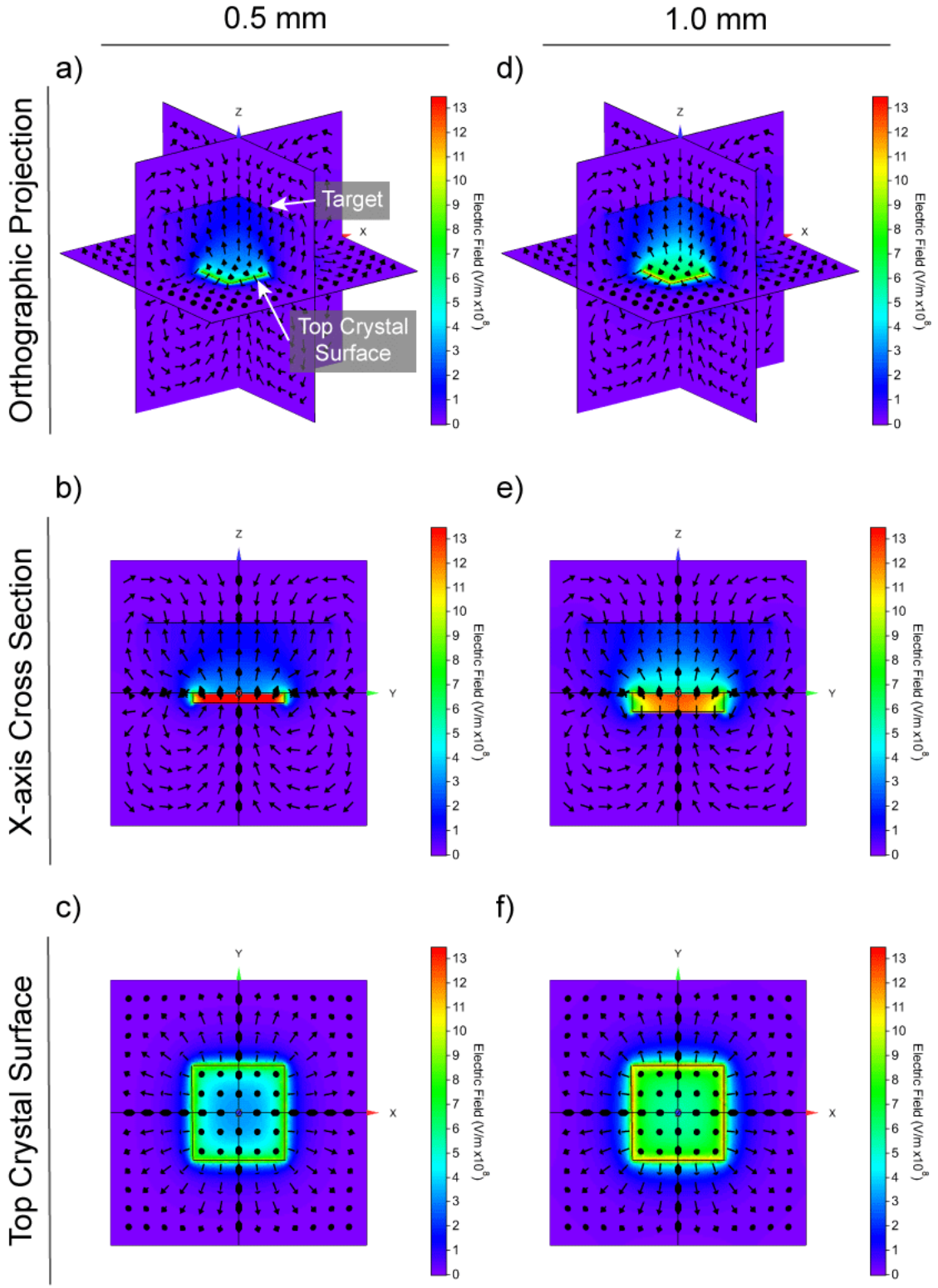

Figure 4-4 Series of electric field distributions produced from $LiTaO_3$ with thicknesses of 0.5 mm (a-c), 1.0 mm (d-f), 2.0 mm (g-i) (next page) and 5.0 mm (j-l) (next page). The threshold electric field applied to all distributions is 13.38×10^8 V/m.

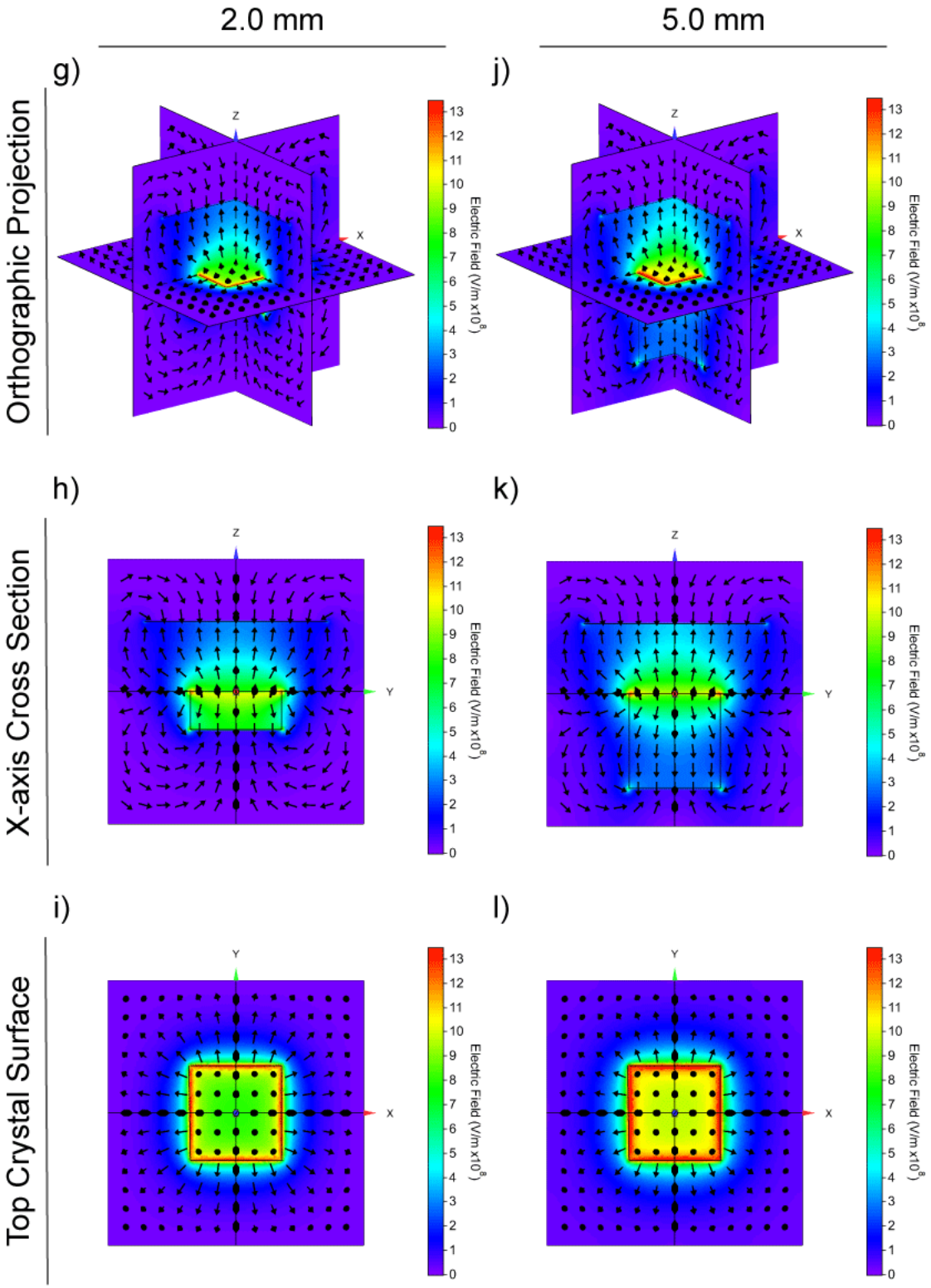

Figure 4-5 Series of electric field distributions produced from $LiTaO_3$ with 0.5 mm (a-c) (previous page), 1.0 mm (d-f) (previous page), 2.0 mm (g-i) and 5.0 mm (j-l) thicknesses. The threshold electric field applied to all distributions is 13.38×10^8 V/m.

In Chapter 3, the figures-of-merit as a function of crystal thickness follows a linear relationship, as was shown in Figure 3-23 and Figure 3-25. That is, the electric field in the gap would increases linearly with crystal thickness. Taking the mode electric field, or most frequently occurring, from the histograms of the electric field distributions at the top crystal surface and the target, it can be seen in Figure 4-8 that the electric field increases in a more logarithmic manner. The differences could be accounted by the assumption applied in Chapter 3, which was the crystal surface and the target were infinite plates. The electric field across the gap would then be uniform. However, in these simulations, they are finite, which causes the electric field to decay from the top crystal surface to the target.

The X-ray energies produced is dependent on the energy of the electrons as they accelerate through the gap. Since the potential difference between the crystal and the target determines the energy of the electrons, the potential difference will be extracted from the simulated models. Using the same volume of data points as for electric fields, the electric potentials at the top crystal surface and the target are distributed into histograms, as shown in Figure 4-7. The bin width for the top crystal surface and target electric potentials are 500 V and 50 V, respectively. The histograms can be found in Appendix B. The mode electric potential at the top crystal surface and target from their respective histograms will then be used to calculate the potential difference. The potential difference as a function of crystal thickness, presented in Figure 4-9, is of a linear relationship. It is then expected that the end-point energy should also increase linearly with crystal thickness.

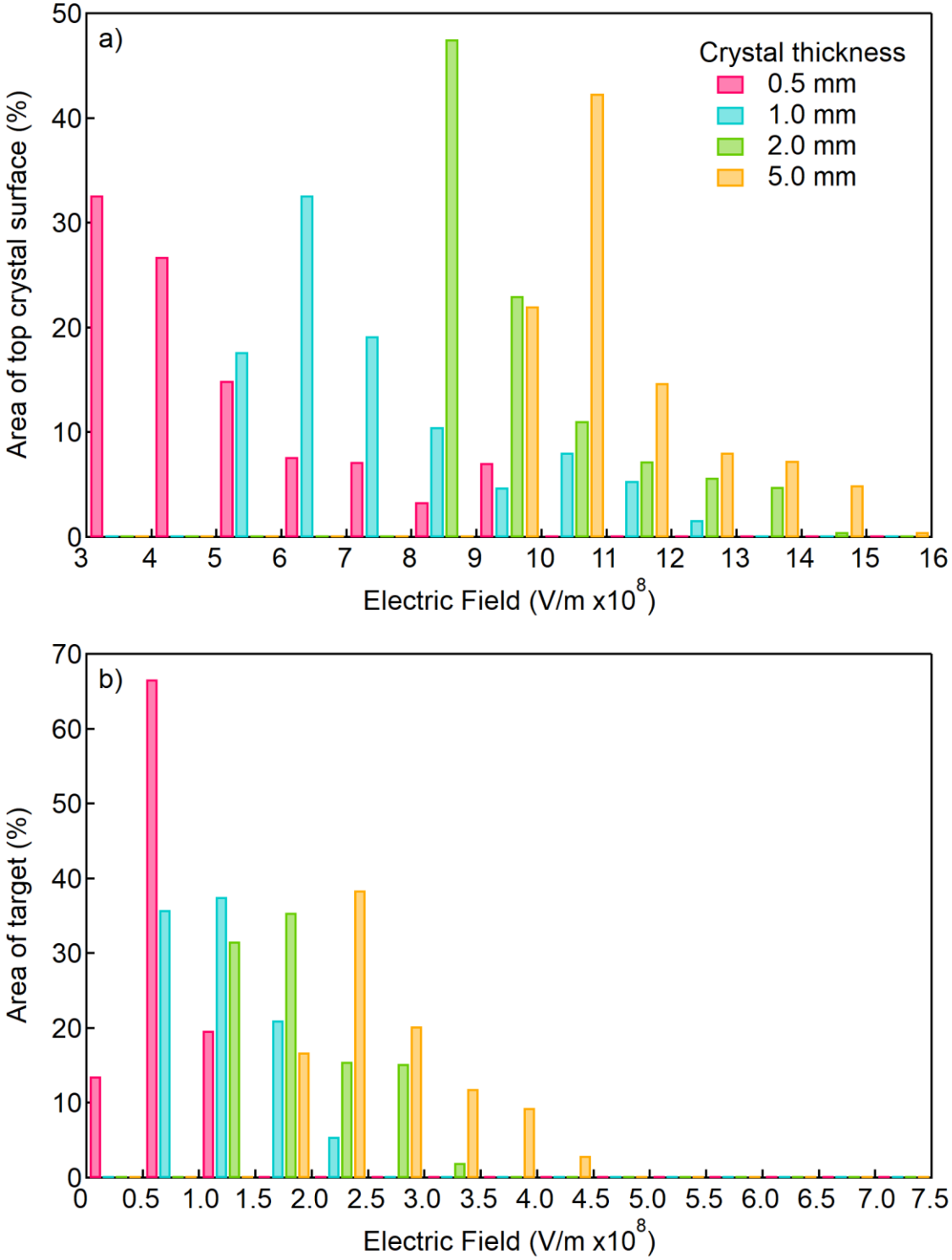

Figure 4-6 Histogram of the electric field distribution produced by $LiTaO_3$ of four different thicknesses, which are 0.5, 1.0, 2.0 and 5.0 mm. Histogram (a) is of the top crystal surface with histogram bin width is 1×10^8 V/m, and histogram (b) is of the target with histogram bin width of 0.5×10^8 V/m.

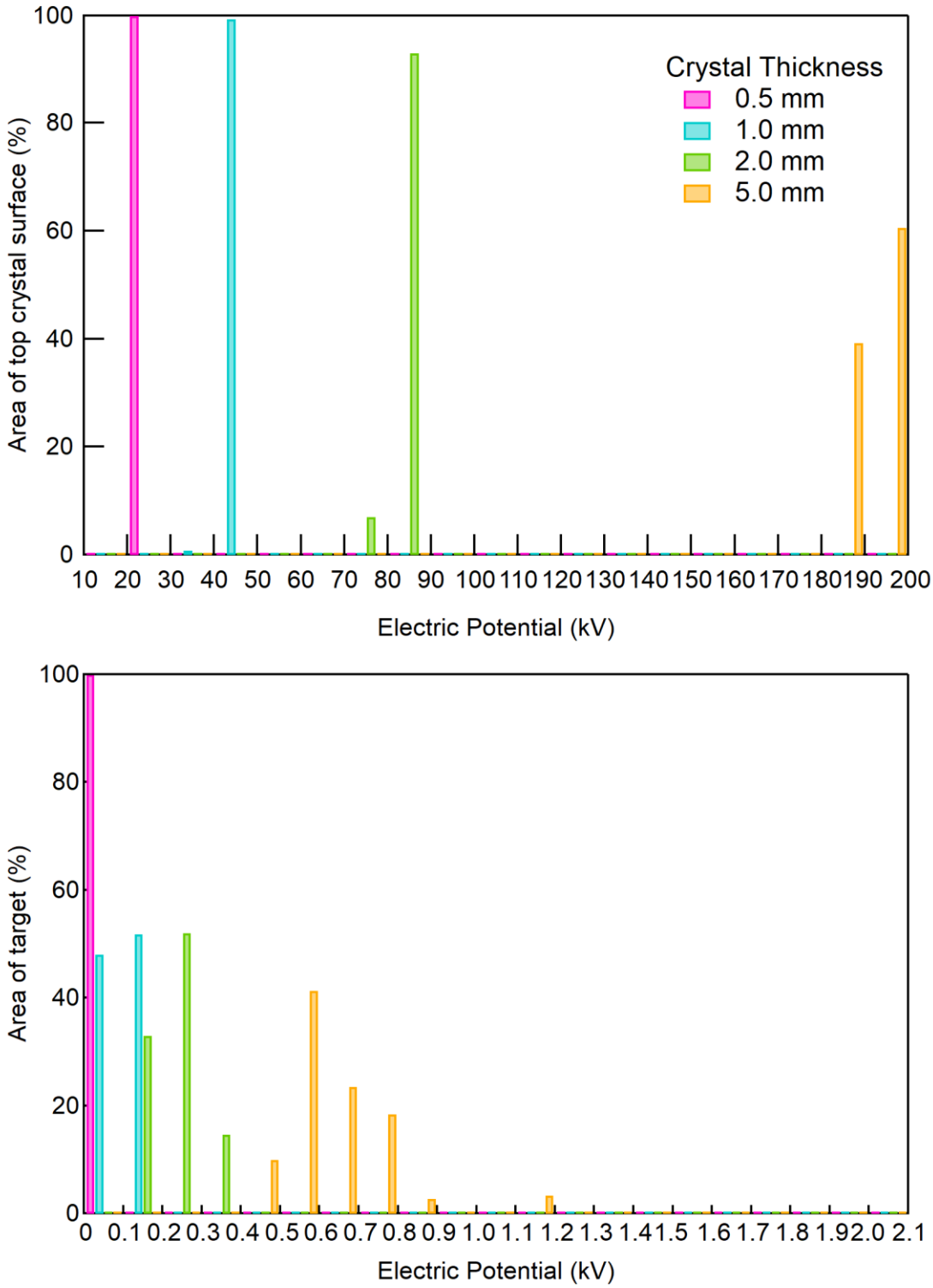

Figure 4-7 Histogram of the electric potential distribution produced by $LiTaO_3$ of four crystal thicknesses at the top crystal surface (top) and at the target (bottom). The bin widths for the top and bottom histograms are 10 kV and 0.1 kV, respectively.

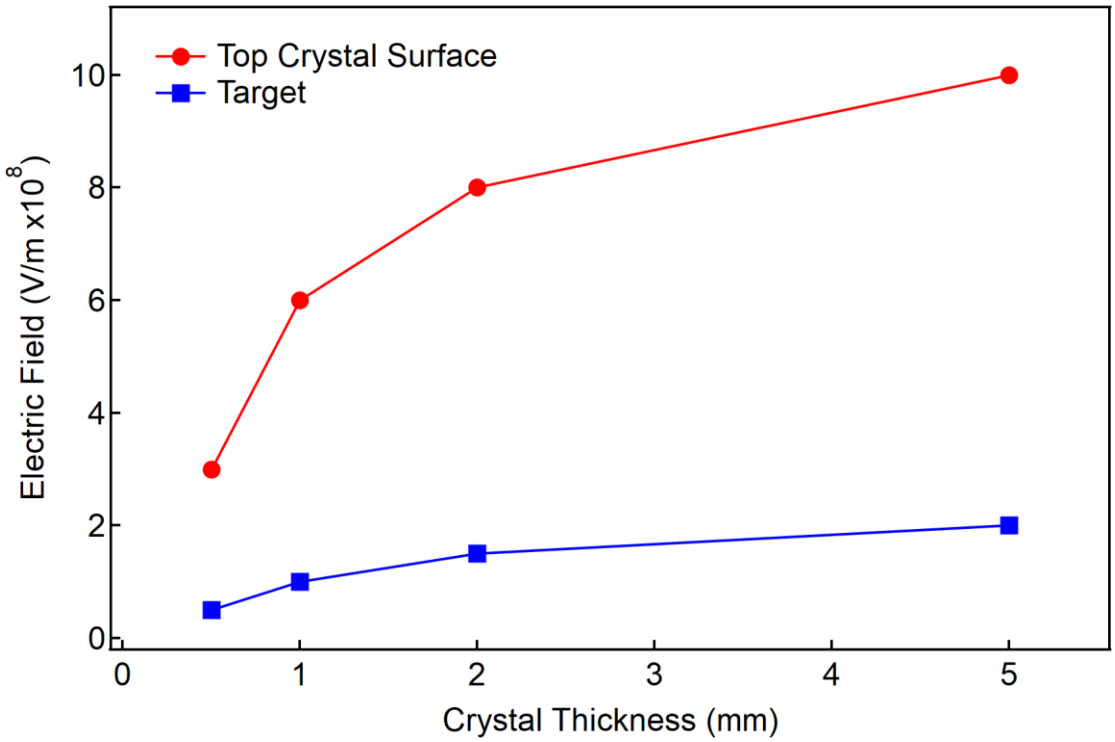

Figure 4-8 The electric field covering the greatest surface area at the top crystal surface and target, obtained from their respective histograms in Figure 4-6.

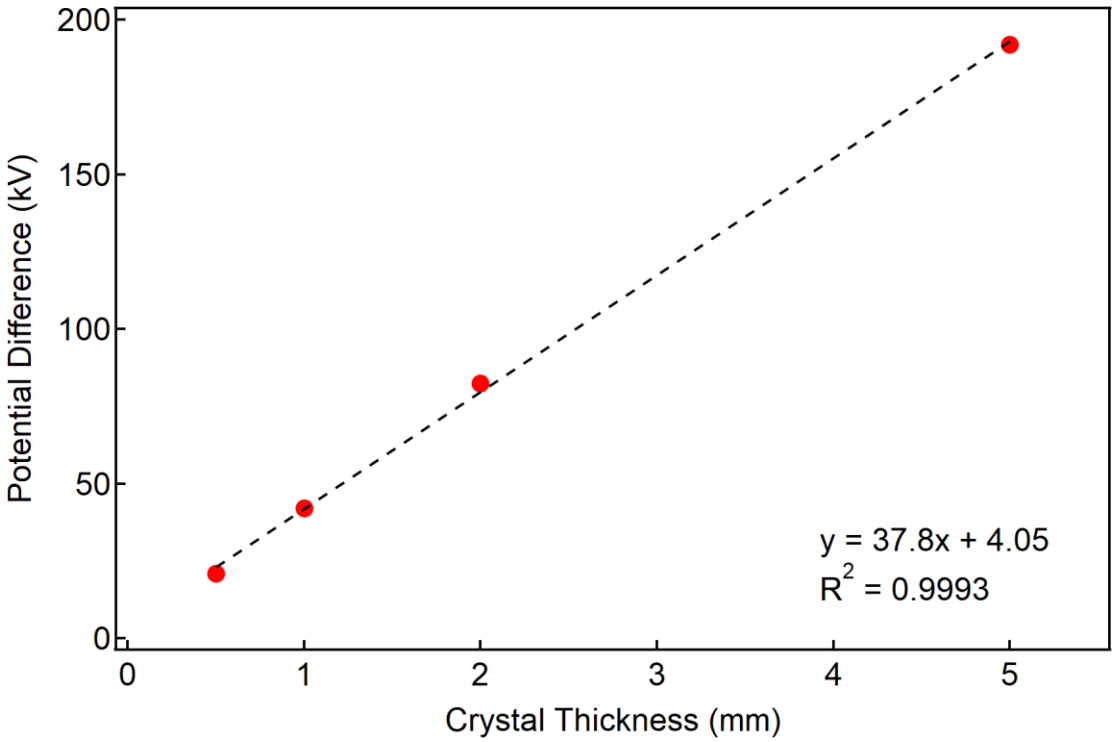

Figure 4-9 Potential difference between the electrical potential mode at the top crystal surface of $LiTaO_3$ and the target, with increasing crystal thickness.

Table 4-3 The minimum and maximum electric field on the top crystal surface and target, and potential difference across the gap obtained from the two crystal thicknesses. The potential difference is taken as the difference in the mode electric potential at the top crystal surface and the target. The gap distance is 3.7 mm.

Crystal Thickness (mm)	Top Crystal Surface		Target		Potential Difference (kV)	F_ε ($\mu C/m^2K$)	F_σ (V/m)
	Min Electric Field (V/m)	Max Electric Field (V/m)	Min Electric Field (V/m)	Max Electric Field (V/m)			
0.5	3.25×10^8	10.1×10^8	0.421×10^8	1.70×10^8	21.0	0.516	19.8×10^6
1.0	5.61×10^8	12.5×10^8	0.717×10^8	2.91×10^8	42.0	1.05	39.7×10^6
2.0	8.03×10^8	14.7×10^8	1.13×10^8	4.61×10^8	82.3	2.07	79.3×10^6
5.0	9.74×10^8	15.7×10^8	1.73×10^8	7.30×10^8	192	–	–

4.3.3 Effect of crystal composition

The figures-of-merit of various pyroelectric crystals were determined in Chapter 3. In the electrostatic simulations, selected crystal compositions to be measured in the X-ray generator were modelled and the electric field and potential difference produced will be discussed. Earlier results consistently showed that $LiTaO_3$ had the highest figure-of-merit of F_ε and F_σ, followed by $LiNbO_3$ and lastly PMN-30PT. The simulation results of $LiNbO_3$ and PMN-30PT are shown in Figure 4-10.

The histogram in Figure 4-11 show the electric field ranges created by the three compositions at the top crystal surface, which do not overlap each other. PMN-30PT produced the lowest electric fields and the smallest range that was less than 10^7 V/m. This led to 100% area of the top crystal surface of PMN-30PT to sit in one bin width, which was 10^8 V/m. The histogram of PMN-30PT in Figure 4-11 was re-distributed into small bin widths. As presented in Figure 4-12, the maximum electric field achieved was 1.10×10^7 V/m. Values of interest obtained from the simulation results are listed in Table 4-4.

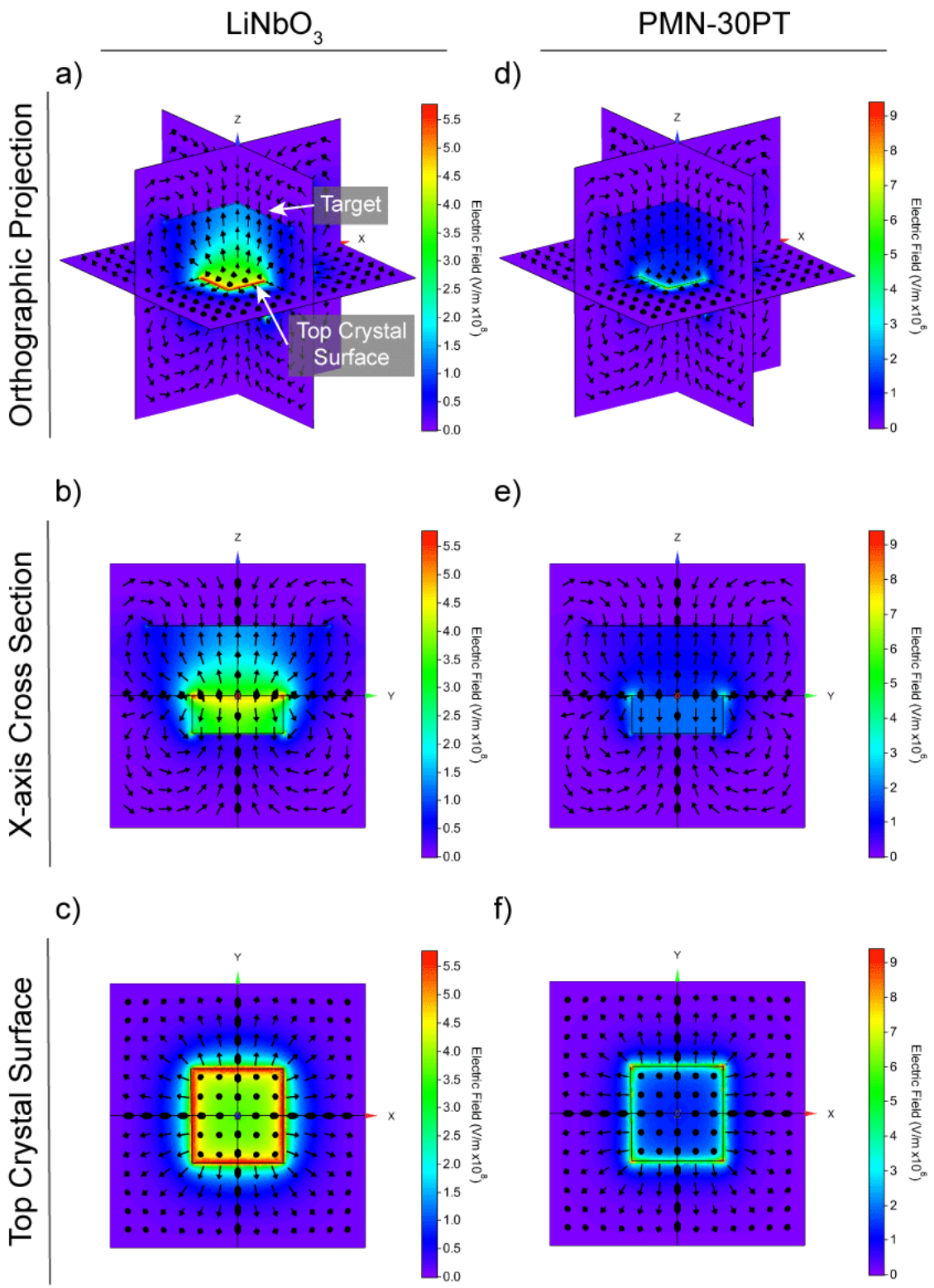

Figure 4-10 Electric field distributions produced by $LiNbO_3$ (a – c) and PMN-30PT (d – f). The top pair are orthographic 3D projections (a, d), the middle pair are cross-sections normal to the X-axis (b, e) and the bottom pair is a top view of the top crystal surface (c, f). The threshold electric field magnitude of $LiNbO_3$ and PMN-30PT are 5.75×10^8 V/m and 9.363×10^6 V/m, respectively. The electric field distributions produced by $LiTaO_3$ can be seen in Figure 4-5(g – i).

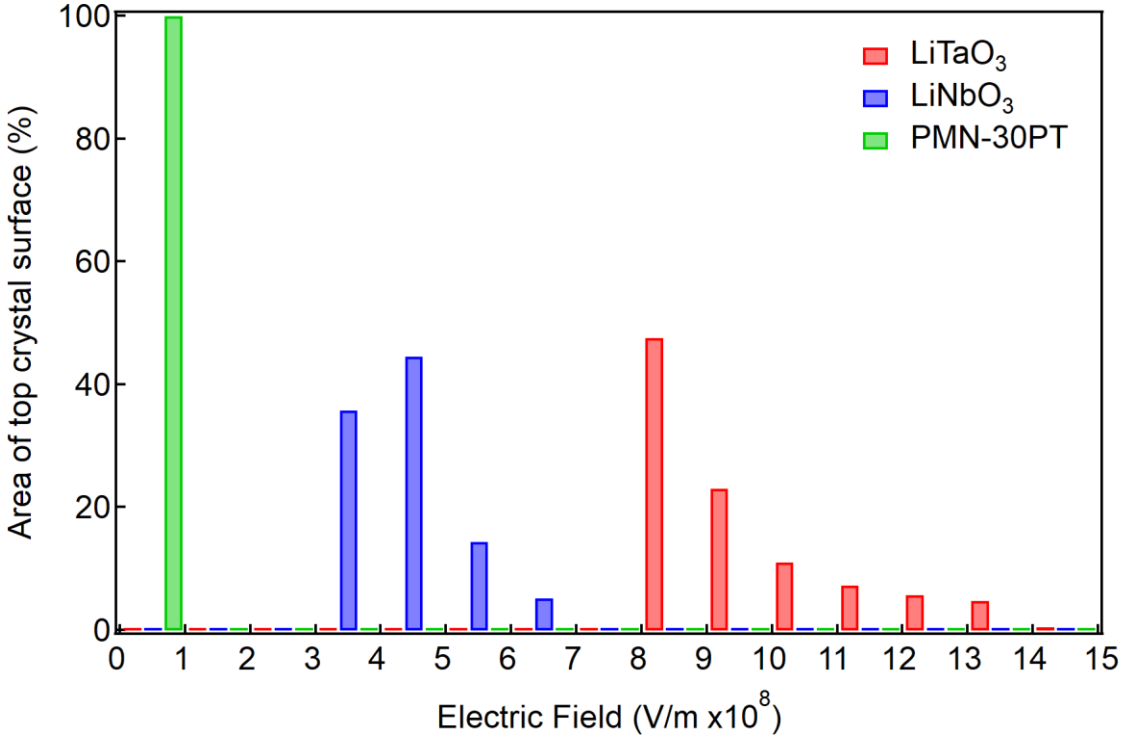

Figure 4-11 Combined histogram of the electric field distribution produced by $LiTaO_3$, $LiNbO_3$ and PMN-30PT. The thickness of the simulated crystals is 2.0 mm. The histogram bin width is 1×10^8 V/m.

In the later part of Chapter 3.4.5, it was shown that materials with higher F_σ tended to be in the 10^7 V/m range, which was one magnitude lower than the critical value mentioned in literature [142]. In the simulation results, both $LiTaO_3$ and $LiNbO_3$ create electric fields with magnitudes from 10^8 V/m and above. It is expected that the simulation results should fall in line with the F_σ calculations, using Equation 3-14. However, this difference could be because the bulk conductivity of the material is not taken into consideration. Since the simulation is a stationary calculation, time is also not considered. That is, the simulation is an ideal scenario where compensation of surface charges by the bulk conductivity does not occur and the resultant electric fields would be higher.

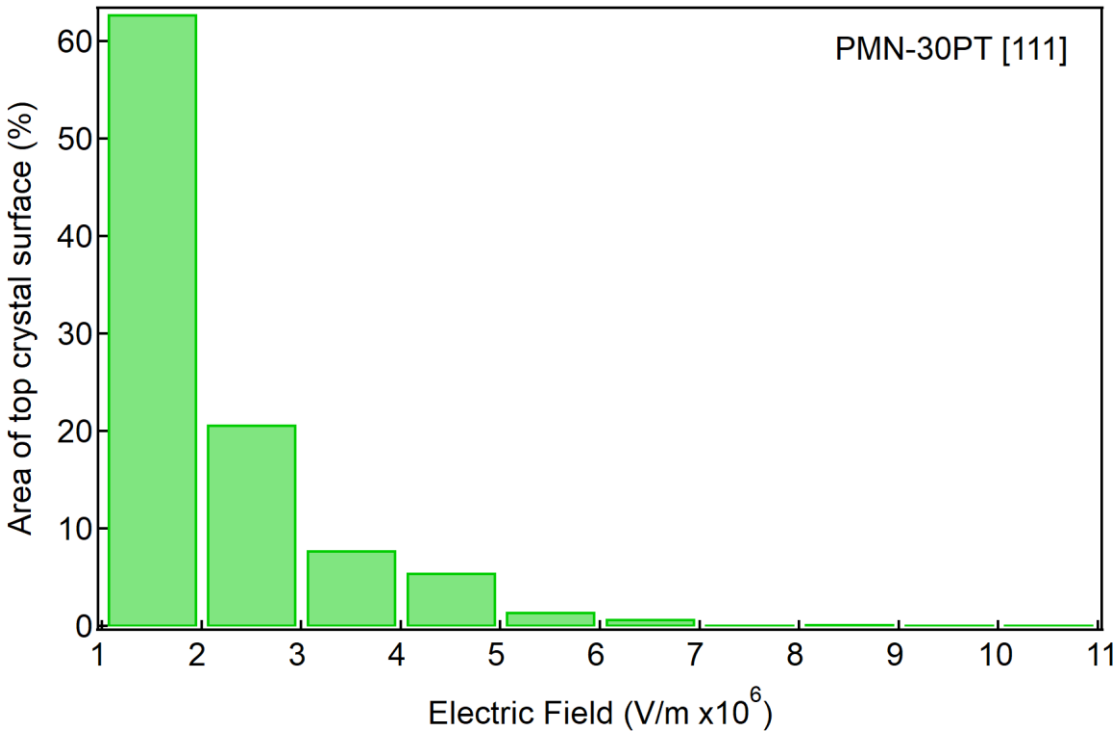

Figure 4-12 Histogram of the electric field distribution produced by PMN-30PT at the top crystal surface. The histogram bin width is 1×10^6 V/m.

The F_σ of PMN-30PT at all gap distances were calculated to be in the 10^3 V/m range. If bulk conductivity and time are taken into consideration, it can be estimated that the electric field over the entire top crystal surface could be at least one magnitude lower than its 10^6 V/m range.

$LiNbO_3$ resides in the middle amongst the three compositions. Its minimum electric field is just above 3.00×10^8 V/m, which when estimated with bulk conductivity of the crystal may overcome the critical F_σ value. So, it is expected for X-rays to be observed, which holds true as an X-ray spectrum with distinct peaks is reported in Chapter 5.4.2. It has been previously reported in literature that the electric field on the surface of $LiNbO_3$ is estimated to be 1.35×10^9 V/m [54]. This is much larger than the maximum electric field determined in the electrostatics simulation, which was 6.77×10^8 V/m. However, this difference could be attribute to the different ΔP_s value applied. The literature estimation used ΔP_s of 0.015 C/m^2, while the simulation used 0.00755 C/m^2.

$LiTaO_3$ again outperforms the other compositions as it had the highest maximum and minimum electric field intensities. It also produced an electric field range of 6.65×10^8 V/m, which is about double that of $LiNbO_3$ of 3.07×10^8 V/m. This confirms that a material with a higher figure-of-merit can produce higher and wider range of overall electric fields such that electrons can be emitted faster and be accelerated to a greater extent.

As mentioned earlier, the electrostatics simulation is a stationary analysis and does not consider changing temperatures and time. The electric field intensities determined only show the materials' potential at the peak of its thermal cycling. That is, the electric field produced by pyroelectric crystal when the temperature is at zero or 100°C. Even if the electric field produced overcame the critical value, there would be three conditions hindering the material's performance in X-ray generation. First, the magnitude of the electric field should be substantially high throughout the heating and cooling phases such that electrons are not only emitted near the peak of the thermal cycle. And secondly, though also dependent on the thermal cycling rate, there would be a waiting time for the generated electric field to overcome the threshold. Thirdly, the bulk conductivity of the material should be small such that charge compensation internally through the bulk does not reduce the potential net surface charge as the material is being thermally cycled. Therefore, a material with higher figures-of-merit is preferred because it can emit electrons earlier and accelerate to higher electric fields. Thus, higher counts and energy of X-rays can be produced.

Table 4-4 The minimum and maximum electric field at the top crystal surface, and potential difference across the gap achieved by the three crystal compositions with a crystal thickness of 2.0 mm and gap distance of 3.7 mm. The corresponding figures-of-merit from Chapter 3 are also included.

Crystal Composition	Min Electric Field (V/m)	Max Electric Field (V/m)	Potential Difference (kV)	F_ε ($\mu C/m^2K$)	F_σ (V/m)
$LiTaO_3$	8.01×10^8	14.7×10^8	82.3	2.07	7.93×10^7
$LiNbO_3$	3.70×10^8	6.77×10^8	51.2	1.47	8.73×10^6
PMN-30PT	1.30×10^6	11.0×10^6	3.90	0.378*	74.2×10^2

* F_ε of PMN-30PT is taken as the F_ε of PMN-28PT [111].

4.3.4 Effect of gap distance

Like in Chapter 3.4.5, the gap distance was parameterised. The crystal composition that will be studied is $LiTaO_3$. It was found in Chapter 3 that F_ε and F_σ decayed in a negative exponential manner as the gap distance increases. The two trends were shown in Figure 3-24 and Figure 3-26.

The electric field distribution from each model of increasing gap distance are presented in Figure 4-13 and Figure 4-14. Looking at the X-axis cross sections (Figure 4-13(b, e), Figure 4-14(h)), it appears that the electric field between the top crystal surface and the target decays as the gap distance widens. However, taking a closer look at the electric fields by displaying them as histograms, as in Figure 4-15, reveals the electric field distributions produced at the top crystal surface and the target are very similar to one another. This is unlike the decaying trend from the figures-of-merit, which suggested that the likelihood for electron emission reduces as the gap distance increases. Instead, it could be possible for electron emission to occur at similar rates in the dynamic X-ray generation process. As was also the case with the effect of crystal thickness in Chapter 4.3.2, this discrepancy could be due to the non-uniform electric field distribution across the gap as the top crystal surface and the target have finite widths in the simulation model.

The potential difference listed in Table 4-5 is approximated using the mode electric potential from the histograms in Figure 4-16. Like the electric field distributions, the electric potential distributions across the three gap distances are also similar. Although the histogram bin width is quite coarse, it still provides a relatively good estimation of the potential difference across the gap. This resulted in either the same or very close potential difference values at the three gap distances.

Since there appears to be minor difference in the electric field and potential difference, adjusting the gap distance may not have a significant effect on the X-ray counts and end-point energies. However, the electrostatics simulation findings exhibited contradicting results from the trend displayed by the figures-of-merit as a function of gap distance. Thus, it is only by undertaking the X-ray generator experiments can it be confirmed if it is more likely for the performance of the X-ray generator to decay as the gap distance widens.

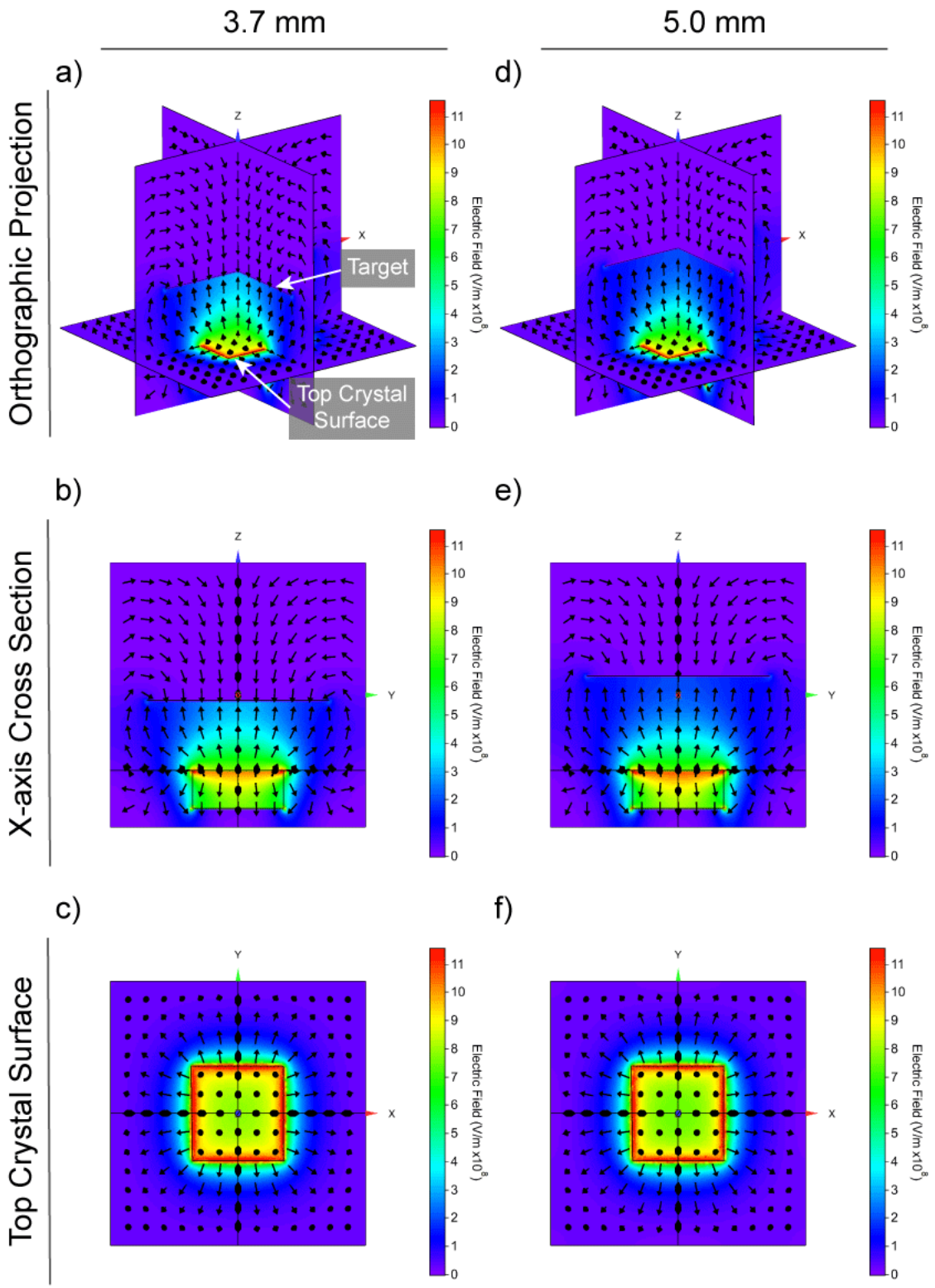

Figure 4-13 Electric field distributions produced by $LiTaO_3$ at gap distance of 3.7 mm (a – c, left vertical series), 5.0 mm (d – f, right vertical series) and 10.0 mm (g – i, next page). The crystal thickness is 2.0 mm. The top figures are orthographic 3D projections (a, d, g), the middle pair are cross-sections normal to the X-axis (b, e, h) and the bottom pair is a top view of the top crystal surface (c, f, i). The threshold electric field applied to all distributions are 11.5×10^8 V/m.

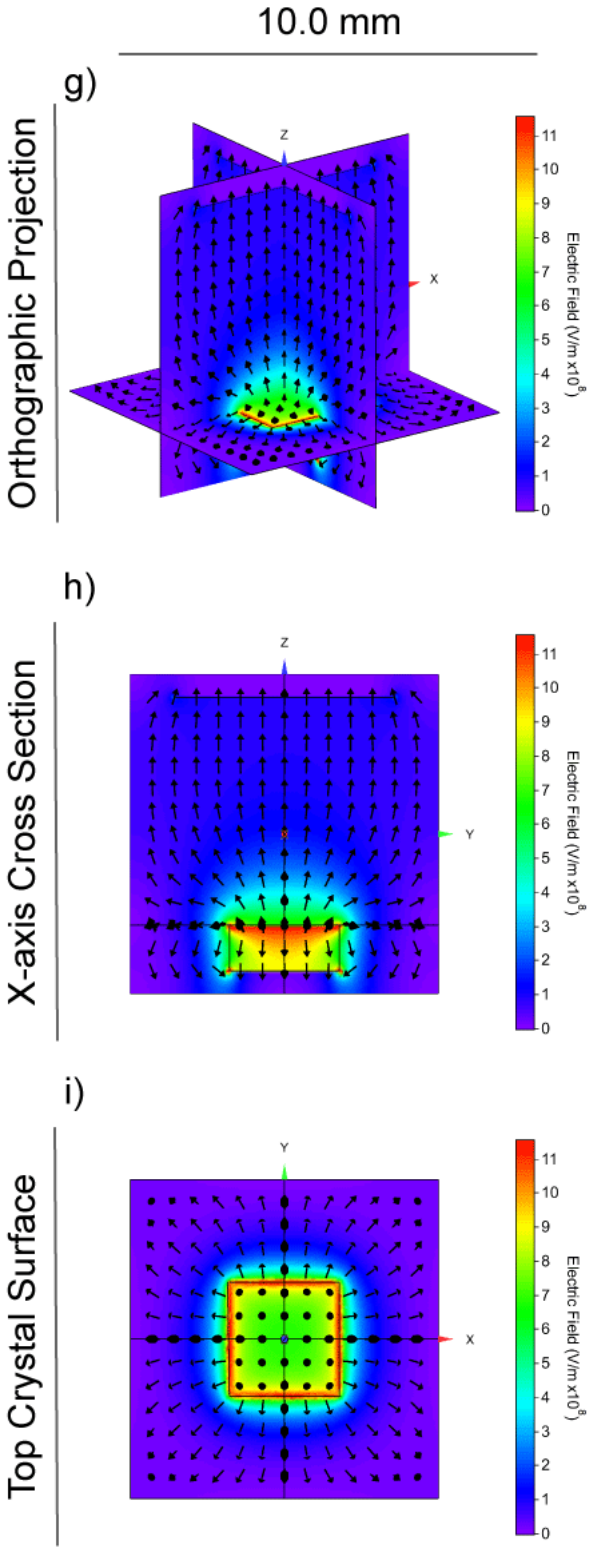

Figure 4-14 Electric field distributions produced by $LiTaO_3$ at gap distance of 3.7 mm (a – c, previous page), 5.0 mm (d – f, previous page) and 10.0 mm (g – i). The crystal thickness is 2.0 mm. The top figures are orthographic 3D projections (a, d, g), the middle pair are cross-sections normal to the X-axis (b, e, h) and the bottom pair is a top view of the top crystal surface (c, f, i). The threshold electric field applied to all distributions are 11.5×10^8 V/m.

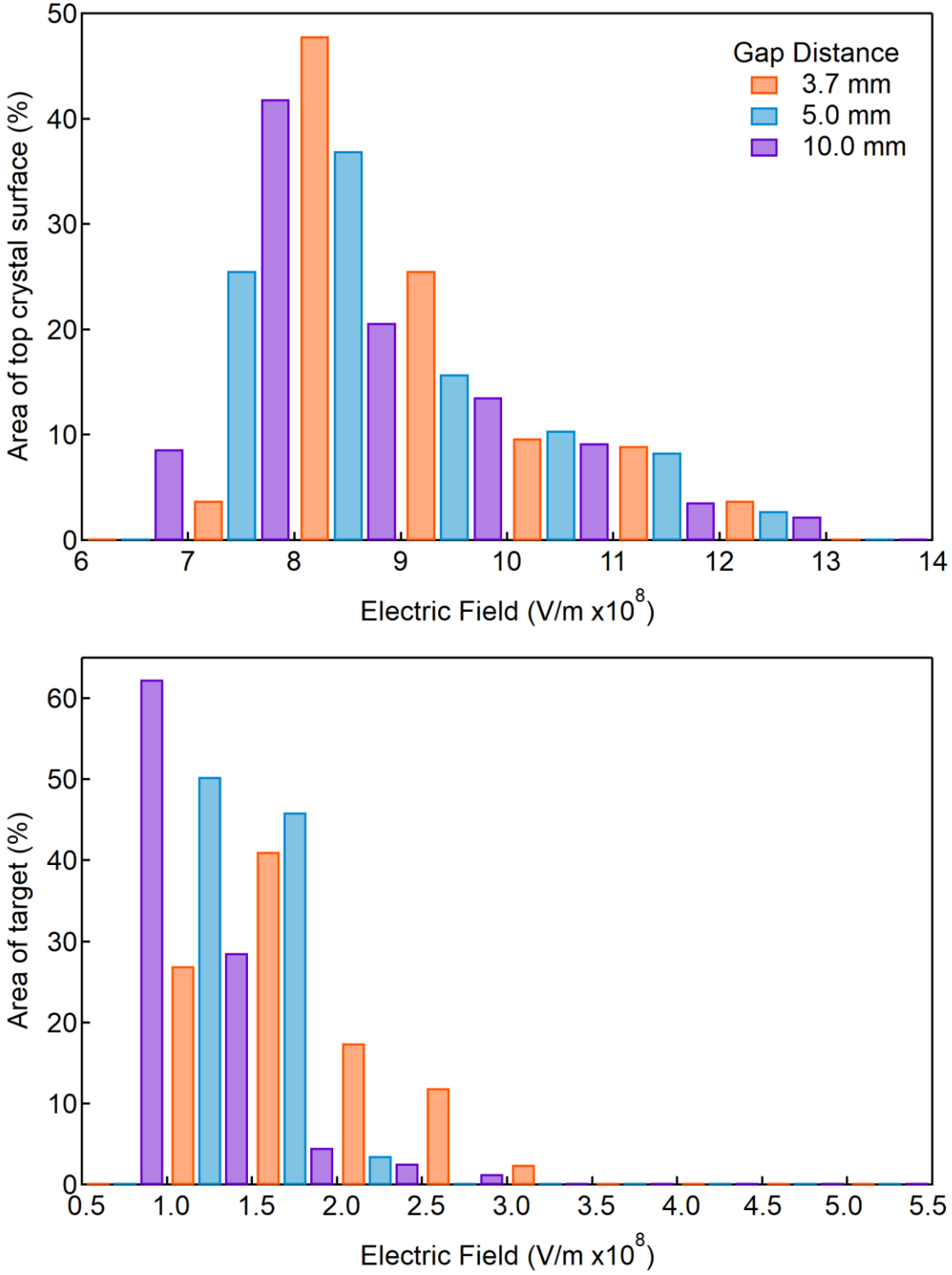

Figure 4-15 Histogram of the electric field distributions at the top crystal surface (top) and the target (bottom) produced by $LiTaO_3$, when arranged at gap distances of 3.7, 5.0 and 10.0 mm. The bin width for the top and bottom histograms are 1×10^8 V/m and 0.5×10^8 V/m, respectively.

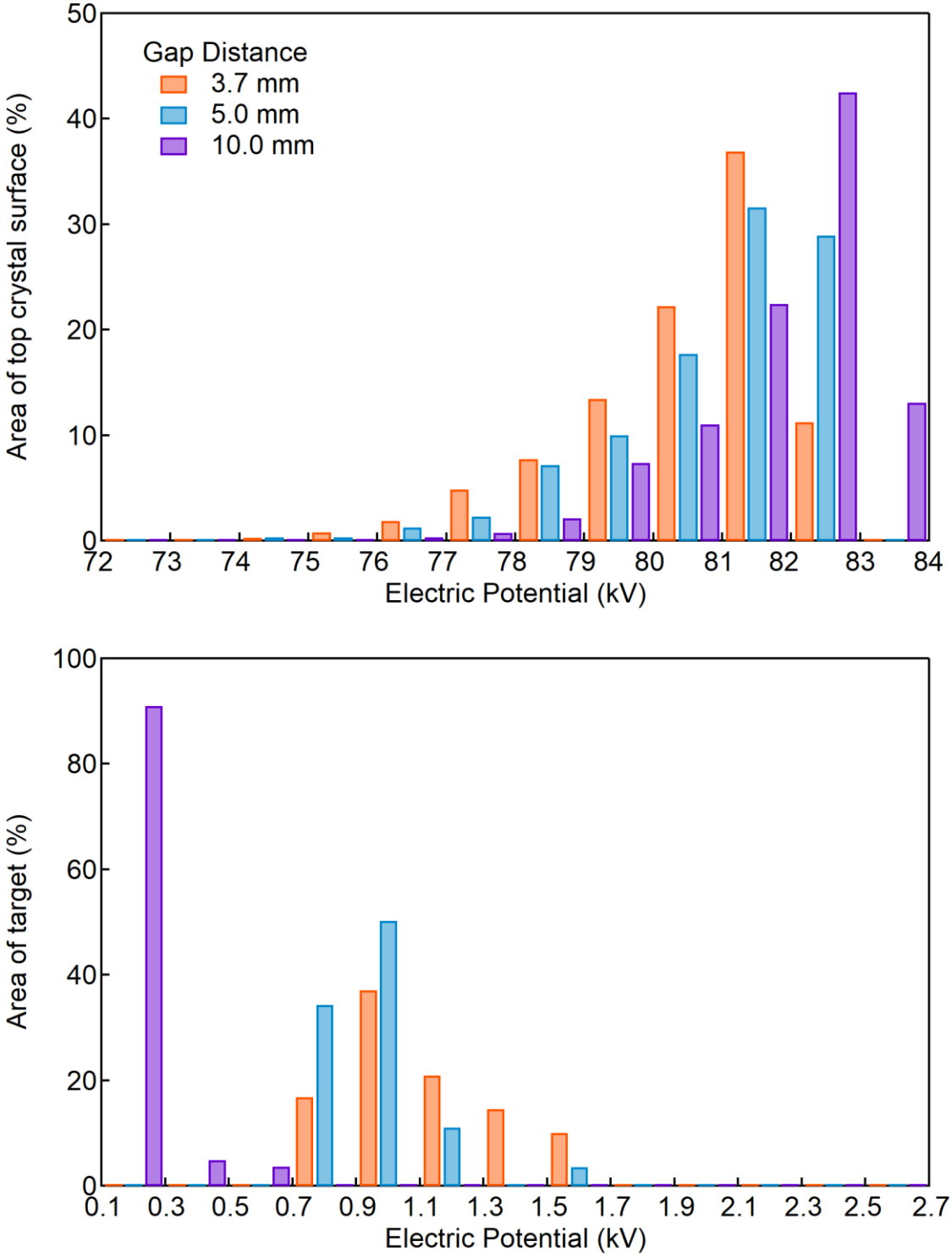

Figure 4-16 Histogram of the electric potential produced at the top crystal surface (top) and the target (bottom), arranged at three gap distances of 3.7, 5.0 and 10.0 mm. The bin widths for the top and bottom histogram are 1 kV and 200 V, respectively.

Table 4-5 The minimum and maximum electric field at the top crystal surface and potential difference across the gap. The corresponding figures-of-merit determined in Chapter 3 are included. The potential difference is taken as the difference in the mode electric potential at the top crystal surface and the target from Figure 4-16.

Gap Distance (mm)	Top Crystal Surface		Target		Potential Difference (kV)	F_ε ($\mu C/m^2K$)	F_σ (V/m)
	Min Electric Field (V/m)	Max Electric Field (V/m)	Min Electric Field (V/m)	Max Electric Field (V/m)			
3.7	7.95×10^8	13.5×10^8	1.18×10^8	3.12×10^8	80.1	2.07	7.93×10^7
5.0	7.56×10^8	12.9×10^8	1.22×10^8	2.64×10^8	80.1	1.53	5.87×10^7
10.0	6.86×10^8	13.0×10^8	0.902×10^8	5.08×10^8	81.9	0.767	2.94×10^7

5

X-RAY GENERATOR APPARATUS

"Everything that can possibly go wrong, will go wrong"

– Murphy's Law

5.1 Overview

Chapter 5 details the design, construction and operation of an experimental testbed for prototyping and characterising pyroelectric X-ray generators. The testbed consists of three main systems; a vacuum system, a temperature control system and a data acquisition system. The system was designed to explore the impacts of various parameters, such as pressure and gap distance, on the X-ray output. Other parameters, such as temperature change rate and duration of measurement were kept constant to allow comparison between measurements. Sub-chapter 5.5 will cover the general experimental setup, while the independent variables will be detailed for each specific experiment. Specific preparation of the crystals will be described in the subsequent chapters.

5.2 Vacuum System

X-ray generation required a low-pressure environment to reduce the rate of charge compensation on the pyroelectric crystal surface from ionised gas particles. But lower pressures also increase the likelihood of an electric breakdown [32, 57]. Therefore, optimisation of the pressure inside the vacuum chamber is critical to maximise X-ray counts, energy and duration of X-ray production while minimising the probability of an electric breakdown.

The vacuum system was built around a high vacuum 304 stainless steel vacuum chamber (Trinos High Vacuum Chamber (Vertical, KVH, DN320), Trinox Vakuum-Systeme GmbH, Göttingen, Germany) customised with a six chamber ports positioned in a ring around the side wall. The complete vacuum system is pictured in Figure 5-1. One port was connected to a pump station (Edwards T-Station 75, Edwards Limited, West Sussex, U.K.), which incorporated a turbo-molecular pump backed by a diaphragm roughing pump. The pump was connected to the chamber via a gate valve, allowing the pump to be throttled or completely isolated from the chamber.

The pressure in the chamber was measured using two vacuum gauges, the first being a combined Penning/Pirani wide-range gauge (Edwards WRG-S-DN40-CF, Edwards Limited, West Sussex, U.K.). This wide-range gauge could measure pressures from atmospheric (10^5 Pa) to ultra-high vacuum range (10^{-7} Pa). The pressure reading by the wide-range gauge was displayed on the control panel of the Edwards T-Station 75. The gauge was configured to turn on the turbo-molecular pump once the roughing pump has brought the chamber pressure to an appropriate level.

The second gauge was a temperature-controlled capacitance gauge (Pfeiffer Vacuum CCR375, Pfeiffer Vacuum GmbH, Asslar, Germany) with a full-scale range of 13 Pa. This was selected to give improved accuracy in the high vacuum range (1.33×10^{-3} to 13.3 Pa) that most pyroelectric X-ray generators have been studied at. The capacitance gauge was connected to a control unit (CenterOne Control Unit, Pfeiffer Vacuum GmbH, Asslar, Germany) which displayed the pressure reading. Additionally, this reading was recorded every second by a laptop, via serial communications.

The supply of dry air into the chamber was regulated by a pair of mass flow controllers, with flow ranges of 10 sccm and 200 sccm (MKS Mass-Flo Controller 1129A, MKS Instruments, Inc., MA, U.S.A.). Depending on the pressure desired in the vacuum chamber, the supply flow rate of the mass flow controllers was controlled by a digital readout controller (MKS Type 247D Four-Channel Readout, MKS Instruments, Inc., MA, U.S.A.). As seen in Figure 5-2, there were several valves attached from the dry air supply valve to the dedicated vacuum chamber port.

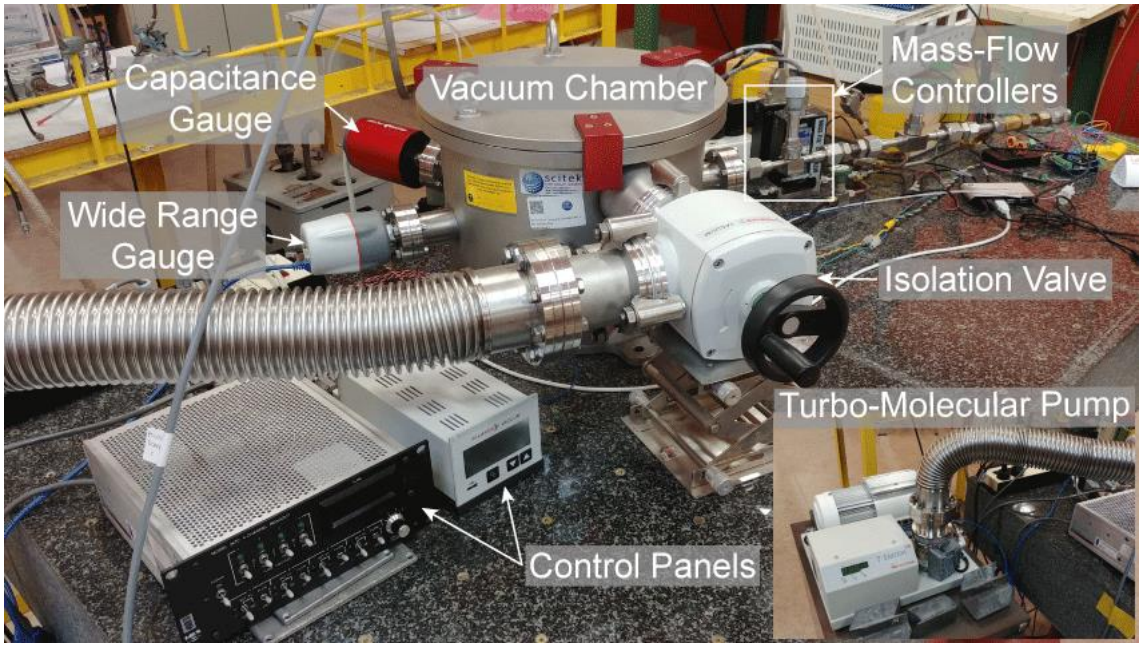

Figure 5-1 Components of the vacuum system.

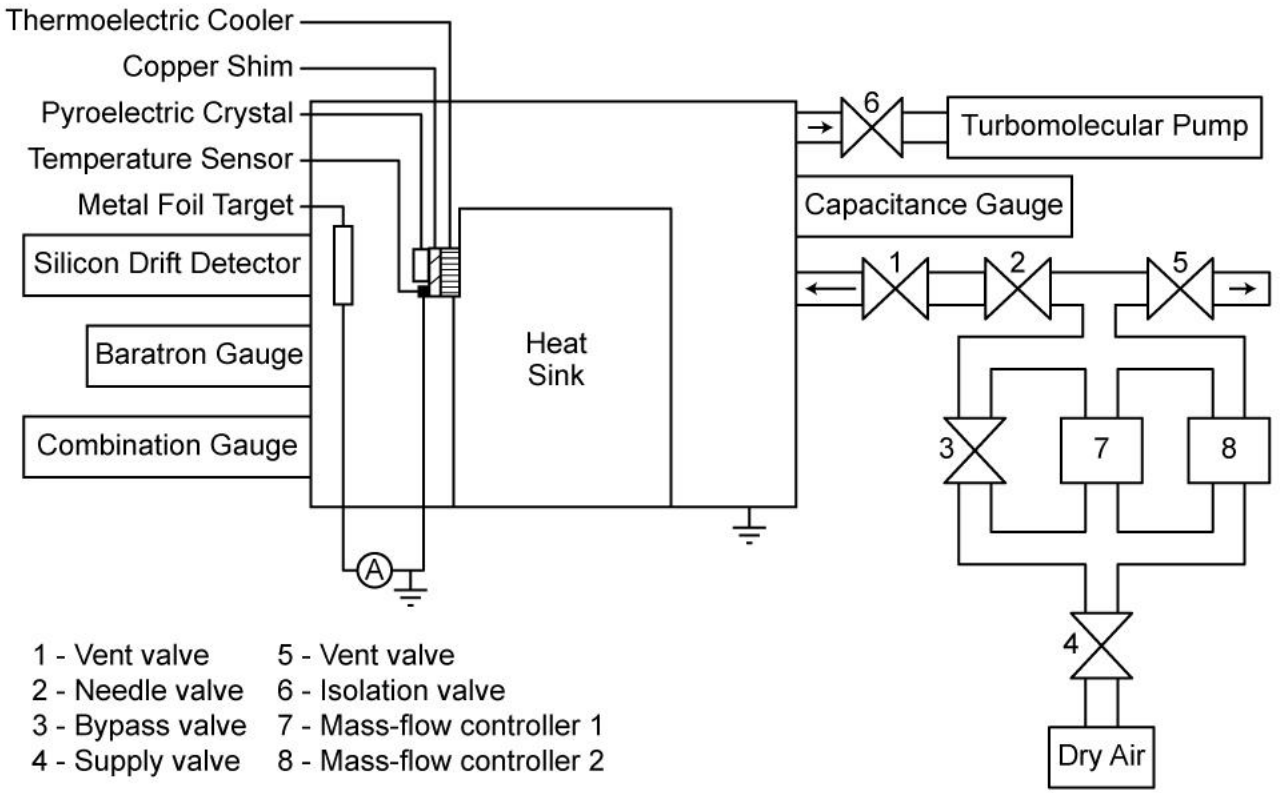

Figure 5-2 Schematic diagram of the vacuum system and the experimental setup inside the vacuum chamber.

5.3 Temperature Control System

The temperature control system was responsible for thermally cycling the pyroelectric crystal, which ultimately triggers the production of X-rays. The primary system components were a thermoelectric cooler (TEC), a temperature sensor and an Arduino microcontroller. The crystal is mounted to a copper shim on the top side of TEC. The Arduino microcontroller was programmed to cycle and monitor the stage temperature. Arduino was an open-source electronics platform and used an Arduino-integrated development environment (IDE), which was derived from other open-source programming environments such as Java and Processing. The Arduino Uno microcontroller board (Arduino AG, Italy) was used to operate the generator.

The temperature sensor was a platinum resistance temperature detector (RTD) (PT100 thin film, Class A, Labfacility Ltd., West Sussex, U.K.). The sensor was a four-wire configuration and used a RTD-to-digital converter peripheral module (MAX31865, Maxim Integrated Products, Inc., CA, U.S.A.) to convert the resistance of the sensor element to digital values that was read into the Arduino [200] via serial peripheral interface (SPI) communication [201]. The sensor was placed on the copper shim near the crystal, indicated in Figure 5-6. As the extension RTD cable was a three-wire configuration, the sensor was converted into a three-wire configuration by combining the terminals of the two white wires together. Similarly, the peripheral module was adjusted to a three-wire RTD connection. In early experiments, a TO-92 package temperature sensor (TMP36, Analog Devices, Inc., MA, U.S.A.) was used. It was placed in the same location as the current temperature sensor.

The power supply and heating and cooling function of the TEC (Model 03111-9L31-04CG, Custom Thermoelectric, MD, U.S.A.) was controlled by an H-bridge and pulse-width-modulation (PWM) signal [202]. The PWM signal modulated the appropriate duty cycle of the power supplied to the TEC. The TEC can receive a PWM signal between zero and 255, however in this case it was limited to 158 to keep the TEC power draw below its specified maximum. The frequency of the PWM is locked at 18500 Hz. The PWM signal and direction was sent via the H-bridge motor driver (Pololu Dual VNH5019 Motor Driver Carrier, Pololu Corporation, NV, U.S.A.) to the TEC with a low-resistance low-pass filter (LC filter) connected in series between the H-bridge

motor driver output and the TEC. The H-bridge motor driver was used to drive the TEC as it can reverse the direction of thermal phase. This allowed automatic control of heating and cooling cycles using limit and tuning parameters as noted in the Arduino code, Generator8, and can be found in Appendix C The H-bridge was used to switch a 6 V DC voltage from a benchtop power supply. The low-pass filter was constructed using 100 μH toroidal inductors and capacitor. The low-pass filter was used to smooth the PWM output of the H-Bridge, maximising the efficiency of the TEC. Part of the temperature control system and the electric circuit schematic driving this system can be seen in Figure 5-3 and Figure 5-4.

A feedback loop was established between the Arduino, temperature sensor and an H-bridge motor driver. A proportional-integral-derivative (PID) library [203] was utilised for precise and smooth temperature control. The PID algorithm was setup to ramp the stage temperature up and down at a rate of 10°C/min, approximating a triangle wave. The Arduino was programmed to set the new temperature every second and took the input temperature, which was an average of 10 readings measured every 100 ms from the temperature sensor. The PID algorithm will calculate an error difference between the measured input and the desired set point, and depending on the tuning applied, will output a value to reduce the error. This output value was the PWM signal.

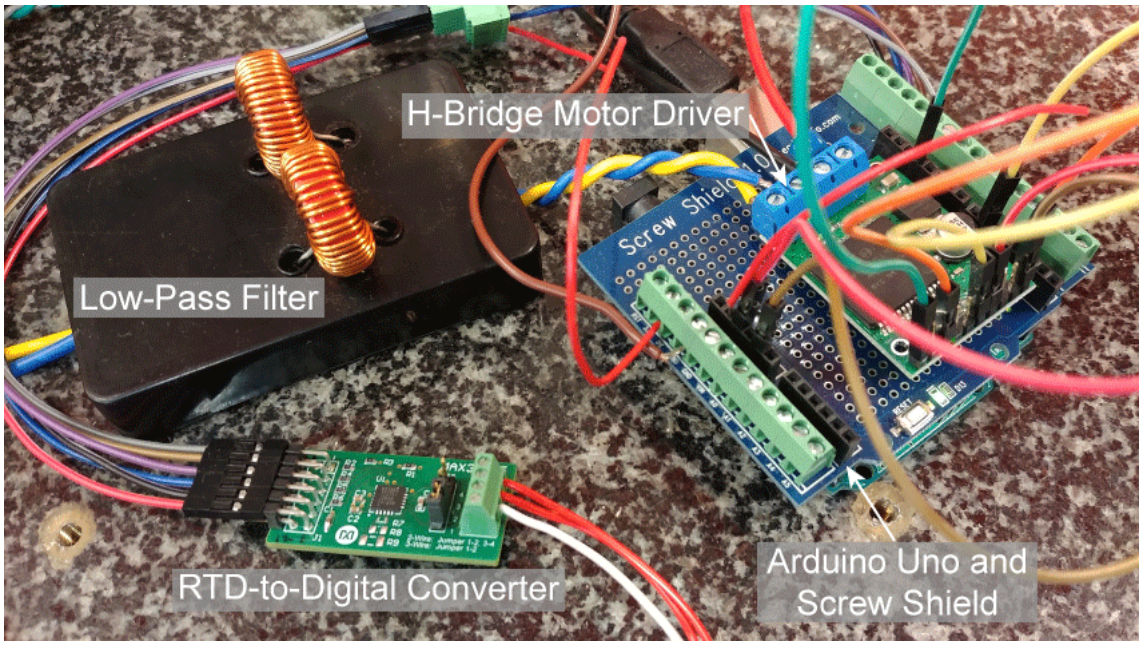

Figure 5-3 Electrical components of the temperature control system that sit outside the vacuum chamber.

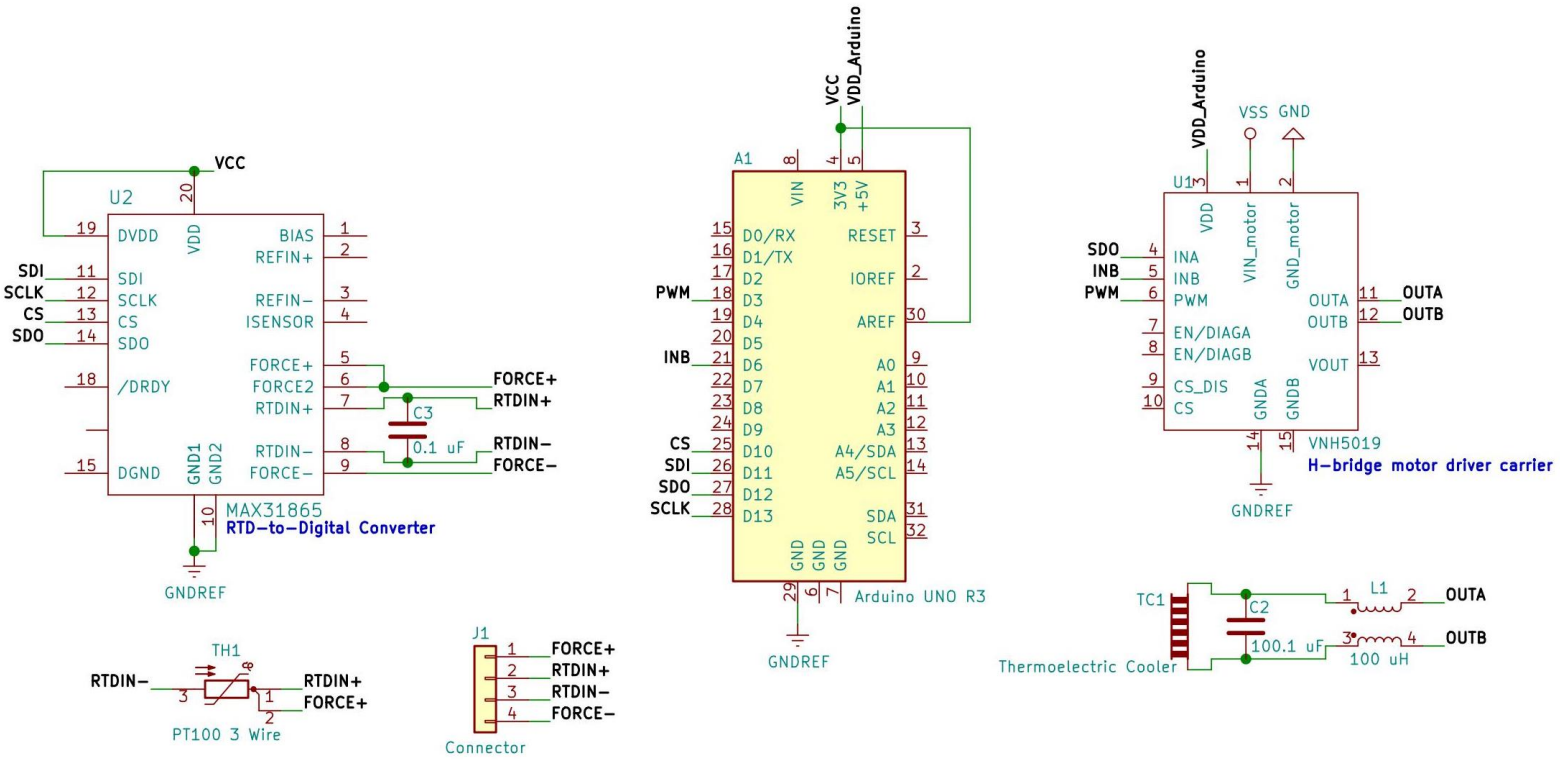

Figure 5-4 Electrical circuit schematic of the temperature control system.

5.4 Data Acquisition System

The role of the data acquisition system was to collect real-time data from various equipment in the testbed to support thorough characterisation of the experimental X-ray generator. Recorded parameters include the crystal temperature, pressure in the vacuum chamber, electron emission current, and X-ray output. The data was logged from the device to the computer via serial communication. To set up parallel serial communications, an open source SSH, Telnet, Rlogin client (or terminal emulator), ExtraPuTTY [204] and PuTTY Session Manager [205], were used. ExtraPuTTY was an extension of the more common PuTTY SSH client [206] while the PuTTY Session Manager was to organise and launch multiple PuTTY sessions simultaneously. Each device was connected to a different serial COM port in the computer and logs real-time data into separate text files. If the device had its own user interface to display and record data, the program will be used instead. The data setup and collection from each device will be mentioned in detail below.

5.4.1 Temperature control

In addition to controlling the temperature of the TEC, the Arduino was programmed to record various parameters relating to its operation. These included the set point temperature, the PWM signal, the TEC voltage and the crystal temperature. The data was collected every second as a new setpoint temperature was assigned each second. Only the temperature sensor and TEC of the temperature control system were located inside the vacuum chamber and connected to the Arduino and laptop via a sub-D feedthrough.

5.4.2 X-ray detection

The detection and measurement of X-rays was achieved using a silicon drift detector (SDD)-based X-ray spectrometer (X-123SDD, Amptek, Inc., MA, U.S.A.). This spectrometer incorporated a TEC-cooled silicon drift X-ray detector, preamplifier, digital pulse processor and multichannel analyser (MCA). An SDD-based spectrometer was selected for this experiment, as it provides both high-resolution and high efficiency detection for the 1 to 30 keV X-rays typically produced by pyroelectric X-ray generators. The spectrometer was customised with an extended probe and conflat compression O-ring vacuum feedthrough. This allowed the spectrometer to be positioned near the

X-ray generator inside the chamber for maximum detection efficiency, while the electronics enclosure remained on the outside.

The spectrometer was calibrated using the radioisotopes, iron-55, americium-241 and barium-133. The detector gain was first adjusted so that the energy spectrum covered the range between 0 and 86.87 keV: 0 keV corresponds to channel zero and 86.87 keV corresponded to channel 8191. After configuring this setting, the channels corresponding to iron-55 Kα decay energy (5.899 keV), americium-241 gamma emission energy (59.54 keV) and barium β decay energy (80.998 keV) were recorded and used to calibrate energy channel numbers in terms of energy. The acquisition setting of the spectrometer was set to a peaking time of 0.8 μs. The energy resolution achieved at this peaking time was about 186 eV FWHM at the nickel Kα line (7.47 keV).

The X-123SDD also included eight single-channel analysers (SCA), each could be configured to generate a digital pulse each time an X-ray inside a user-specified energy range is detected. The output of an SCA was connected to an Arduino Nano (Arduino AG, Italy) microcontroller to record X-ray counts as a function of time. The Arduino Nano used a Frequency Counter library to determine the number of detected X-rays in a gate time of 10 ms. Due to this gate time and compensation of the frequency counter, there will be a difference in counts collected from the multichannel analyser and the single channel analyser. The total counts collected from the SCA was consistently approximately 17% less than the MCA counts, shown in Figure 5-5. The difference in counts can be attributed to measurement errors associated with the frequency counter such as a quantisation error as some counts are missed as the gate time closes [207].

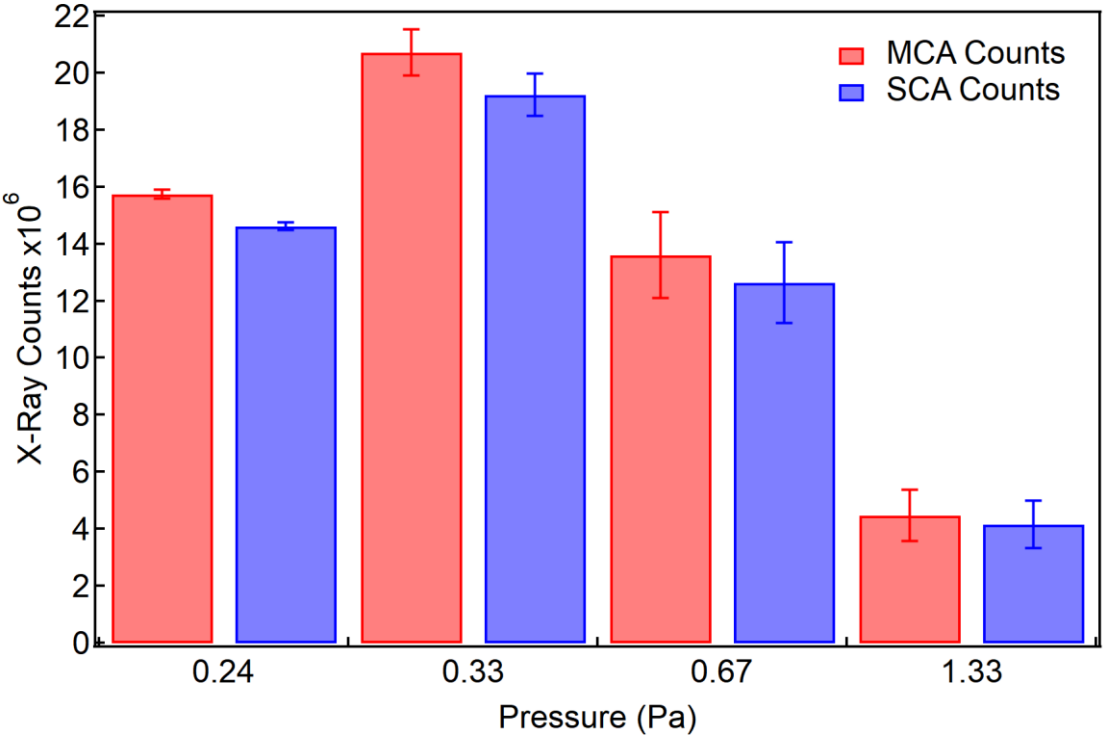

Figure 5-5 Total X-ray counts collected from the multi-channel analyser (MCA) and single-channel analyser (SCA).

5.4.3 Ion current measurement

A picoammeter (Model 9103 Picoammeter, RBD Instruments, Inc., OR, U.S.A.) was employed to measure the current at the metal target. This will give insight to the direction and magnitude of the electrons and ions travelling between the crystal and target. The picoammeter was connected between the otherwise electrically isolated metal target holder and the grounded copper shim located on top of the TEC.

The picoammeter had a Graphics User Interface software called Actuel. Through this software, the settings for the data acquisition was set up in the following manner:

- Range: 2 nA
- Sampling rate: 100 ms
- Filter: 32
- Input: Normal
- Bias: Off

5.5 Generator Setup

The generator was set up such that the polar surfaces of the pyroelectric crystal were parallel and in line with the face of the X-ray spectrometer. As the pyroelectric crystal have positively and negatively charged surfaces on opposite faces, the positively charged surface was attached with silver conductive paint (Electrolube, Leicestershire, U.K.) to an oxygen-free copper shim that was 0.3 mm thick. The copper shim was attached to the thermoelectric cooler using silver conductive epoxy (CircuitWorks® Conductive Epoxy, Chemtronics, GA, U.S.A.). It was important that any excess silver conductive paint and silver conductive epoxy on the edges of the pyroelectric crystal, copper shim and thermoelectric cooler must be removed. As such, these surfaces were cleaned using acetone.

The temperature sensor and crimp connector, indicated as the ground pin in Figure 5-6 and Figure 5-7, were also mounted onto the copper shim using silver conductive epoxy. The silver conductive epoxy here acted as a thermal conductive adhesive to hold the temperature sensor in place and as an electrically conductive adhesive to connect the copper shim to ground. Both the temperature sensor and connector were then insulated with Kapton® tape to prevent any electrical breakdown due to the large electric field formed around the pyroelectric crystal.

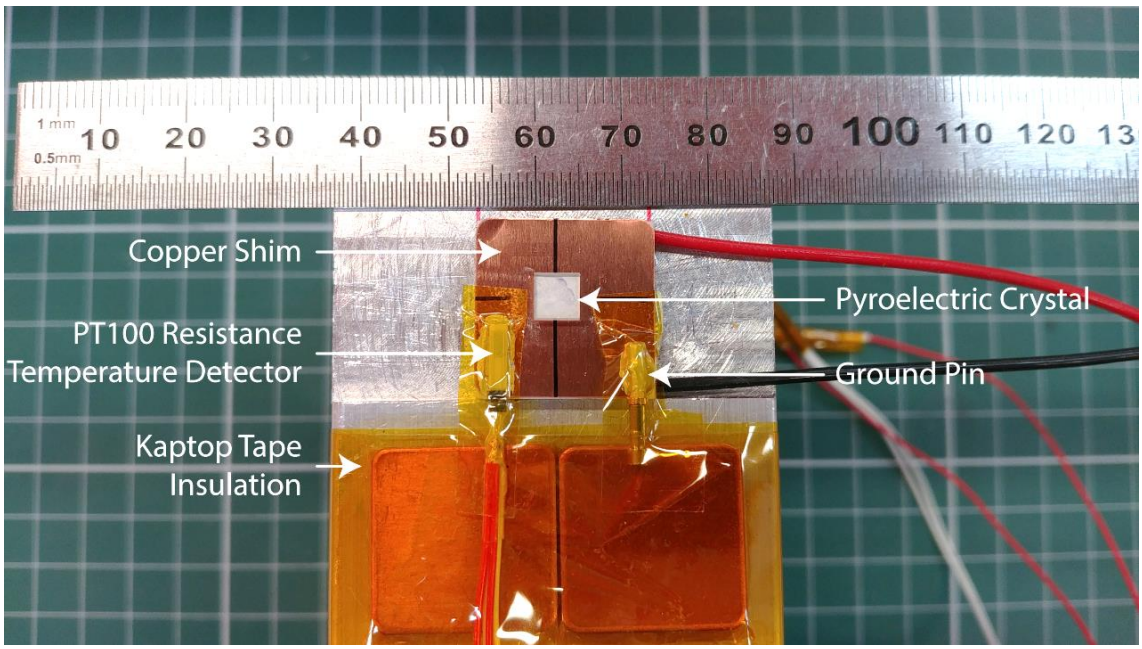

Figure 5-6 Front view of the experimental setup.

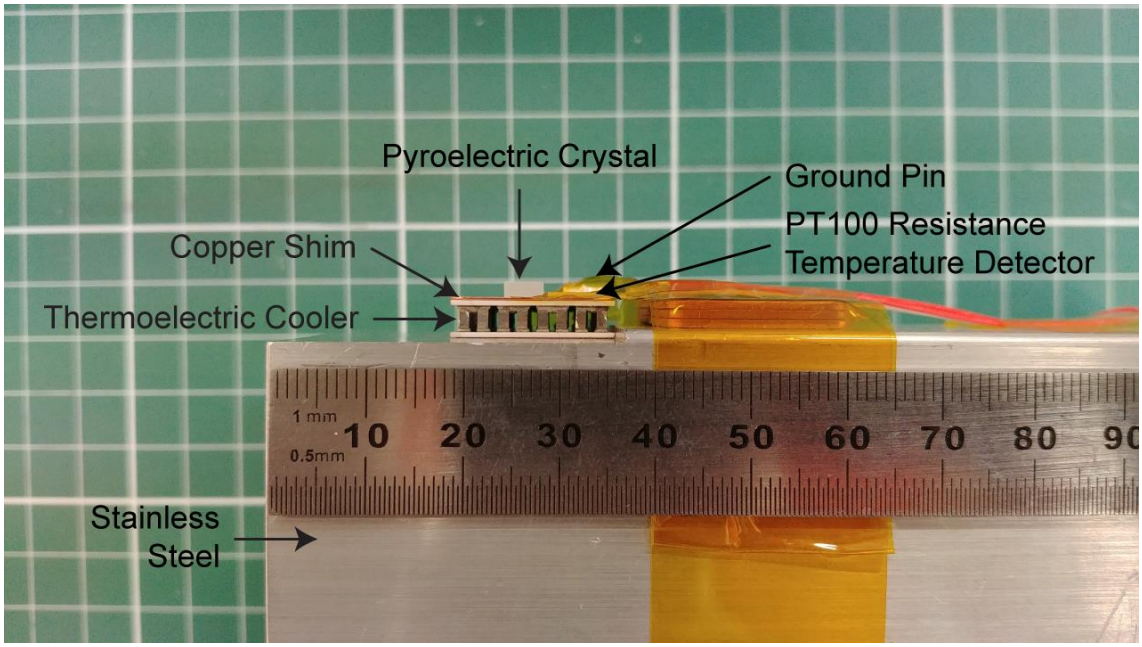

Figure 5-7 Side view of the experimental setup.

The sample stage was then mounted onto an aluminium heat sink using double-sided thermal conductive tape (Double coated tissue tape 9448A, 3M™, MN, U.S.A.). The aluminium heat sink serves two purposes; first was to absorb the heat exhausted from the thermoelectric cooler, and second was to hold the sample stage in position aligned with the detector. In between the pyroelectric crystal and the detector sat a thin metal foil. This metal foil was clamped between two stainless steel plates that was connected to a PTFE block and subsequently to a triple-axis crossed-roller bearing linear stage (Model AKSM13(A)-40LLZ, Zolix Instruments Co., Ltd., Beijing, China). Figure 5-8 and Figure 5-9 show the assembly inside the vacuum chamber.

Vacuum-compatible wires must be used in the vacuum chamber to prevent outgassing of materials such as polymer sheath. Outgassing is the desorption of vapours and gases from surfaces in a vacuum environment and is known to impede the performance of a vacuum system. The in-vacuum wire used in this experimental setup was a Kapton® insulated 7 stranded core wire (LewVac Components Limited, East Sussex, U.K.). All exposed metallic end connectors were insulated with Kapton® tape.

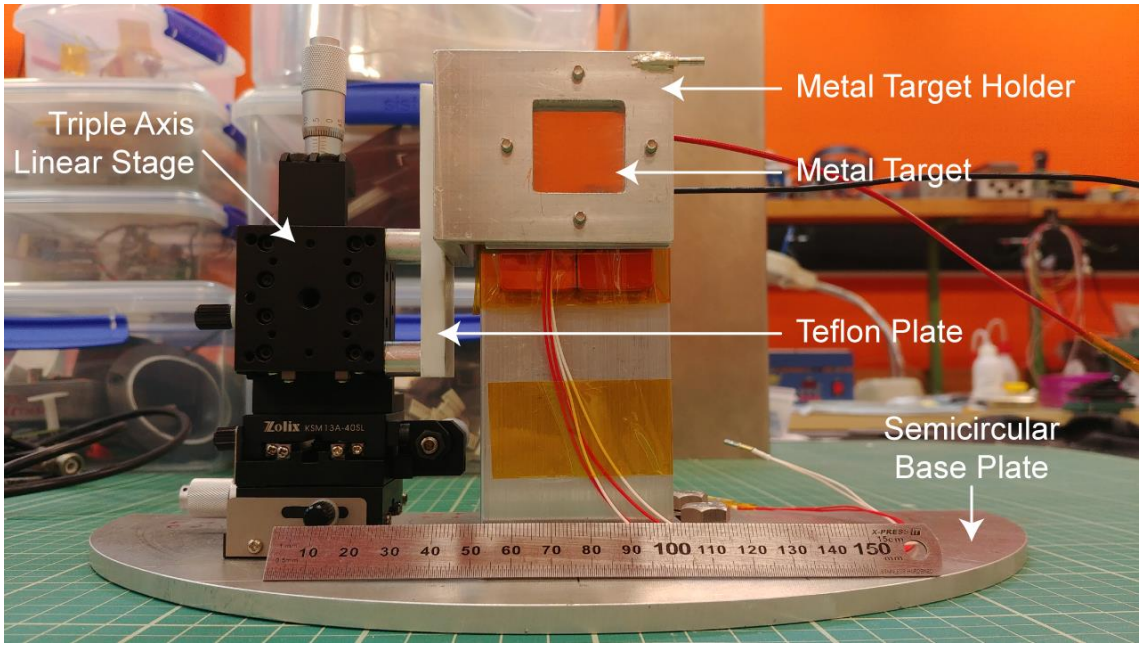

Figure 5-8 Front view of the complete experimental apparatus that sits inside the vacuum chamber.

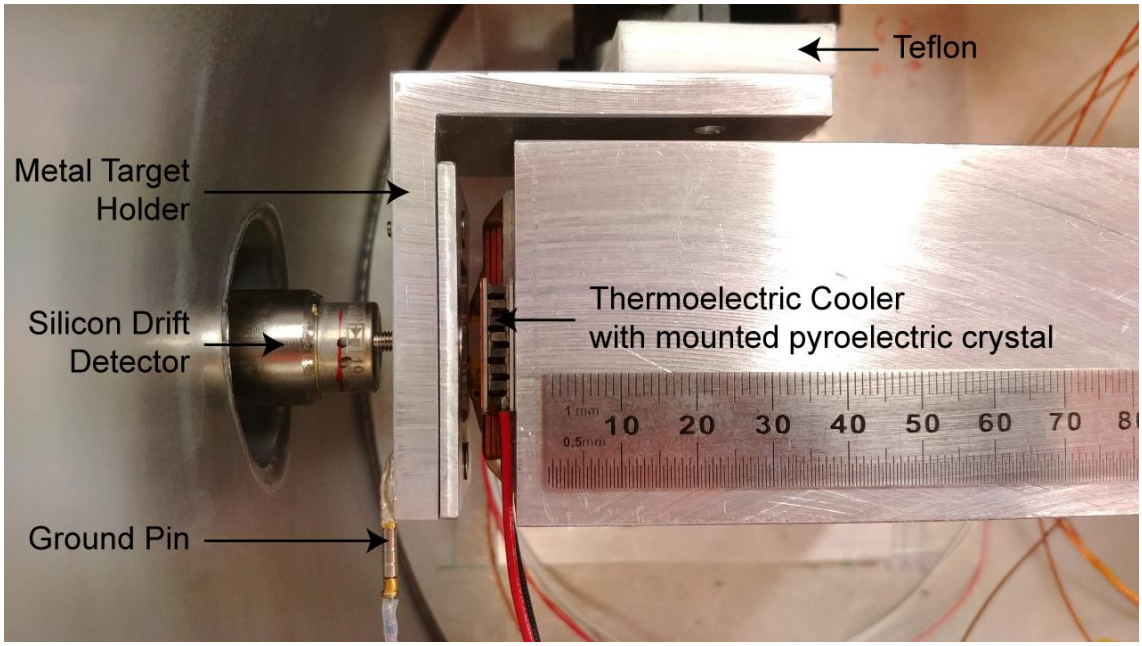

Figure 5-9 Top view of the experimental apparatus sitting inside the vacuum chamber, and the pyroelectric crystal and the metal target in line with the X-ray detector.

5.6 Vacuum setup

The experiments began with pumping the chamber down to a hard vacuum and allowing the entire system to warm-up. This typically took 1 h to complete. Warm-up was recommended for the vacuum gauge, mass-flow controllers, picoammeter and power supply to ensure stable and accurate operation.

Once the vacuum chamber had settled, turbo-molecular pump was choked by turning the gate valve one and a half turns from open. The vent valve was slowly opened followed by the needle valve. This operation must be carried out slowly to avoid a sudden increase in pressure and potentially damaging the beryllium window on the X-ray detector.

After the vent valve and needle valve were fully opened, the pressure in the vacuum chamber was controlled by adjusting the amount of gas flowing through the mass-flow controllers. Depending on the pressure, either Channel One or Channel Two was only used.

6

CHARACTERISATION AND OPTIMISATION OF THE X-RAY GENERATOR

"One's destination is never a place but another way of looking at things."

– *Henry Miller*

6.1 Overview

In this chapter, the pyroelectric X-ray generator constructed will be characterised and optimised in terms of several parameters. The experimental method to study the effect of these parameters will firstly be introduced. This will be followed by the analytical methods of the results. The X-ray generator's performance as a function of the various parameters will then be assessed by the produced X-ray counts and end-point energy to determine the best combination of parameters.

6.2 Experimental Methodology

As alluded to in the early sub-chapters, an X-ray generator required three main components; an accelerating electric field, an electron source and a target. In order to improve and optimise the X-ray generator, the parameters affecting these three main components must be explored. They were determined by a combination of factors such as the properties of the pyroelectric crystal and thin metal target, the distance between the crystal and metal target, and the pressure and gas filled inside the vacuum chamber.

A shortlist of parameters was selected, and the X-ray generator was tested as a function of:

- Crystal thickness
- Crystal composition
- Pressure of the vacuum chamber
- The distance between the exposed crystal face and metal target, otherwise known as the gap distance

The parameters that were kept constant were the:

- Surface area of the pyroelectric crystals, set at 25 mm^2
- Gas filled inside the vacuum chamber, using dry air
- Material and thickness of the metal target, using 7.5 μm nickel of 99.9% purity (Advent Research Materials Ltd, Oxford, England)

The crystals acquired for the experiments were listed in Table 6-1. The crystals were prepared as single domain single crystals with two mirror-polished faces perpendicular to the Z-axis for lithium tantalate ($LiTaO_3$) and lithium niobate ($LiNbO_3$), and perpendicular to the [111] direction for lead manganese niobate – lead titanate (PMN-30PT). The direction of spontaneous polarisation for $LiTaO_3$ and $LiNbO_3$ were parallel with the Z-axis [208]. The [111] direction was chosen for PMN-30PT because, as shown in Chapter 3 Figure 3-22, it produced higher calculated charge density and electric field than PMN-30PT prepared in the [001] direction.

The material of the target was selected such that the X-ray generator would produce different characteristic X-rays from the copper shim and confirm the direction of electron movement during thermal cycling of the crystal. The thickness of the metal target was chosen based on optimum transmission of X-rays determined via Monte Carlo simulation, as well as cost and availability.

Table 6-1 Crystal compositions and their dimensions and orientations tested.

Sample	Area (mm^2)	Thickness (mm)	Orientation	Manufacturer
LiTaO3	5.00×5.00	0.5, 2.0	Z-cut	HeFei Crystal Technical Material Co., Ltd., HeFei, China
LiNbO3	5.00×5.00	2.0	Z-cut	HeFei Crystal Technical Material Co., Ltd., HeFei, China
PMN-30PT	4.95×5.04	2.0	[111]	Innovia Materials Co., Ltd, Shanghai, China

The combination of parameters at which the X-ray generator was tested were listed in Table 6-2. The crystal, $LiTaO_3$, with a crystal thickness of 0.5 mm was not tested at a gap distance of 3.7 mm due to the limitation of the experimental setup and the closest distance achievable is 5.3 mm.

Table 6-2 The values of the parameters tested for each crystal.

Crystal Composition	Crystal Thickness (mm)	Gap Distance (mm)	Pressure (Pa)
$LiTaO_3$	0.5	5.3, 10.0	0.24, 0.33, 0.67, 1.33
$LiTaO_3$	2.0	3.7, 5.0, 10.0	0.24, 0.33, 0.67, 1.33
$LiNbO_3$	2.0	3.7, 5.0, 10.0	0.24, 0.33, 0.67, 1.33
PMN-30PT	2.0	3.7, 5.0, 10.0	0.24, 0.33, 0.67, 1.33

6.3 X-ray Spectra

6.3.1 Characteristics of the X-ray spectra

As described in Chapter 4.4.2, the generator output was measured using a silicon drift detector (SDD)-based X-ray spectrometer. The spectrometer produces a histogram, or spectrum, of detected X-ray counts as a function of energy collected over the measurement time. Figure 6-1 shows the spectrum of X-rays measured over several thermal cycles of a pyroelectric crystal. The spectrum shows two primary features: a broad bremsstrahlung continuum and characteristic peaks due to X-ray fluorescence.

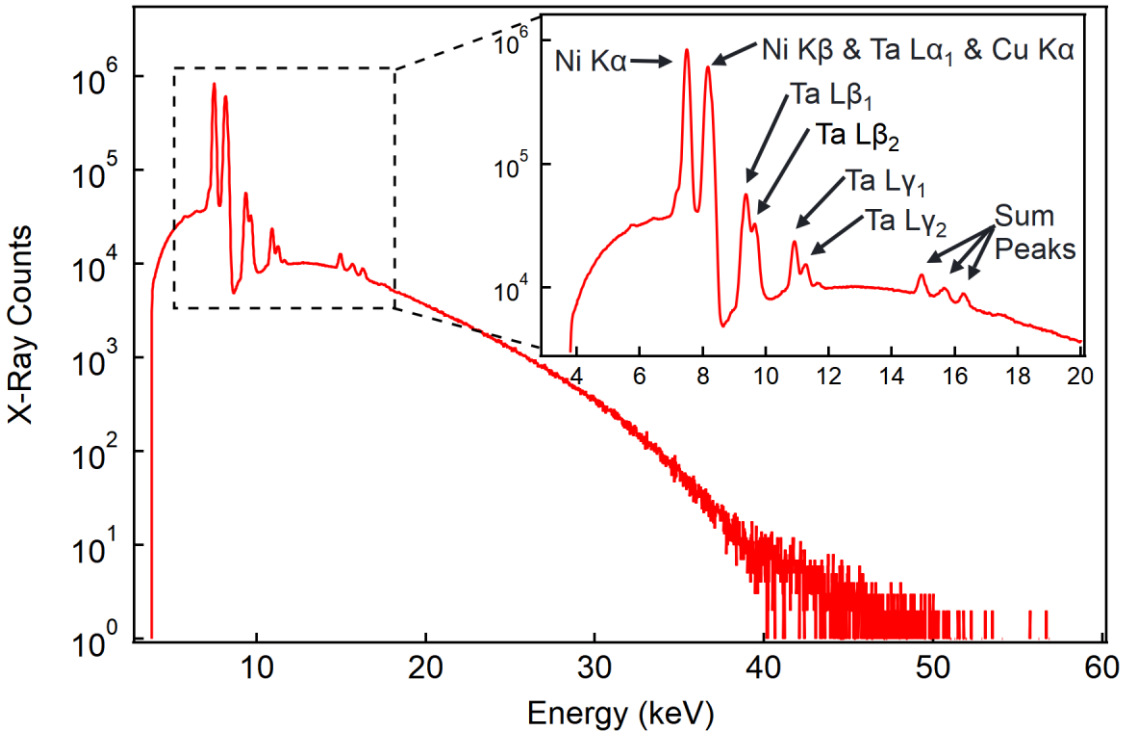

Figure 6-1 An X-ray spectrum of the X-rays produced from the pyroelectric X-ray generator. The collection time was over 1 h or 3 heating-cooling cycles. The inset shows characteristic X-ray emission lines predominantly from nickel and tantalum. The bremsstrahlung reaches to energies of approximately 55 keV.

The characteristic peaks of the X-ray spectra were characterised by fitting a polynomial function to the bremsstrahlung continuum and Gaussian profiles to each X-ray peak. The polynomial function of up to six degrees was applied and its coefficients were determined using the lmfit package for Python, which uses the non-linear least-squares fitting method [209, 210]. The Gaussian function employed was

$$G(x) = A\frac{1}{\sqrt{2\pi}\sigma}e^{\frac{-(x - x_0)^2}{2\sigma^2}} \quad (6\text{-}1)$$

where σ is the peak resolution, A is the area of the X-ray peak and x_0 is the energy of the corresponding X-ray peak. The area of each X-ray peak was also calculated with lmfit.

During the heating and cooling phases, different characteristic X-rays are produced. The spectrum collected during the heating phases, shown in Figure 6-2, exhibits emission lines corresponding to nickel and copper. The nickel Kα and Kβ lines at energies 7.47 keV and 8.26 keV, respectively, indicate that electrons are travelling from the crystal towards the nickel target. This is because the rising temperature increases the spontaneous polarisation, which makes the exposed crystal face more negatively charged. This causes the exposed face to attract positive ions and repel electrons. Therefore, it confirms that ferroelectric electron emission occurs during the heating phase when the -Z crystal face is exposed to compensate for the changes in surface charges.

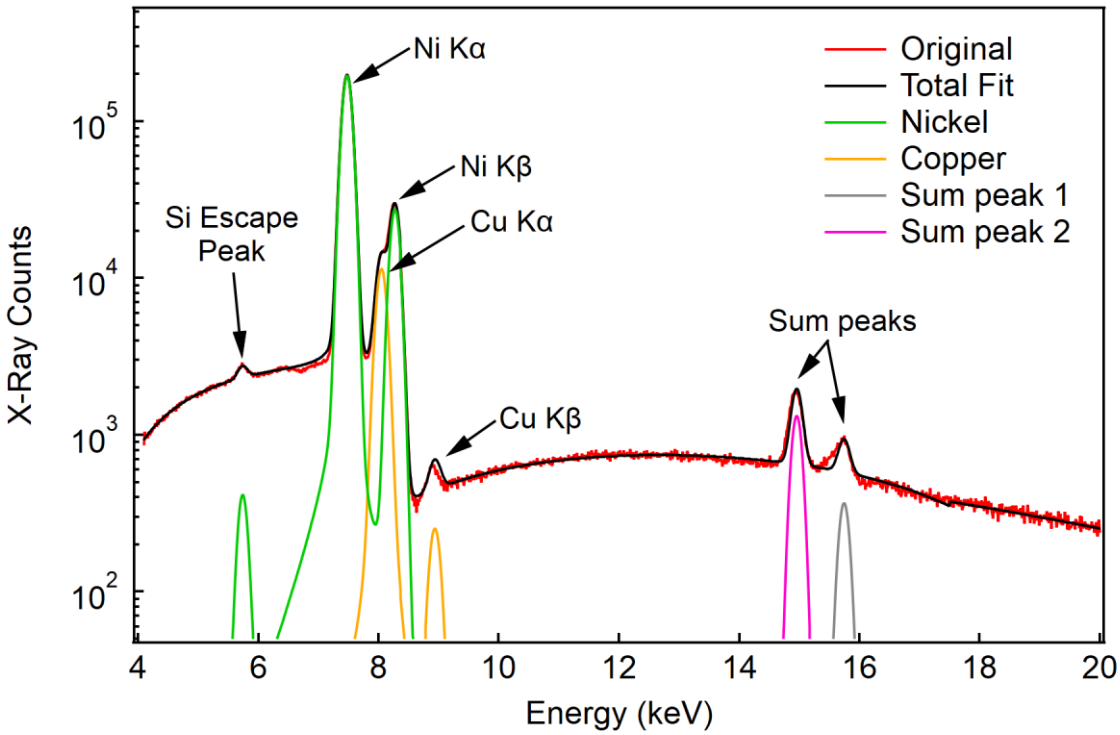

Figure 6-2 X-ray spectrum collected during heating phase and fitted with elemental characteristic peaks.

For the copper Kα and Kβ lines with energies of 8.04 keV and 8.90 keV respectively, it is suspected that the electrons travel around the edges of the pyroelectric crystal and collide with the copper shim, which is attached to the +Z face of the pyroelectric crystal. The drop in the X-ray intensity at approximately 8.3 keV coincides with the K-absorption edge of nickel.

The two additional types of lines existing in the spectra are sum peaks and silicon escape peaks. The sum peaks are a combination of full energy lines, where the peak at 14.93 keV consists of nickel (Kα + Kα) lines and the peak at 15.74 keV is a sum of nickel (Kα + Kβ) lines. The sum peaks can be apparent for different reasons such as due to the pile-up effect or X-rays arriving too closely that the detector is unable to discriminate them. Thus, two X-rays are recorded as one X-ray energy. Upon reducing the peaking time to 0.8 μs to better discriminate incoming X-rays, the sum peaks were still apparent.

It has been mentioned previously by Brownridge and Raboy [81, 103] of the possibility that the electrons travel in packets or "clusters" during the emission. This possibility can be estimated by applying the Poisson distribution to determine the probability of two X-rays arriving in the same time period. The assumption here is all events are independent and random. The digital pulse processor of the X-ray spectrometer is set with "Pile-Up Rejection" enabled, which means it will utilise the "Fast Channel" to determine if two closely-occurring events are accepted or rejected. The fast channel pulse pair resolving time is 120 ns. Using the spectrum in Figure 6-2, the count rate of the nickel Kα line is 395.1133 cps within an accumulation time of 495.263 s. This translates to 47.4136×10^{-6} counts per 120 ns period, which is the rate parameter. Therefore, the probability of two counts arriving in the same 120 ns period is 1.124×10^{-9} and the expected count rate of a nickel (Kα + Kα) line is 4.44×10^{-7} cps. However, the actual count rate of this sum peak is 2.675 cps, which is much greater than the expected value. This suggests it is likely the events do not occur independently and reinforces the possibility of electrons, and subsequently, X-rays travel in packets.

Silicon escape peaks are generated from incoming X-rays fluorescing the silicon element in the detector, producing a 1.74 keV silicon Kα X-ray. If this Kα X-ray subsequently escapes the detector, the energy deposited in the detector is reduced by 1.74 keV. Figure 6-2 exhibits a silicon escape peak at 5.73 keV.

An X-ray spectrum was also collected during the cooling phase from 100°C until 0°C. Apart from the nickel and copper lines still apparent, a set of tantalum L-shell lines can be seen. The energies that correlate to the lines in Figure 6-3 from left to right are 7.19, 8.14, 9.35, 9.64, 10.88, 11.262 keV. The observation of tantalum lines confirms the direction of the electric field in the gap has reversed such that electrons travel and collide with the surface of the lithium tantalate single crystal. This suggests that electrons originate from field ionisation of the gas molecules present in close vicinity to the crystal face. As the surface charge on the -Z crystal face is becoming less negatively charged during the cooling phase of the thermal cycle, the electrons produced will be attracted to the crystal face and accommodate for the change in charge.

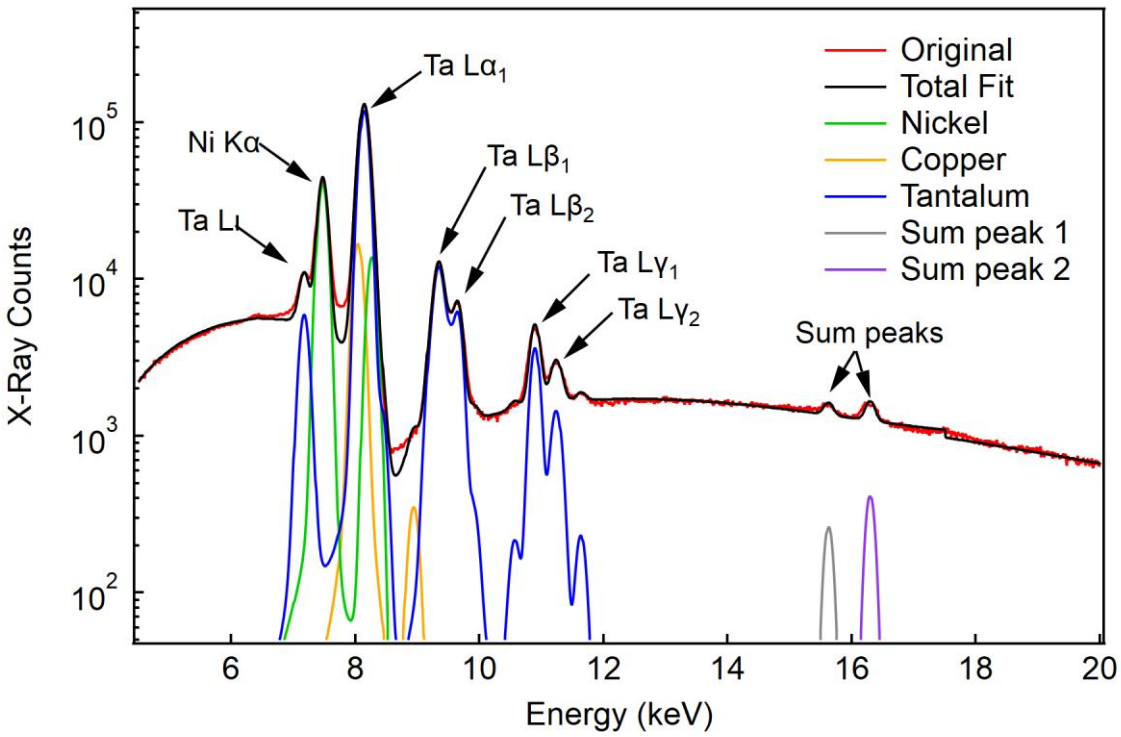

Figure 6-3 X-ray spectrum collected during the cooling phase.

The sum peaks in this figure are different to the sum peaks collected during the heating phase. In this case, sum peak 1 is a combination of tantalum ($L\alpha_1$ + $L\iota$) at energy 15.61 keV and sum peak 2 is of tantalum ($L\alpha_1$ + $L\alpha_1$) at energy 16.26 keV. Nickel lines are still observed because the reversal of the electric field direction is a transitional effect where the intensity of the electric field developed in the heating phase is still present at the beginning of the cooling phase, before it can decrease and change polarity, as exhibited in Figure 6-4. This means some of the emitted electrons will still be travelling towards the target and have sufficient energy to produce characteristic X-rays of the target.

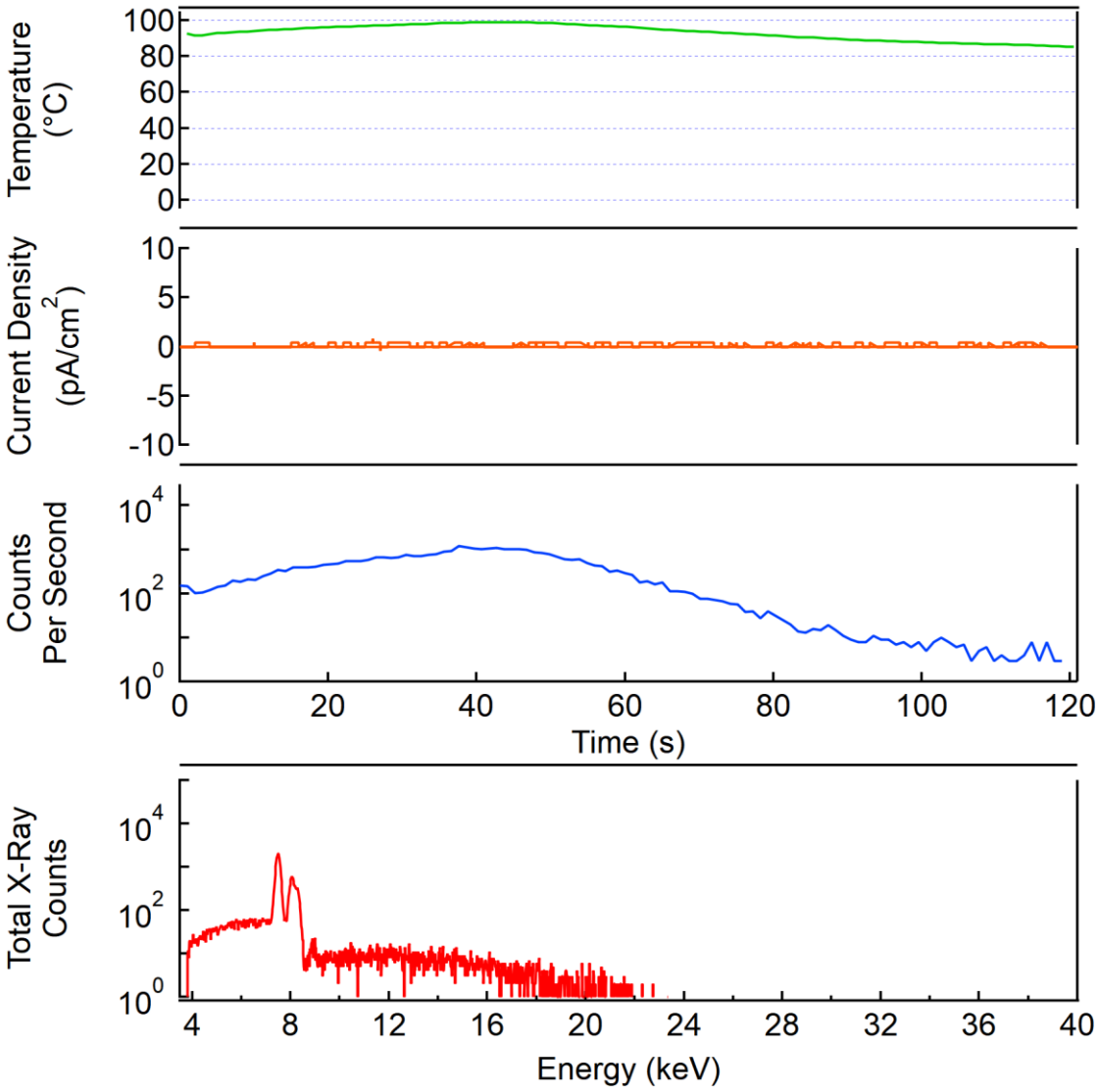

Figure 6-4 Recorded temperature, current density, time-resolved counts and energy-resolved spectrum (bottom) measured for 2 min. The X-ray counts detected per second follows the same profile as the temperature cycle where it increases as the temperature approaches 100°C and decreases upon cooling.

6.3.2 End-point energy evaluation

The end-point energy of the spectra is determined by employing the Baseline Fitting package (Version 3.08) in IGOR Pro. A smoothing spline is fitted over the upper region of the bremsstrahlung continuum of the normalised X-ray spectrum, as exemplified in Figure 6-5. The same region is used for each respective crystal composition and configuration. The end-point energy is then selected as the energy at which the normalised X-ray count drops below 5×10^{-7}. This value was selected in order to exclude the pile-up effect in the assessment of the end-point energy.

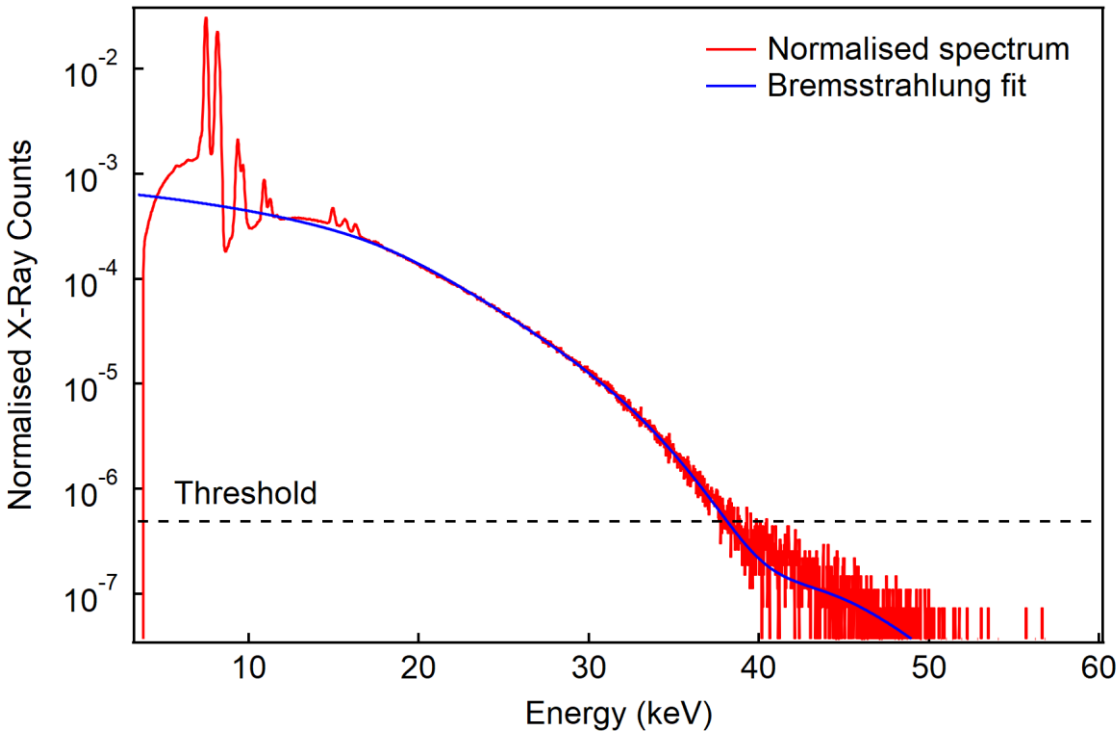

Figure 6-5 Fitting of the bremsstrahlung continuum in a normalised X-ray spectrum.

6.3.3 Variation of count rate and end-point energy with temperature and time

In Chapter 3, it was introduced that the pyroelectric coefficient and therefore, the net surface charge, increased with increasing ΔT. A similar observation can be made for the increase in end-point energy through the thermal cycling of the pyroelectric crystal. Figure 6-6 displays the X-rays counts collected as a function of time and energy in intervals of 2 min through the heating phase. It is evident that at the onset of X-ray production, the energy range is initially narrow and continues to broaden as the temperature rises, as seen through Figure 6-6(a) to (c). Also noticeable in Figure 6-6(c) is a sharp diminished drop in count rate. This drop suggests an electrical breakdown and will be discussed in the later part of the chapter. However, another feature apparent is that when X-rays are being generated again, the count rate rises slightly faster from 70°C to 90°C and achieves a higher end-point energy than when the temperature was increasing from 30°C to 50°C. The end-point energy of (b) and (d) are 26.32 keV and 27.98 keV, respectively. This confirms a comment made in Chapter 3 that thermal cycling the pyroelectric crystal at higher temperatures and perhaps closer to its T_C will produce higher energy X-rays and at a faster rate. Likewise, the count rate and end-point energy follow a similar profile during the cooling phase, as displayed in Figure 6-7.

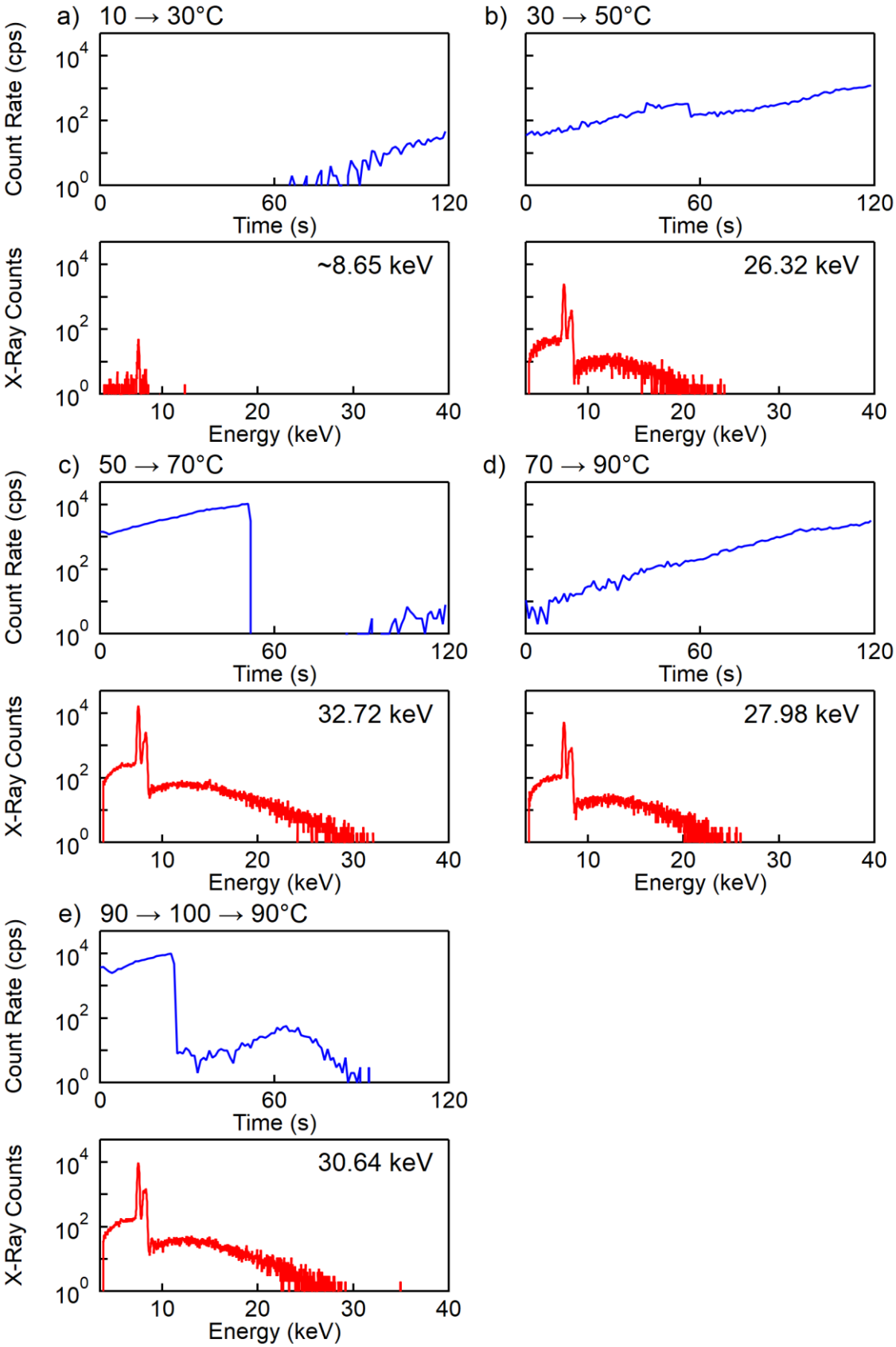

Figure 6-6 Two-minute interval time-resolved and energy-resolved measurements of the heating phase. The end-point energy of each measurement is indicated in the top right corner of the spectrum.

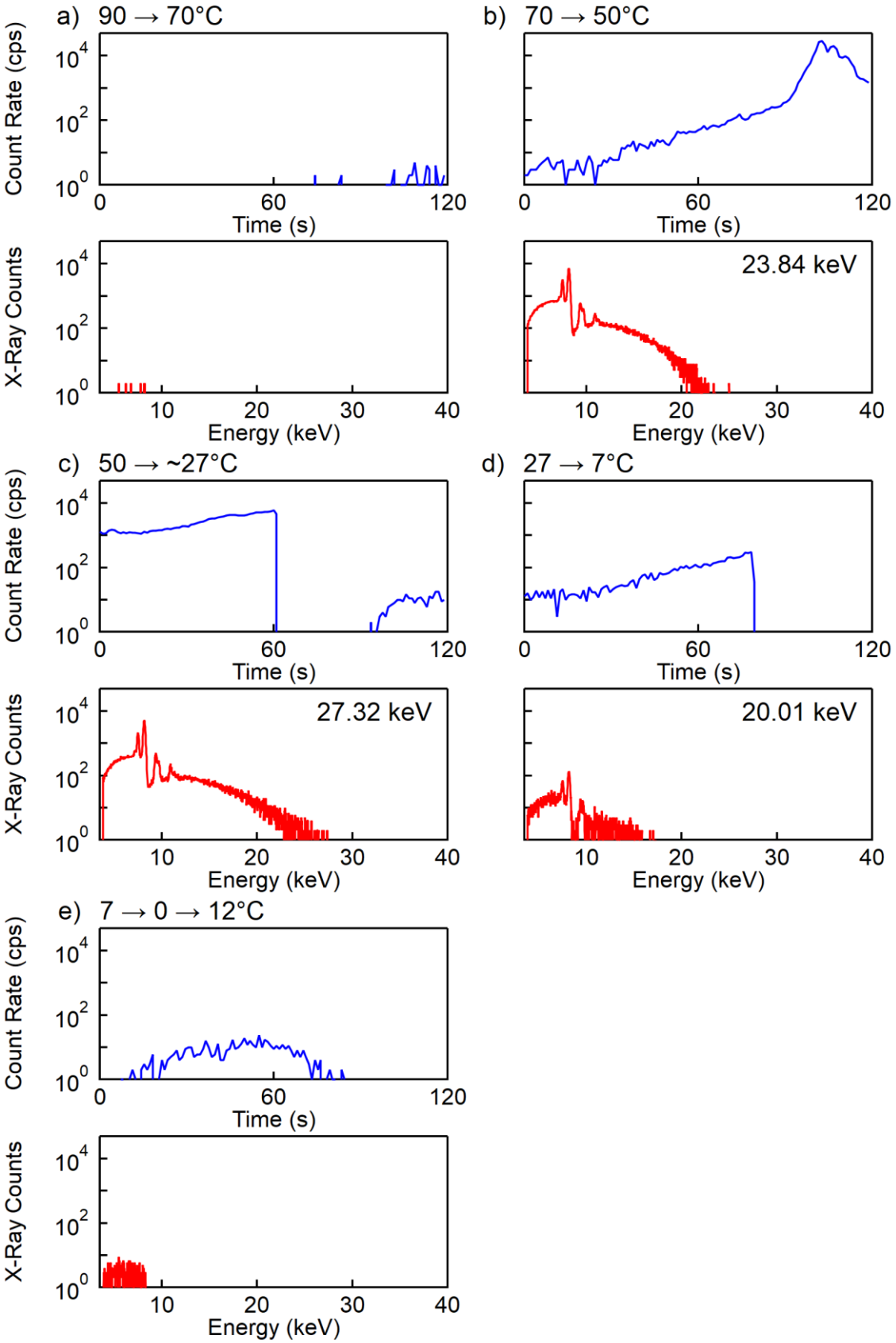

Figure 6-7 Two-minute interval time-resolved and energy-resolved measurements of the cooling phase, following from Figure 6-6. The end-point energy of each measurement is in the top right corner of the spectrum, unless left indeterminable.

6.4 X-ray Spectra Correction

Not all X-rays impinging on the detector are successfully detected and recorded producing a count in the accumulated spectrum. In the following experiments there were two main factors that contributed to a reduction in detection efficiency: absorption of X-rays in the beryllium window (before they could reach the detector), and the chance that the X-rays pass through the detector volume without interacting.

The intrinsic detection efficiency of the X-123 SDD was calculated using the mass attenuation coefficients provided by NIST [211]. A thin beam model was used calculate the probability that X-rays of different energies pass through the beryllium window and undergo photoelectric absorption in the detector volume, producing a signal in the detector. As the experiments were undertaken at high vacuum, the absorption of air was considered to be negligible. The model also assumed that the X-rays travel perpendicular to the detector.

Figure 6-8 shows the calculated efficiency of the detector used in all the experiments and how it affects the energy spectrum collected. The lower energies can be attributed to the lack of X-rays transmitted through the beryllium window as they are easily absorbed. On the other hand, at higher energies, the efficiency decreases due to reduced attenuation through the active volume of the detector, causing an increasing proportion of X-rays to pass through without interacting. The correction was applied by dividing the measured counts in each bin by the calculated efficiency at that particular energy.

As can be seen in Figure 6-9, the counts above 10 keV are given a greater weight, as the higher energy X-rays are more likely to pass through the detector without being detected. This suggests that the pyroelectric X-ray generator has the propensity to produce relatively high X-ray energies. The results reported in the following sections will not have the correction applied to the X-ray spectra and will be discussed as the raw collected X-ray counts. The raw spectra can be used for comparisons because the same detector with the same settings are applied for all experiments.

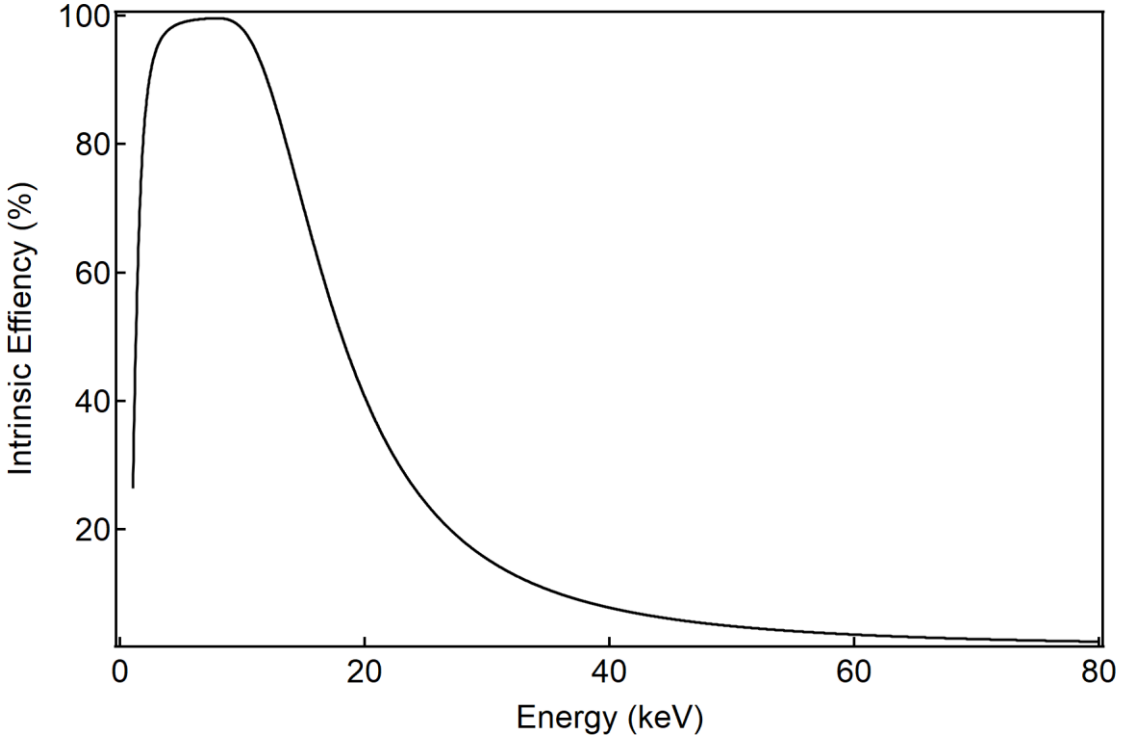

Figure 6-8 Intrinsic efficiency over photon energy of the Amptek X-123 silicon drift detector with a 12.7 μm beryllium window and 500 μm silicon detector.

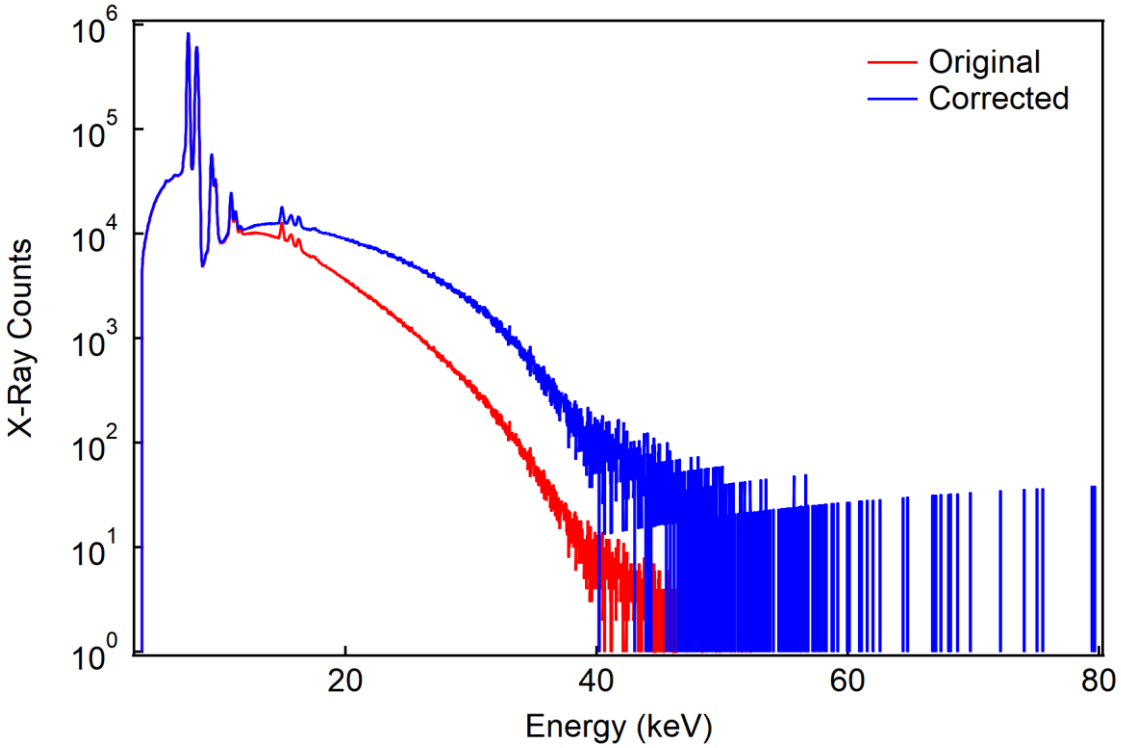

Figure 6-9 Comparison of the original energy spectrum collected from $LiTaO_3$ and its corrected version.

6.5 X-ray Generation as a Function of Various Parameters

The production of X-ray generation via the pyroelectric effect is dependent of several parameters, as mentioned in Chapter 4. Some of these parameters are set as variables, which are studied, while others remain constant. While many of these parameters are highly related to one another, the effects of each variable parameter will first be presented and discussed individually. The relationship between all variable parameters will then be tied together at the conclusion of this sub-chapter. It should also be reiterated that the term, electron emission, includes both ferroelectric electron emission during the heating phase and field ionisation during the cooling phase.

6.5.1 Effect of crystal thickness

The effect of the crystal thickness on the output of the X-ray generator was studied using two thicknesses, 0.5 mm and 2.0 mm, of $LiTaO_3$ single crystals. In Figure 6-10 and Table 6-3, the output from the $LiTaO_3$ with a crystal thickness of 2.0 mm dominates over the 0.5 mm thick crystal. The 2.0 mm thick crystal produced a maximum of ~7360 cps at a pressure of 0.33 Pa compared to the 0.5 mm thick crystal only achieving a maximum of 16.1 cps at a pressure of 0.67 Pa for the same gap distance of 5.0 mm. The 0.5 mm thick crystal also showed little variation across the pressure range it was measured at. Both crystal thicknesses also exhibited relatively stable end-point energies across the measured pressure range.

The difference in count rate between the two crystal thicknesses agrees with the figures-of-merit and electrostatics simulation findings from Chapter 3.4.5 and Chapter 4.3.2. A crystal of greater thickness creates a higher electric field in the gap, and therefore, emit electrons earlier. However, the results in the earlier chapters lied within the same magnitude whereas the count rate here was two orders of magnitude in difference. This could be because the emitted electrons from thicker crystal are able to cause secondary electron emission and amplify the X-ray generation process.

In Chapter 3.4.5, Figure 3-23 showed a linear trend between the figure-of-merit F_ε, $\frac{p}{\varepsilon}\frac{L_{crystal}}{L_{gap}}$, and crystal thickness at a fixed gap distance. The F_ε calculated for a 2.0 mm thick $LiTaO_3$ crystal was approximately four times greater than the 0.5 mm thick crystal. The electrostatics simulations in Chapter 4.3.2 also exhibited a linear trend between the potential difference and crystal thickness. The X-ray generation results here are in relatively good agreement with the theoretical findings. As shown in Figure 6-11 and Table 6-3, the end-point energy from the 2.0 mm thick crystal is approximately 40 keV, compared to the 0.5 mm thick crystal that managed to produce energies up to about 14 keV. The magnitude difference here is close to three times. Geuther *et al.* [82] has also shown this linear correlation between the end-point energy and the crystal thickness.

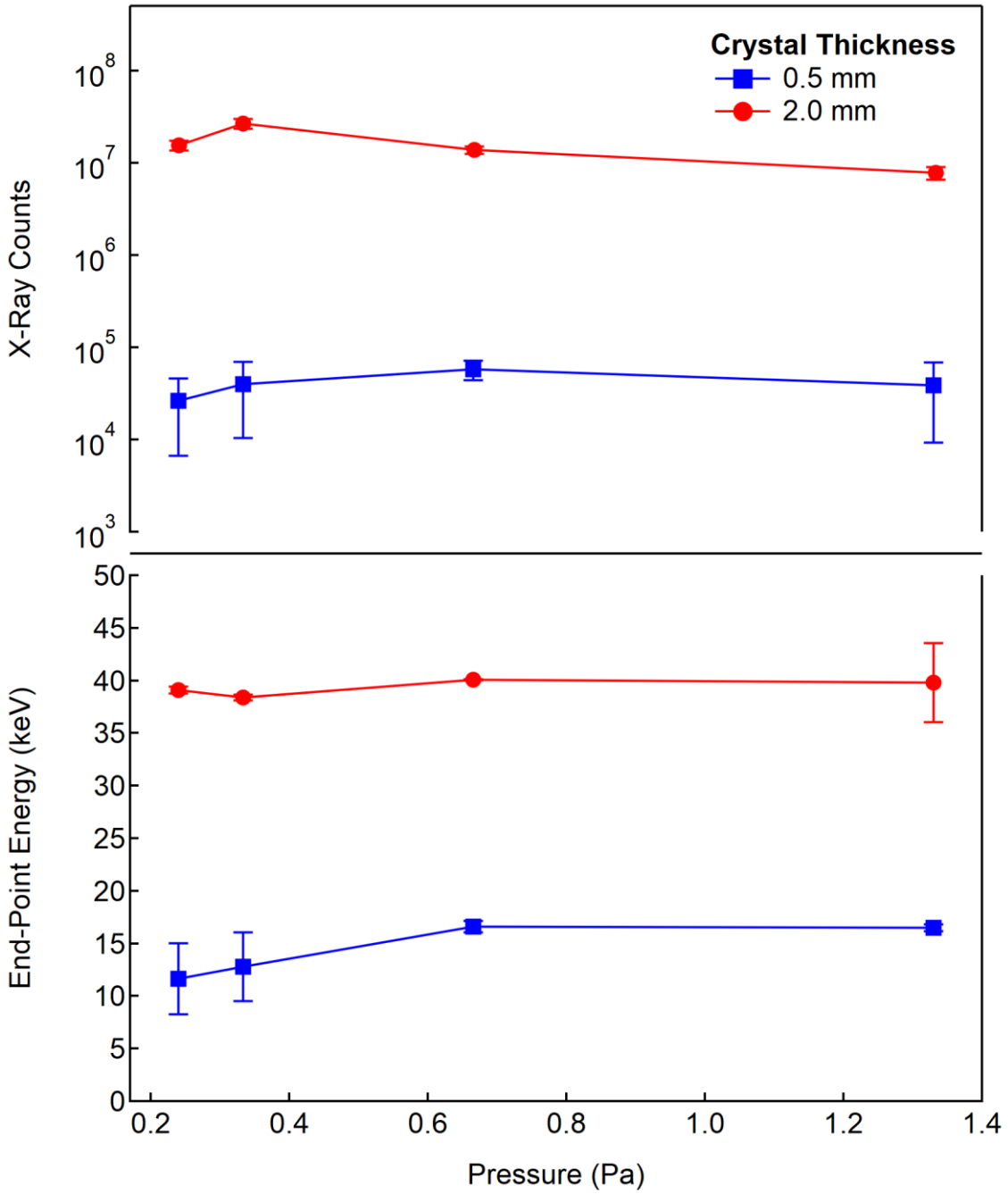

Figure 6-10 Comparison of the total X-ray counts and end-point energy produced by $LiTaO_3$ single crystal of two thicknesses, 0.5 mm and 2.0 mm, at a gap distance of 5.0 mm. Error bars represent a standard deviation over three repeated measurements.

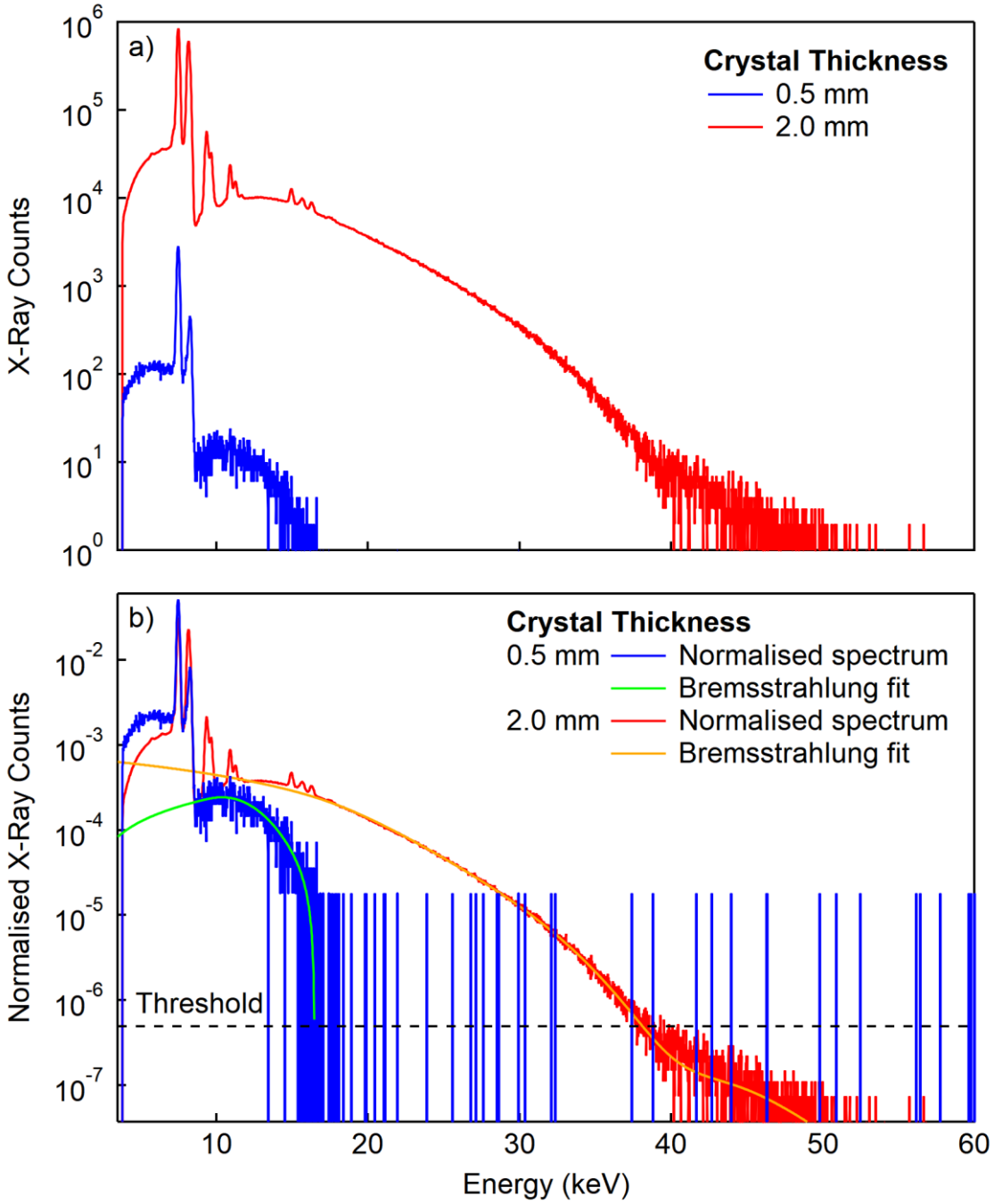

Figure 6-11 Comparison of the energy spectra (a) and its normalisation (b) produced by $LiTaO_3$ of two crystal thickness at a pressure of 0.33 Pa and gap distance of 5.0 mm.

Table 6-3 Summary of the total X-ray counts, count rate and end-point energy produced by $LiTaO_3$ of two crystal thicknesses at varying pressures and gap distance fixed at 5.0 mm. The figures-of-merit from Chapter 3, as well as the max electric field at the crystal surface, E_{max}, and potential difference, ΔV, from Chapter 4 are included.

Crystal Thickness (mm)	Pressure (Pa)	Total X-ray Counts	Count Rate (cps)	End-Point Energy (keV)	F_ε ($\mu C/m^2K$)	F_σ (V/m)	E_{max} (V/m)	ΔV (kV)
0.5	0.24	$(2.66\pm1.98)\times10^4$	7.38 ± 5.50	11.7 ± 3.37	0.382	14.7×10^6	10.1×10^8	21.0
	0.33	$(3.98\pm2.94)\times10^4$	11.1 ± 8.17	12.8 ± 3.24				
	0.67	$(5.80\pm1.39)\times10^4$	16.1 ± 3.87	16.6 ± 0.518				
	1.33	$(3.89\pm2.95)\times10^4$	10.8 ± 8.20	16.5 ± 0.340				
2.0	0.24	$(1.55\pm0.185)\times10^7$	$(43.0\pm5.14)\times10^2$	$39.1\pm0..325$	1.53	58.7×10^6	14.7×10^8	82.3
	0.33	$(2.65\pm0.319)\times10^7$	$(73.6\pm8.85)\times10^2$	38.4 ± 0.266				
	0.67	$(1.39\pm0.135)\times10^7$	$(38.6\pm3.75)\times10^2$	40.1 ± 0.0746				
	1.33	$(0.785\pm0.119)\times10^7$	$(2.18\pm3.31)\times10^2$	39.8 ± 3.76				

6.5.2 Effect of crystal composition

The X-ray generator system was tested using different pyroelectric materials with the same crystal thickness of 2.0 mm. Energy-resolved and time-resolved X-ray counts were collected over the same range of pressures and gap distances.

Figure 6-12 presents the spectrum collected from $LiNbO_3$ where the distinct peaks from the nickel target and the crystal can be seen. There are also two sum peaks that come from a sum of nickel (Kα + Kα) lines and sum of nickel (Kα + Kβ) lines. Compared to $LiTaO_3$, shown in Figure 6-1, $LiNbO_3$ cannot produce as high energy of X-rays with its cut-off at approximately 32.0 keV, whereas a fresh $LiTaO_3$ can reach approximately 42.0 keV.

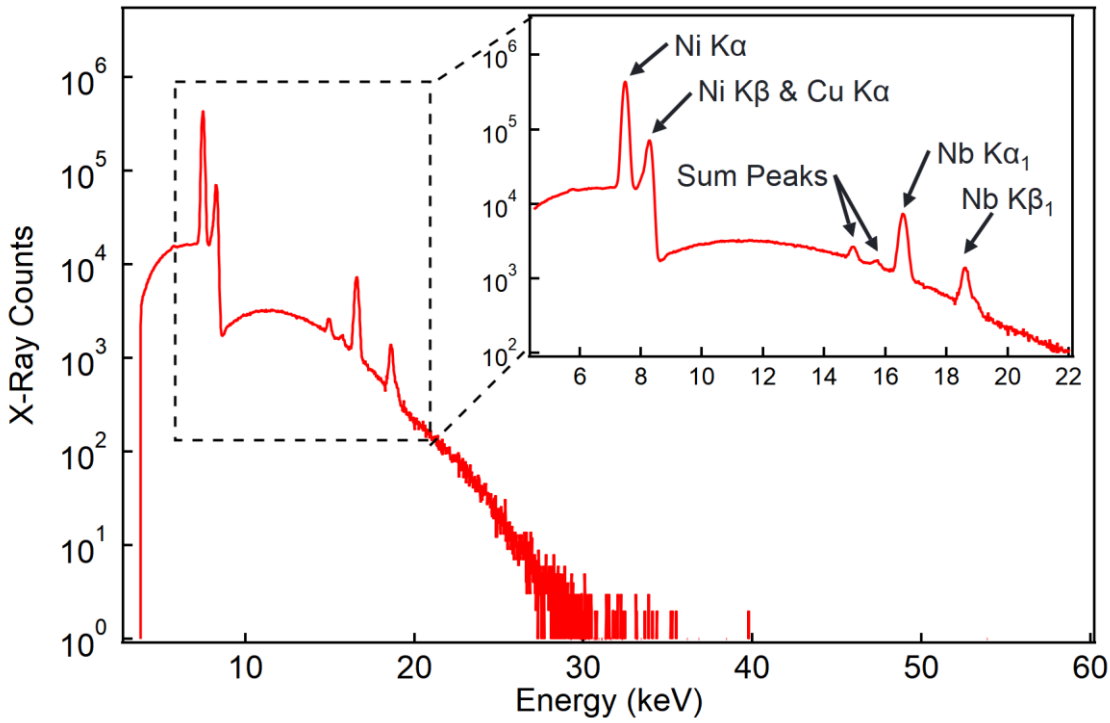

Figure 6-12 X-ray spectrum produced by $LiNbO_3$ crystal with a thickness of 2.0 mm. It was collected for 1 h at a gap distance of 3.7 mm and a pressure of 0.24 Pa. The inset shows a magnified view of characteristic peaks.

Unlike $LiTaO_3$ and $LiNbO_3$, PMN-30PT produced little-to-no X-rays. In the X-ray spectrum pictured in Figure 6-13, no characteristic X-rays and bremsstrahlung are observed. Measurements taken at two pressures, 0.24 Pa and 1.33 Pa, and at the two gap distances, 3.7 mm and 5.0 mm, produced an average of 0.00917 cps.

A background survey of the experimental setup while the generator is running without a crystal is taken. The average count from the background survey is 0.0108 cps. This reveals that the counts collected from PMN-30PT is most likely background counts and that PMN-30PT is unable to create an electric field sufficient to emit electrons and generate usable X-rays. Because of this, measurements at a gap distance of 10.0 mm is not taken and its end-point energies are not determined.

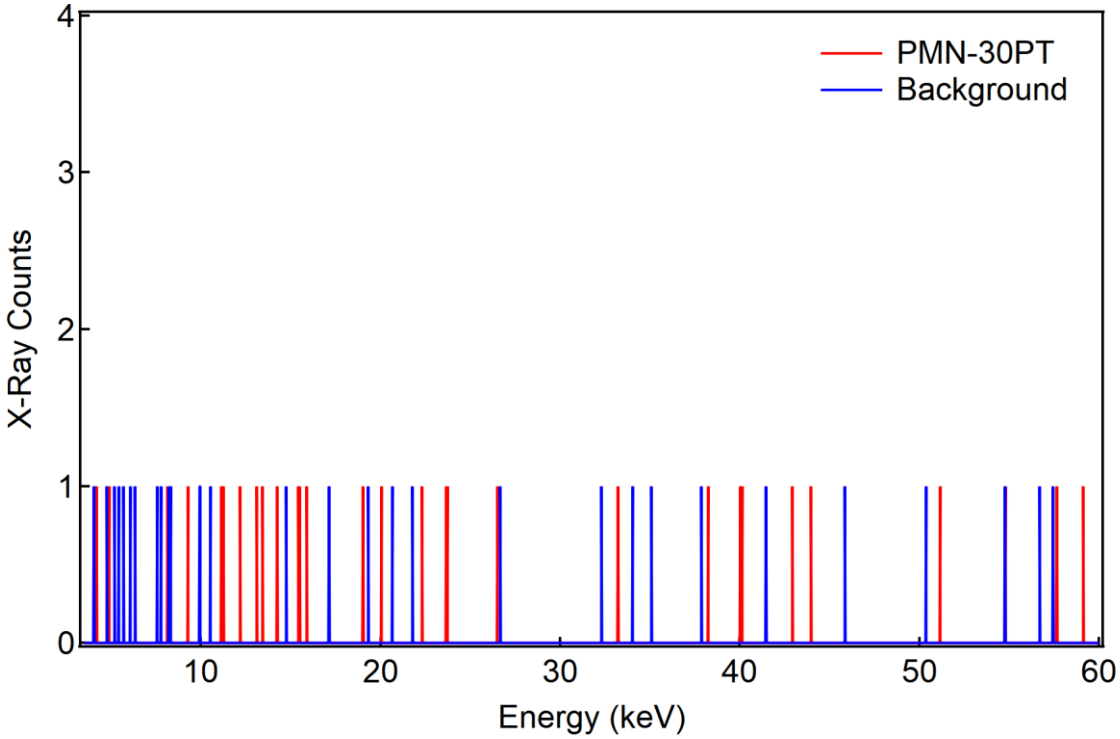

Figure 6-13 Spectrum of X-rays produced by PMN-30PT with a crystal thickness of 2.0 mm. It is collected at a gap distance of 3.7 mm and pressure of 0.24 Pa.

Referring to Figure 6-14 and Table 6-4, $LiTaO_3$ dominates over $LiNbO_3$ and PMN-30PT over all the measured pressures in terms of the total X-ray counts and end-point energies. This matches very well with the figure-of-merit study and electrostatics simulations discussed in Chapter 3.4.5 and Chapter 4.3.3, respectively. $LiTaO_3$ was calculated to have the highest F_ε and F_σ, as well as the highest electric field, if excluding PZT. This is then followed by $LiNbO_3$ and subsequently PMN-28PT [111]. As two other PMN-PT compositions had their pyroelectric properties measured, the F_ε of PMN-30PT would be considered equivalent to PMN-28PT as they fall in the same crystallographic phase. This also suggests that, while more materials need to be tested to discern which of the two

figures-of-merit is more suitable, both figures-of-merit used as a relative measure of the electric field in the gap can be closely applied for pyroelectric X-ray generation.

In terms of end-point energy, the X-ray generation results agree quite well with the potential difference determined from the electrostatics simulations. The average end-point energies from $LiTaO_3$ and $LiNbO_3$ across the four listed pressures in Table 6-4 are 39.5 keV and 32.7 keV, respectively. The ratio of the end-point energy from the two crystal compositions is about 1.2 while the ratio of their potential difference is approximately 1.6. If taking the ratio of the potential difference between $LiTaO_3$ and PMN-30PT, it is approximately 21.1. This means the possible end-point energy from PMN-30PT is only 1.88 keV.

The X-ray generator results here reveal that PMN-30PT is unable to produce any significant X-ray counts, unlike $LiTaO_3$ and $LiNbO_3$. A F_σ value of 10^7 V/m was established in Chapter 3 as a critical value to observe X-rays. As listed in Table 6-4, the F_σ of PMN-30PT is 10^3 V/m. On the other hand, $LiNbO_3$ managed to produce a considerable amount of X-rays and its F_σ is in the 10^6 V/m range. This implies that when applying F_σ, the critical value to observe X-rays needs to exceed a value greater than 10^6 V/m. Since characteristic lines of the pyroelectric crystal were observed using $LiTaO_3$ and $LiNbO_3$, it also suggests that field ionisation can occur when F_σ is of at least 10^6 V/m.

Although the figure-of-merit can be used as an indicator to estimate if a pyroelectric crystal with a set of material properties is capable of electron emission, it uses a model that assumes the crystal and the target have infinite widths. The electrostatics simulation presented earlier in Chapter 4 showed that the electric field produced by $LiNbO_3$ is in the 10^8 V/m range. The difference by two orders of magnitude between the two models is because the electrostatics simulation takes into account of the dimensions of the pyroelectric crystal and the target alongside their material properties. This shows that the electric field is actually more intense at the top crystal surface and its distribution is non-uniform. Therefore, the electric field required for electron emission to occur is much greater than the critical value determined by the figure-of-merit.

Very few studies have demonstrated the use of pyroelectric compositions and crystalline forms other than $LiTaO_3$ and $LiNbO_3$ in pyroelectric X-ray generators. The investigation by Vokhmyanina *et al.* [184] demonstrate the potential of using polycrystalline PZT-19 ceramics, instead of single crystals, for pyroelectric X-ray generators. It must be noted that their ceramic samples were 15 mm in thickness compared to the maximum crystal thickness of 2.0 mm measured in the experiments in this project. The X-ray spectra collected from using PZT-19 show lower end-point energies compared to $LiTaO_3$ and $LiNbO_3$. Using the pyroelectric coefficient determined by Vokhmyanina *et al.* [184], F_ε, $\frac{p}{\varepsilon}\frac{L_{crystal}}{L_{gap}}$ (assuming $\frac{L_{crystal}}{L_{gap}}$ is equal to 1), resulted in a ratio of 0.694 $\mu C/m^2K$ compared to 3.52 $\mu C/m^2K$ and 2.53 $\mu C/m^2K$ for $LiTaO_3$ and $LiNbO_3$ respectively. Although it is uncertain whether using a polycrystalline material affects the output of the X-ray generator, the difference in results reinforces that the pyroelectric coefficient and the relative permittivity of the material are key determining properties. Furthermore, the p/ε ratio of PMN-28PT is 0.573 $\mu C/m^2K$. Since Vokhmyanina *et al.* [184] was able to produce an X-ray spectrum with visible characteristic lines using a thicker crystal, and PZT-19 and PMN-28PT have similar p/ε ratios, it confirms that increasing the $L_{crystal}$ does increase the X-ray output.

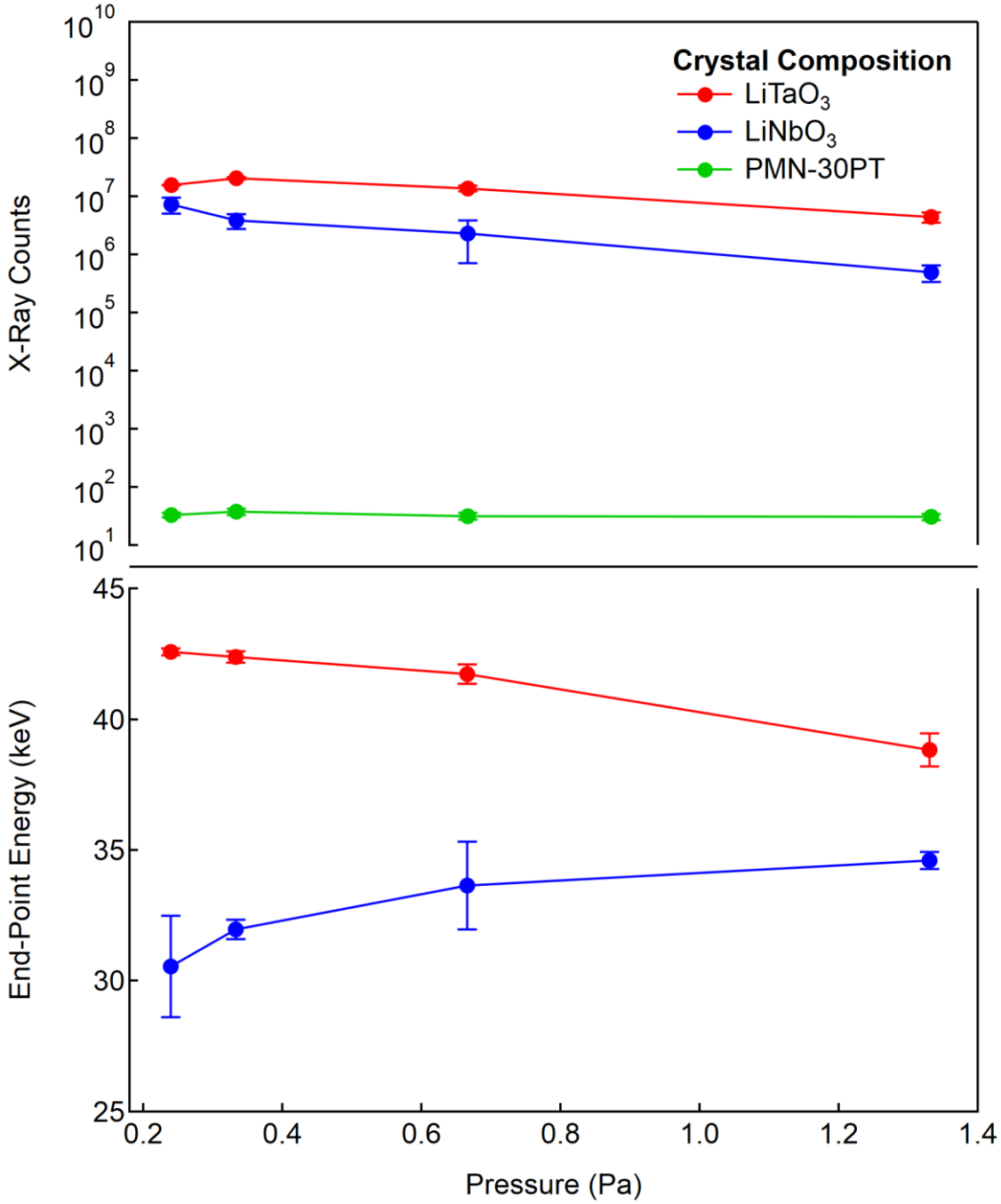

Figure 6-14 Comparison of the total X-ray counts and end-point energies produced over a range of pressures and collected from three different compositions at a gap distance of 3.7 mm. The end-point energy of PMN-30PT is not included. Error bars represent a standard deviation over three to four repeated measurements.

Table 6-4 Summary of the total X-ray counts, count rate and end-point energy produced by each crystal composition at different pressures and gap distance of 3.7 mm. The corresponding figures-of-merit from Chapter 3, as well as the max electric field, E_{max}, at the top crystal surface and potential difference, ΔV, from Chapter 4 are included.

Crystal Composition	Pressure (Pa)	Total X-ray Counts	Count Rate (cps)	End-point Energy (keV)	F_ε ($\mu C/m^2K$)	F_σ (V/m)	E_{max} (V/m)	ΔV (kV)
$LiTaO_3$	0.24	$(1.58\pm0.0149)\times10^7$	$(43.8\pm0.414)\times10^2$	39.4±0.252	2.07	7.93×10^7	14.7×10^8	82.3
	0.33	$(2.07\pm0.0801)\times10^7$	$(57.5\pm22.2)\times10^2$	38.2±0.348				
	0.67	$(1.36\pm0.152)\times10^7$	$(37.8\pm4.22)\times10^2$	40.4±0.386				
	1.33	$(0.447\pm0.0908)\times10^7$	$(12.4\pm25.2)\times10^2$	40.1±0.277				
$LiNbO_3$	0.24	$(7.33\pm2.17)\times10^6$	$(20.4\pm6.04)\times10^2$	30.6±1.93	1.46	8.73×10^6	6.77×10^8	51.2
	0.33	$(3.89\pm1.13)\times10^6$	$(10.8\pm3.13)\times10^2$	32.0±0.372				
	0.67	$(2.31\pm1.60)\times10^6$	$(6.43\pm4.44)\times10^2$	33.6±1.68				
	1.33	$(0.493\pm0.155)\times10^6$	$(1.37\pm0.430)\times10^2$	34.6±0.323				
PMN-30PT	0.24	32.8±3.10	0.00910±0.000860	–	0.378	7.42×10^3	11.0×10^6	3.90
	0.33	37.8±4.57	0.0105±0.00127	–				
	0.67	31.5±4.20	0.00875±0.00117	–				
	1.33	30.8±3.86	0.00854±0.00107	–				

6.5.3 Effect of pressure and gap distance

The three crystal compositions were investigated over a range of pressures and gap distances. Here, the effect of pressure and gap distance will be explored by presenting the total X-ray counts and end-point energies as a function of pressure. Similar studies on the dependence of pressure has been reported previously but at a pressure range of 0.0133 – 20 Pa [77, 82, 107]. However, it is important to note that the dimensions of the crystal and the experimental setup varied and would contribute to the differences in trends.

The measurement taken from $LiTaO_3$ and $LiNbO_3$ were also tested in the high vacuum regime, with pressures below 5.32 mPa. This was achieved by turning off the dry air supply, opening the gate valve and allowing turbomolecular pump to pump the chamber down unthrottled. A series of four measurements at each gap distance was undertaken with the initial pressure at approximately 5.32 mPa and would continue to decrease until approximately 2.0 mPa. These pressures are recorded from the wide range gauge as the pressure reading from the capacitance gauge had gone beyond its measurement range.

The maximum total X-ray count generated by $LiTaO_3$ was measured at a pressure of 0.33 Pa and with a gap distance of 5.0 mm, shown in Figure 6-15. At this pressure, it is also the optimum when the gap distance is set at 3.7 mm. However, when the gap distance is adjusted to 10.0 mm, the X-ray counts is greater at a pressure of <5.32 mPa. The end-point energies produced by $LiTaO_3$ tended to increase with increasing pressure. The X-ray energies produced are dependent on the initial energy the electron possessed at the moment of emission as well as the magnitude of the electric field. The end-point energies produced at gap distances of 3.7 mm and 5.0 mm were within one standard deviation of each other. While at the gap distance of 10.0 mm, the end-point energies were consistently lower but only by a difference of 2 keV at most. Comparisons of the shape of their normalised spectra can be found in Appendix D.

For $LiNbO_3$, the optimum pressure for all gap distances is at 0.24 Pa. Setting the gap distance to 3.7 mm has a more significant effect on the X-ray production as the total X-ray count tapers in an exponential manner, rather than linearly, with increasing pressure, as seen in Figure 6-16. The end-point energies produced as a function of

pressure generally increased at gap distances of 3.7 mm and 10.0 mm, but there is no clear trend across the three gap distances.

As alluded to in Chapter 6.5.2, PMN-30PT produced insignificant X-rays at all measured configurations. This is further evident in Figure 6-17 as the average and its variance are spread far apart. The end-point energies for PMN-30PT are not evaluated.

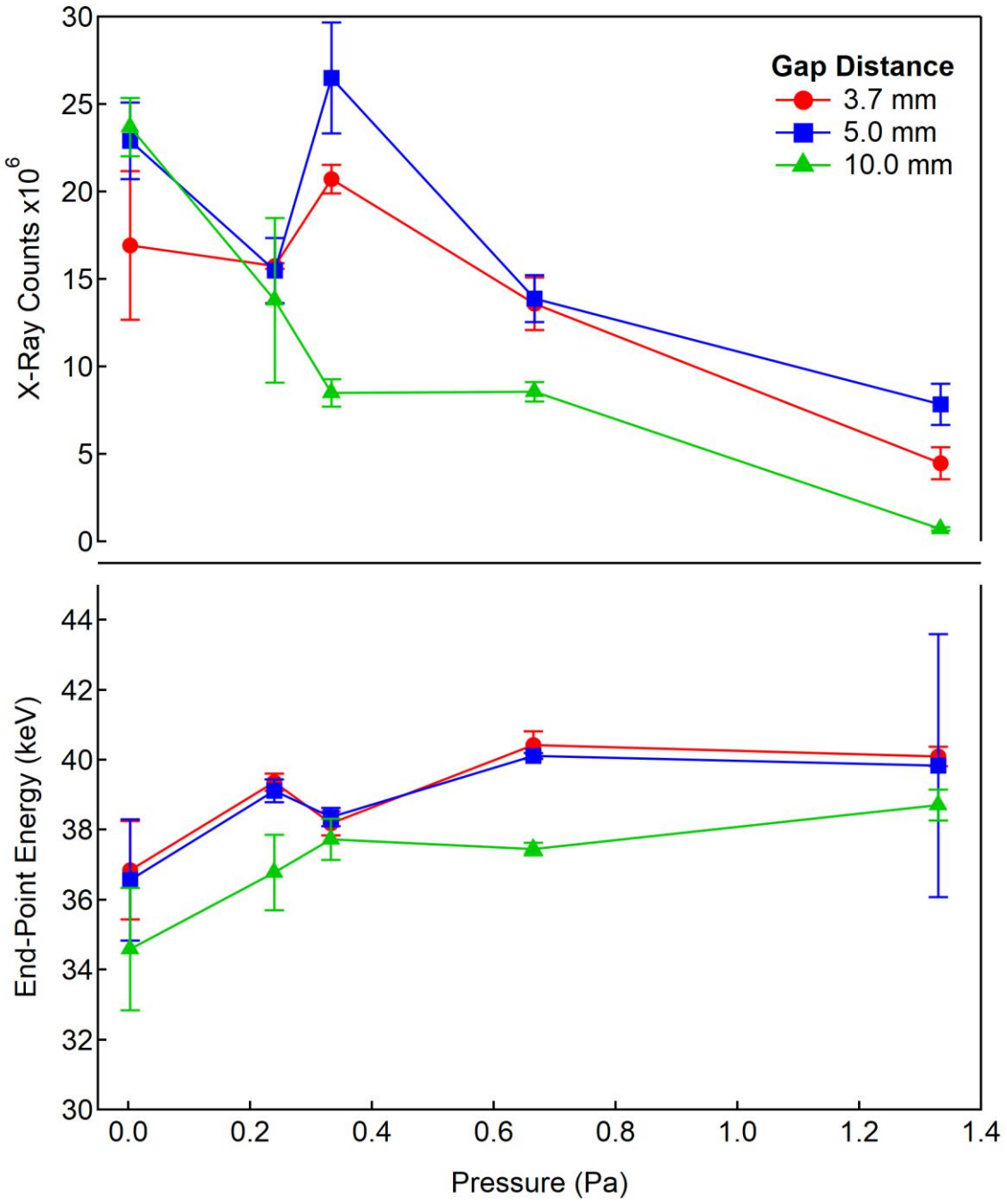

Figure 6-15 Total X-ray counts and end-point energy as a function of pressure measured at three different gap distances from $LiTaO_3$ with a thickness of 2.0 mm. Error bars represent a standard deviation over three repeated measurements.

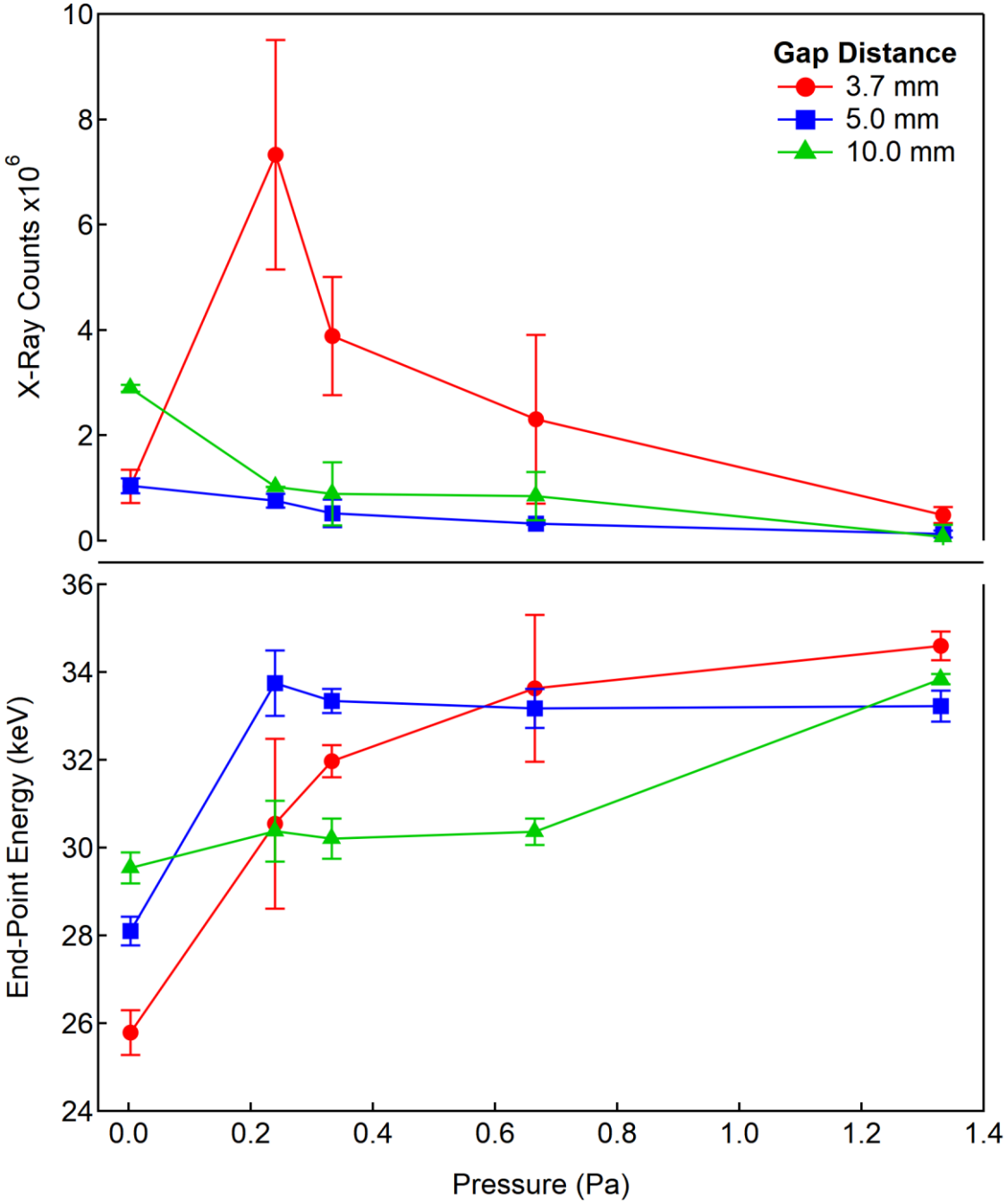

Figure 6-16 Total X-ray counts and end-point energy as a function of pressure measured at three different gap distances from $LiNbO_3$ with a thickness of 2.0 mm. Error bars represent a standard deviation over three to four repeated measurements.

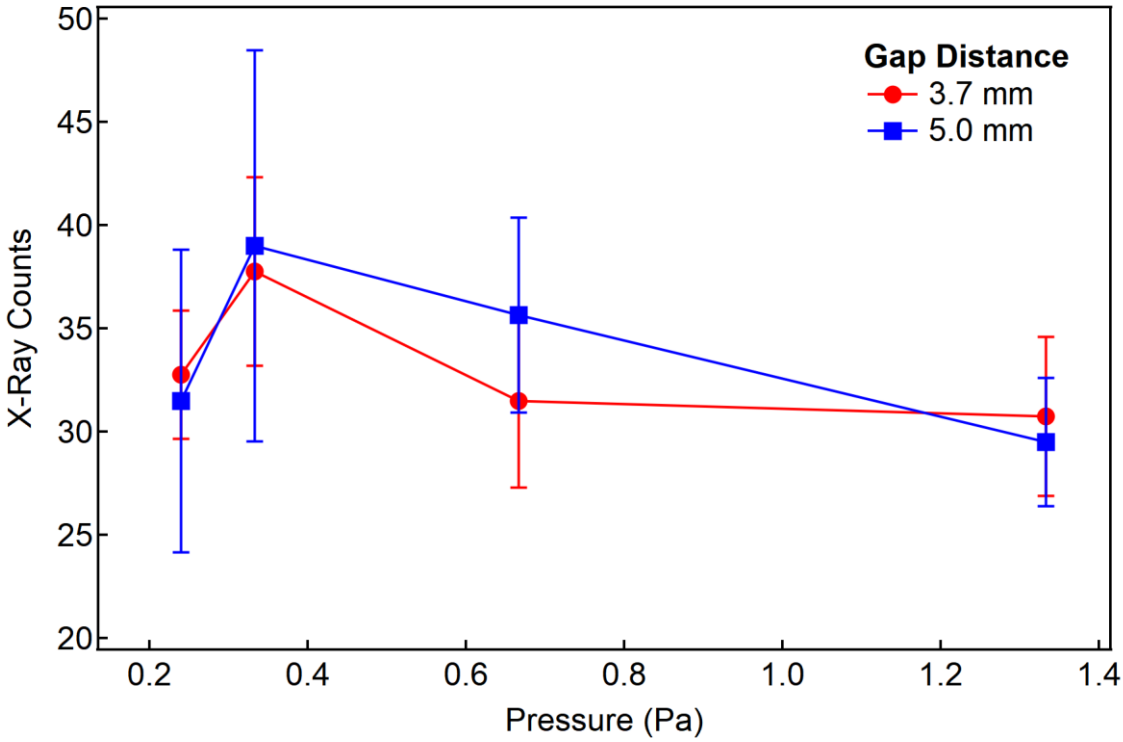

Figure 6-17 Total X-ray counts as a function of pressure measured at two gap distances from PMN-30PT with a thickness of 2.0 mm. Error bars represent a standard deviation over three repeated measurements.

When a pyroelectric crystal is thermally cycled at atmospheric pressure, the net surface charge is subjected to immediate charge compensation, also known as charge neutralisation. This renders the pyroelectric crystal ineffective as an X-ray generator as it is dependent on the magnitude of the uncompensated surface charge, and in turn the electric field in the gap, to emit electrons [16]. As has been explored in Chapter 3, there are several processes in which charge compensation can occur and demonstrated by Equation 3-10. However, the focus here will be by charge compensation from the surrounding ionised gas molecules. By limiting the pressure surrounding the pyroelectric crystal, it will reduce the rate of charge compensation. On the other hand, if the pressure is low, the lack of ionised gas molecules available will reduce the production of X-rays.

Since the X-ray generator has a potential difference in the gap and operates at high vacuum, it is subjected to electrical breakdowns. This means that the pressure in the vacuum chamber cannot be optimised alone and gap distance must be considered. When an electron is emitted either by ferroelectric electron emission or field ionisation, it has the probability to ionise more gas molecules and cause further secondary electron emission before impacting on the target or crystal surface. As the number of ions increase

and the voltage in the gap reaches a critical value, an electric current can quickly flow from one electrode to another and short-circuit the system. In this case, it would be between the surface of the pyroelectric crystal to the target. It is usually marked by a sharp change in current followed by a sudden halt in the production of X-rays, as observed in Figure 6-6 and Figure 6-18. This heavily affects the repeatability of the X-ray generator's output because it essentially causes the X-ray generation process to restart with dwelling time for enough surcharge charge to rebuild. This issue has been mentioned in several studies [19, 105, 107, 117, 212].

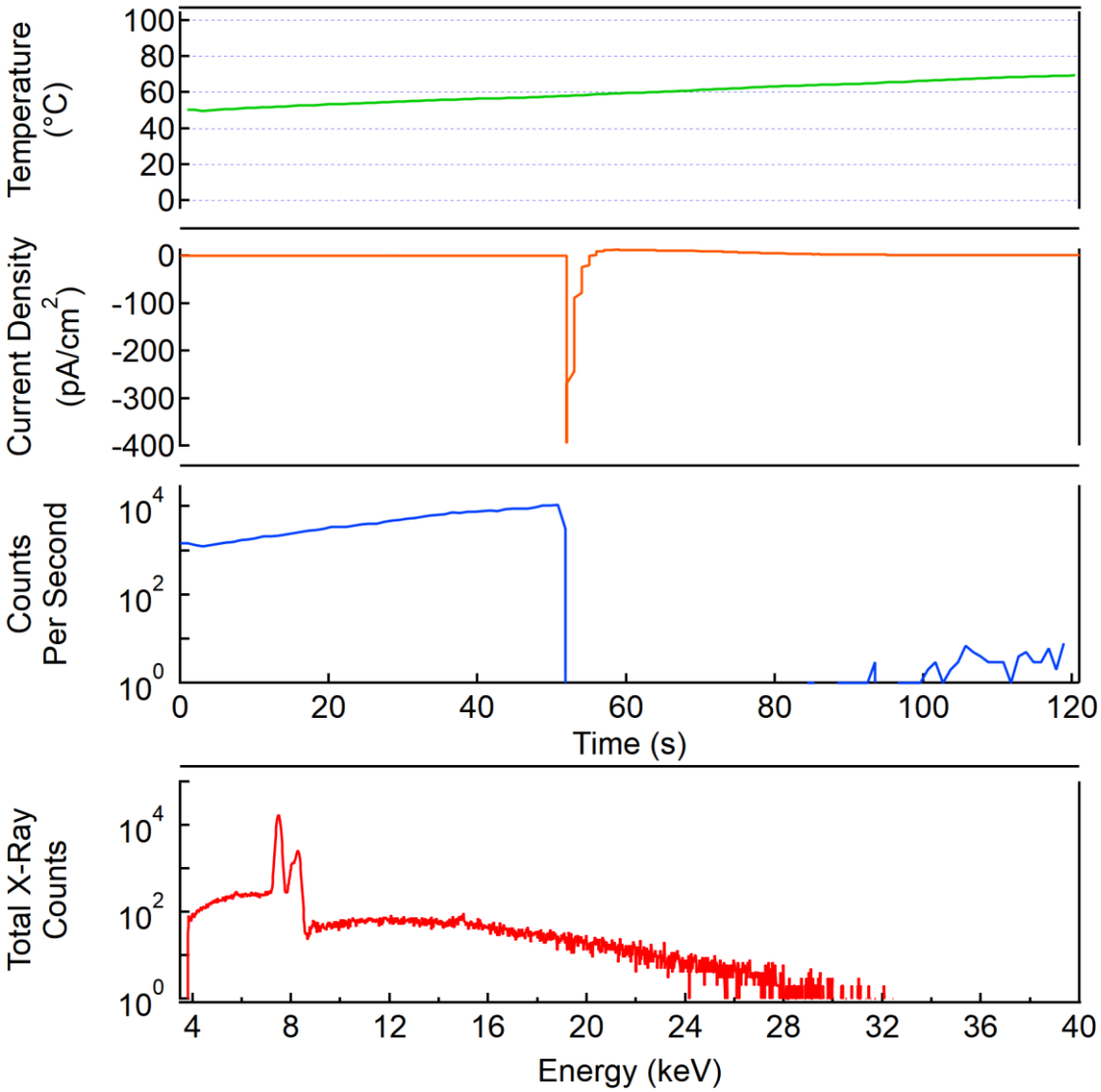

Figure 6-18 A sharp change in the current density is quickly followed by a sudden halt in X-ray production. The X-ray generator system will then need to rebuild enough charges to continue producing X-rays.

The critical voltage in the gap at which breakdown occurs is known as the breakdown voltage. The relationship of the breakdown voltage with the pressure in the chamber and gap distance is known as Paschen's Law. By understanding Paschen's Law, an optimised X-ray generator can be designed to avoid electric breakdowns while achieving a high X-ray yield. Figure 6-19 shows a typical curve of the dependence of the breakdown voltage in air with the product of pressure and gap distance. The position of the Paschen curve varies with the composition of the gas and the material of the electrodes, which in this system are the pyroelectric crystal and the metal target.

Assuming the gap distance is fixed and an electrical breakdown does not occur, changing the pressure will affect the mean free path of electrons. When the pressure is above the Paschen curve minima, the electron mean free path is short. Introducing more gas molecules into the vacuum chamber does increase the number of collisions. However, the electrons are not able to accelerate to an energy sufficient to ionise the gas molecules [32, 213]. Therefore, the number of X-rays produced decreases.

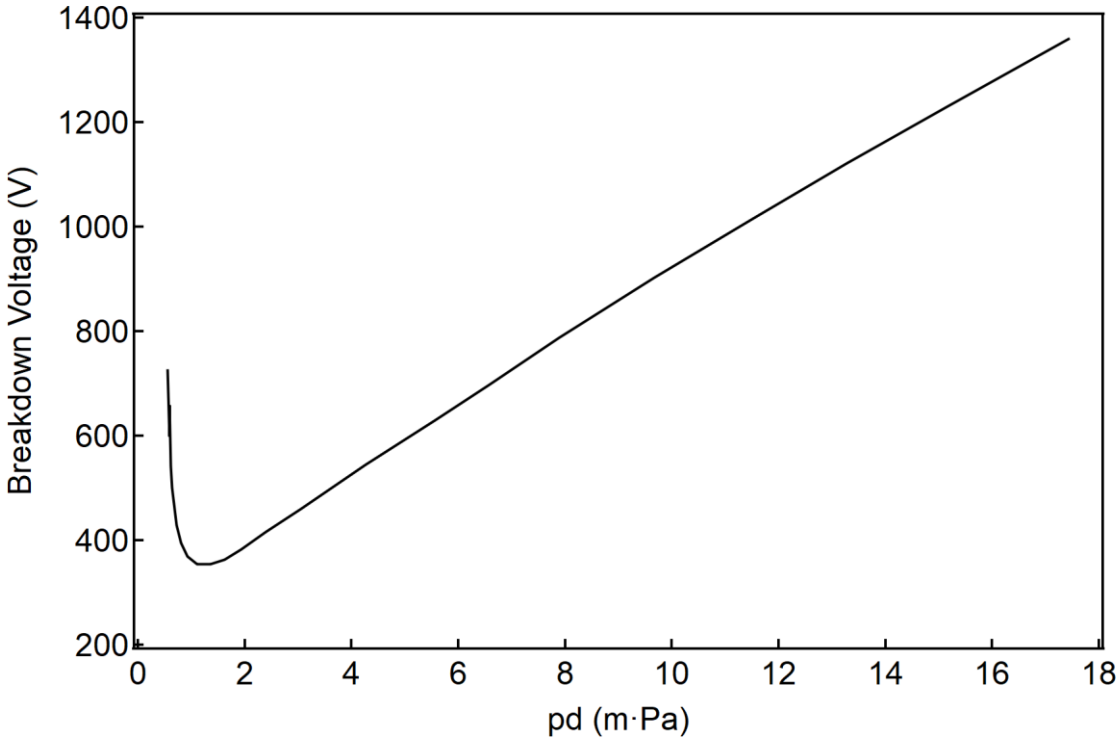

Figure 6-19 A typical Paschen curve of air showing the breakdown voltage between two parallel electrodes as a function of the product of pressure, p, and distance between the electrodes, d. Image reproduced from [213].

On the other hand, if the pressure is low, the electron mean free path would be long. During the heating phase, the production of X-rays would be more reliant on the electrons emitted from the crystal surface as it travels straight to the target with few interactions with the gas molecules. This can be seen in the bottom plot of Figure 6-20 where the nickel K-shell lines and corresponding sum peaks at pressures below 5.32 mPa are more dominant compared to the spectra collected at other pressures. But if the gap distance is increased, the electrons will have accelerated to energies that can ionise more gas molecules. This has also been observed as the count rate increases from about 4700 cps at a gap distance of 3.7 mm to about 6000 cps at 10.0 mm, as from Figure 6-15 and Table 6-5 (found in Chapter 6.5.4). While this agrees with trends reported by others [68, 212, 214], it should be noted that the pressures and gap distances used differ from those implemented in literature.

In the same spectra collected at the pressure below 5.32 mPa, there are no visible tantalum L-shell lines. These tantalum lines are observed during the cooling phase and electrons are sourced from field ionisation of the gas molecules. The time-resolved X-ray counts shown in Figure 6-21 indicate that X-rays are still produced. This suggests that while electrons are still produced, the quantity and energy are insufficient to produce more electrons and emit characteristic X-rays of the crystal.

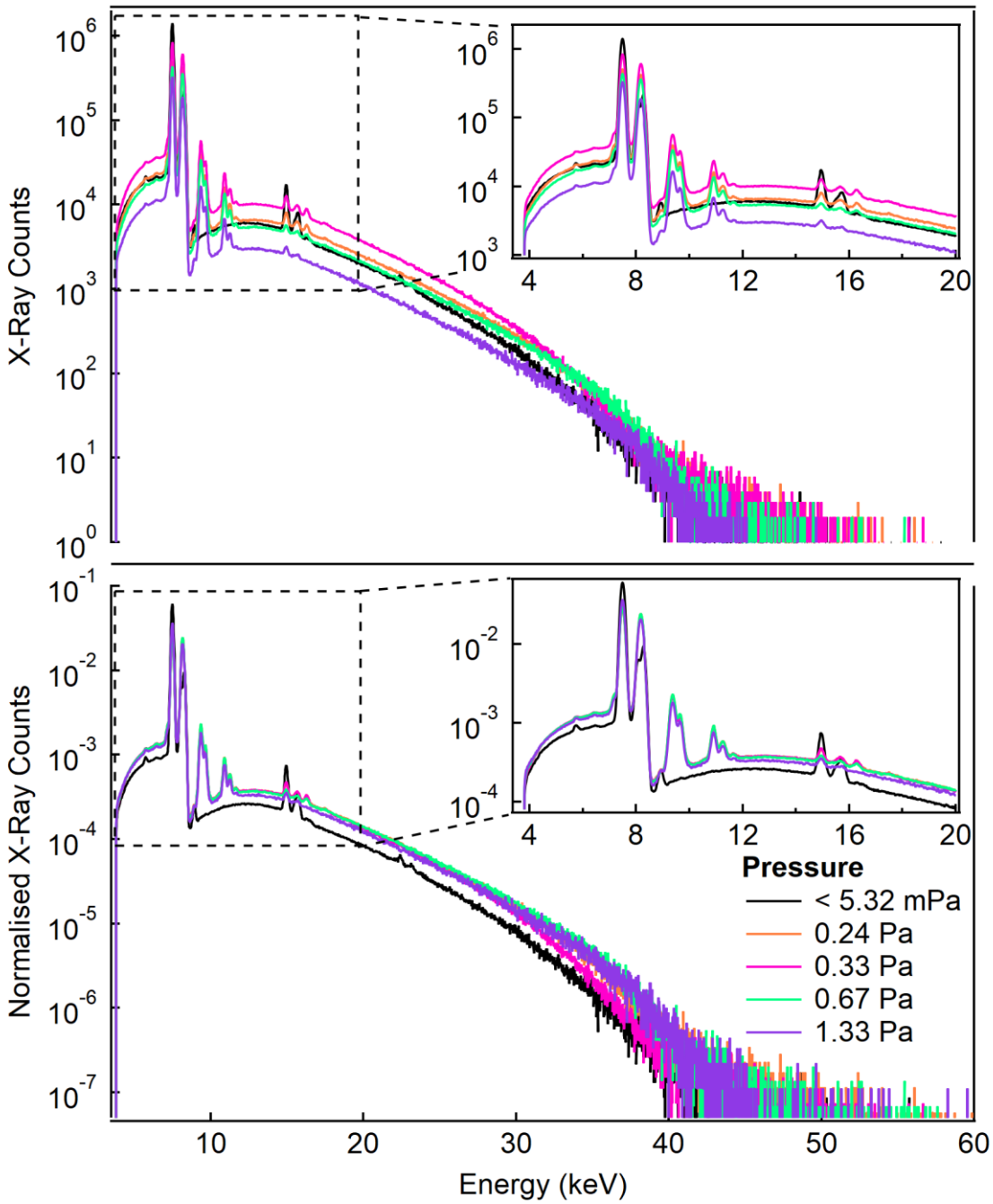

Figure 6-20 Spectra (top) collected from $LiTaO_3$ over five pressures at a gap distance of 5.0 mm. The bottom plot is of the same spectra normalised to each spectrum's total X-ray counts.

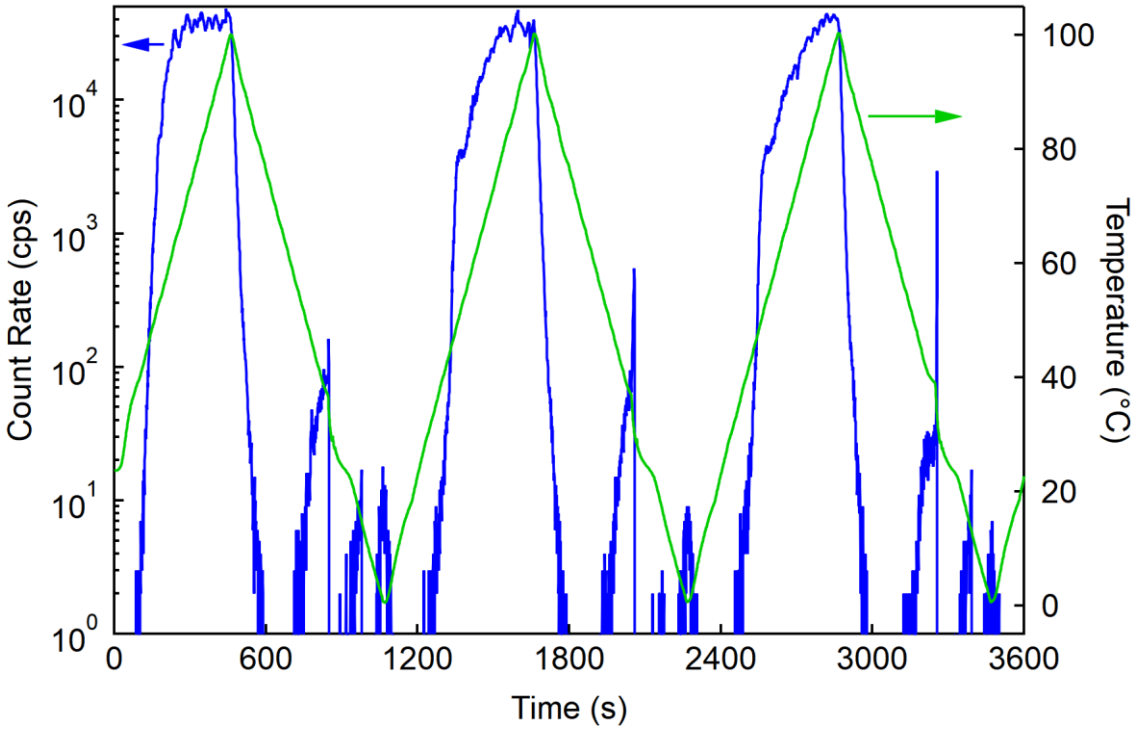

Figure 6-21 Count rate and temperature measured from $LiTaO_3$ at pressure of <5.32 mPa and gap distance of 5.0 mm. It corresponds to the black energy spectrum in Figure 6-20.

The material used as the electrodes can also affect the magnitude of the breakdown voltage. Hackam and Altcheh [215] studied the variation of DC breakdown voltage with pressure, gap distances and different metallic electrodes. Focusing on nickel as the electrode material, it was found that although the breakdown voltage increased with larger gap distances, the breakdown voltage dropped more abruptly at pressures increasing from 0.0133 - 1.33 Pa when the gap distance was greater than 2.03 mm. This pressure range sits in the same high vacuum range as the experiments are operating at.

Another consideration to take into account is that the electron emission phenomenon is a dynamic process. Given that ionisation of the gas molecules takes place and causes a chain production of electrons, positive ions would also be produced and could be screening out the opposing charges on the crystal surface. This would then reduce the surface charge and the electric field in the gap, ultimately reducing the potential for electrons to accelerate to energies that can generate X-rays.

In practical application, it would be very difficult to avoid electric breakdowns. Gas molecules are required to accentuate the ionisation process in order to produce more

electrons and therefore, X-rays. Decreasing the gap distance will increase the figures-of-merit, and therefore the generation of X-rays, but it also increases the likelihood of electrical breakdown by reducing the magnitude of the breakdown voltage. But the appropriate gap distance is also required to allow the electrons to accelerate to energies enough to ionise the gas molecules.

6.5.4 Combination of crystal composition, pressure and gap distance

In Chapter 3, it was predicted that the electric field in the gap, dictated by both figures-of-merit, should increase as the gap distance decreases. This was shown in Figure 3-24 and Figure 3-26. On the contrary, varying the gap distance in the electrostatics simulations exhibited minimal effect on the electric field and potential difference across the gap. However, the results in Chapter 4.3.3 and Chapter 5.5.2 showed that the X-ray output should correspond with the figures-of-merit of different compositions.

In this section, it will be shown if there is correlation between the total X-ray counts, figure-of-merit, gap distance and pressure. Figure 6-22, Figure 6-23 and Figure 6-24 display the X-ray counts and end-point energy from $LiTaO_3$ and $LiNbO_3$, including $LiTaO_3$ with a crystal thickness of 0.5 mm. As the relationships exhibited for both figures-of-merit have very similar trends, only F_ε will be presented here with the understanding that F_σ follows similarly. The total X-ray counts and end-point energy values presented are from measurements that experienced the least electrical breakdowns. The counting of electrical breakdowns is deduced using the current and time-resolved X-ray data. An electrical breakdown is deemed to have occurred if there is a coupling sharp change in current of at least 2 pA/cm^2 and in the time-resolved counts, in a timeframe of about 5 s (includes rise and fall of the current peak). It should be reinforced that an electrical breakdown is counted regardless of whether a complete or partial breakdown happened. A complete summary of the results measured at all parametric combinations can be found in Table 6-5.

Firstly, focusing on $LiTaO_3$ with a crystal thickness of 2.0 mm in Figure 6-22, the total X-ray counts tended to peak at a gap distance of 5.0 mm for all pressures except at 0.24 Pa. For $LiNbO_3$, it is presented in Figure 6-23 that the X-ray yield dips marginally

at a gap distance of 5.0 mm before rising again at 3.7 mm. This is not the case for pressures below 5.32 mPa. The correlation from the measurements taken using $LiTaO_3$ with crystal thickness of 0.5 mm is not very clear since it is only at pressures of 0.67 Pa and 1.33 Pa the X-ray counts does increase with a higher figure-of-merit.

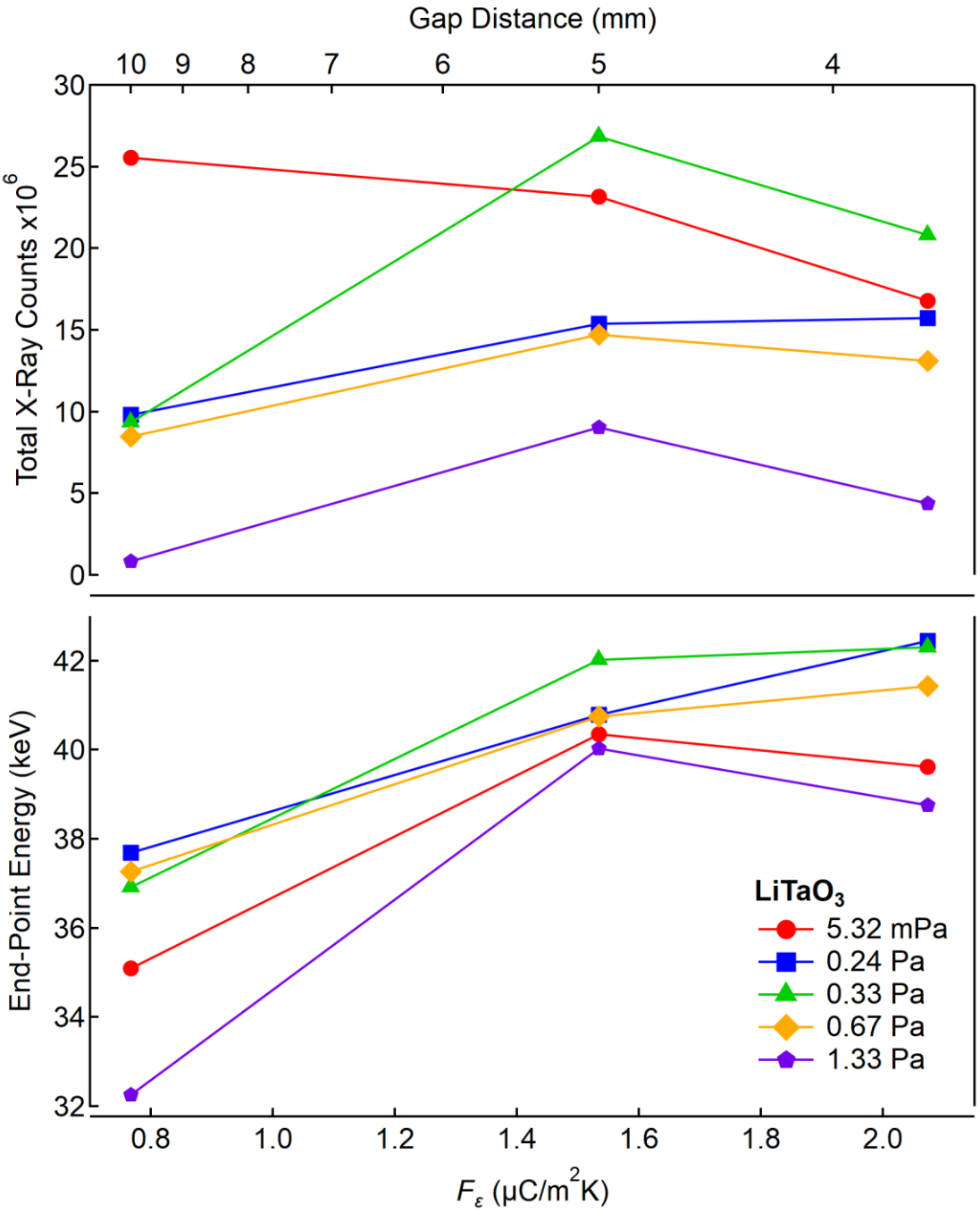

Figure 6-22 Total X-ray counts and end-point energy produced by $LiTaO_3$ at all combinations of gap distance and pressure with the least electrical breakdowns, compared to the figure-of-merit, F_e. The crystal thickness is 2.0 mm.

Out of the three configurations displayed, $LiNbO_3$ is the closest to agreeing with the relationship of increasing figures-of-merit with narrower gap distances across the three gap distances and majority of the pressures it measured at. $LiTaO_3$ with a crystal thickness of 2.0 mm does exhibit that rise in counts but only from gap distance of 10.0 mm to 5.0 mm. Therefore, based off the results presented here, it is fair to say that while the figures-of-merit can predict which materials and crystal thicknesses may perform better, they do not necessarily correlate to the X-ray output within each material and crystal thickness combination. A reason for this would be due to the occurrence of electrical breakdowns that were discussed in the earlier sub-chapter.

For each crystal composition and crystal thickness characterised, their end-point energies over the range of gap distances and pressures measured are approximately within error of each other. Back in Chapter 4.3.4, the electrostatics simulation study found that the potential difference is consistent regardless of the gap distance. This confirms that it provided a good representation of the effect of gap distance. Additionally, the slight variation could be due to pressure introducing additional phenomena such as electrical breakdowns, which was explored earlier.

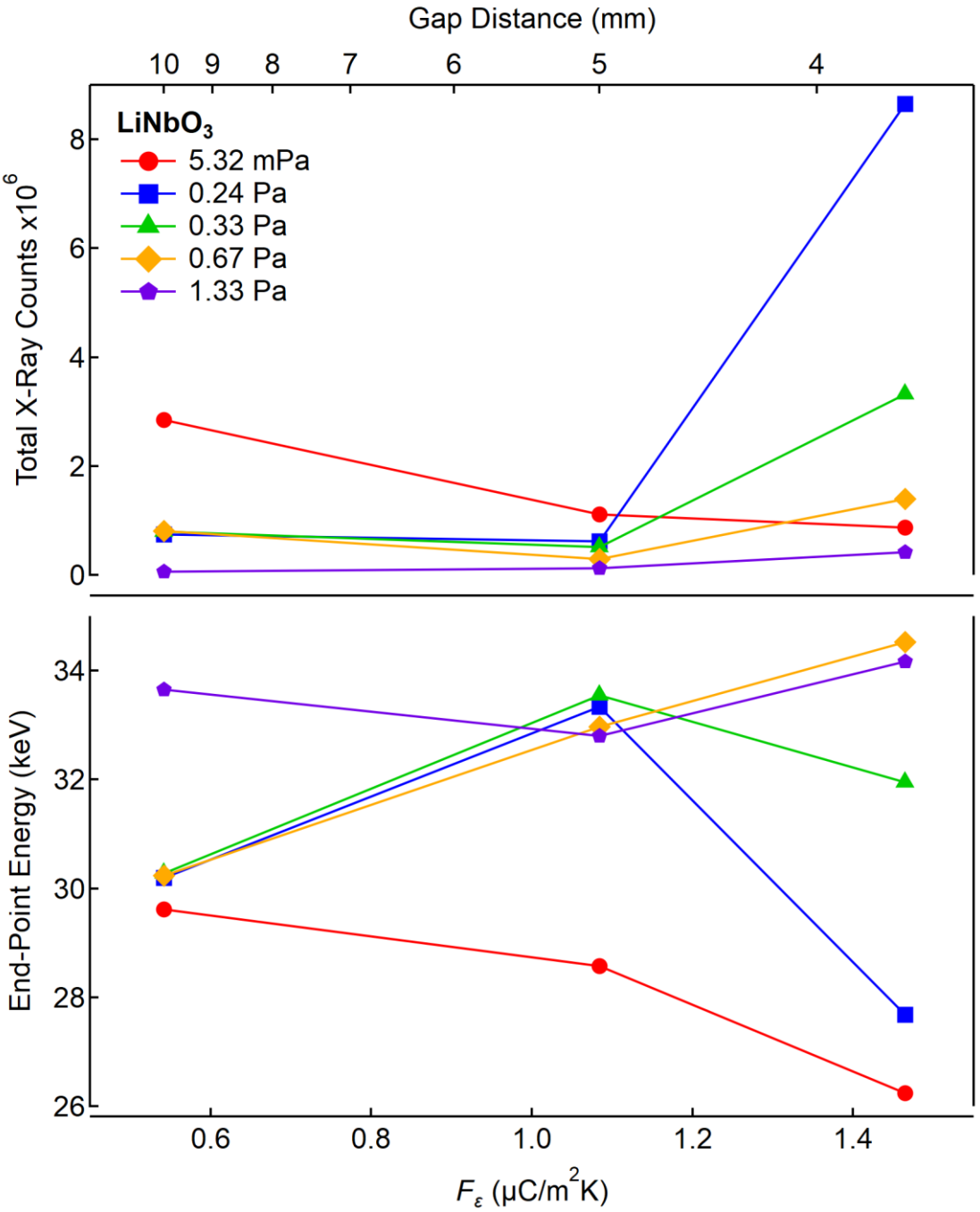

Figure 6-23 Total X-ray counts and end-point energy produced by $LiNbO_3$ at all combinations of gap distance and pressure with the least electrical breakdowns, compared to the figure-of-merit, F_e. The crystal thickness is 2.0 mm.

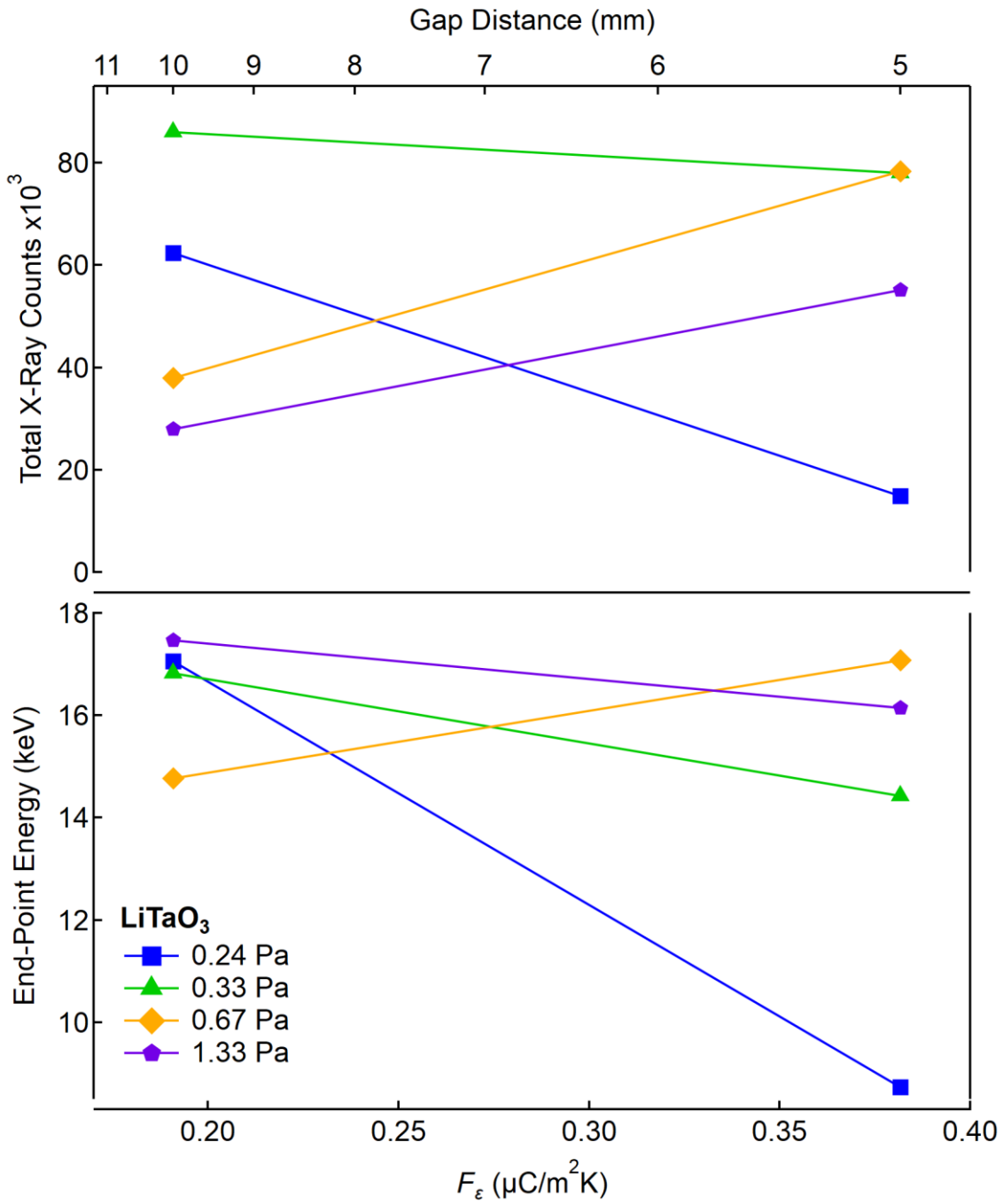

Figure 6-24 Total X-ray counts and end-point energy produced by $LiTaO_3$, with a crystal thickness of 0.5 mm, at all combinations of gap distance and pressure with the least electrical breakdowns, compared to the figure-of-merit, F_ε.

In selecting the optimum conditions for maximum X-ray counts and end-point energy, it is obvious that $LiTaO_3$ with a crystal thickness of 2.0 mm is the preferred crystal composition and crystal thickness. Based off Figure 6-22, the optimum gap distance and pressure for $LiTaO_3$ are 5.0 mm and 0.33 Pa, respectively. On the other hand, when selecting the optimum gap distance and pressure for maximum end-point energy produced by $LiTaO_3$, then it would be 3.7 mm and 0.67 Pa. But since the difference in

end-point energies between the gap distances of 3.7 mm and 5.0 mm at all pressures are only at most about 4.0 keV, it is a reasonable compromise to have the most optimum gap distance and pressure be 3.7 mm and 0.33 Pa, respectively. At this combination, the X-ray flux collected at the detector determined using the corrected spectrum with least number of electrical breakdowns is 1.22×10^5 cm^2/s.

Although the X-ray output generated by $LiTaO_3$ will continue to be limited by electrical breakdowns, it is also recommended that more measurements should be undertaken at each parametric combination to confirm its reliability. Figure 6-25 displays moments during the heating phase when X-rays are sometimes produced. The lack of X-ray production can also occur sometimes for the cooling phase. It could be that if there is greater consistency in the X-ray production, the predictions set by the figures-of-merit may be true. Therefore, even if further optimisation measurements are undertaken around the mentioned optimum settings, there should be an investigation into why the X-ray output is inconsistent when the same parameters are applied.

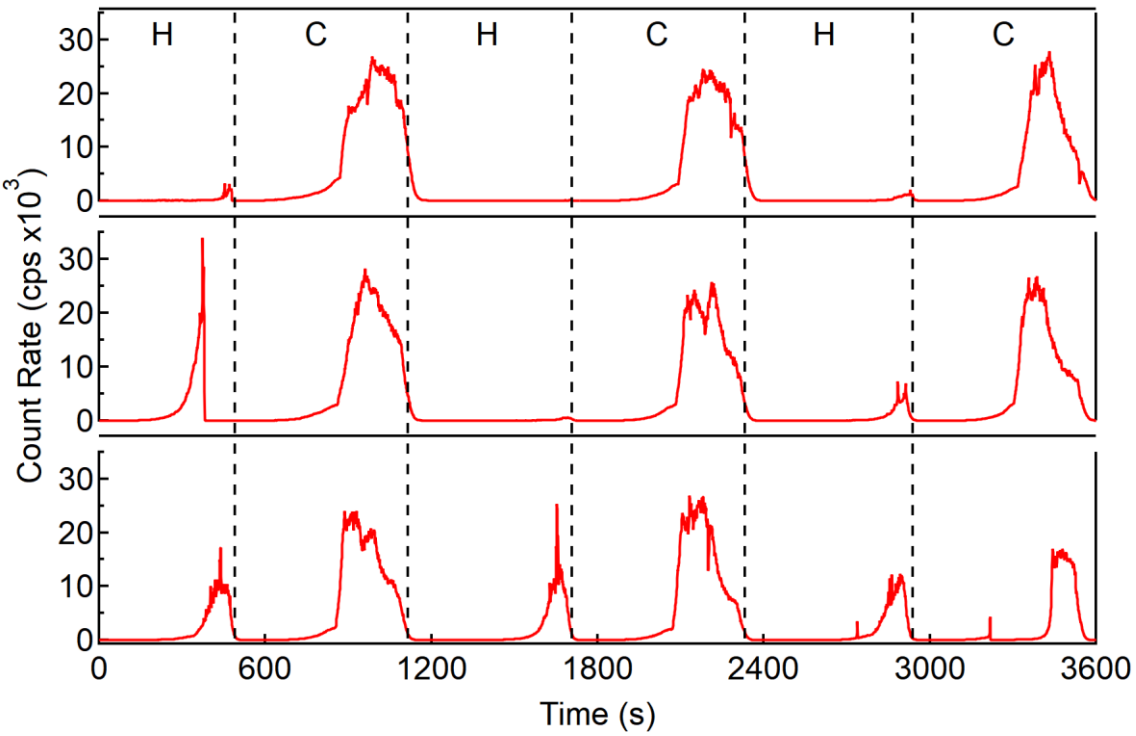

Figure 6-25 Three repeated measurements of time-resolved counts generated from $LiTaO_3$ (2.0 mm thickness) at gap distance of 3.7 mm and pressure of 0.33 Pa. The dotted lines separate the heating (H) and cooling (C) phases.

This page is intentionally left blank.

Table 6-5 A complete summary of the total X-ray counts, count rate, end-point energy and average number of electric breakdowns, N_B, over three repeated measurements produced from all measured configurations. The figures-of-merit from Chapter 3, and the max electric field at the top crystal surface, E_{max}, and potential difference, ΔV, from Chapter 4 are included. L_{gap} refers to gap distance. This table spans over two pages and is to be read portrait-wise.

Crystal Composition	L_{gap} (mm)	Pressure (Pa)	Total X-ray Counts	Count Rate (cps)
$LiTaO_3$	3.7	<0.00532	$(1.69\pm0.425)\times10^7$	$(47.1\pm11.8)\times10^2$
(2.0 mm)		0.24	$(1.58\pm0.0149)\times10^7$	$(43.8\pm0.414)\times10^2$
		0.33	$(2.07\pm0.0801)\times10^7$	$(57.5\pm22.2)\times10^2$
		0.67	$(1.36\pm0.152)\times10^7$	$(37.8\pm4.22)\times10^2$
		1.33	$(0.447\pm0.0908)\times10^7$	$(12.4\pm25.2)\times10^2$
	5.0	<0.00532	$(2.29\pm0.218)\times10^7$	$(63.6\pm6.06)\times10^2$
		0.24	$(1.55\pm0.185)\times10^7$	$(43.0\pm5.14)\times10^2$
		0.33	$(2.65\pm0.319)\times10^7$	$(73.6\pm8.85)\times10^2$
		0.67	$(1.39\pm0.135)\times10^7$	$(38.6\pm3.75)\times10^2$
		1.33	$(0.785\pm0.119)\times10^7$	$(21.8\pm3.31)\times10^2$
	10.0	<0.00532	$(2.37\pm0.471)\times10^7$	$(65.8\pm4.65)\times10^2$
		0.24	$(1.38\pm0.471)\times10^7$	$(38.3\pm13.1)\times10^2$
		0.33	$(0.848\pm0.0775)\times10^7$	$(23.6\pm2.15)\times10^2$
		0.67	$(0.856\pm0.0540)\times10^7$	$(23.8\pm1.50)\times10^2$
		1.33	$(0.00718\pm0.0979)\times10^7$	$(0.199\pm0.272)\times10^2$
$LiNbO_3$	3.7	<0.00532	$(1.03\pm0.316)\times10^6$	$(2.86\pm0.877)\times10^2$
		0.24	$(7.33\pm2.17)\times10^6$	$(20.4\pm6.04)\times10^2$
		0.33	$(3.89\pm1.13)\times10^6$	$(10.8\pm3.13)\times10^2$
		0.67	$(2.31\pm1.60)\times10^6$	$(6.43\pm4.44)\times10^2$
		1.33	$(0.493\pm0.155)\times10^6$	$(1.37\pm0.430)\times10^2$

End-point Energy (keV)	N_B	F_ε ($\mu C/m^2K$)	F_σ (V/m)	E_{max} (V/m)	ΔV (kV)
36.8±1.40	3.00	2.07	7.93×10^7	13.5×10^8	80.1
39.4±0.252	2.33				
38.2±0.348	3.33				
40.4±0.386	1.00				
40.1±0.277	4.33				
36.6±1.74	6.67	1.53	5.87×10^7	12.9×10^8	80.1
39.1±0.325	2.00				
38.4±0.266	7.33				
40.1±0.0746	2.67				
39.8±3.76	8.00				
34.6±1.76	5.33	0.767	2.94×10^7	13.0×10^8	81.9
36.8±1.07	2.00				
37.7±0.595	0.33				
37.6±0.185	1.67				
38.7±0.436	2.33				
25.8±0.512	3.00	1.46	8.73×10^6	6.77×10^8	51.2
30.6±1.93	3.75				
32.0±0.372	1.00				
33.6±1.68	0.75				
34.6±0.323	3.75				

Table 5-5 (Continued)

Crystal Composition	L_{gap} (mm)	Pressure (Pa)	Total X-ray Counts	Count Rate (cps)
$LiNbO_3$	5.0	<0.00532	$(1.04\pm0.126)\times10^6$	$(2.89\pm0.349)\times10^2$
		0.24	$(0.759\pm0.262)\times10^6$	$(2.11\pm0.728)\times10^2$
		0.33	$(0.525\pm0.0172)\times10^6$	$(1.46\pm0.0478)\times10^2$
		0.67	$(0.327\pm0.0640)\times10^6$	$(0.908\pm0.178)\times10^2$
		1.33	$(0.135\pm0.00353)\times10^6$	$(0.375\pm0.00981)\times10^2$
	10.0	<0.00532	$(2.89\pm0.595)\times10^6$	$(8.04\pm1.65)\times10^2$
		0.24	$(1.03\pm0.458)\times10^6$	$(2.85\pm1.27)\times10^2$
		0.33	$(0.894\pm0.230)\times10^6$	$(2.48\pm0.640)\times10^2$
		0.67	$(0.849\pm0.0407)\times10^6$	$(2.36\pm0.113)\times10^2$
		1.33	$(0.0779\pm0.0377)\times10^6$	$(0.216\pm0.105)\times10^2$
$LiTaO_3$ (0.5 mm)	5.0	0.24	$(2.66\pm1.98)\times10^4$	7.38±5.50
		0.33	$(3.98\pm2.94)\times10^4$	11.1±8.17
		0.67	$(5.80\pm1.39)\times10^4$	16.1±3.87
		1.33	$(3.89\pm2.95)\times10^4$	10.8±8.20
	10.0	0.24	$(2.85\pm2.57)\times10^4$	7.92±7.13
		0.33	$(5.77\pm2.39)\times10^4$	16.0±6.64
		0.67	$(5.00\pm0.934)\times10^4$	13.9±2.60
		1.33	$(2.52\pm0.577)\times10^4$	7.01±1.60
PMN-30PT	3.7	0.24	32.8±3.10	0.00910±0.000860
		0.33	37.8±4.57	0.0105±0.00127
		0.67	31.5±4.20	0.00875±0.00117
		1.33	30.8±3.86	0.00854±0.00107
	5.0	0.24	31.5±7.33	0.00875±0.00203
		0.33	39.0±9.49	0.0108±0.00264
		0.67	35.7±4.73	0.00991±0.00131
		1.33	29.5±3.11	0.00819±0.000864

End-point Energy (keV)	N_B	F_e ($\mu C/m^2K$)	F_σ (V/m)	E_{max} (V/m)	ΔV (kV)
28.1±0.743	3.25	1.08	6.46×10^6	–	–
33.8±0.280	2.25				
33.3±0.451	0.67				
33.2±0.357	4.25				
33.2±0.687	4.33				
29.5±0.462	4.00	0.542	3.23×10^6	–	–
30.4±0.301	4.75				
30.2±0.112	1.00				
30.4±0.138	1.67				
33.8±0.298	1.50				
11.7±3.37	7.00	0.382	14.7×10^6	10.1×10^8	21.0
12.8±3.24	6.00				
16.6±0.518	2.75				
16.5±0.340	5.33				
15.4±1.44	2.33	0.191	7.34×10^6	–	–
16.5±0.259	3.50				
15.9±0.776	4.75				
16.9±0.431	5.25				
–	–	0.378	7.42×10^3	11.0×10^6	3.90
–	–				
–	–				
–	–				
–	–	0.2798	5.49×10^3	–	–
–	–				
–	–				
–	–				

This page is intentionally left blank.

7

EDGE EFFECT OF THE PYROELECTRIC CRYSTAL

"I don't believe there would be any science at all without intuition."

– *Rita Levi Montalcini*

7.1 Overview

Results from the characterisation measurements in Chapter 6 suggested that X-rays could be produced from electrons travelling around the edges of the crystal and colliding with the copper shim, which is attached to the positively charged (+Z) surface of the pyroelectric crystal. The significance of the edges of the crystal in the production of X-rays will be explored by generating X-rays using a crystal with insulated edges. Next, a method to potentially improve the X-ray yield using this edge effect will be demonstrated by introducing more edges to the crystal. Both measurements will be studied through experiments and electrostatics simulations.

7.2 X-Ray Generation with Insulated Edges

7.2.1 X-ray generation experimental methodology

The edge effect of the pyroelectric crystal in generating X-rays will be tested by covering the edges of the crystal with an insulating material and placing it in the same X-ray generator apparatus. Applying the insulating material on the edge faces of the pyroelectric crystal was achieved by using a silicone potting compound (RTV 615 silicone rubber compound, GE Silicones, NY, U.S.A.). A silicone potting compound was used as it does not permanently adhere to the surface of the pyroelectric crystal, is easily shaped and insulating.

To achieve encapsulation around the edges of the pyroelectric crystal, a single crystal of $LiTaO_3$ with dimensions of 5×5×2 (thickness) mm^3 was sandwiched between two polyurethane blocks, wrapped with low-density polyethylene film (Figure 7-1(a)). This prevented the silicone potting compound bonding with the polymeric blocks and reduced the chance for it to seep into the top and bottom surfaces of the pyroelectric crystal, as these surfaces should be clean. The silicone potting compound in its liquid state was slowly dripped into the small opening between the two polymeric blocks to avoid formation of air bubbles. Once the compound was applied, the encapsulation setup was slowly rotated to ensure the compound reached the edges of the pyroelectric crystal. The silicone potting compound was then left to cure for 24 h into a high strength silicone rubber, as shown in Figure 7-1(b). The surrounding silicone was then cut down to a 2.0 mm width around the crystal edges with the positive face coated with silver paint.

The edge effect was tested by comparing the results of using the same crystal composition without and with silicone around its edges, and with and without a metal target in place. The target used for this experiment was nickel with a thickness of 7.5 μm. The experiment was tested at pressures of 0.33 Pa but at one fixed gap distance of 3.7 mm. When the target was removed from the setup, the placement of the crystal did not change.

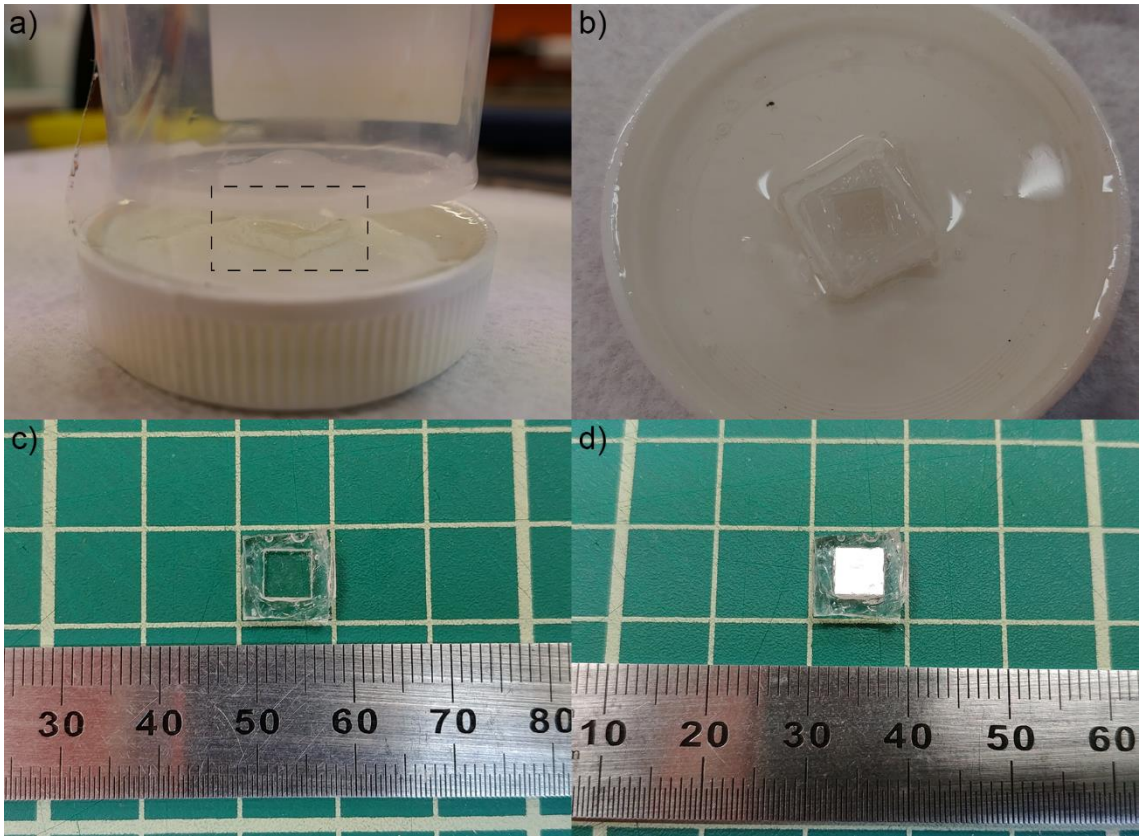

Figure 7-1 Process of sample preparation: (a) Sample is mounted and encapsulated with silicone potting compound, (b) Result of cured silicone surrounding the sample, (c) Cured silicone is cut to width of approximately 2.0 mm around the edge of the crystal, (d) Silver paint is applied only on the +Z polar face of the crystal.

7.2.2 Insulated edge measurement results and discussion

To ensure the polar faces are free of silicone and other foreign materials, Figure 7-2 shows two micrographs belonging to one of the crystal faces before and after it is cleaned.

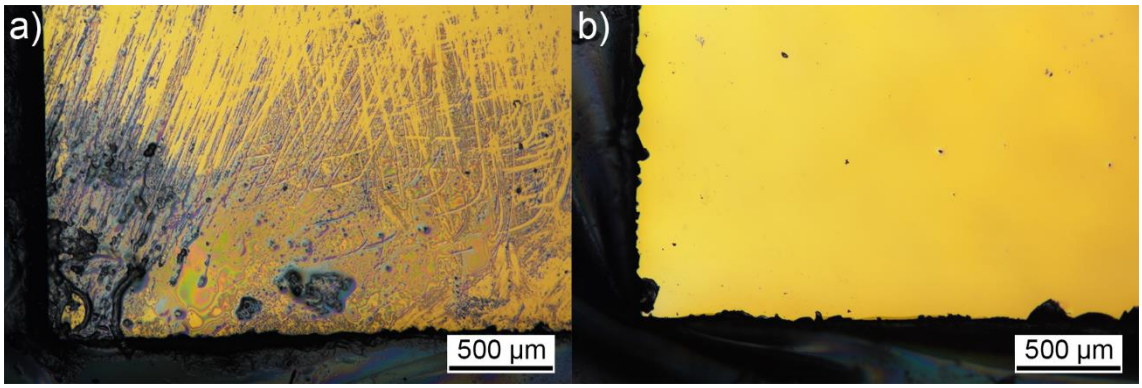

Figure 7-2 Before (a) and after (b) cleaning silicone on $LiTaO_3$ polar surfaces.

The spectra shown in Figure 7-3 have their X-ray counts normalised to each individual spectrum. The fitted elemental spectral lines presented in Figure 7-5, Figure 7-6, Figure 7-7 and Figure 7-8 are relative to the total X-ray counts. The total fit labelled in the mentioned figures represents the sum of all the contributions from each elemental fit and bremsstrahlung.

In both target and no-target configurations, adding the silicone insulation drastically decreased the endpoint energy and total X-ray counts produced by the generator. This suggests that the edges of the crystal play a significant role in producing higher intensity and energy X-rays compared to inner area of crystal face. This should be expected since electric fields tend to concentrate at sharp points or regions of small radius curvature [216, 217]. It has also been observed previously by Shur and Rosenman [142] where they captured electrons emitted from the edges of a circular PLZT ceramic.

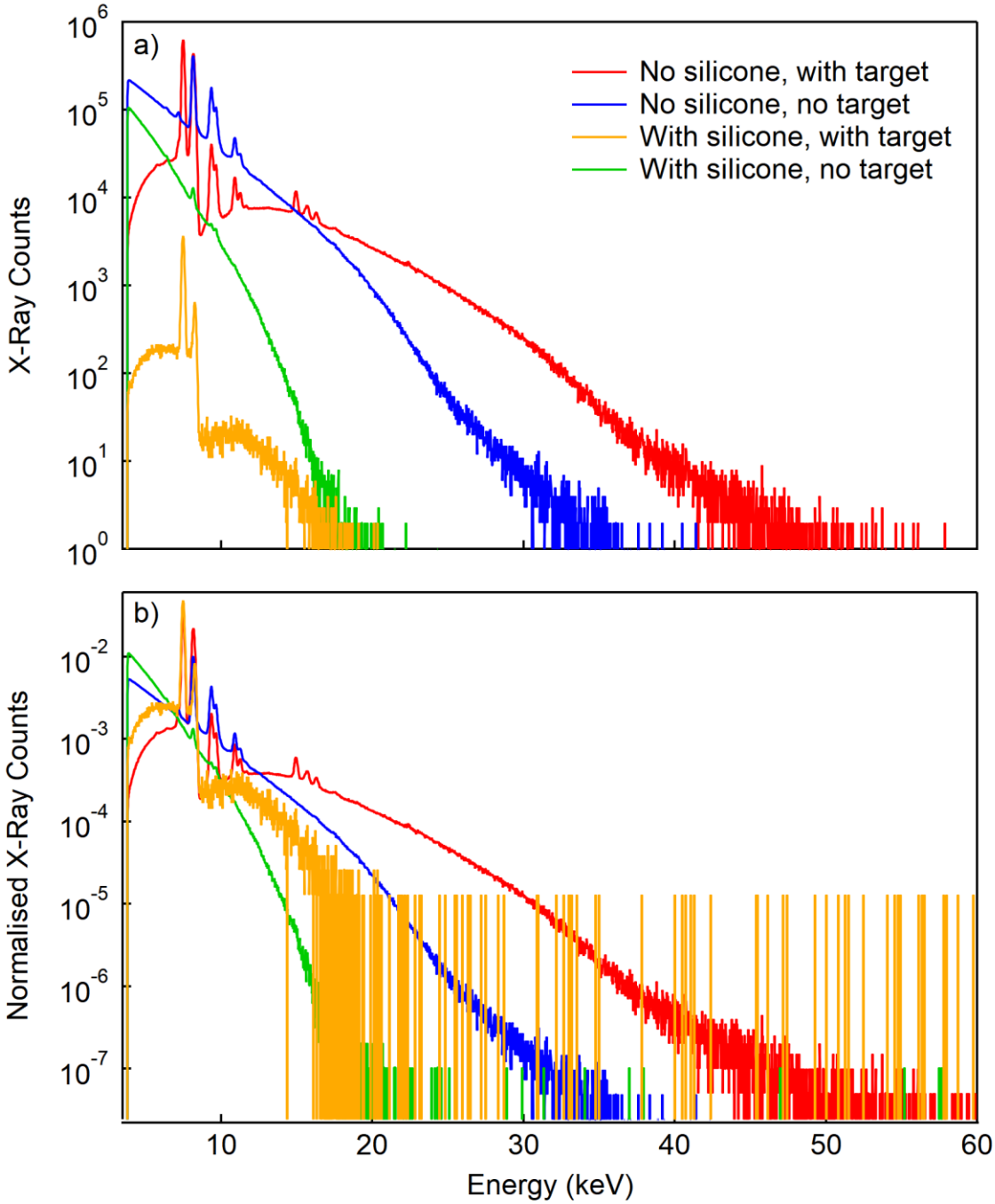

Figure 7-3 Spectra collected from the measurement variations with and without silicone insulation, and with and without a metal target. The bottom figure plots the spectra normalised to each spectrum's total X-ray counts.

Table 7-1 Total X-ray counts, count rate and end-point energy produced from each configuration, with and without silicone and target.

Target	Silicone Insulation	Total X-ray Counts	Count Rate (cps)	End-point Energy (keV)
With target	No silicone	$(20.7\pm0.801)\times10^{6}$	$(57.5\pm22.2)\times10^{2}$	42.4±0.225
With target	With silicone	$(44.4\pm24.8)\times10^{3}$	12.3±6.89	21.4±1.68
No target	No silicone	$(31.8\pm8.83)\times10^{6}$	$(88.3\pm24.5)\times10^{2}$	27.0±3.82
No target	With silicone	$(8.78\pm1.20)\times10^{6}$	$(24.4\pm3.32)\times10^{2}$	16.3±0.454

As discussed in Chapter 6.3, it is understood that the electrons would collide with the crystal during the cooling phase to produce characteristic X-rays of the elements of the pyroelectric crystal [81]. The spectra collected from these four experimental setups bring clarity to the location of interaction. The addition of insulation around the edge faces of the $LiTaO_3$ crystal produced no tantalum L-shell lines when tested with a target in place. Comparing the normalised X-ray counts of tantalum $L\alpha_1$ line in Figure 7-7 and Figure 7-8 where the nickel target is in place and removed, respectively, there is a reduction by an order of magnitude. In the heating phase, some of the emitted electrons would travel directly towards the target and some would circle around to meet the other polar face, much like how the magnetic field lines of a bar magnet would travel from the North Pole to the South Pole, as demonstrated in Figure 7-4. It would then be expected for the electric field distribution around the crystal to be the same in the cooling phase but with the direction reversed. That is, the electrons from the ionised gas molecules near the exposed -Z crystal face would travel directly to the crystal, and the electrons located near the side of the crystal would travel to the edges of the crystal face. If the crystal has insulation around its edges, the electrons coming in from the side would be blocked from colliding with the crystal.

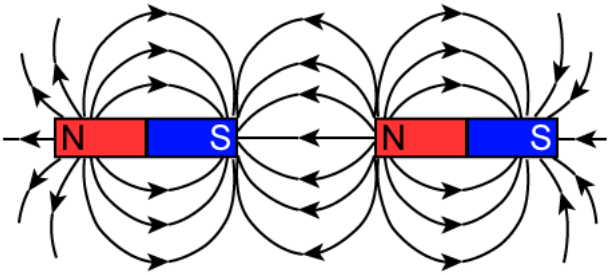

Figure 7-4 Analogy of the electric field created by the pyroelectric crystal alike to magnetic field lines between two unlike poles and around individual bar magnets.

Similarly, electrons travelling around the crystal edges would also account for the presence of copper lines in the heating-phase spectra, as mentioned in Chapter 6.3. This would originate from the electrons accelerating around the edge of the crystal and colliding with the copper shim. When there is insulation around the crystal, the electrons should be blocked from hitting the copper shim. This is seen as no copper is observed in Figure 7-6 and Figure 7-8. The reverse direction of the electric field confirms that no copper lines should also be seen during the cooling phase.

In the measurements taken without the nickel target for both non-insulated and insulated crystals, X-rays are still generated. It was introduced in Chapter 2 that the electron emission originates from electric field in the gap developed by the crystal, such that ferroelectric electron emission and field ionisation can occur. In the absence of the nickel target, the beryllium window of the X-ray spectrometer may be acting as the target. Since copper and tantalum characteristic lines are present in Figure 7-7 and Figure 7-8, it signifies that the electric field in the gap is still intense enough for electron emission to occur. As the gap distance is wider, the electrons may have a greater probability of interacting with other materials nearby. In this case, it is likely that the electrons collided with the steel components of and within the vacuum chamber during the heating phase because there are iron Kα lines present in both spectra (Figure 7-7, Figure 7-8). Conversely, the electrons would collide with the crystal in the cooling phase.

The reduction in end-point energy from the non-insulated crystal test with a target, about 42 keV, to being tested without a target, about 27 keV, could be because the beryllium window of the spectrometer is now acting as the target. This means the detector element would be closer to the location of X-ray production, being at the beryllium window. In Chapter 5.4, the efficiency of the detector for photon energies below 10 keV is close to 100%. Additionally, having no target skips the filtration of the lower energy photons [218, 219]. The effect of filtration at the different sections of an X-ray tube was explored in Chapter 2.2. The combination of these two effects will allow the bremsstrahlung continuum to dominate over the characteristic peaks and skew towards the lower energies.

This page is intentionally left blank.

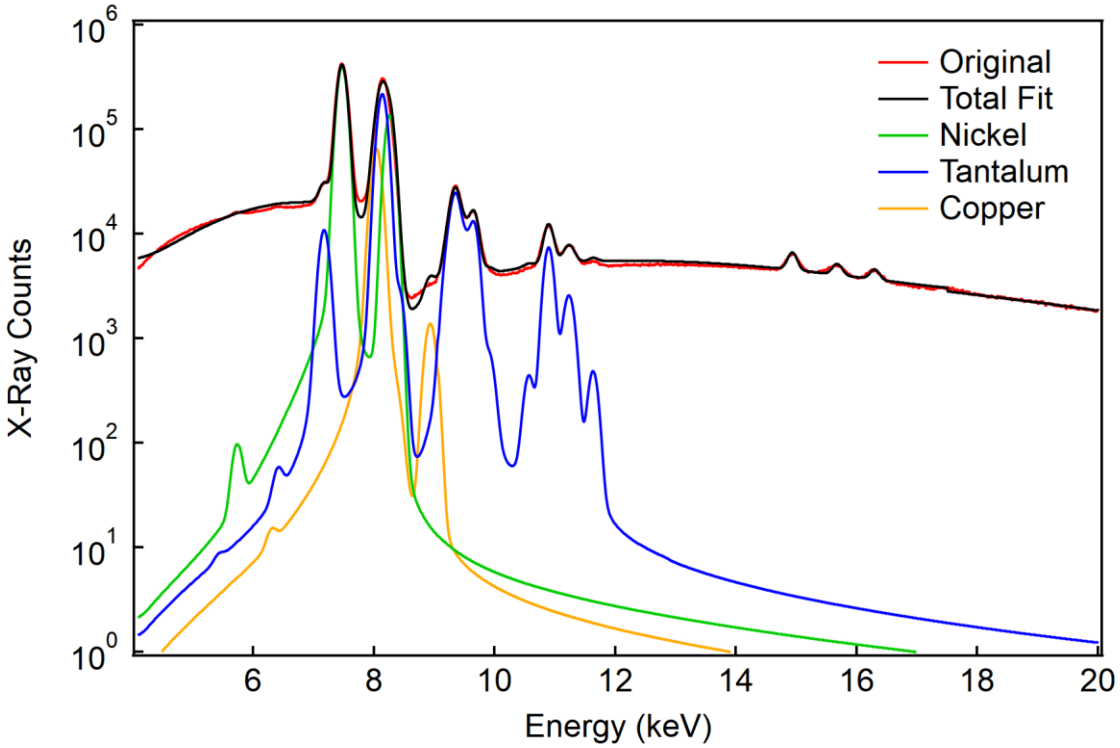

Figure 7-5 Spectral fitting of X-rays produced from a non-insulated $LiTaO_3$ crystal with a nickel target, normalised to the total X-ray counts.

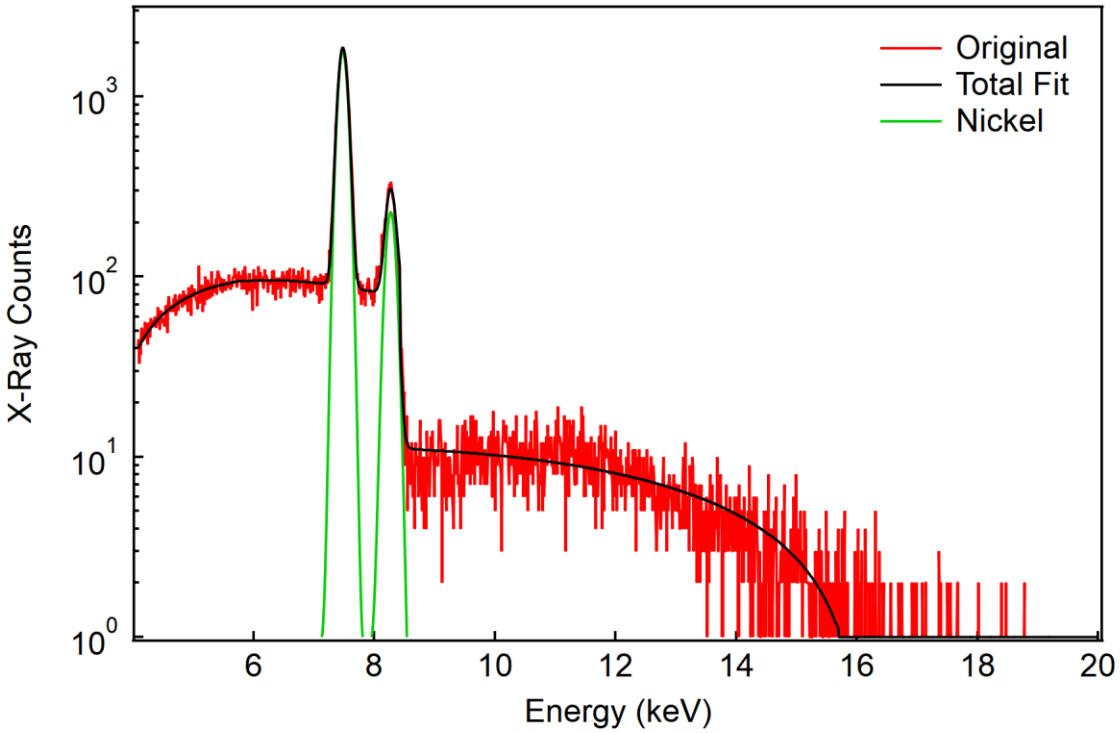

Figure 7-6 Spectral fitting of X-rays produced from $LiTaO_3$ with silicone insulation around the crystal edge faces and a nickel target, normalised to the total X-ray counts.

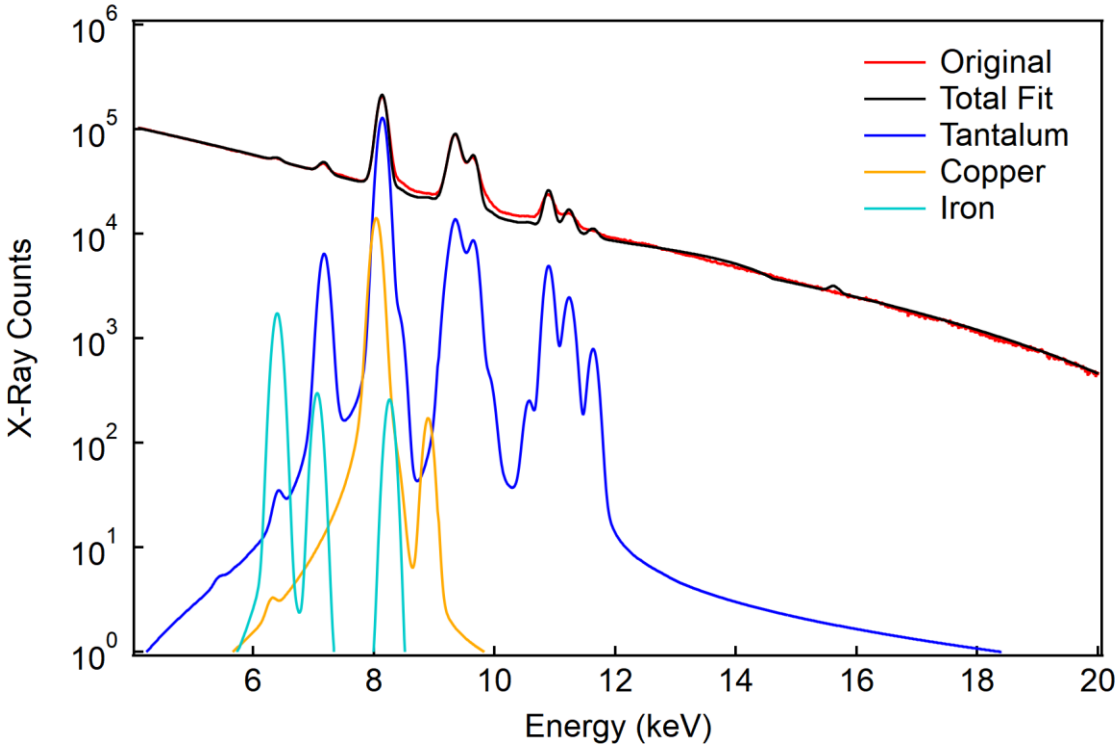

Figure 7-7 Spectral fitting of X-rays produced from $LiTaO_3$ with no insulation and no target.

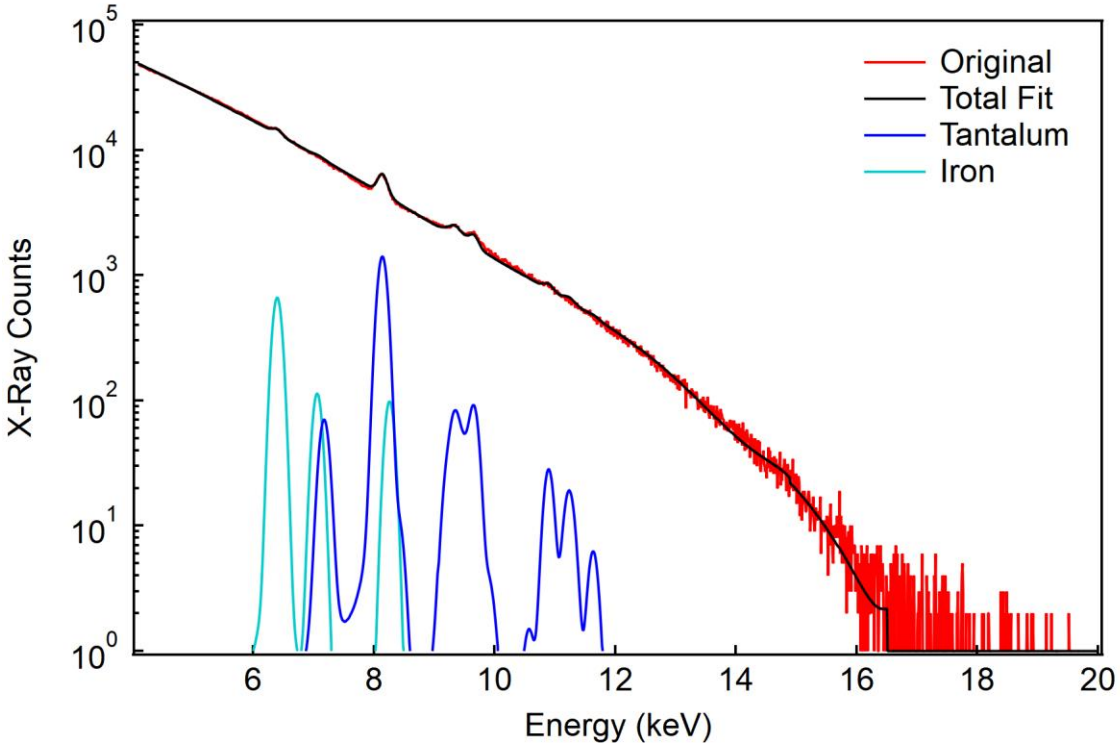

Figure 7-8 Spectral fitting of X-rays produced from $LiTaO_3$ with silicone insulation around the crystal edge faces and no target.

7.2.3 Electrostatics simulation model

To further understand the results observed in Chapter 7.2.2, the pyroelectric crystal was simulated with silicone insulation around its edge faces, as displayed in Figure 7-9, and the electric field distribution will be studied. The width of the silicone was 2.0 mm. The properties of silicone were taken from COMSOL's library of materials. The applied surface charge density was tested with a positive and negative polarity, like in Chapter 6.

The constant parameters were the same as in Chapter 6 with the addition of:

- Crystal composition, which was $LiTaO_3$
- Crystal thickness, set at 2.0 mm
- Gap distance, fixed at 3.7 mm

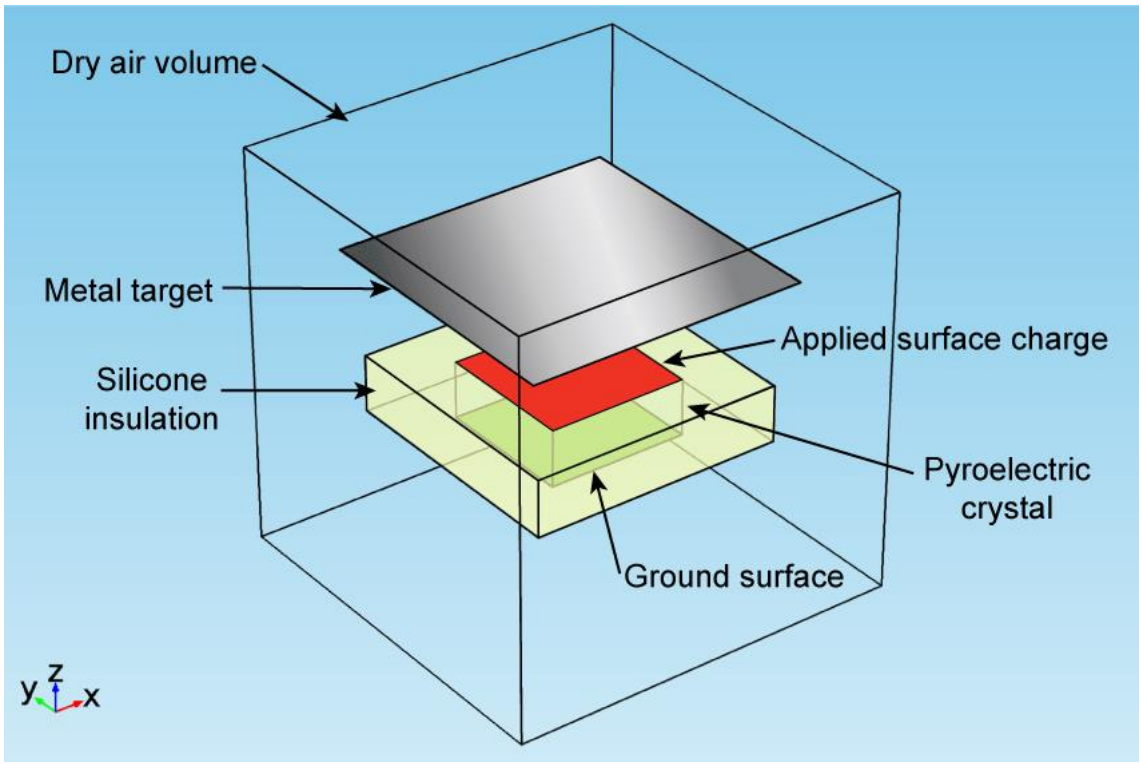

Figure 7-9 Geometry of the pyroelectric crystal with insulation around its edge faces.

As was conducted in the X-ray generator experiment earlier, a non-insulated and insulated crystal were simulated without a metal target. Instead the beryllium window of the spectrometer was put in place, as pictured in Figure 7-10 and Figure 7-11. The dimensions of the window are 7.0 mm in diameter and 12.5 μm in thickness. As the spectrometer is always placed 5.0 mm away from the target and the gap distance is 3.7 mm, the distance between the top crystal surface and the beryllium window is set at 8.7 mm. The configuration is shifted similar to the simulation study on the effect of gap distance so that it can fit within the same volume.

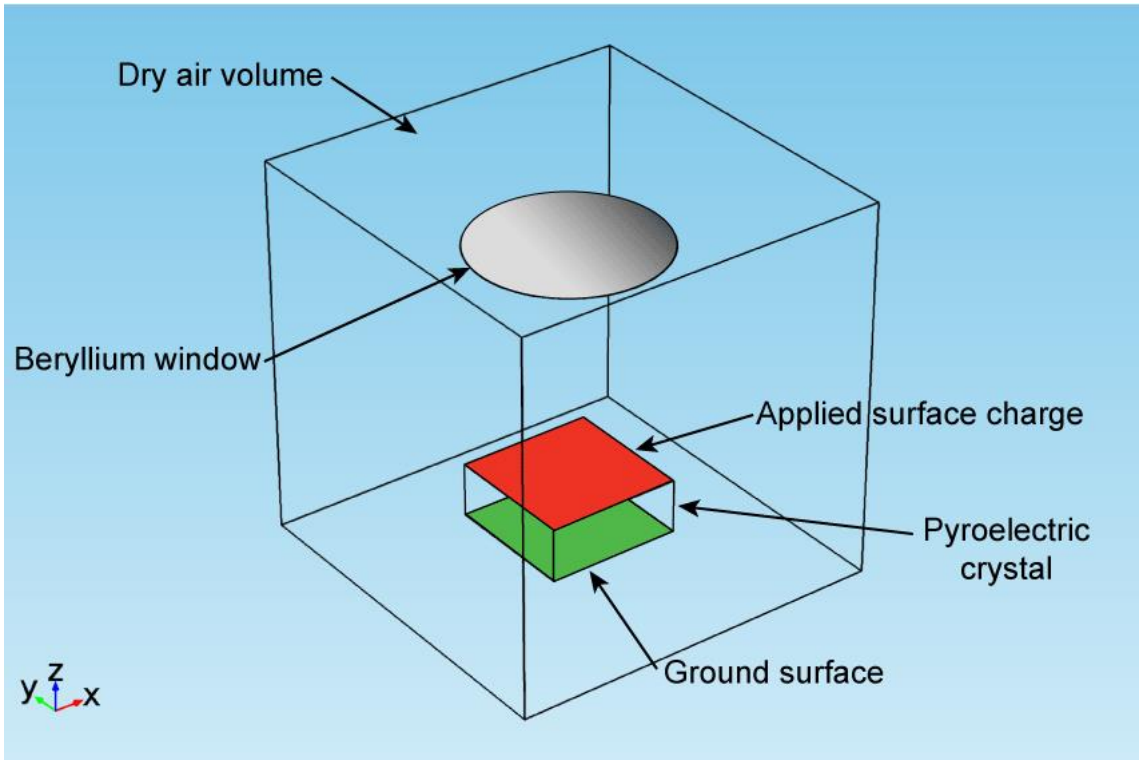

Figure 7-10 X-ray generator model using a non-insulated crystal with the beryllium window of the spectrometer replacing the metal target.

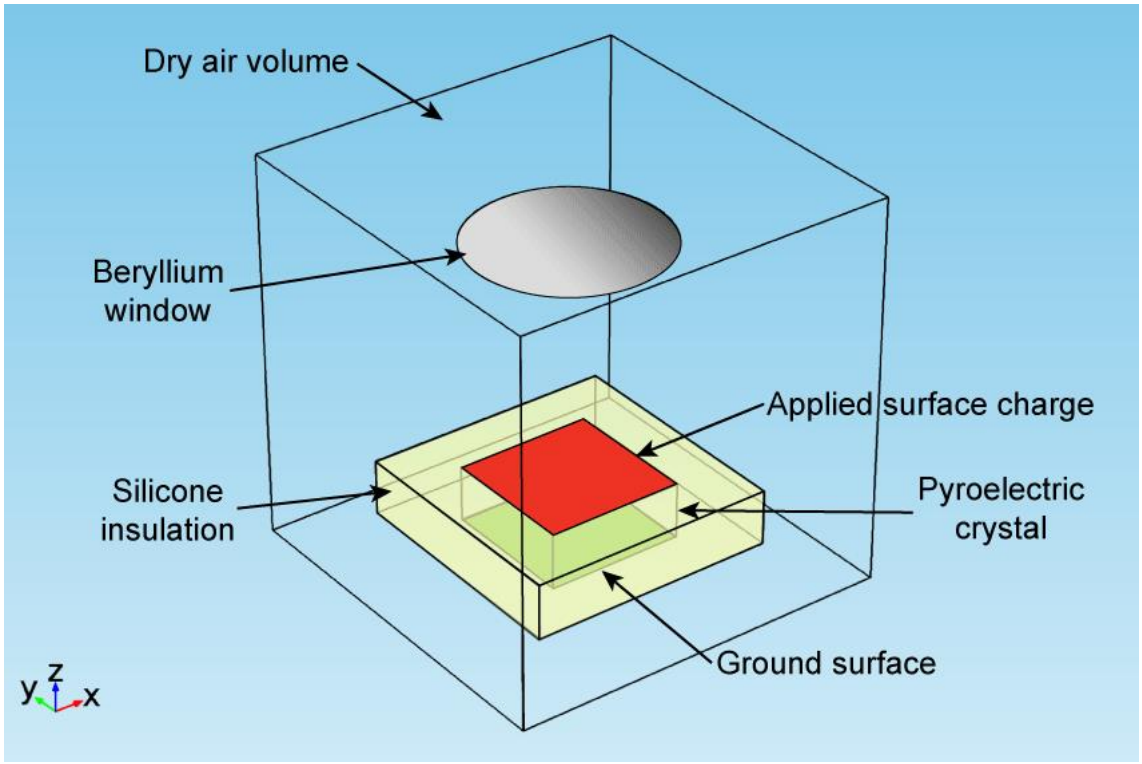

Figure 7-11 X-ray generator model with insulated crystal and beryllium window.

7.2.4 Simulation results and discussion

The edge effect of the pyroelectric X-ray generation was simulated to confirm the observations seen in experiments with and without silicone insulation around the edge faces of the pyroelectric crystal. The electric field distribution presented in Figure 7-12, Figure 7-13 and Figure 7-15 do reinforce the results discussed in Chapter 7.2.2. It also gives insight into the distribution of the electric field around the pyroelectric crystal.

In Chapter 7.2.2, when the insulated crystal was tested with the nickel target in place, no copper and tantalum lines were observed unlike its non-insulated counterpart. A probable reason mentioned was because the silicone was blocking the electrons from colliding with the copper shim during the heating phase, and the $LiTaO_3$ crystal during cooling. This reasoning agrees with the results presented here. Figure 7-12 shows the electric field distribution during the heating phase. With silicone added around the edge faces of the pyroelectric crystal, the electric field distribution around the crystal and silicone is alike to the non-insulated crystal configuration. That is, there are electrons travelling either upwards towards the target or around edge faces of the crystal. The electric field also permeates through the silicone in an unperturbed manner. However, because of the insulating properties and location of the silicone, the electrons are prevented from

travelling through the silicone. Therefore, if the copper shim was placed behind the +Z crystal face, the electrons would not be able to collide with it, reinforcing the lack of copper lines observed when using the insulated crystal.

Figure 7-13 shows the electric field distribution during the cooling phase, where electrons are now attracted to the top crystal surface. As was the case in the heating phase model, the electrons generally travel in the same manner as the non-insulated crystal. This means there would be fewer electrons colliding with the edges of the crystal as they would be obstructed by the silicone. The electrons produced around the more central part of the crystal would travel with little disruption.

The series of electric field distribution figures of the insulated crystal continue to show that the electric field does concentrate at the edges of the crystal. However, the histogram in Figure 7-14 show that only a very small area of 0.923% of the top crystal surface has an electric field above 10^8 V/m and nearly 50% of the top crystal surface has an electric field below 3.5×10^7 V/m . Since the electric field magnitudes here is between that of $LiNbO_3$ and PMN-30PT, it is expected for fewer X-rays to be seen.

Therefore, an insulated pyroelectric crystal will still be able to create a sufficiently intense electric field for electron emission throughout the thermal cycle, but the electrons are not energetic enough to produce characteristic X-rays of the copper shim and the pyroelectric crystal. Instead, bremsstrahlung would be generated.

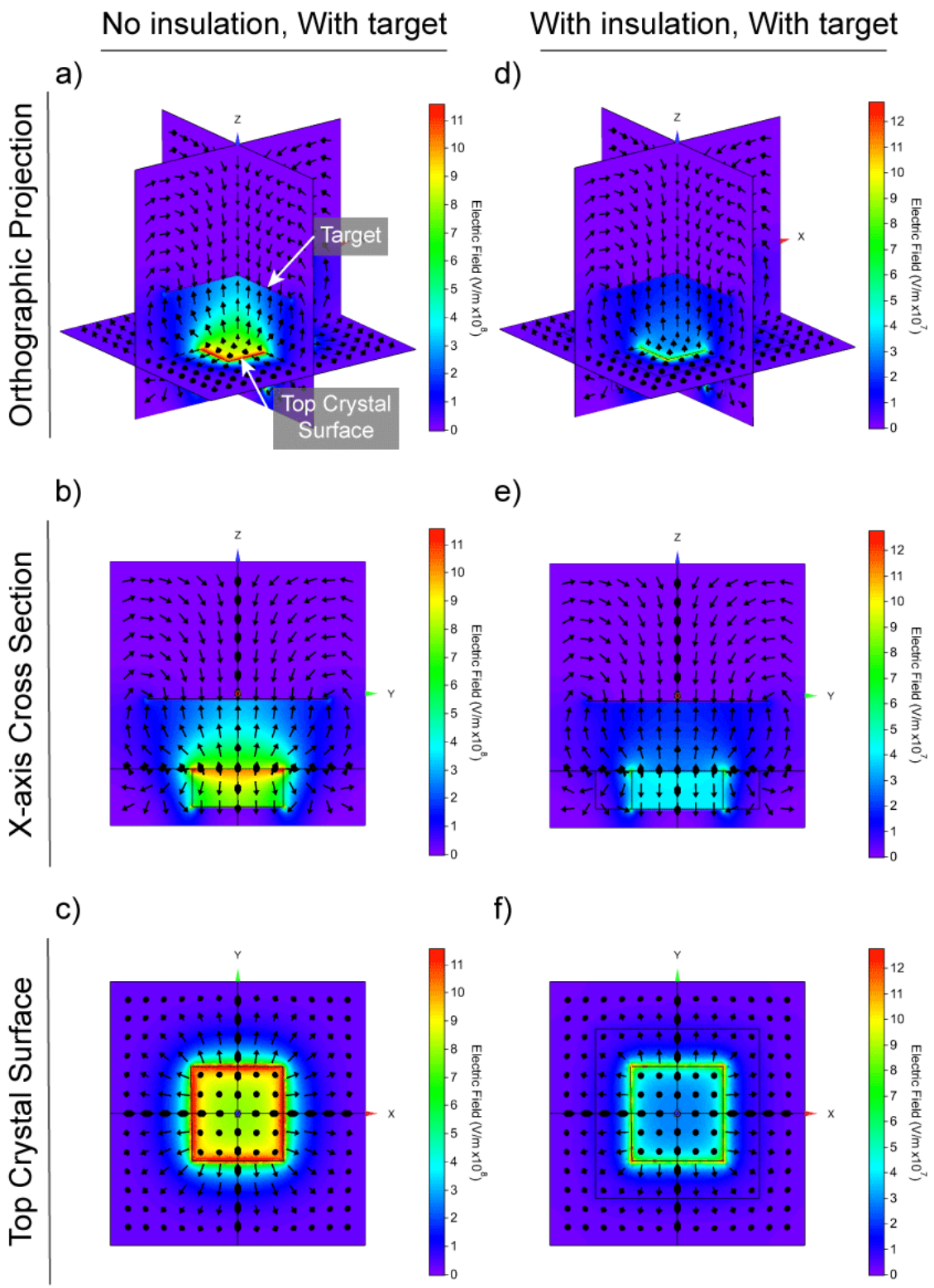

Figure 7-12 Comparison of the electric field distribution of a non-insulated crystal (left vertical series) and silicone insulated crystal (right vertical series) during the heating phase. The vectors represent electrons, which are travelling towards the target. The bottom pair is a top view of the top crystal surface (c, f). The threshold electric field of the non-insulated and insulated crystals are 11.5×10^8 V/m and 12.7×10^7 V/m, respectively.

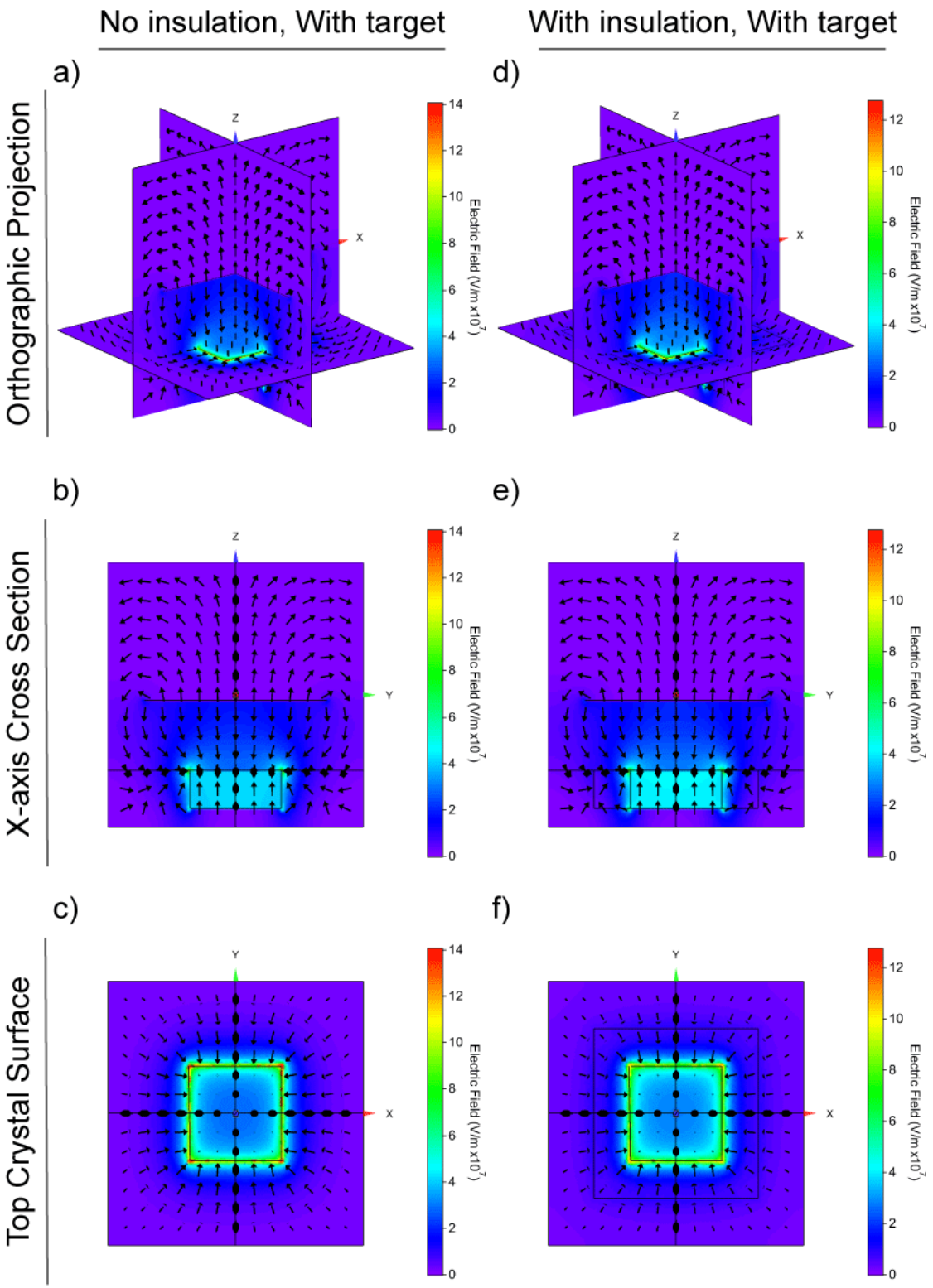

Figure 7-13 Comparison of the electric field distribution of a non-insulated crystal (left vertical series) and silicone insulated crystal (right vertical series) during the cooling phase. The vectors represent electrons, which are travelling towards the top crystal surface. The bottom pair is a top view of the top crystal surface (c, f). The threshold electric field of the non-insulated and insulated crystals are 14.0×10^7 V/m and 12.7×10^7 V/m, respectively.

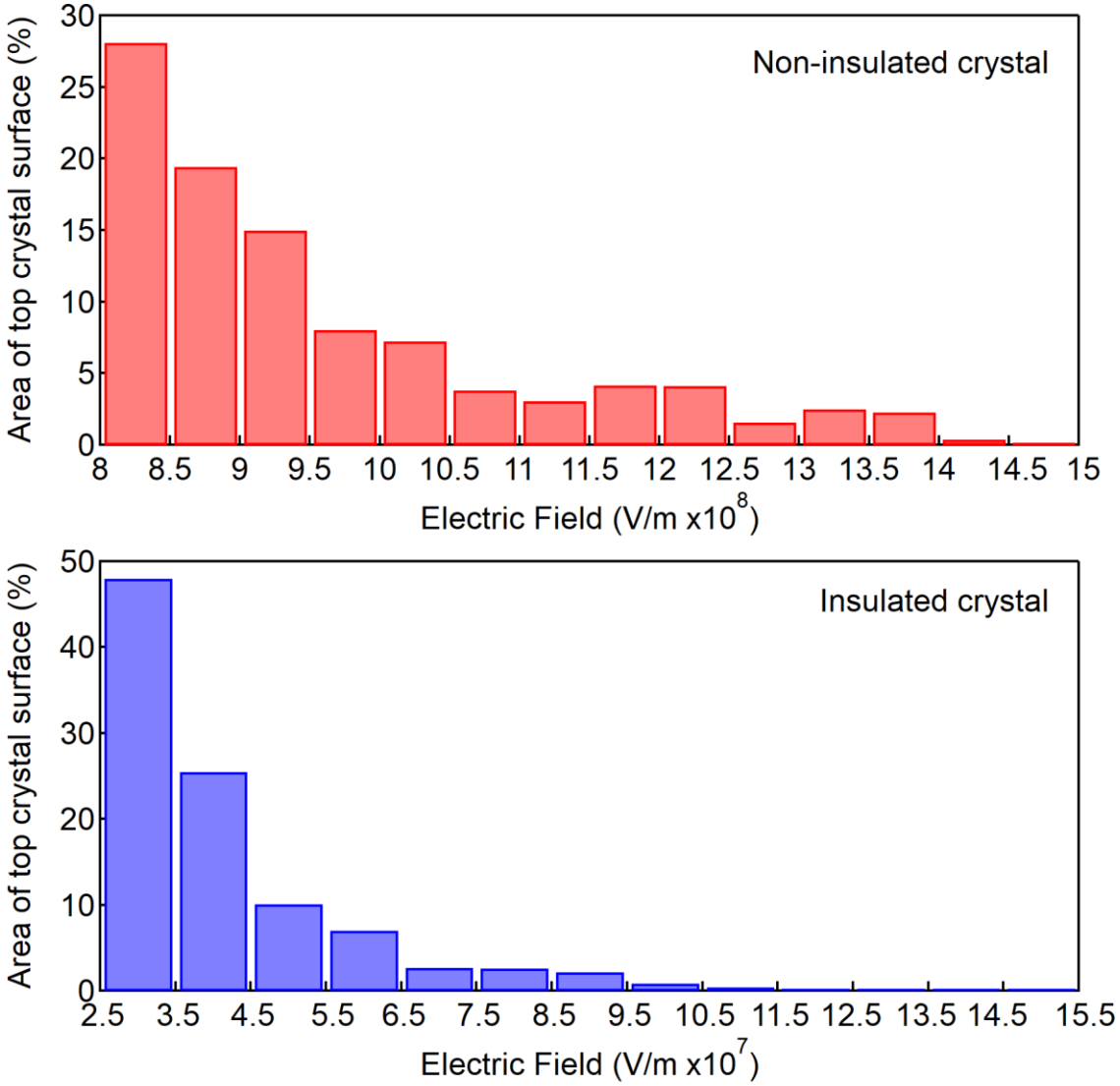

Figure 7-14 Histograms of the electric field produced by non-insulated (top) and insulated (bottom) crystals at the top crystal surface. Their bin widths are 0.5×10^8 V/m and 1×10^7 V/m, respectively.

The non-insulated and insulated pyroelectric crystals were also modelled with no nickel target in place. Instead a beryllium piece was used to represent the window of the spectrometer. This is because in Chapter 7.2.2, it was speculated that the beryllium window is acting as the target but located at a wider gap distance. The electric field distributions from both crystals are shown in Figure 7-15. In conjunction with Table 7-2, the electric field at the top crystal surface from both configurations are within close ranges. The major difference is at the beryllium window where the electric field created by the non-insulated crystal is able to sustain over the wider gap compared to the insulated crystal. This suggests that insulating the edges of the crystal not only reduces

the electric field at the crystal but diminishes the electric field across the gap to a further extent.

Between the non-insulated and insulated crystal models, with the target in place, there is a close to one magnitude difference of the electric field at the top crystal surface and the target. This corresponds with the difference in the count rate, as listed in Table 7-2. When the target was substituted for the beryllium window in the model, the resulting electric field at the top crystal surface and the target were very close to each other. However, the count rate produced by the insulated crystal was still half that of the non-insulated crystal. This reinforces the edge effect of the pyroelectric crystal where a contribution of the X-ray counts came from electrons interacting around the crystal's edges.

The potential difference across the gap for the four models were also determined using the same method as described in Chapter 4. The bin widths of 500 V for the top crystal surface and 50 V for the target were applied. The histograms of the electric potential distributions at the top crystal surface and target of the non-insulated and insulated crystals can be found in Appendix E. The potential difference across the gap of the four models were found to be very similar to each other. This suggests that the end-point energies should also exhibit a corresponding trend. However, the model with no silicone insulation and a nickel target appears to be an anomaly.

It is uncertain as to the cause for the difference, but there could be several contributions at play. Like the diminishing effect on the X-ray counts by applying insulation on the crystal edges, there could be an equivalent effect on the end-point energy. As was mentioned earlier in Chapter 7.2.2, removing the nickel target allows the electrons to collide directly with the beryllium window of the spectrometer. This means X-rays being produced much closer to the detector component. Additionally, an absent target in the X-ray generator configuration allows the X-rays to bypass the filtration of low-energy photons. This causes the energy spectra to skew towards the low photon energy range, where the detector would also have excellent detector efficiency.

This decrease in the X-ray generator performance when the pyroelectric crystal edges are insulated reinforce that the edges do play a part in enhancing the electric field created by the pyroelectric crystal and amplifies the X-ray generator output.

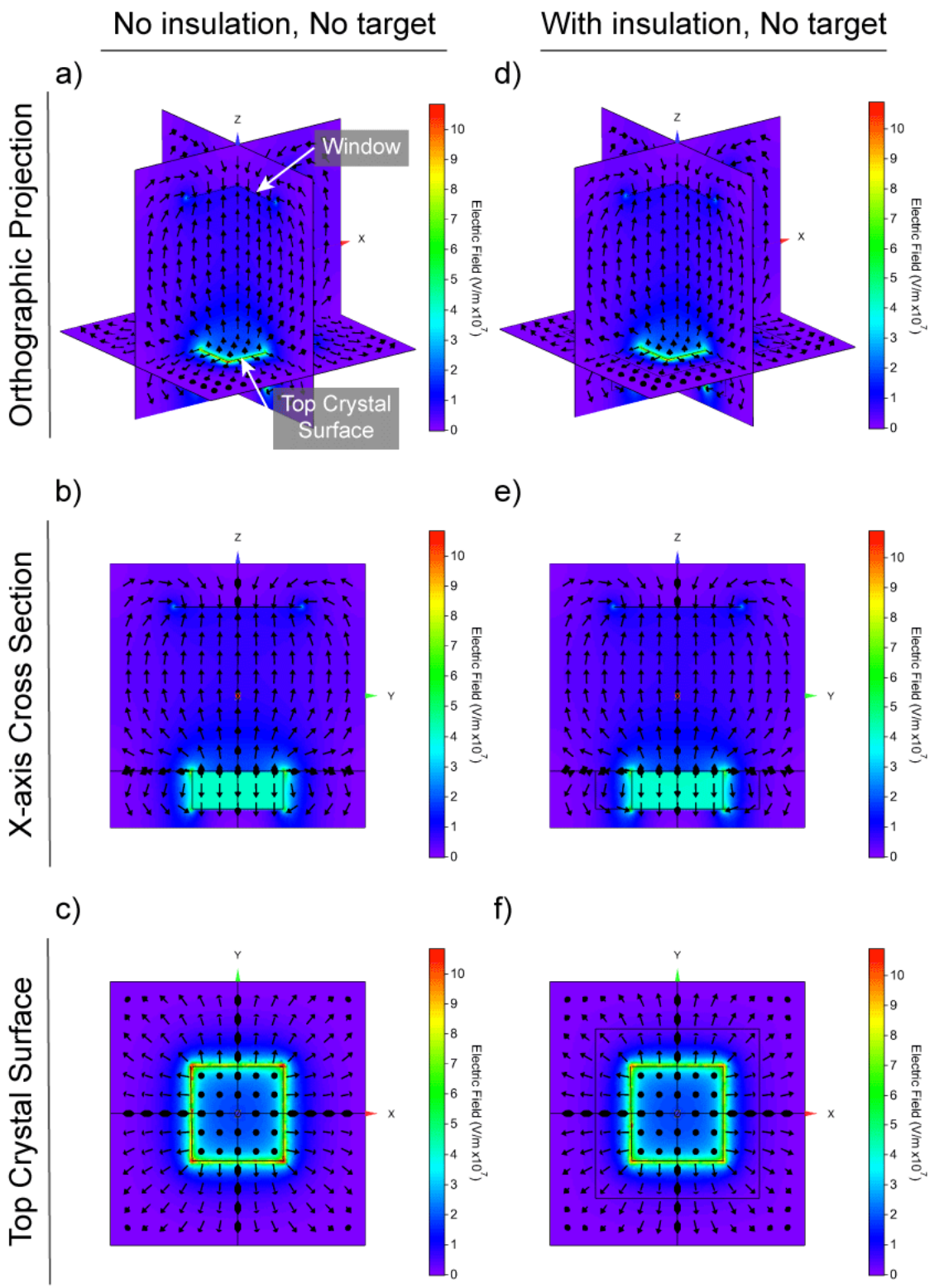

Figure 7-15 Comparison of the electric field distribution of a non-insulated crystal (left vertical series) and silicone insulated crystal (right vertical series) with no metal target. The beryllium detector window is replaced instead. The bottom pair is a top view of the top crystal surface (c, f). The threshold electric field of both models is 10.8×10^7 V/m.

Table 7-2 The minimum and maximum electric field produced at the top crystal surface, and the target or detector window depending on the model. The count rate and end-point energy collected from the corresponding measurements are included.

Target	Silicone Insulation	Gap Distance (mm)	Top Crystal Surface		Target/Detector Window		Potential Difference (kV)	Count Rate (cps)	End-point Energy (keV)
			Min Electric Field (V/m)	Max Electric Field (V/m)	Min Electric Field (V/m)	Max Electric Field (V/m)			
With target	No	3.7	7.95×10^{8}	13.5×10^{8}	1.18×10^{8}	3.12×10^{8}	80.6	$(57.5\pm22.2)\times10^{2}$	42.4±0.225
With target	Yes	3.7	2.81×10^{7}	1.49×10^{8}	0.991×10^{7}	2.19×10^{7}	80.0	12.3±6.89	21.4±1.68
No target	No	8.7	1.84×10^{7}	1.27×10^{8}	0.383×10^{7}	4.05×10^{7}	82.3	$(88.3\pm24.5)\times10^{2}$	27.0±3.82
No target	Yes	8.7	1.82×10^{7}	1.28×10^{8}	0.385×10^{7}	4.22×10^{7}	81.8	$(24.4\pm3.32)\times10^{2}$	16.3±0.454

7.3 X-ray Generation using a Diced Crystal

7.3.1 X-ray generation experimental methodology

As it was noticed that the edges of the pyroelectric crystal played a part in the electron emission phenomenon, one potential idea to increase the X-ray counts and X-ray energy was to add more edges in the element. In conjunction with electrostatic simulations computed using COMSOL Multiphysics, an experimental test was performed to confirm this hypothesis.

To prepare for this experiment, a single crystal of $LiTaO_3$ with thickness of 2.0 mm was partially diced in a (1-3) structure from its negative polar face [220]. The sample was cut using a diamond wire saw with a diamond wire diameter of 0.125 mm (Diamond Wire Saw Model STX-202A, MTI Corporation, CA, U.S.A.). The single crystal was then set up in the same manner as described in Chapter 4.5.

It was tested under the following combination of parameters:

- Pressure (Pa) – 0.24, 0.33, 0.67, 1.33
- Gap distance (mm) – 3.7, 5.0, 10.0

Micrographs of the prepared crystal was inspected under the optical microscope. The kerf width and depth could then be measured using Photoshop (Adobe Photoshop CC 2014).

7.3.2 Diced pyroelectric crystal results and discussion

The contribution from the edges of the crystal in X-ray production led to the hypothesis that adding more edges to a crystal would improve the X-ray yield and end-point energy. This would be tested by making several cuts through the crystal from the -Z face of the crystal and not cutting completely through its thickness.

Micrographs of the prepared diced crystal are shown in Figure 7-16 and Figure 7-17. The damage should be taken into account when discussing the experiment results. The kerf width is approximately 0.17 mm and the average pillar width of 0.525 ± 0.0585 mm.

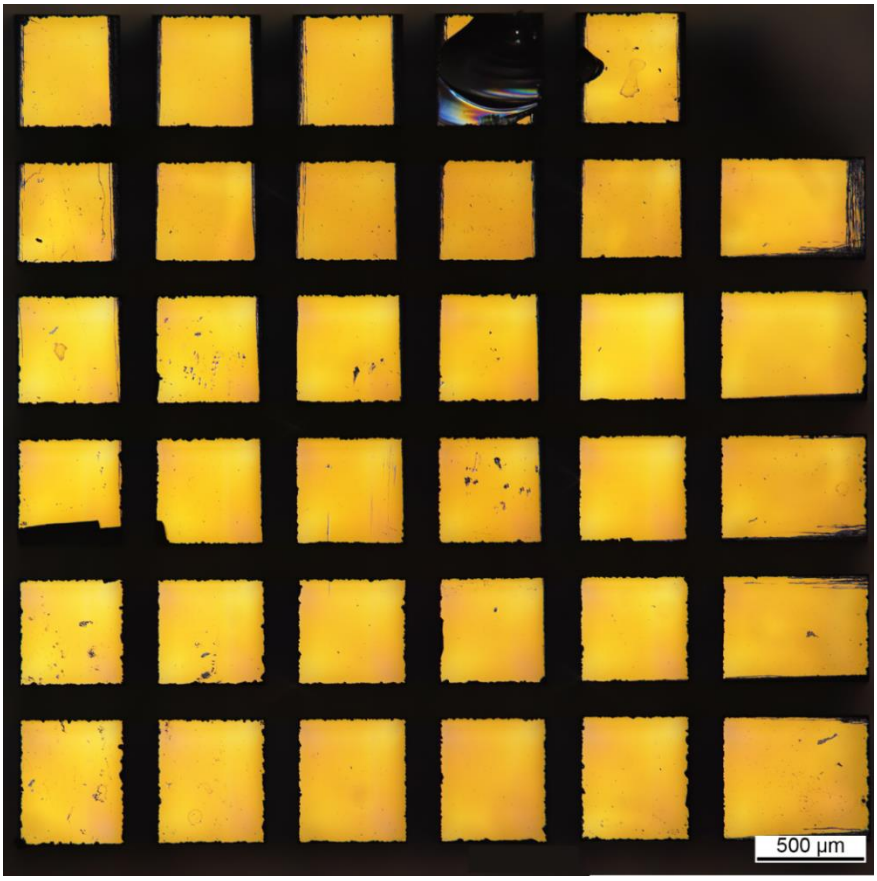

Figure 7-16 Blended micrographs of the diced $LiTaO_3$. Damage occurred during the machining and cleaning process where a pillar and a half was broken off.

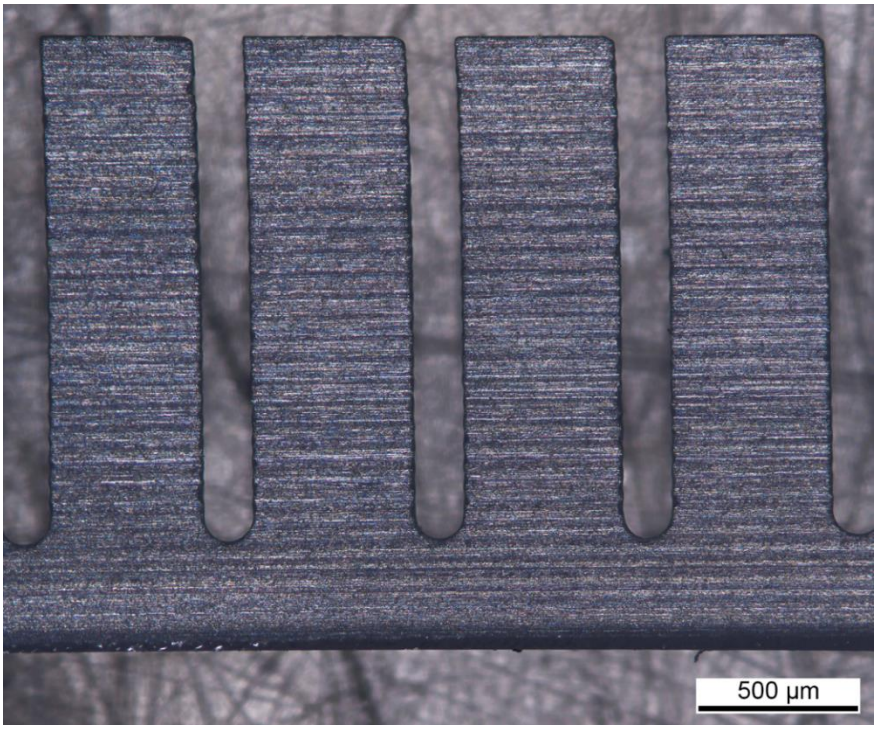

Figure 7-17 Blended micrograph of a side view of the diced $LiTaO_3$ crystal with a kerf depth of approximately 0.13 mm.

The X-ray counts and end-point energies produced by the diced crystal is shown in Figure 7-18. Increasing the pressure inside the vacuum chamber did not display a strong effect in the X-ray production and end-point energy when using the diced crystal. On the other hand, increasing the gap distance to 10.0 mm unusually increased the X-ray counts at all tested pressures. This is contrary to the gap distance variation trend exhibited by the non-diced counterpart where increasing the gap distance generally had lower counts, as can be seen in Figure 7-19. Additionally, both figures-of-merit, F_σ and F_ε, for a non-diced crystal also decayed with greater gap distances. That is, the magnitude of the electric field in the gap decreases as the gap distance widens. It is uncertain as to why the X-ray yield increased but it may be associated with the number of electrical breakdowns. As listed in Table 7-3, the number of electrical breakdowns for measurements at gap distance of 3.7 mm and 5.0 mm sat within a closer range than at a gap distance of 10.0 mm. However, it can also be said that the number of electrical breakdowns at gap distance of 10.0 mm is not drastically fewer as well. It should also be noted that it was only the X-ray counts that increased while the end-point energy was still within standard deviation of the other two gap distances. This suggests that only the electron emission current increased. Therefore, the electric field in the gap would have been of similar intensity amongst the three gap distances but it was an optimum combination such that more electrons could be produced and few electrical breakdown events interrupting the generation of X-rays [32].

In comparison to the original non-diced crystal, the diced crystal exhibited lower X-ray output in all conditions, as seen in Figure 7-19. The diced crystal produced a maximum of 105 cps at pressure of 0.33 Pa and gap distance of 10.0 mm. At the same parameters, the non-diced crystal produced 2360 cps. The results produced by the non-diced crystal can be found in Table 6-5 from Chapter 6.5.4. A possible explanation for the difference could be due to a reduction in the surface area of the exposed -Z crystal face and the number of electrical breakdowns being higher with the diced crystal. Since the surface charge is proportionally related to the surface area of the crystal, as introduced in Chapter 3, the 63.9% surface area reduction would result in a lower electric field in the gap and subsequently, fewer electrons emitted. As a result, the end-point energy of the diced crystal is half the end-point energy from the original crystal.

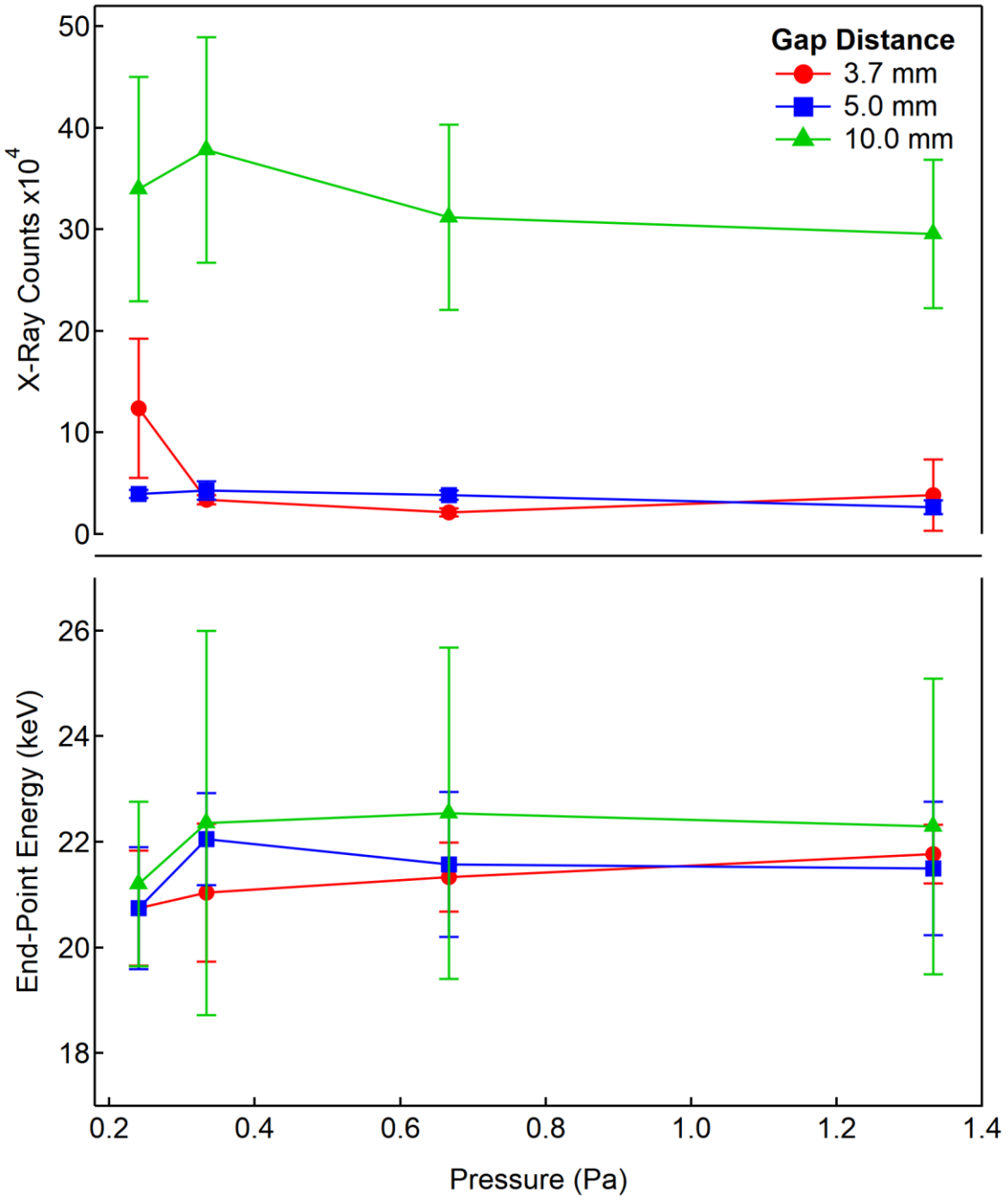

Figure 7-18 Total X-ray counts produced by the diced $LiTaO_3$ crystal presented as a function of pressure over a range of gap distances. Error bars represent a standard deviation over three repeated measurements.

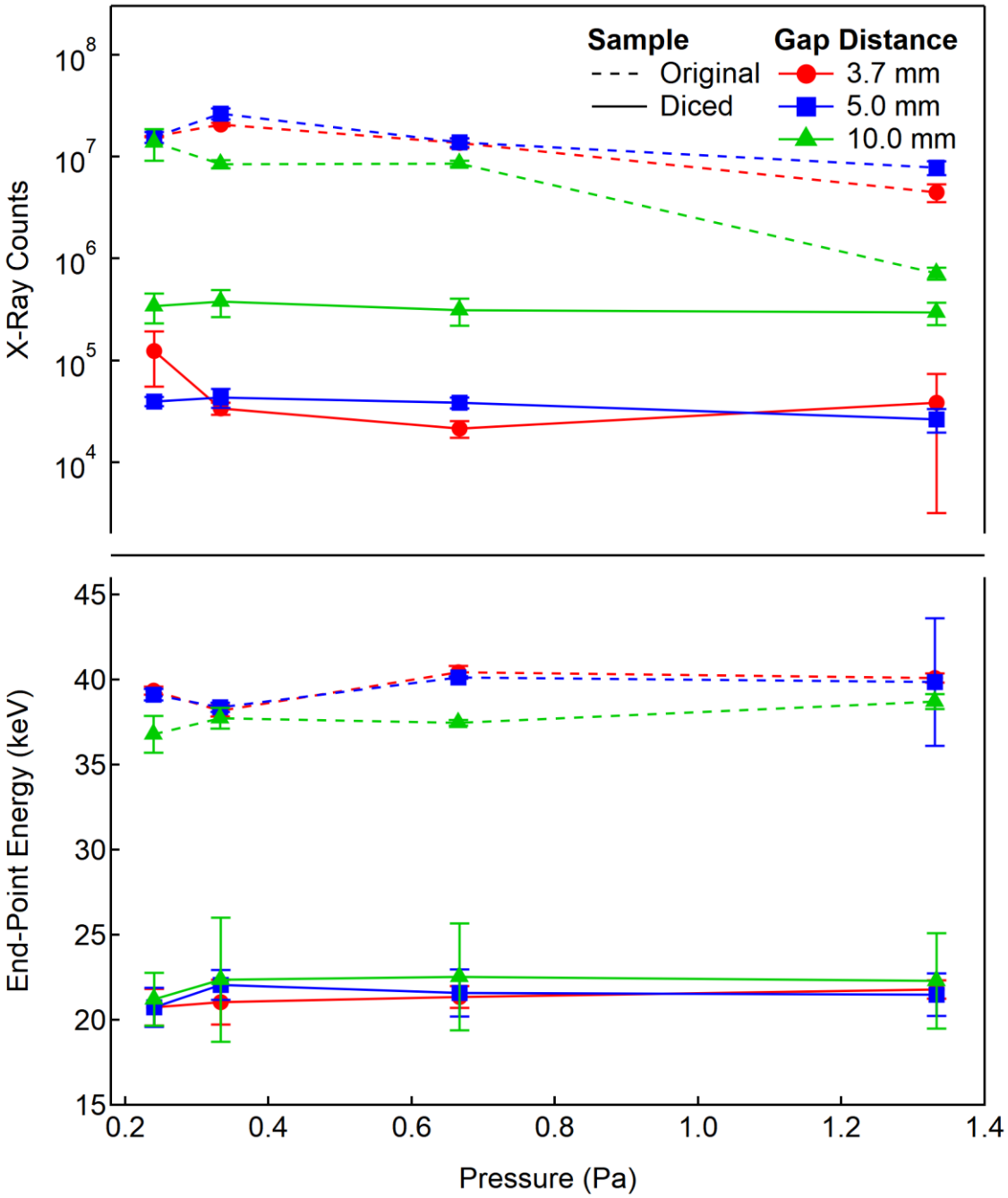

Figure 7-19 A comparison of the total X-ray counts and end-point energies produced by the original and diced $LiTaO_3$ crystal. Error bars represent a standard deviation over three repeated measurements.

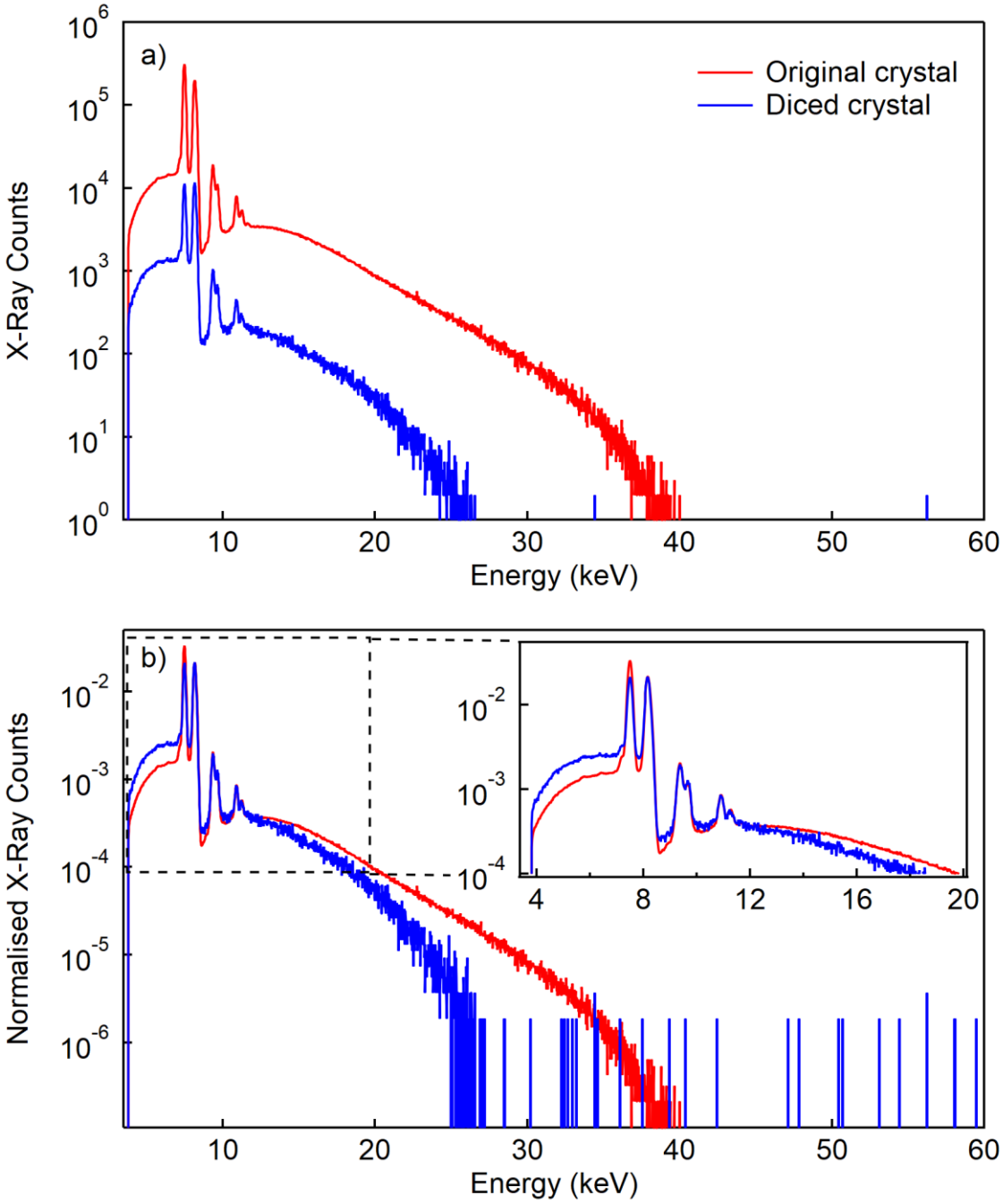

Figure 7-20 Spectra from the original non-diced crystal and the diced crystal, collected at pressure of 0.33 Pa and gap distance of 10.0 mm. The bottom figure plots the spectra normalised to each spectrum's total X-ray counts.

Table 7-3 Summary of the X-ray generator output from the diced crystal, including the average number of electrical breakdowns over three repeated measurements.

Gap Distance (mm)	Pressure (Pa)	Total X-ray Counts	Count Rate (cps)	End-point Energy (keV)	No. of Breakdowns
3.7	0.24	$(12.4\pm6.85)\times10^4$	34.5±19.0	20.8±1.09	8.75
	0.33	$(3.40\pm0.469)\times10^4$	9.45±1.30	21.0±1.30	7.00
	0.67	$(2.15\pm0.397)\times10^4$	5.96±1.10	21.3±0.656	8.00
	1.33	$(3.86\pm3.54)\times10^4$	10.7±9.83	21.8±0.556	12.5
5.0	0.24	$(3.97\pm0.409)\times10^4$	11.0±1.14	20.8±1.15	8.50
	0.33	$(4.32\pm0.971)\times10^4$	12.0±2.55	22.1±0.871	10.8
	0.67	$(3.88\pm0.454)\times10^4$	10.8±1.26	21.6±1.38	10.0
	1.33	$(2.64\pm0.677)\times10^4$	7.33±1.88	21.5±1.26	10.0
10.0	0.24	$(34.0\pm11.0)\times10^4$	94.4±30.7	21.2±1.56	4.50
	0.33	$(37.8\pm11.1)\times10^4$	105±30.8	22.4±3.64	6.25
	0.67	$(31.2\pm9.11)\times10^4$	86.6±25.3	22.5±3.14	8.50
	1.33	$(29.6\pm7.30)\times10^4$	82.1±20.3	22.3±2.80	10.3

7.3.3 Electrostatics simulation model

In Chapter 7.3.1, the machining of a $LiTaO_3$ single crystal into a 1-3 structure similar to that of a reticulated piezoelectric structure was described. This diced crystal was then tested under a series of varying pressures and gap distances. It was of interest to investigate the intensity and distribution of the electric field produced by a diced crystal of varying kerf widths and number of kerfs, and to understand the results from the X-ray generator experiment. The geometry and constant parameters remained the same as in the simple generator model and insulated edge model. However, the main difference between the model and the machined crystal was the kerfs of the crystal volume was cut through the entire crystal thickness, as shown in Figure 7-21. All the bottom surfaces of the diced crystal were also electrically grounded. The variable parameters used in this model are listed in Table 7-4.

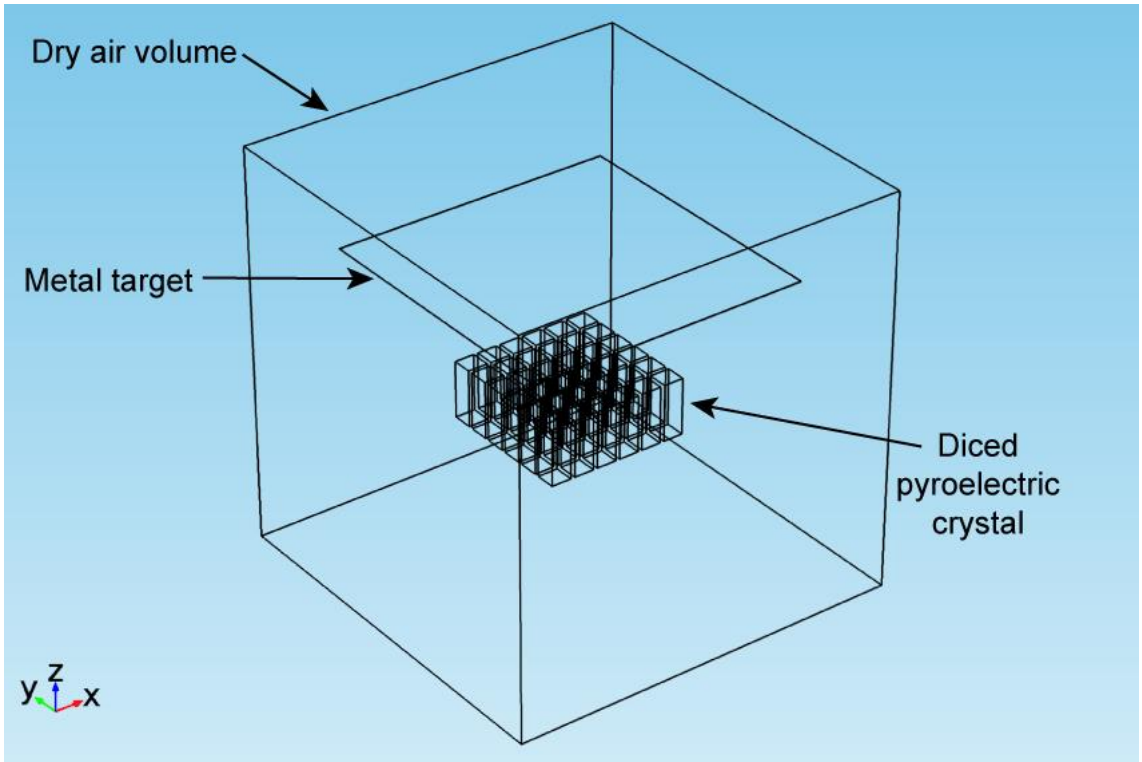

Figure 7-21 Geometry of the model of the diced pyroelectric crystal.

Table 7-4 Variable parameters of the diced crystal simulation model.

Variable Parameter	Value
Number of kerfs in X and Y axes	5, 10, 15, 20
Kerf width (μm)	50, 100, 150, 200

7.3.4 Effect of number of kerfs and kerf widths

Figure 7-22 to Figure 7-25 show corresponding electric field distributions and histograms of the electric field produced at the top surface with changing values of the two parameters of interest. To view the transition of increasing number of kerfs, it should be viewed horizontally along row of indicated kerf width. The transition of increasing kerf widths should then be viewed vertically down.

The specified value of kerfs in all discussions and figures refer to the number of kerfs along the X and Y axes. The electric field at the top surface of the crystal is of interest because it is the determining location for electrons to be emitted from the crystal surface. Whereas the electric field between the top surface and the target determines the acceleration of the electrons. In discussing the electric field distributions, the squares will refer to the sectioned pillars.

In Chapter 6, it was hypothesised that increasing the number of edges on the top surface of the crystal would create more regions of high electric fields at the edges. As the electric field distributions show, the higher electric fields continue to concentrate more so at the outermost edges than the edges of the inner squares. When the crystal was cut with 5 kerfs, the electric field distribution of the second outermost ring of squares follows a similar distribution as the outermost ring of squares where the edges closer to the outside have higher intensities than the inner edges. Furthermore, the overall intensity of the second outermost ring of squares is marginally lower than the outermost ring of squares. This appears to follow the same manner with every progression inward, though difficult to discern for the higher number of kerfs. So, although all the edges do not have the same magnitude of electric field, the outer edges of each square do continue to have a higher intensity than the inner edges.

However, the model with 15 kerfs and a kerf width of 50 μm pictured in Figure 7-22(d) is an exception. The second outermost ring of squares manages to maintain very close electric field intensities as the outermost ring of squares. Looking at the histogram of this model, it also manages to cover a greater area of the top crystal surface at an electric field magnitude of 14.5×10^8 V/m compared to all the other models. This may suggest that machining a pyroelectric crystal into this structure may produce improved results.

Another general trend that can be seen with increasing number of kerfs and kerf widths is more regions of electric fields with low intensities. This is especially accentuated for the model with 20 kerfs with a width of 200 μm since it has very little material remaining. In the histograms, the proportion of electric fields below 5×10^8 V/m, estimated from Figure 7-22 and Figure 7-23, gradually covers a greater area of the top surface. These low magnitudes represent the kerf regions that is void of material. Going across the number of kerfs series, in Figure 7-24(a), the histogram peak is at 8.5×10^8 V/m indicating most of the squares produce this electric field intensity. This magnitude seems to maintain consistently as the peak in Figure 7-24(b) and Figure 7-25(a) until the model reaches 15 kerfs with a kerf width of 150 μm. This indicates a good area of the top crystal surface can still produce the same minimum electric field as the model with no kerfs.

In Figure 7-24(a), the shape of the histograms can be described as having a major peak with small peaks at both extremes. The distribution of the histogram for the models with 5 and 10 kerfs is generally maintained with increasing kerf widths. But for the models with 15 and 20 kerfs, their histograms transition into a bimodal distribution and subsequently into left-skewed when the kerf width broadens to 150 μm and 200 μm. Although the electric field in the kerfs is still above 1.00×10^8 V/m, it could be said that the pyroelectric crystal prepared with these parametric values would not make a significant contribution to the generation of X-rays since there is little pyroelectric material to create a sufficiently intense electric field.

The prepared $LiTaO_3$ crystal that was tested in the X-ray generator had 5 kerfs and kerf width of approximately 170 μm. The output of this crystal can be closely compared to the model with 5 kerfs and kerf width of 150 μm. Its histogram in Figure 7-25(a) shows a peak at 8.50×10^8 V/m and tapering until approximately 13.0×10^8 V/m. Compared to its no-kerfs counterpart, it has slightly greater area of the top crystal surface with electric fields of 8.50×10^8 V/m to 9.50×10^8 V/m before dropping rather quickly. On the other hand, the model with no kerfs has a greater surface area of higher electric field intensities as it has 37.4% of its top crystal surface area above 9.50×10^8 V/m and reaching up to 15.0×10^8 V/m. This dominates over the diced crystal that has 24.5% of its top crystal surface area between 9.50×10^8 V/m and 14.0×10^8 V/m. In Chapter 7.3.2, the

comparison of the total X-ray output showed about a magnitude difference across all pressures between the original and diced crystal. The end-point energy generated by the diced crystal was also 15 keV lower than the original crystal.

The difference in model results agrees rather well with the X-ray generator results. The diced crystal could still achieve a substantial electric field to emit electrons, but it would produce more low energy X-rays and not be able to produce as high energy X-rays as the original crystal. Figure 7-20(b) in Chapter 7.3.2 demonstrates this as the normalised X-ray spectra of the diced crystal is higher at energies below 8 keV but its end-point energy drops out earlier than the original crystal. Since it has similar area proportion of electric fields between 8.50×10^8 V/m and 9.50×10^8 V/m, the nickel and tantalum lines from the normalised X-ray spectra of both original and diced crystal would also be very close. The reasoning mentioned in Chapter 7.3.2 where the surface area reduction resulting in less electrons emitted also still stands. Therefore, it is the combination of less material available to provide electrons and less area of the top crystal surface with high electric field that produces less total X-ray counts and of lower X-ray energies.

In Chapter 2, the various approaches to improve the X-ray generator's performance were described. Some of these approaches included introducing additional pyroelectric crystals or low work-function materials in the shape of a tip or cone. Those methods saw an increase in both the X-ray counts and end-point, and in the case of adding carbon nanotubes, extended the longevity of the X-ray generator. The purpose of increasing the number of edges was to increase the area of enhanced electric field regions, and thereby, increase X-ray output. As gathered from the earlier discussions, dicing the crystal to increase the number of edges produced poorer results compared to its non-diced counterpart.

A notable difference between the diced crystal and the other approaches is the surface area is not reduced. Although there are other system parameters that differs with the settings applied in this experiment, this reinforces that a crystal of sufficient surface area is still necessary to provide a considerable net surface charge as it is thermally cycled. The electric field can instead be enhanced by adding another material of small radius curvature rather than modifying the shape of the crystal.

This page is intentionally left blank.

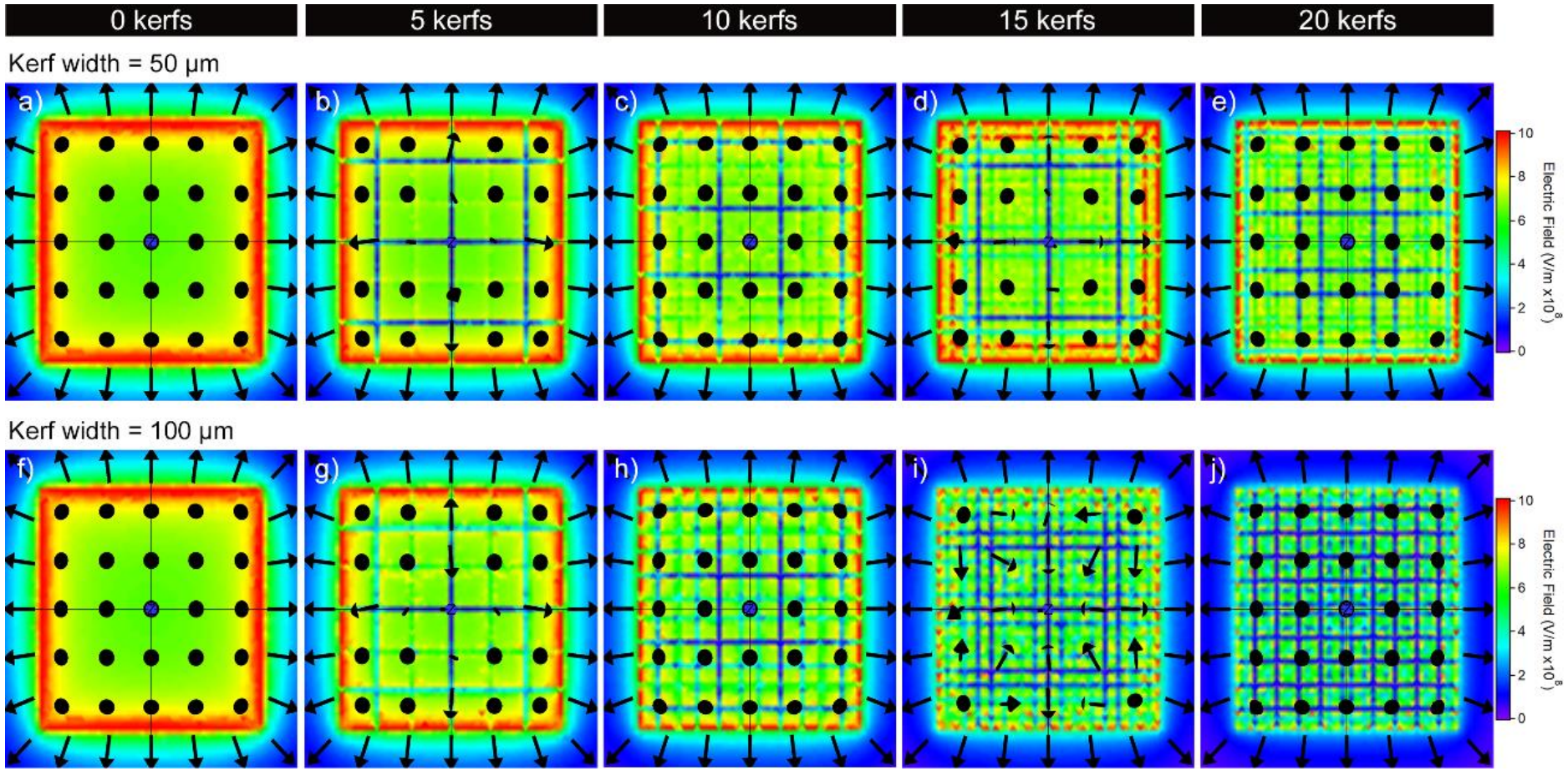

Figure 7-22 Electric field distribution of the top crystal surface with varying number of kerfs and kerf widths. The top and bottom horizontal series show kerf widths of 50 µm and 100 µm, respectively. The figure continues onto Figure 7-23.

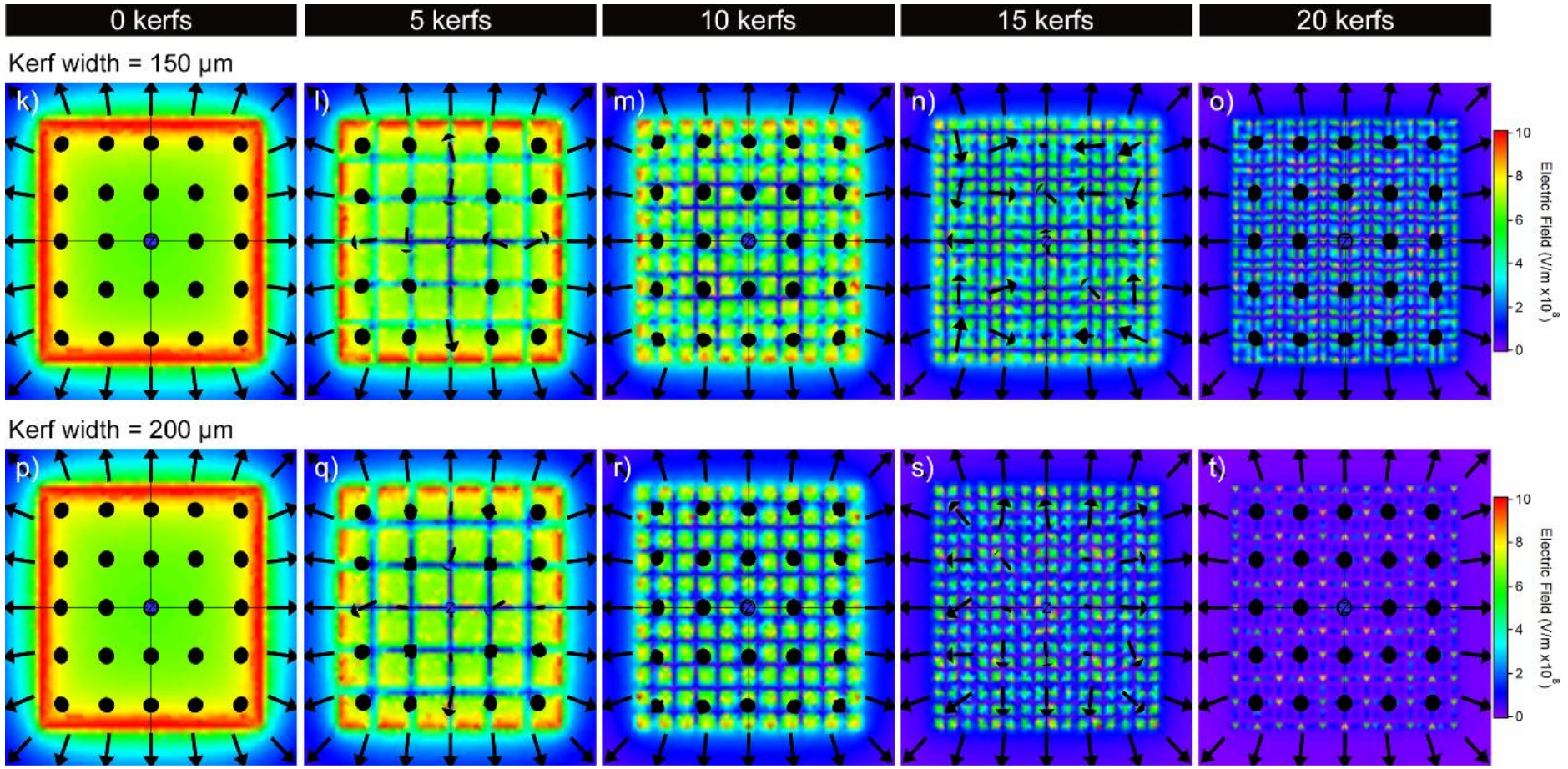

Figure 7-23 Electric field distribution of the top crystal surface with the number of kerfs and kerf width parameterised. This figure is a continuation from Figure 7-22. The top and bottom horizontal series show kerf widths of 150 µm and 200 µm, respectively.

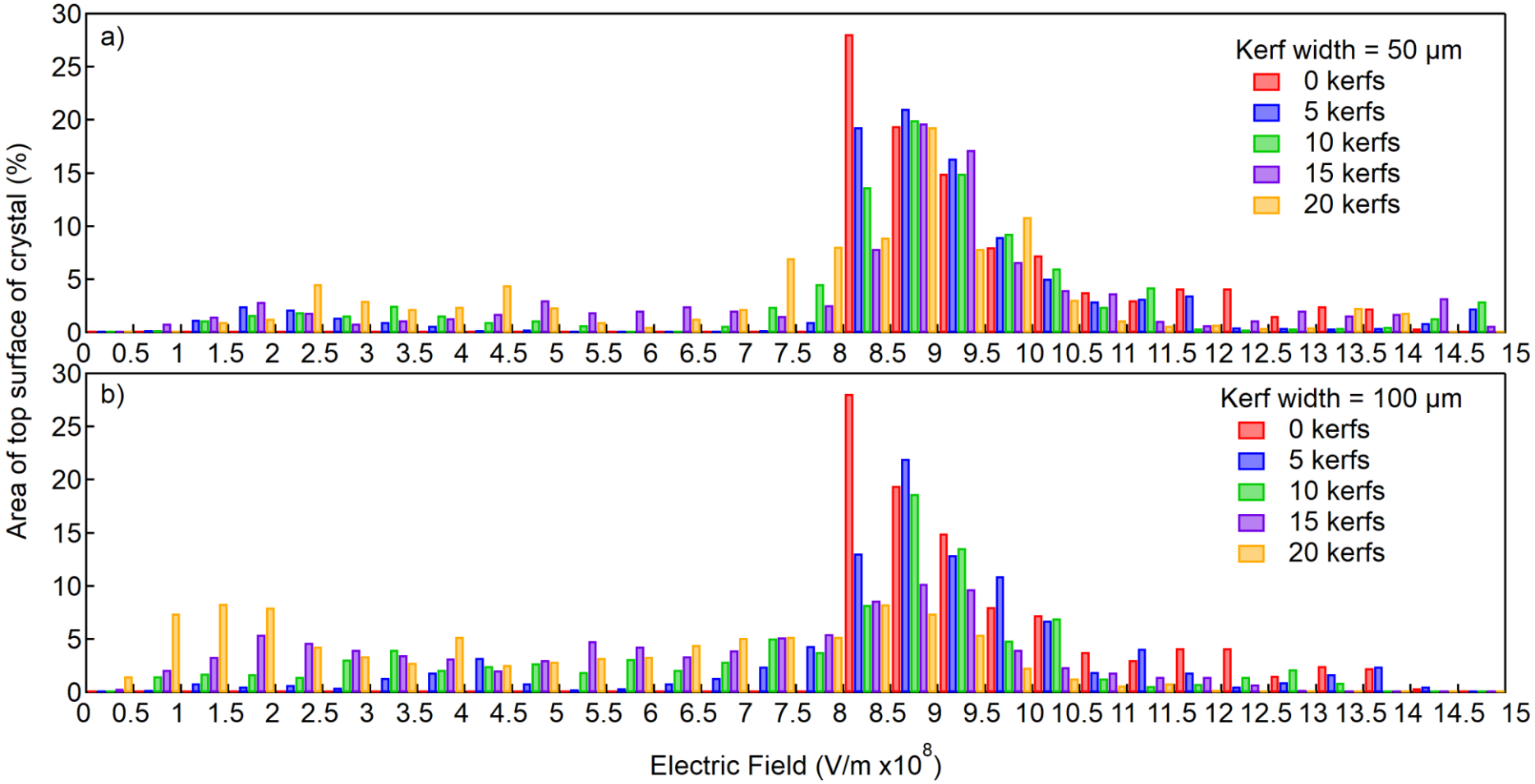

Figure 7-24 Histogram of the electric field distribution at the top crystal surface. (a) correlates to Figure 7-22 (a – e) series and (b) correlates to Figure 7-22 (f – j) series.

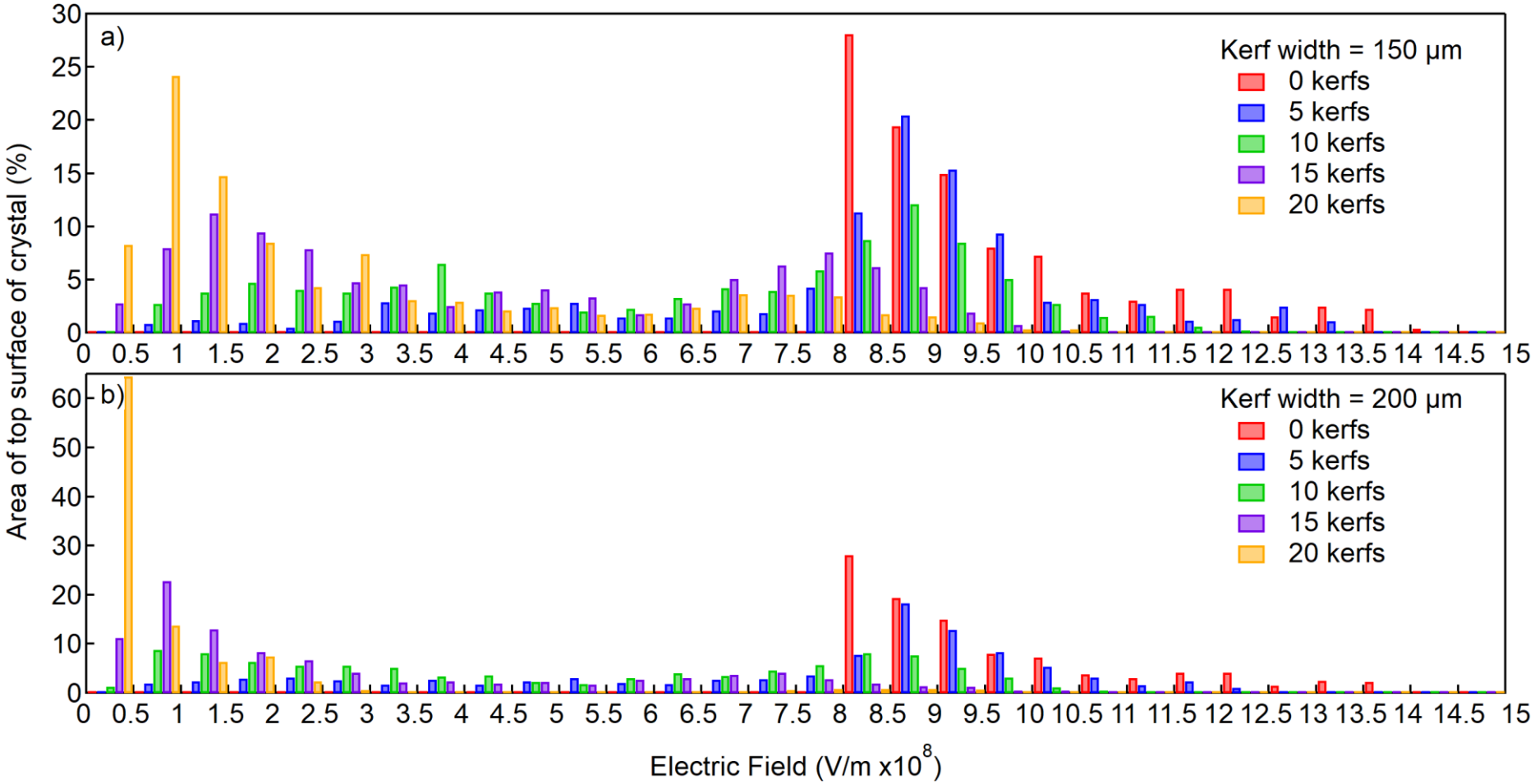

Figure 7-25 Histogram of the electric field distribution produced at the top crystal surface. (c) correlates to Figure 7-23 (k – o) series and (d) correlates to Figure 7-23 (p – t) series.

This page is intentionally left blank.

8

FATIGUE TEST OF THE X-RAY GENERATOR

"Life is a like a box of chocolates. You never know what you're gonna get."

– *Forrest Gump*

8.1 Overview

In the development of the X-ray generator using the pyroelectric effect, several studies had been undertaken to optimise the design to maximise X-ray flux and end-point energy. One important characteristic not yet measured is how the X-ray output varies over a longer time period. Undertaking a fatigue test is a necessary step to assess the X-ray generator's suitability for potential applications, particularly in ones where it would be required to operate over an extended period of time. In addition to taking continuous measurements, the state of the pyroelectric crystal is also characterised.

8.2 Experimental Methodology

Fatigue tests were conducted to determine the pyroelectric X-ray generator's performance over continuous thermal cycles. Amptek Inc. specifies that the lifetime of the commercial Cool-X under continuous use is "approximately 200 hours" [14]. The results that were of interest were the X-ray counts, end-point energy and state of the -Z exposed crystal surface. The fatigue characterisation was performed over a series of long-running measurements, each lasting up to 24 h with an energy spectrum collected every hour. Over 200 h of measurements was accumulated to closely match Amptek Inc.'s specified lifetime under continuous use.

These measurements were largely unattended, that is no experimenters present, so reliable synchronisation between the thermal cycling and data acquisition was important. The following procedure was introduced to ensure each 24 h experiment ran to completion. To set up the data acquisition for this experiment, the module in Amptek Inc.'s digital pulse processor (DP5) called "Repeat Measurements" was be used. A delay of 60 s between hourly measurements was used to facilitate synchronisation between the temperature control Arduino and the X-ray detection software. The delays were also used to ensure that the starting crystal temperature was consistent between measurement cycles. The Arduino held the temperature at a constant 21°C between measurements.

The automated control of the thermal cycling and data acquisition was upgraded from ExtraPuTTY to another external operating program. It was created such that it was able to log the same data as the ExtraPuTTY but also track each X-ray spectrum measurement. The Arduino code was updated to Version 12 (Appendix F). The operating program was written in Igor Pro (Version 7.0.8.1, Wavemetrics, Inc., Oregon, U.S.A.) and used its extension, VDT2, to communicate to the Arduino via serial communication. The operating program code can be found in Appendix G. VDT2 works in a similar way to PuTTY but can also perform additional controls in conjunction to acting as a terminal.

Upon establishing the automatic experimental system, some issues were encountered. They included disconnection of the serial communication between the computer and instruments, and de-synchronisation of the thermal cycling and collection of X-ray spectra. This led to some discrepancies that meant the results gathered were not fully representative of the intended measurements. Some of the inconsistencies were:

- Not all 24 h series of measurements ran for the full duration,
- Loss of data as thermal cycling of the crystal continued to operate when the data acquisition system and X-ray spectrometer were not collecting, and
- Collection of data when the thermal cycling paused between hourly measurements

In terms of setting up the configuration of fatigue tests, the crystal, $LiTaO_3$, with a thickness of 2.0 mm was selected, and a gap distance of 3.7 mm and pressure of 0.33 Pa were applied. This combination of parameters was chosen, because as calculated in sub-chapter 3.4.5, it was predicted to have the highest figure-of-merit. The crystal was mounted in a similar manner as mentioned in Chapter 5.

After each 24 h measurement, the crystal was removed and inspected under an optical microscope (Eclipse ME600L, Nikon Corporation, Tokyo, Japan). The crystal was removed carefully with small amounts of acetone, so as not to damage other electrical components. The crystal was then cleaned with acetone, followed by ethanol in an ultrasonic bath for 5 min each.

At the conclusion of the fatigue characterisation of the X-ray generator, the crystal was inspected under a confocal laser scanning microscope (VK-X200 microscope unit with VK-X250K control unit, Keyence Corporation, IL, U.S.A.). Profile measurements were undertaken to further investigate the features apparent on the crystal brought about from the X-ray generation process.

8.3 Results and Discussion

8.3.1 X-ray intensity

A fatigue test was undertaken to monitor how the X-ray generator performs over prolonged periods of time. Each alphabet-labelled measurement in Figure 8-1 consists of a continuous measurement lasting up to 24 h. A total of 213 h of operation was accumulated. In each fatigue measurement conducted, there appears to be a maximum achieved within the first 5 hourly experimental run before experiencing a decline in the total X-ray counts. Comparing the average between each fatigue measurement, there is no clear trend as the total counts dip between D to H before increasing again in I and J, before subsequently falling again.

The X-ray end-point energy also fluctuates throughout the entire test, as seen in Figure 8-1. However, the fluctuation between each hourly measurement is not as significant as the total X-ray counts. The end-point energy across the entire test generally straddles at an average of 36.92 ± 3.55 keV. There is some correlation of the end-point energy with total X-ray counts, especially at events where there is a large drop in X-ray counts. This can be seen in the comparison between experimental runs, A–4 and C–16.

The experimental run, A–4, produced the highest total X-ray counts of 34.3×10^6 and achieved an end-point energy of approximately 40.2 keV, as indicated in Figure 8-2. This is far better than experimental run, C–16, which only produced 0.179×10^6 counts and had an end-point energy of approximately 24.1 keV.

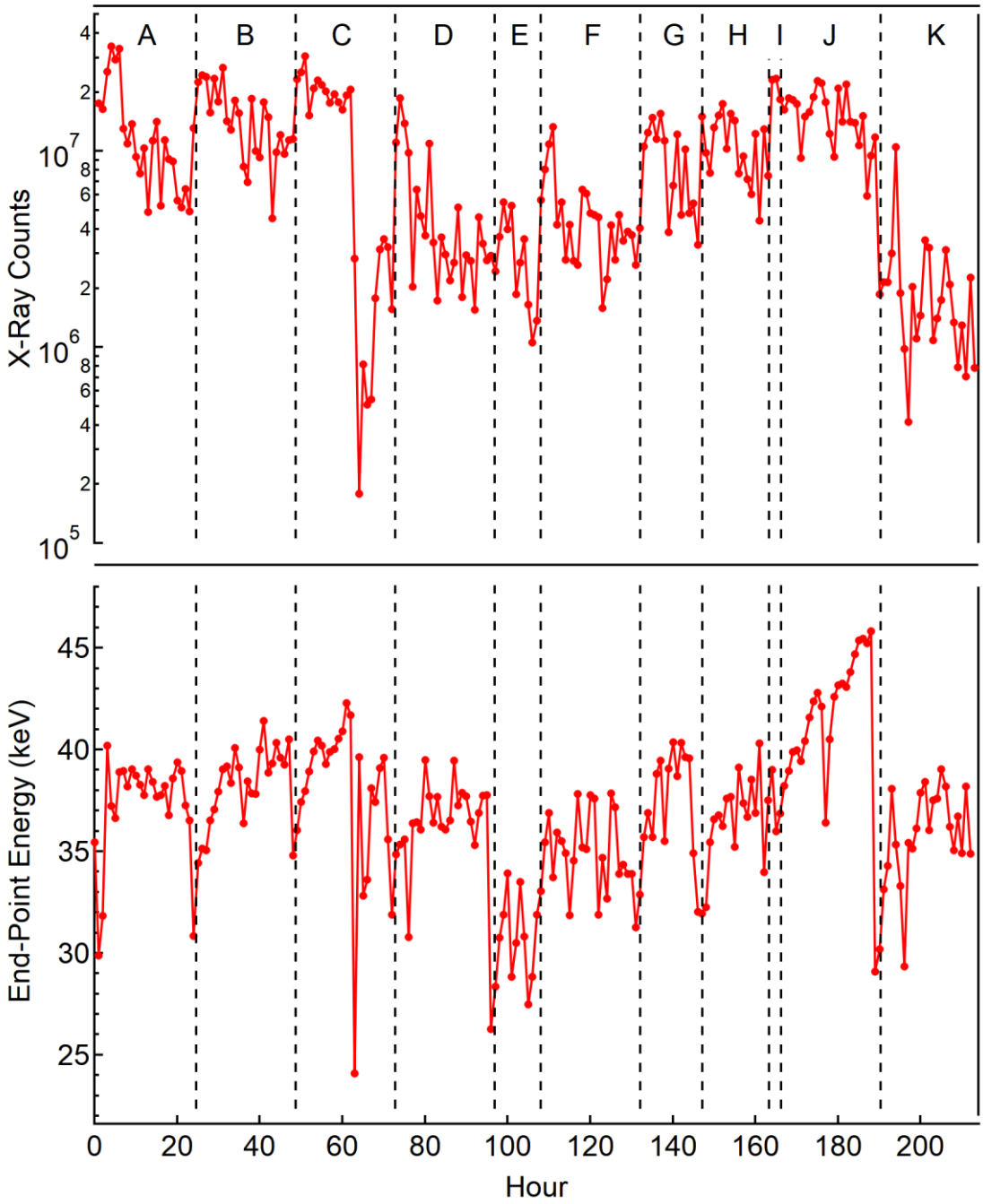

Figure 8-1 Total X-ray counts and end-point energy collected for each individual hourly experimental run indicated by the marker. The dotted lines represent the break between each fatigue measurement.

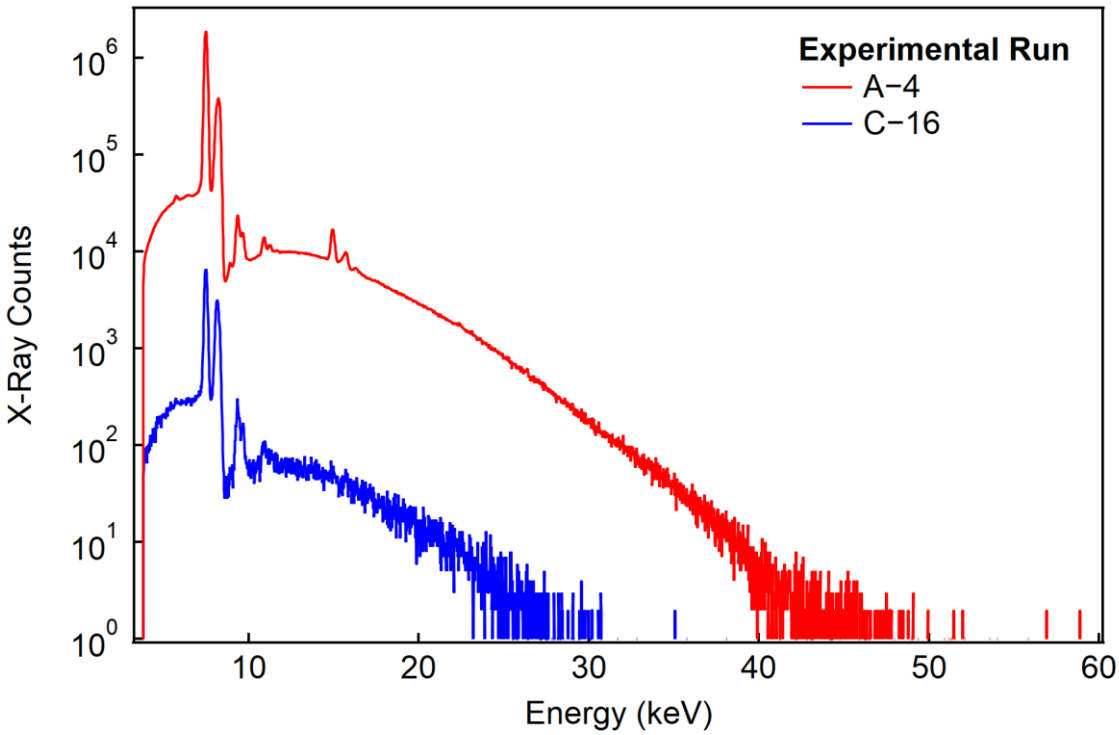

Figure 8-2 Energy spectra of the experimental run corresponding to the highest (A-4) and lowest (C-16) total X-ray counts.

It has been previously commented before of the inconsistency and difficulty to accurately compare the output from each measurement conducted. When the pyroelectric crystal is thermally cycled, the rise of the surface charges is compensated by the electron emission current produced via ferroelectric electron emission during the heating phase and via field ionisation during the cooling phase and the bulk conductivity of the material, introduced in Chapter 3. Although the surface charge screening by the bulk material is not a significant factor, the total X-ray counts does begin to deplete with more measurements because of the bulk charge screening effect continuing to take place and the bulk charges become more mobile [60]. It has been suggested that better consistency in the X-ray production can be obtained by allowing the experimental setup to relax at either atmospheric pressure or in vacuum [19, 82]. However, using this method in an application setting is not economical and is time-consuming.

While the bulk charge screening effect accounts for the reduction in counts over each 24 h measurement, Figure 8-3 shows variation in the count rate over each thermal cycle. It is ideally desired that the profile of the count rate is uniform over the heating and cooling phases for consistency and reliability. However, in reality as depicted in Figure 8-3, it is clear that this is not the case. This has also been shown at the beginning

of Chapter 5 that the X-ray energy spectrum from the heating and cooling phases are different. In X-ray tubes, increasing the accelerating voltage across the tube will extend the X-ray end-point energy and heighten the intensity, while increasing the beam current will only heighten the intensity. So, in the pyroelectric X-ray generator, this variation in count rate indicates that there is instability in electron emission current and acceleration of electrons across the gap. As it was shown in Chapter 5.3.3 that the count rate affects the end-point energy, the inconsistent X-ray energy can subsequently create issues in X-ray spectrometry applications.

As introduced in Chapter 2, fluorescence yield, or the number of characteristic photon emissions, is dependent on the effect of X-ray absorption and photoelectricity. All elements have an atomic cross section, which consists of X-ray absorption edges. The energy dependence of the atomic cross section is proportional to the probability of fluorescence photon emission [219, 221]. That is, if the end-point energy in one measurement is smaller or larger than in another, the relative intensity of the characteristic lines will not be consistent across repeated measurements. Although the standard deviation of the end-point energy across all the hourly measurements is 3.55 keV, it should be reminded that the end-point energy also varies with the profile of the thermal cycle, as shown in Chapter 6.3.3. Therefore, if the excitation energy is unstable, this can cause difficulties in quantitative measurements such as in X-ray fluorescence analysis.

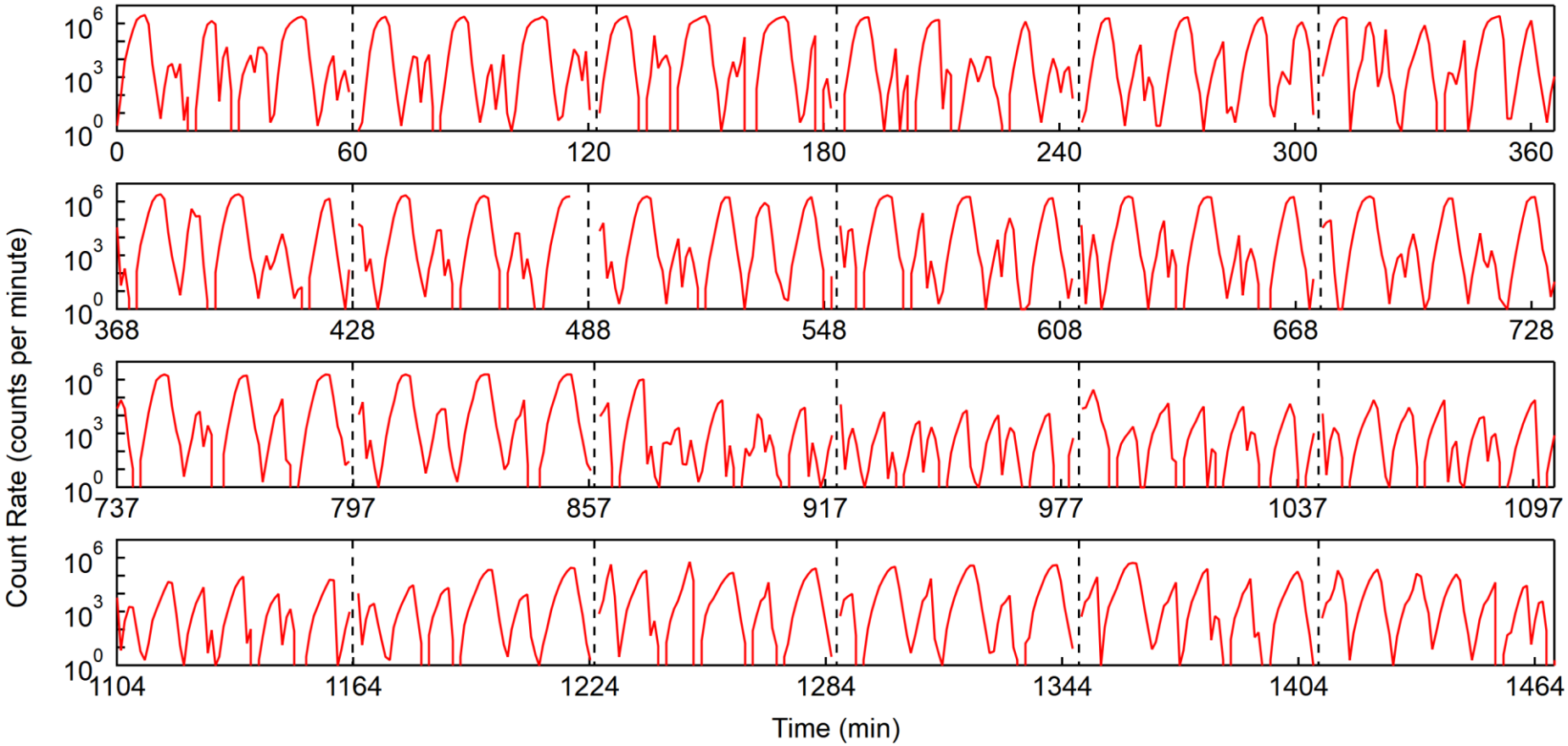

Figure 8-3 Counts produced per minute over one 24 h measurement. It correlates to the third measurement labelled C in Figure 8-1. The dotted vertical lines represent the break between each hourly X-ray spectrum acquisition. The thermal cycle always starts with a heating phase and each hourly measurement goes through three thermal cycles.

8.3.2 Optical micrographs of the crystal surface

A series of micrographs were taken after each fatigue measurement on the optical microscope and combined via a blending technique in Adobe® Photoshop® (Adobe Systems Inc.). Each micrograph square in Figure 8-4 corresponds to each fatigue measurement in Figure 8-1. In these micrographs, there are dark lines that run vertically and diagonally. The number and intensity of these dark lines increases with each progression of fatigue measurement taken. At higher magnification, shown in Figure 8-5, Figure 8-6 and Figure 8-7, many dark spots and finer fern-like lines can be seen.

Interestingly, the fern-like lines intersect each other at an average of 59.98°. After fatigue measurement C, a crack initiating at the corner of the crystal also propagated at the same distinct angles, as magnified in Figure 8-8. Similar observations have been made in other pyroelectric X-ray generation and electron emission investigations. Bourim *et al.* [19] noticed the hexagonal patterns on congruent $LiNbO_3$, however, they were on the +Z surface and this exposed surface was etched. This could mean the phenomena can occur regardless of the polarity of the exposed surface but also makes it uncertain as to whether the patterns existed before the etching procedure. In another additional work, Bourim *et al.* [222] reported tree-like features impacted on E-beam resist from the -Z surface when the electron emission of congruent $LiNbO_3$ was tested.

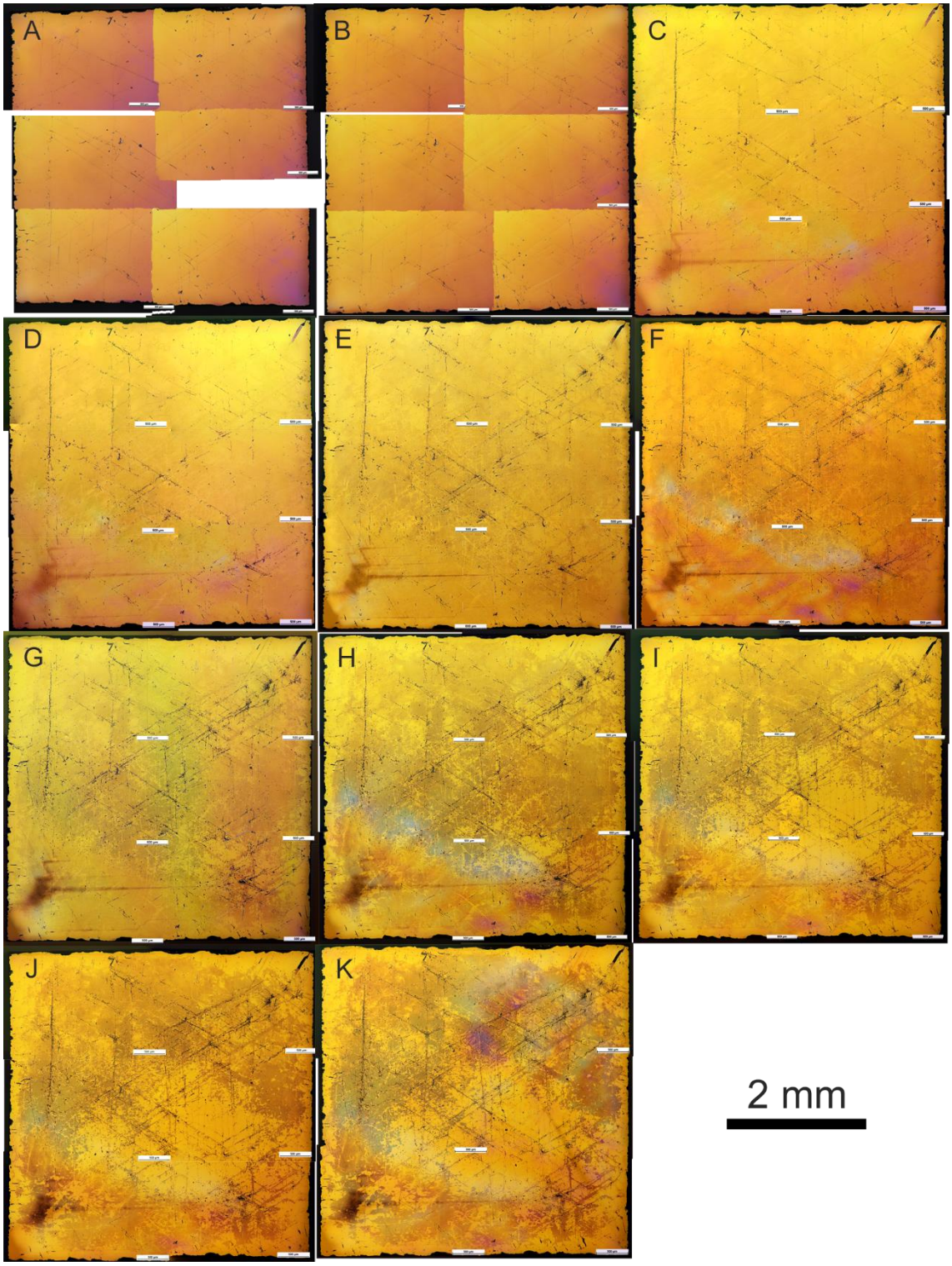

Figure 8-4 Optical micrographs of the electron emitting crystal surface collected after each fatigue measurement. Each labelled image correlates to Figure 8-1 and is a blend of smaller micrograph sections.

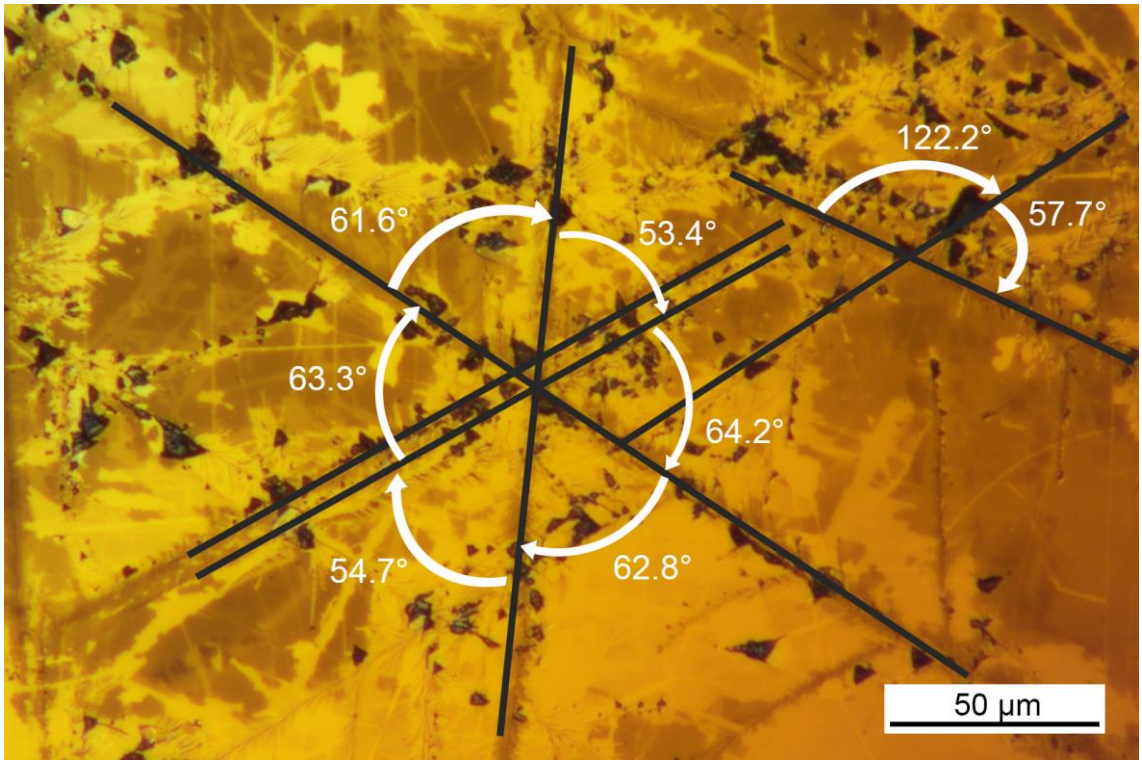

Figure 8-5 Degradation marks on the -Z surface of the crystal.

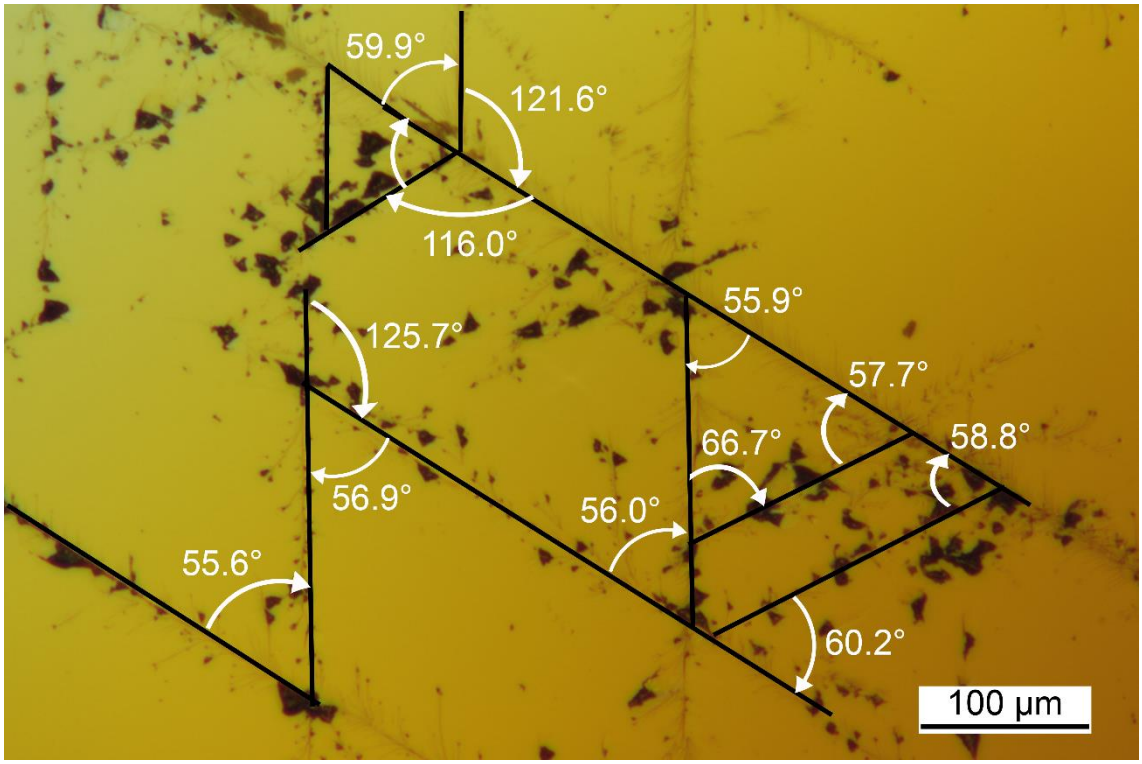

Figure 8-6 Degradation marks on the -Z surface of the crystal with fern-like lines.

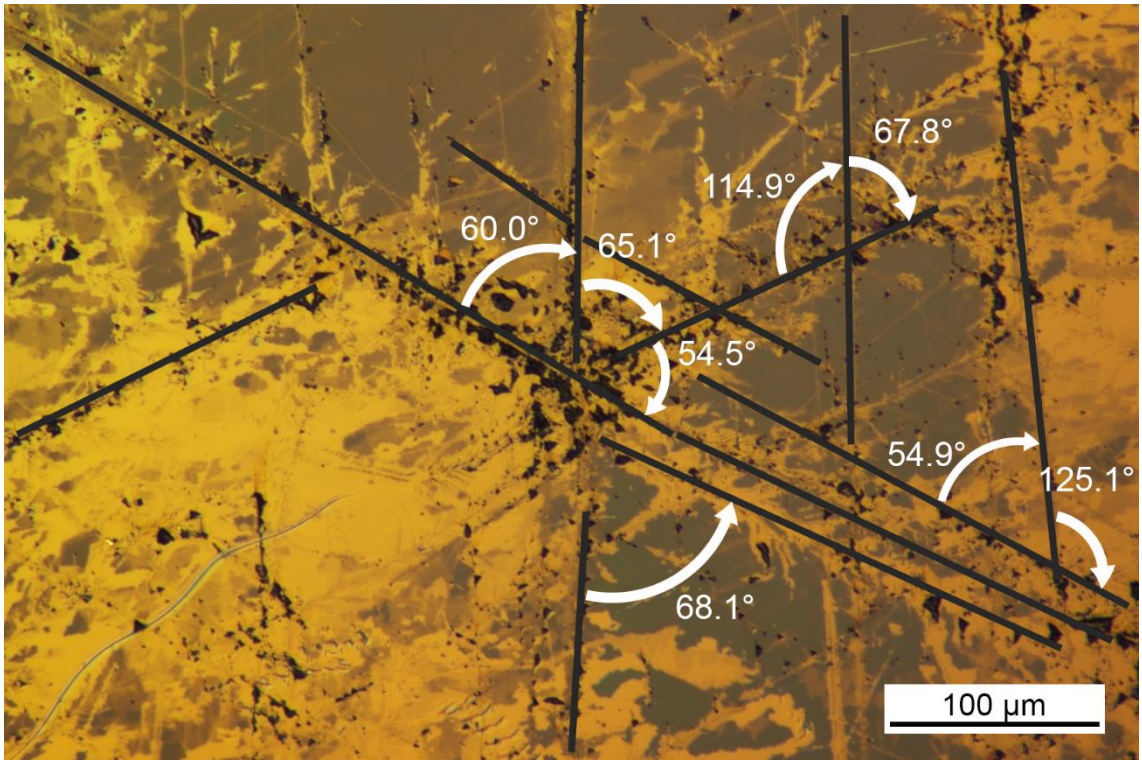

Figure 8-7 Degradation marks on the -Z surface of the crystal with dark defect spots around the degradation lines.

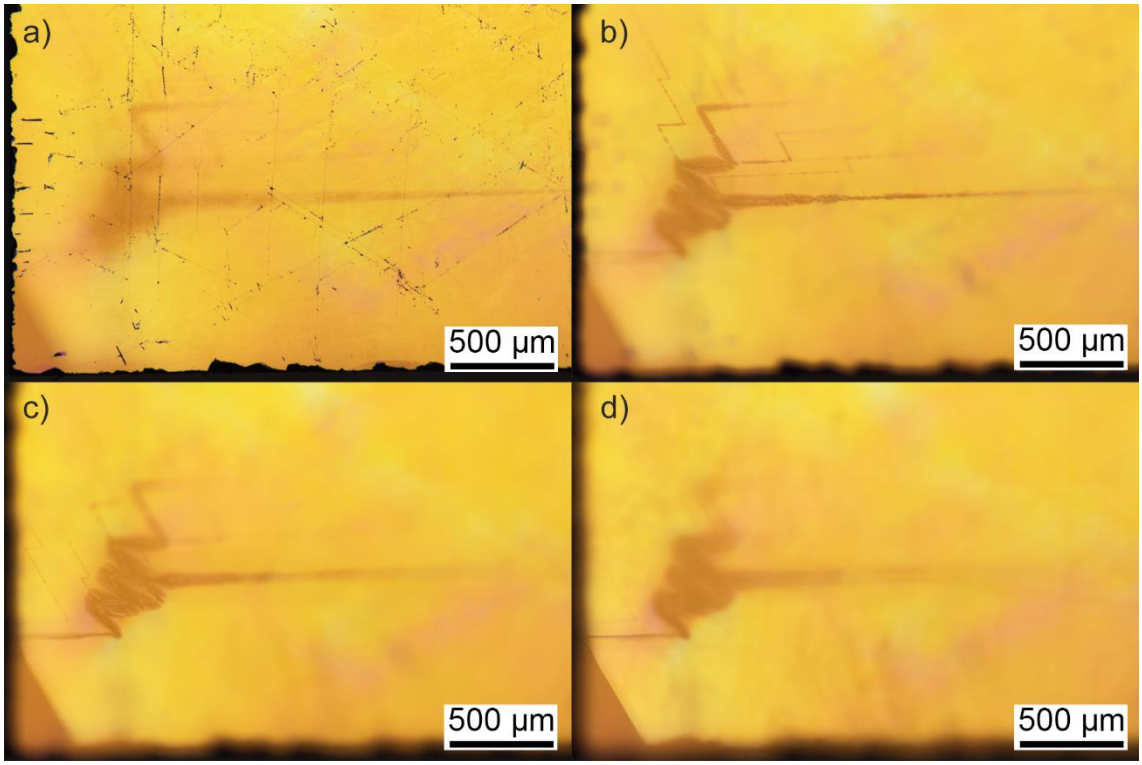

Figure 8-8 Crack propagating from a chipped corner and travelling at an angle through the thickness of the crystal.

Damage in crystal structures, such as by fracture, can occur along well-defined lattice planes known as cleavage planes. These planes in $LiTaO_3$ are $(1\bar{1}02)$, $(\bar{1}012)$ and $(01\bar{1}2)$, where the bonds between the lithium and tantalum atoms are weak [223]. By determining the angle between pairs of the three known planes, they were found to be 56.79°, 56.79° and 36.87°. Based on the findings observed in the micrographs, it is unlikely for there to be ~36° formations. Therefore, the degradation apparent on the crystal surface may not occur along the cleavage planes.

The consistency of these line formations may be related to the crystal symmetry of $LiTaO_3$. This crystal is typically described as having a hexagonal lattice structure, however, this structure belongs under the trigonal system and can be represented with a rhombohedral lattice structure. The relationship between the hexagonal and rhombohedral structure was explored in Chapter 2.3.2. Therefore, if the spontaneous polarisation was along the Z-axis [001] direction in the hexagonal structure, it would be equivalent to the pseudo-cubic [111] direction.

A stereographic projection can be utilised to locate the possible planes giving rise to these formations. It is a projection of a point normal to a crystal face onto a spherical space and represented on a 2D equatorial plane, as exemplified in Figure 8-9. It is beneficial in viewing the angles between crystallographic planes. Looking at Figure 8-10, by using the projection normal to the (111) face such that it is equivalent to a rhombohedral structure in a pseudo-cubic system, one possibility that creates the same geometric pattern is the family of <110> planes. This would suggest that the fern-like tracks tend to preferentially travel in the <110> crystallographic direction.

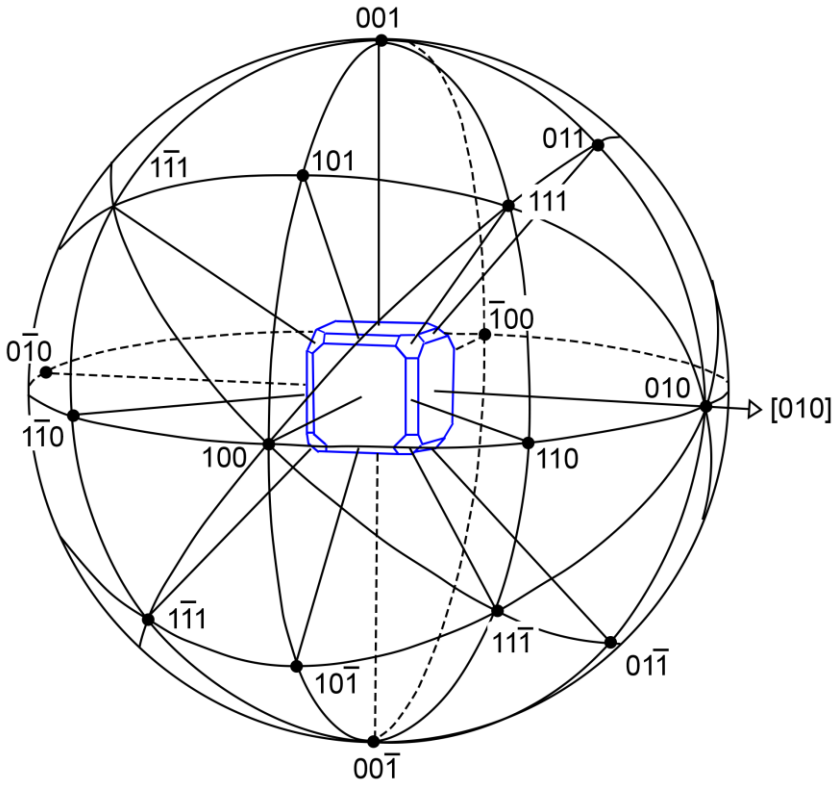

Figure 8-9 Spherical projection of points normal to crystal faces. Reproduced with permission by John Wiley and Sons from [224].

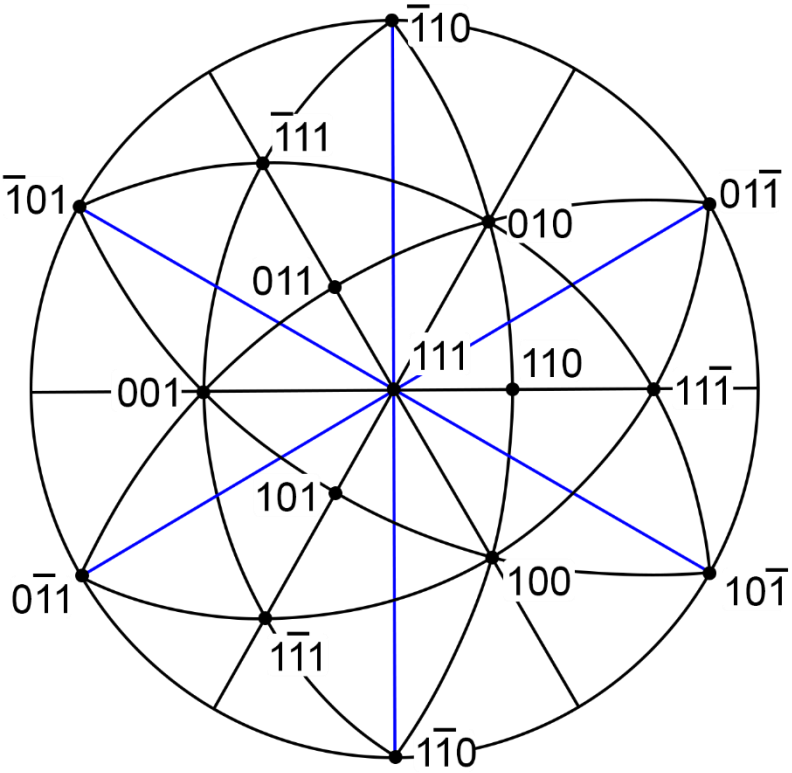

Figure 8-10 Stereographic projection of hkl planes for a cubic crystal perpendicular to the (111) face with the <$\bar{1}$10> family of planes highlighted. Reproduced with permission by Springer Nature from [225].

8.3.3 Confocal laser scanning micrographs of the surface

Confocal laser scanning (CLS) microscopy is utilised to measure the profile of the crystal surface and to validate if the features are domain-related or surface degradation.

The features seen in the optical micrographs only occurred after using the crystal in the X-ray generator as a fresh crystal pictured in Figure 8-11 shows a uniform and clean surface. This is unlike the other CLS micrographs shown later (Figure 8-12, Figure 8-15 and Figure 8-17) which exhibit greater clarity to the features seen in the optical micrographs. The dotted black line in the profile measurements is a linear approximation of the crystal surface. The gradient was set to zero and its approximation was estimated with manually-selected bounds.

The profile measurements presented confirm the features that are characteristic of surface erosion, displaying areas of roughness and material loss. Like in the optical micrographs, two distinct features are observed with greater clarity from the CLS microscope. The first are tree-like tracks travelling in straight lines and the second are irregular shaped craters. It is difficult to discern if the fern-like tracks create pits or bumps. However, based on the magenta profile in Figure 8-14 that crosses over part of the track, it is certain that the tracks cause roughness that is $<1\ \mu m$.

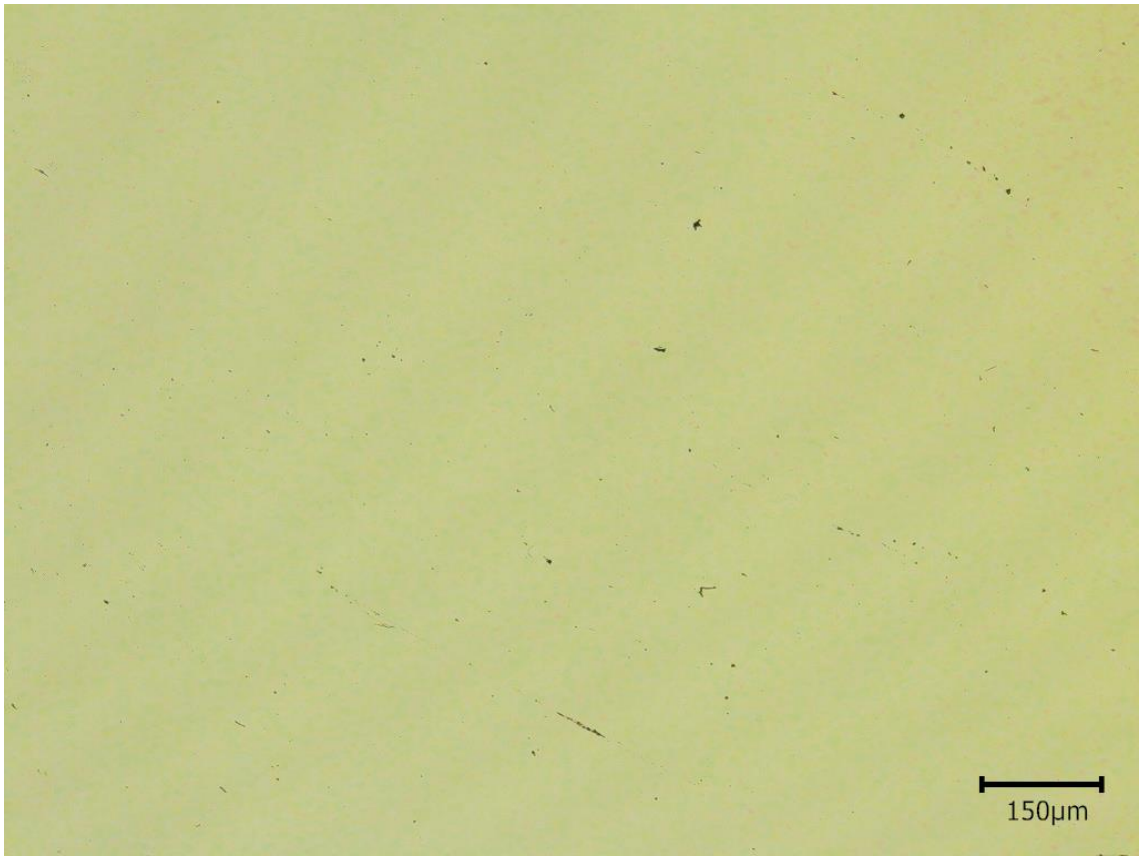

Figure 8-11 CLS micrograph of a fresh $LiTaO_3$ crystal.

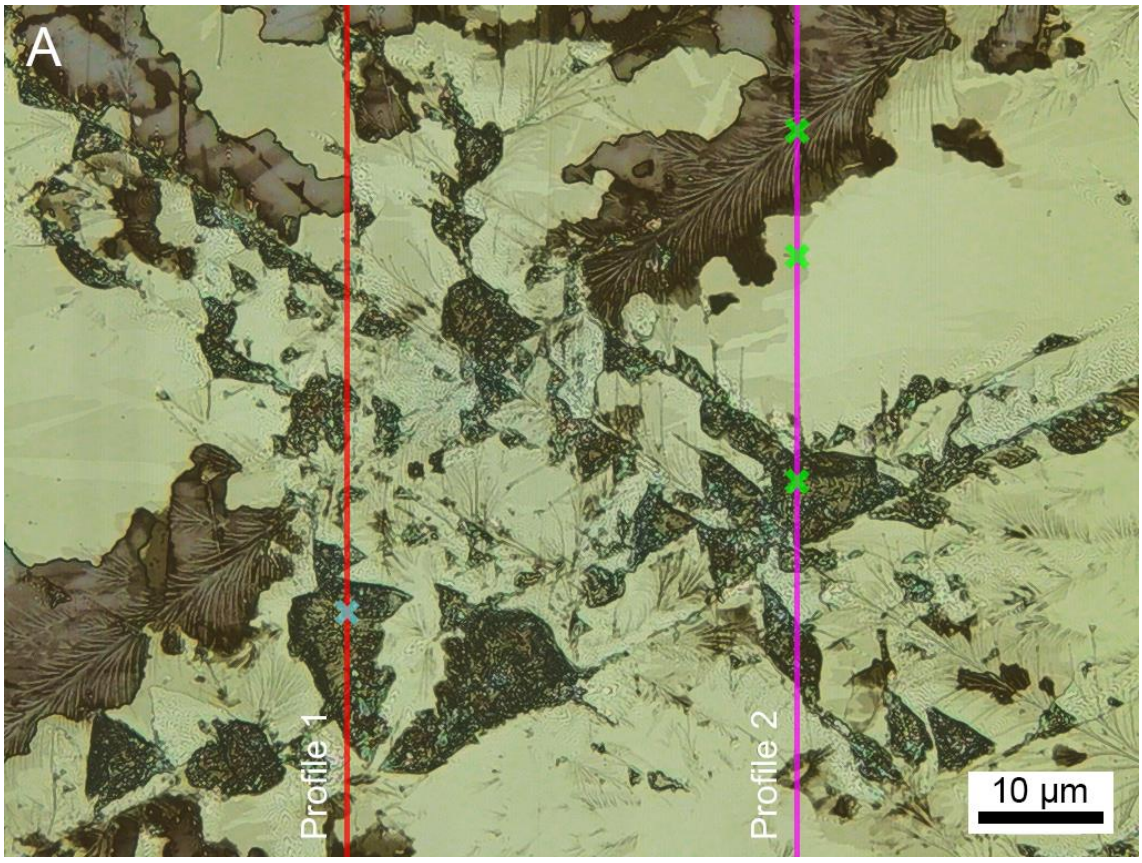

Figure 8-12 CLS micrograph A with two lined profiles.

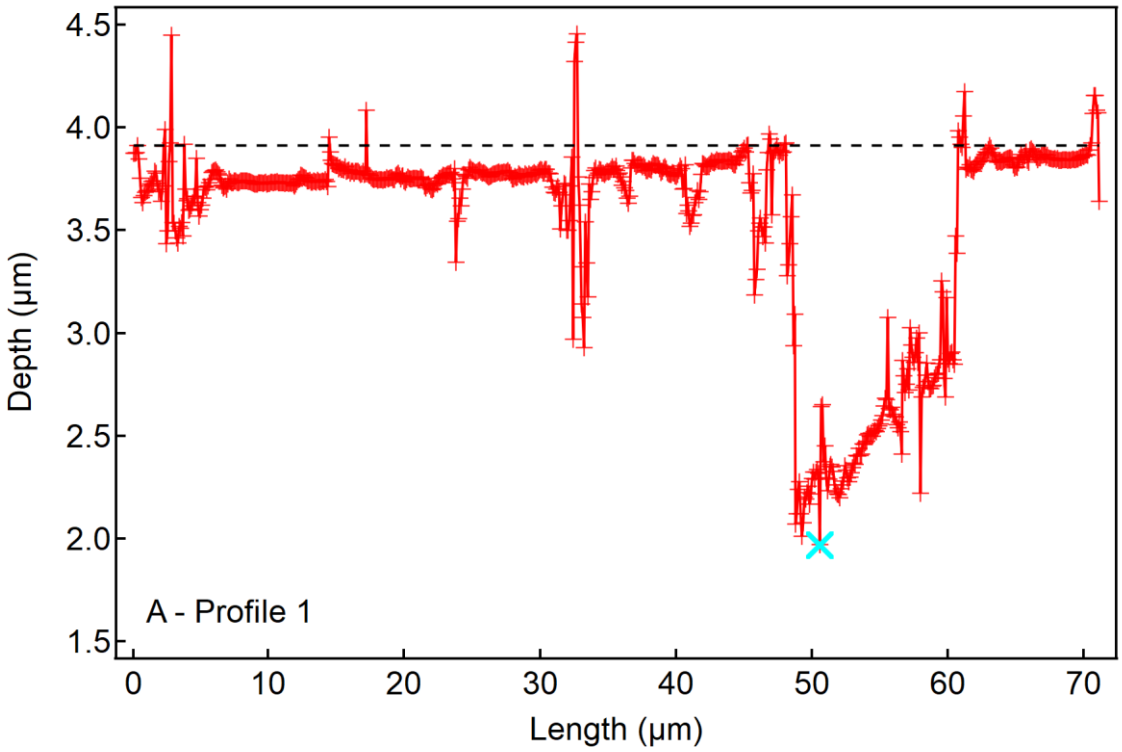

Figure 8-13 Profile measurement corresponding to Profile 1 drawn in red in Figure 8-12. The blue cross is the deepest part from the surface (dotted line).

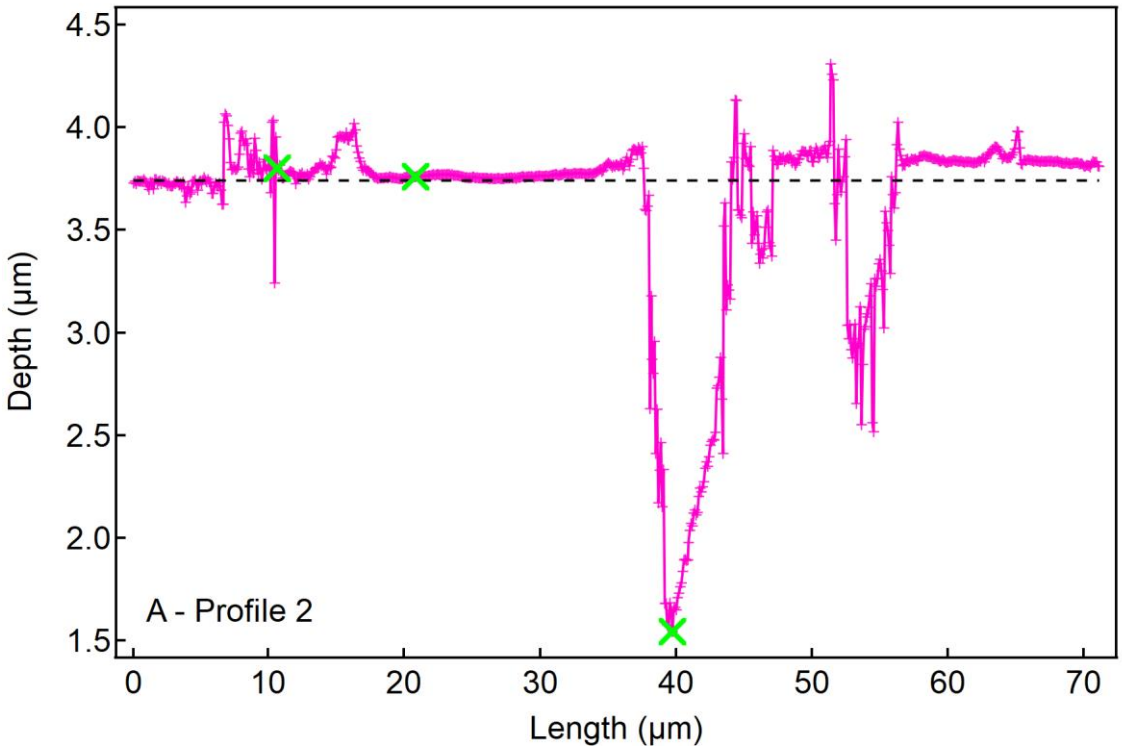

Figure 8-14 Profile measurement corresponding to Profile 2 drawn in magenta in Figure 8-12. The left green cross lies over the stem of the tracking. The green cross on the right lies on the deepest part of the profile from the surface (dotted line).

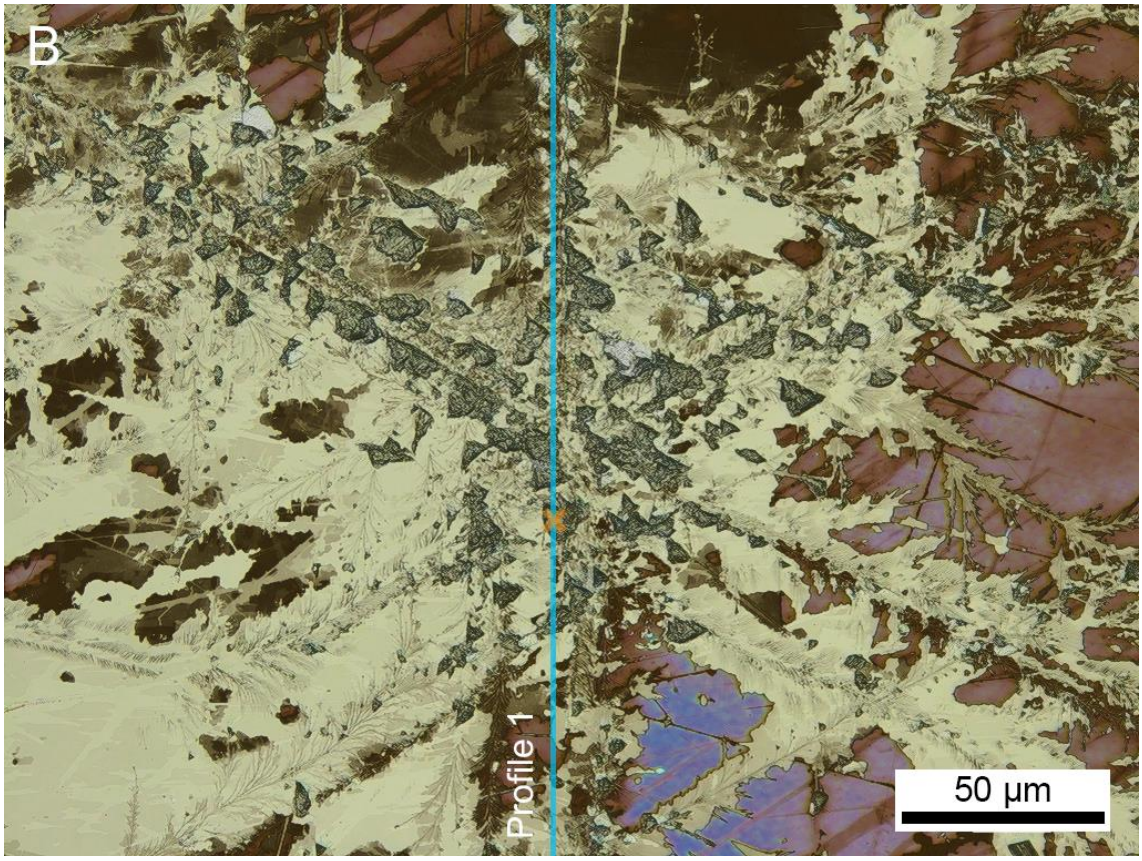

Figure 8-15 CLS micrograph B taken in the same area as Figure 8-7.

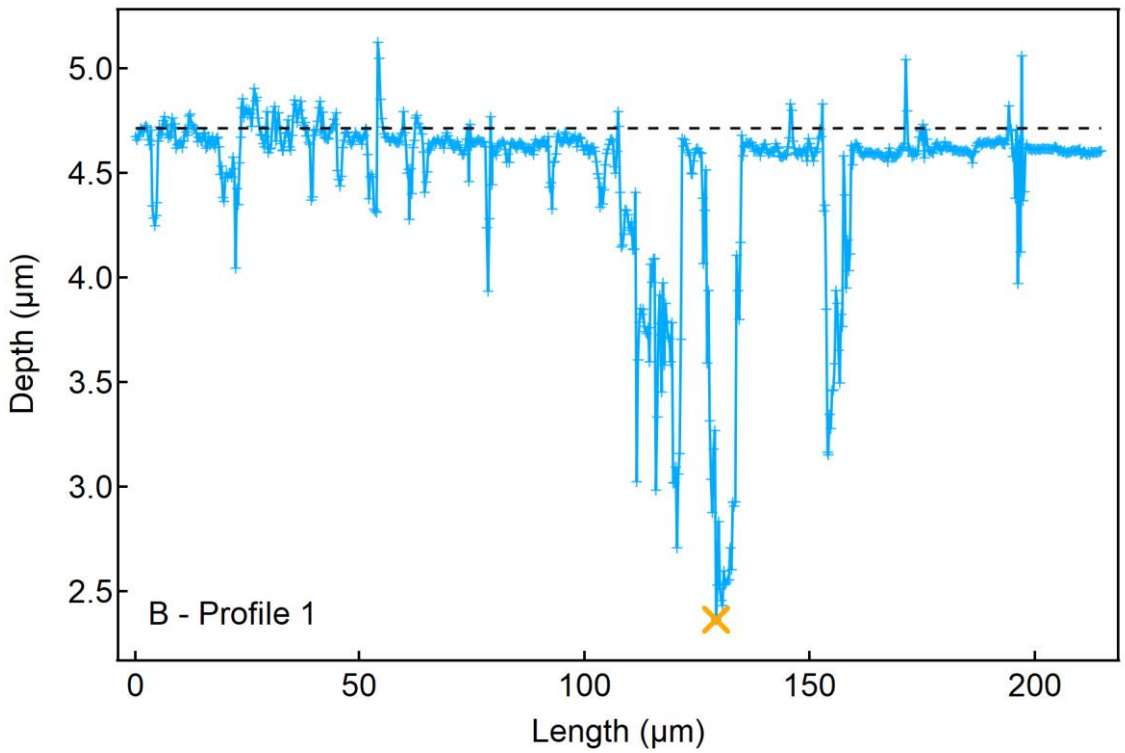

Figure 8-16 Profile measurement of Profile 1 in CLS micrograph B. The yellow cross is the deepest part of the feature from the surface (dotted line).

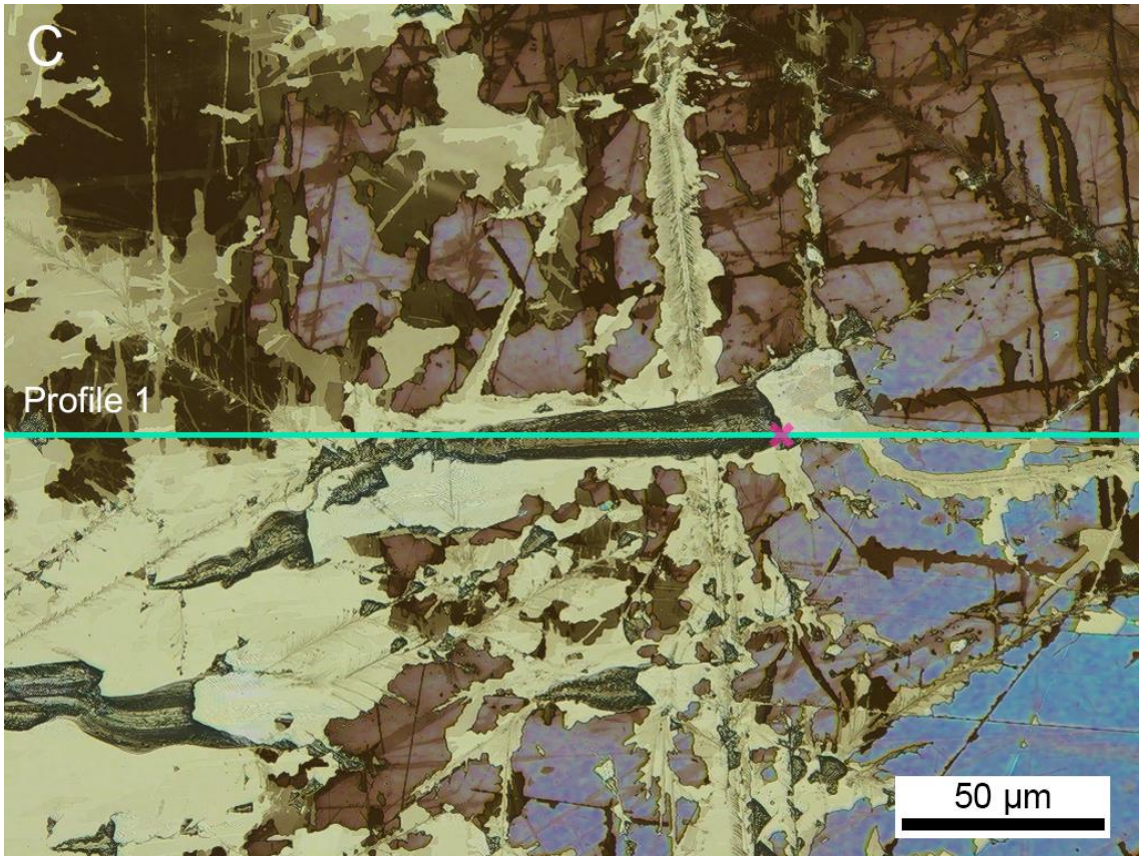

Figure 8-17 CLS micrograph C with a profile line crossing the deepest section of the crater.

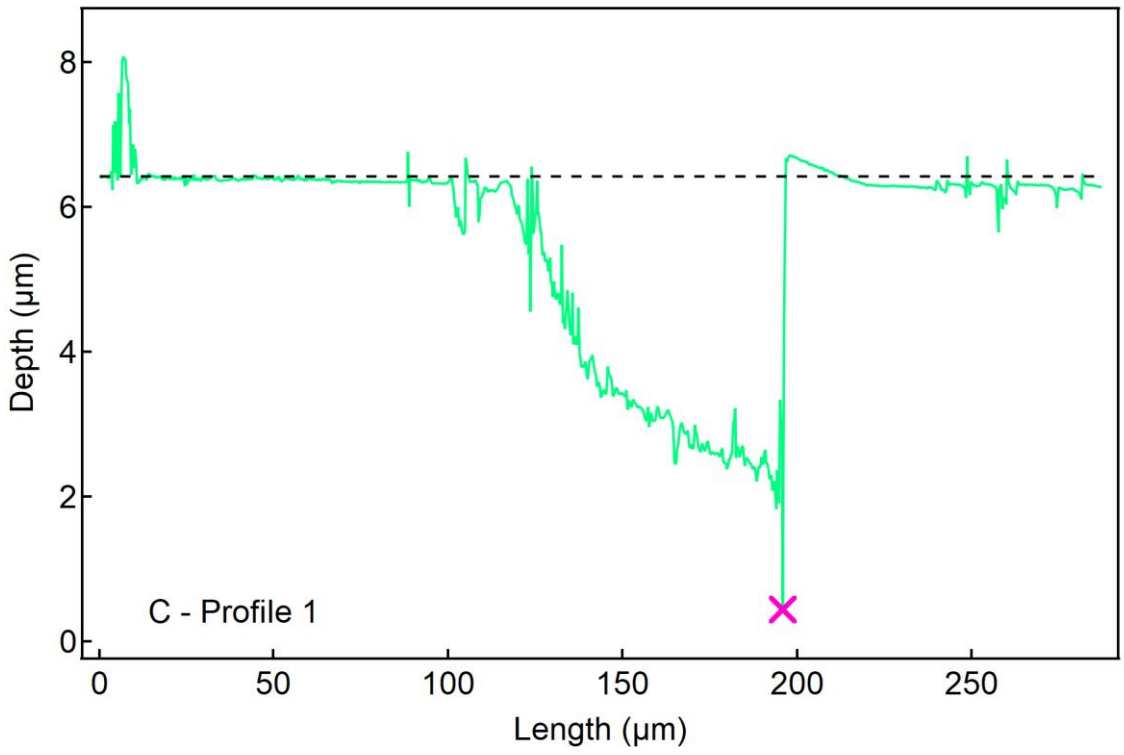

Figure 8-18 Profile measurement corresponding to micrograph C.

The fern-like tracks could also be related to light emission that has been observed in previous studies. The light emission here will be termed as a spark and is seen on the crystal, not from a fluorescence screen. Andrianov *et al.* [226], Naito *et al.* [17] and Ohira *et al.* [227] both captured moments of bright sparks running along the crystal surfaces. Andrianov *et al.* [226] referred to these sparks as electrical breakdowns and causing "scratch-caverns" on the crystal surface. Naito *et al.* [17] found that sparks could be emitted during both heating and cooling phases and appeared to occur either along the crystal surface or at corners. Ohira *et al.* [227] instead describes it as surface creeping discharge but observes the same scratches. Under the naked eye, the fern-like tracks also appear to look like scratches, shown in Figure 8-19. Ohira *et al.* [227] makes a further observation of different coloured luminescence produced along the surfaces of the crystal as it is cooling. It is suspected that the different colours could originate from different discharge processes.

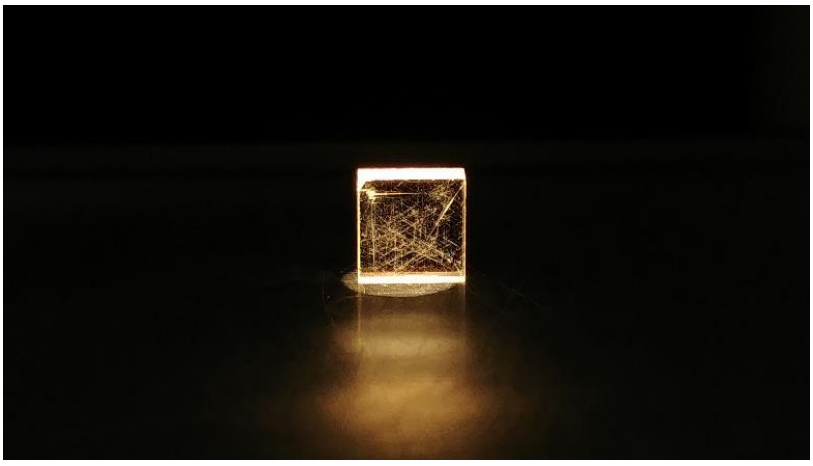

Figure 8-19 $LiTaO_3$ crystal taken with a mobile phone camera at the conclusion of the fatigue measurements.

Here, a theory to explain the causes of these observations will be discussed. The pyroelectric X-ray generator can be thought of as having similar components as a discharge tube. It has been explored in Chapter 3 that the pyroelectric crystal emits electrons, therefore, its exposed surface would act as a cathode when it is being heated. The target would then be the anode. Although the mechanism that starts the emission of electrons is different to a traditional discharge tube, the ionisation of gas particles to create a conducting path of electrons and positive ions can still be considered an electrical discharge. It should be clarified that there are different types of electrical discharges such as the corona, glow and arc to name a few [216, 217].

When an electron is emitted from the crystal, it already possesses an initial energy that is increased by the electric field of the gap. Since the pyroelectric crystal is still heating, the electric field in the gap and the charge at the crystal continues to rise. As the emitted electrons travel through the gap, it will generate sufficient energy to collide and ionise the residual gas molecules. This further produces free electrons and positive ions. The free electrons will continue to travel towards the target while the positive ions travel towards the crystal, forming an electron avalanche [217, 228, 229]. Secondary electron emission can also occur by positive ions bombarding the crystal surface. The secondary electrons will in turn ionise more gas molecules and create more avalanches. The series of avalanches eventually connects to one another and develops into a streamer of positive and negative ions across the gap [229].

Electrical breakdowns can also occur during the cooling phase, as has been shown in Chapter 5. As the process of electron emission is by field ionisation, multiple ionisation events will follow suit and produce electron avalanches. Since electrons would be travelling towards the crystal, the direction of the electron avalanche is in reverse to the direction in the heating phase. When the voltage in the gap reaches a critical value, an electrical breakdown of the discharge occurs and short-circuits the system. The breakdown is usually seen as a spark, or also known as a flashover. The critical value at which the breakdown occurs is known as the breakdown voltage, as has been introduced earlier.

When an insulating material is present in the discharge system, the electrical breakdown is specifically known as a partial breakdown because the current does not travel through the gas and bridge the electrodes. Instead, the unwanted sparks prefer to propagate along the surface of the material [217, 228-230]. They are also referred to as creeping discharges or surface flashovers and results in fern-like or tree-like tracking appearing across the surface. These tracks are conducting channels that erode into the material causing permanent damage. Furthermore, in a uniform electric field, these discharges tend to create nearly straight tracks. Therefore, the fern-like tracks observed could be creeping discharges.

Tracking tends to initiate at contaminated or weak points such as foreign particles, inclusions and protrusions. This is because these small protuberances become localised regions of electric field enhancements. The tracking that appears preferentially along the (111) planes in the <110> directions must indicate that they are regions of weaknesses. As crystal surface continues to degrade with more tracking, it increases the opportunity of partial breakdowns happening because the surface is roughened with more cavities. Ultimately, the ability for the pyroelectric crystal to develop charge on its surface and emit electrons is reduced. Thus, the production of X-rays decreases over increasing thermal cycles.

The second type of degradation are craters that are irregular in shape, and can vary in size and depth. These craters can appear along the fern-like tracks in small sizes and making the surface quite rough. Of the three profile measurements shown (Figure 8-13, Figure 8-14 and Figure 8-16), the average depth of the marked crosses is 2.68 μm. But these craters can also appear in random locations and larger in size. The deepest crater recorded was 5.98 μm, which corresponds to the micrograph in Figure 8-17 and its profile measurement in Figure 8-18. The formation of the craters could occur at the same moment as the creeping discharge. The initiation of a creeping discharge is the bombardment of accelerated charged particles, much like sputtering, that results in material loss [57]. Upon close inspection of some of the tapered-looking craters in Figure 8-17, tracks can be seen travelling from the tips.

Over prolonged periods of thermal cycling, the pyroelectric crystal experiences surface degradation due to the electrical breakdowns occurring in the system causing erosion across the crystal surface. Despite the surface degradation observed on the crystal surface impacting the X-ray output, the X-ray generator continues to function after more than 200 h of operation. However, the issue of the variation in X-ray counts and end-point energy continues to reside. This introduces difficulties in conducting accurate spectral measurements. If the issue is unable to be resolved in the X-ray generator system, alternate methods to correct for this output variation will need to be considered in the application. For example, in an X-ray fluorescence application, a reference material may be measured alongside the sample of interest to adjust the X-ray peak intensities.

9

CONCLUSIONS

"One of the advantages of being disorganised is that one is always having surprising discoveries."

– *A. A. Milne*

The application of the pyroelectric effect for the generation of X-rays was demonstrated and investigated in this project. There were four main areas of exploration that were studied via a combination of experimental measurements and simulation analysis. The material properties of pyroelectric materials that affected the performance and function of the X-ray generator were identified and the use of figures-of-merit were validated. Characterisation of the X-ray generator led to a clearer understanding of the effects of various system parameters, and more importantly, a verification of the mechanisms involved in the phenomenon. Additionally, the method of utilising the edge effect to improve the performance of the X-ray generator was tested. The X-ray generator's ability to perform under extended continuous operating cycles was also examined to determine the effects of long-term usage and behaviour of degradation.

Chapter 3 explored the material properties of the pyroelectric crystals that determine the intensity of the electric field in the gap to produce electrons for X-ray generation. While the net charge density developed on the polar surface of the pyroelectric crystal is important, it is the intensity of the electric field in the gap that is equally crucial. It was found that the relative permittivity and bulk conductivity of a ferroelectric material limit the magnitude of the electric field. Therefore, it is desirable for a material to not only have a high pyroelectric coefficient, but also a small relative permittivity and low bulk conductivity. Of the various compositions measured, $LiTaO_3$ and PZT were estimated to both produce the most intense electric fields, based on F_ε and F_σ, respectively. It was also determined that the configuration of the X-ray generator should have a large crystal thickness and a narrow gap distance to maximise the electric field.

The incorporation of electrostatics simulations presented in Chapter 4 allowed a more accurate representation of the electric field and potential distribution in the X-ray generator system. A simplified model of the X-ray generator was simulated with varying crystal thickness and gap distance on a selection of crystal compositions. The electric field indicated the pyroelectric crystal's ability to produce electrons, and in turn X-rays, while the potential difference across the gap predicted the X-ray end-point energy trend. There was general agreement between the figures-of-merit and the electrostatics simulations. That is, a thicker crystal arranged at a narrow gap distance created a more intense electric field and higher potential difference across the gap. This suggested that more X-rays of greater end-point energy would be generated. Thus, $LiTaO_3$ having the highest F_ε, was able to create the greatest electric field and potential difference across the gap.

In Chapter 6, a selection of the compositions tested in Chapter 3 and Chapter 4 were demonstrated in the X-ray generator constructed in Chapter 5 and characterised over a range of system parameters. The series of experiments confirmed that $LiTaO_3$ produced the highest X-ray counts and end-point energy at all parametric combinations compared to $LiNbO_3$ and PMN-30PT. Although PZT was not selected, it still verified that the figures-of-merit can be applied as an indicator of a material's performance in the X-ray generator. Additionally, new estimations on how well the figures-of-merit can predict the generation of X-rays was brought to light. PMN-30PT was unable to produce any

significant X-rays compared to $LiNbO_3$ and $LiTaO_3$. The criterion value for F_σ should then be at least 10^6 V/m. It was also confirmed that crystals with a larger crystal thickness will produce X-rays of greater yield and energy.

However, arranging the X-ray generator setup with a narrower gap distance did not correlate to better results as the involvement of gas pressure in the generator chamber brought in the limiting behaviour of electrical breakdown. These events have proven to be a disruptive feature as the parametric combination that produced the most optimum performance also experienced one of the highest occurrences of electrical breakdown. Although they can be reduced by appointing a different pressure and gap distance combination, it would also result in a lower X-ray output. The most optimal parametric combination was achieved by lithium tantalate with a crystal thickness of 2.0 mm, at a pressure of 0.33 Pa and gap distance of 3.7 mm. The X-ray flux was 1.22×10^5 cm^2/s and the highest end-point energy was approximately 40 keV.

The mechanism of the X-ray generator was also made clear. The source of electrons originated from two different electron emission phenomena. With the -Z crystal face exposed to the target, electrons were produced via ferroelectric electron emission in the heating phase, and via field ionisation in the cooling phase. This was confirmed by the observation of characteristic emission lines of the target in the heating phase, and of the pyroelectric crystal in the cooling phase.

The X-ray generator experiments and electrostatics simulations of the edge effect in Chapter 7 revealed the significance of the edges in its role to enhance the electric field and X-ray production. However, the approach to amplify the X-ray generator output by utilising this edge effect was rendered ineffective. The reduction in surface area resulted in a decrease in the surface charge density available. This synonymously diminished the electric field in the gap as the X-ray counts dropped by two orders of magnitude and the end-point energy was approximately halved. Therefore, introducing more edges on the crystal did not improve the X-ray generator performance.

The results across Chapter 4, Chapter 6 and Chapter 7 provided a clearer indication of the electric field required to produce X-rays. When PMN-30PT was tested in the X-ray generator, it did not produce any significant X-rays. The maximum electric field it produced at the top crystal surface was approximately 1.1×10^7 V/m. $LiTaO_3$ with a crystal thickness of 0.5 mm had a minimum electric field of 3.25×10^8 V/m and $LiNbO_3$ had a minimum electric field of 3.70×10^8 V/m. Both crystals were able to produce X-rays of approximately 10 cps and 10^2 cps, respectively, across all measured parametric combinations. When $LiTaO_3$ was simulated with insulated edges and a target, the minimum and maximum electric field at the top crystal surface were 2.81×10^7 V/m and 1.49×10^8 V/m, respectively. The corresponding X-ray generator experiment showed that X-rays were produced during the heating and cooling phases. This shows the electric field at the top crystal surface needs to be in the range of at least 10^7 - 10^8 V/m for ferroelectric electron emission and field ionisation to occur. Although it is possible that the interaction mostly occurred at the regions of 10^8 V/m, the values measured agrees well with existing literature.

Finally, in Chapter 8, running the pyroelectric crystal under extended thermal cycles in the X-ray generator gave new insight into its fatigue behaviour. The output of the X-ray generator saw many fluctuations within each individual 24 h fatigue measurement and throughout the entire experiment. There was a general decline in the X-ray counts observed within all 24 h measurements to varying extents. This was attributed to the bulk charge screening effect that continues to occur throughout the thermal cycling process. While there was no clear trend between each fatigue measurement, it was evident from optical microscope inspections that there was a gradual degradation on the exposed crystal surface. Together with the confocal laser scanning micrographs, it was deduced that this degradation behaviour is be linked to electrical breakdowns occurring as tracking along the crystal surface in preferred <110> directions.

The technology behind this type of X-ray generator involves several dependencies ranging from the properties and dimensions of the pyroelectric crystal, to the arrangement of the X-ray generator components and other system parameters. In an ideal scenario, the pyroelectric material selected should have a ratio of pyroelectric coefficient

to relative permittivity of at least 1.5 $\mu C/m^2K$, and a small bulk conductivity in the order of 10^{-15} $\Omega^{-1}m^{-1}$, in order to surpass the minimum electric field requirement and reduce the X-ray output decay over repeated usage. It is preferable for the dimension of the crystal along the axis of its spontaneous polarisation to be at least 2.0 mm, which can also be increased provided a uniform thermal distribution can be achieved. Keeping the gap distance as narrow as possible will further increase the electric field across the gap, and subsequently, the X-ray energy. However, this must be optimised with the pressure of the system to avoid or reduce electrical breakdowns as they can cause disruptive and damaging effects. With these considerations kept in mind, the overall performance of the X-ray generator and the longevity of the pyroelectric material can be increased.

This page is intentionally left blank.

10

FUTURE WORK

"There is much to do, and I am busy, very busy."

- *Wilhelm Röntgen*

While an X-ray generator system that applied the pyroelectric effect was successfully constructed and tested, there are issues that need to be resolved and further improvements to be made. This can be achieved by characterising and optimising more system parameters, using more accurate analytical methods and enhancing the design of the X-ray generator system.

One such system parameter that should be optimised is the thermal cycling rate. As the generation of X-rays is a dynamic process in such a way that the pyroelectric crystal relies of experiencing the temperature change, it is likely that the rate of temperature change will affect the rate of X-ray production. Previous studies either used a resistor or a thermoelectric cooler, meaning the thermal gradient was non-uniform or followed a triangular waveform. When a resistor was used, it was observed that the thermal gradient

was non-uniform and the count rate would peak very quickly and eventually reach a plateau as the temperature neared its set maximum temperature. On the other hand, if a constant thermal gradient was applied using a thermoelectric cooler, there would be a delay in the production of X-rays. Although it was not explicitly noted, it has been observed in some of the experiments conducted in this project that a small increase in the heating or cooling rate did result in a small increase in X-ray count rate. Only recently has this been investigated in more depth by Ghaderi and Davani [18] where they developed an electric potential equation to describe the dynamic production of net charge on the crystal surface. Therefore, the effect of temperature change rate should be investigated in order to optimise a more stable and uniform production of X-rays, as well as to increase the duty cycle.

It was reinforced in this project that a thicker crystal will increase the electric field in the gap, thereby increasing the production of X-rays. This should incline one to swap the 2.0 mm thick pyroelectric crystal with a thicker option. Previous studies have demonstrated using crystals with a thickness of up to 10 mm. However, one issue will continue to preside despite the potential it has. Since the pyroelectric crystal is only heated from one side of the crystal, its poor thermal conductivity will prevent the exposed polar surface from experiencing the full thermal cycle. In conjunction with optimising the temperature change rate, an alternate design to heat and cool the crystal should be thought of before experimenting with a thicker crystal.

Another aspect that should be considered is improving the efficiency of X-ray production. Although the results in this project were presented as X-ray counts and end-point energy, it tended to focus on optimising the system parameters to essentially maximise electron production. In order to further improve the X-ray generator performance, the conversion of electrons to X-rays should also be maximised. This requires optimisation of the target thickness and target element to increase the conversion efficiency while reducing attenuation. One such method is by conducting Monte Carlo simulations followed by experimental validation.

The energy and time-resolved results of the small interval measurements collected throughout a single thermal cycle revealed that both the count rate and end-point energy varied with the changing thermal difference. This has a large implication for applications such as quantitative spectral instruments as it can lead to inaccurate results. The fluctuation in count rate and energy is also one characteristic that does not meet the same capability as conventional X-ray tubes. While it is fair to say that X-ray tubes are still subjected to degradation and failure, it is a slow aging process and their X-ray beam can maintain stability during each interval use. It is also surprisingly to note that there has been little mention of this issue in studies which are integrating the X-ray generator with X-ray spectroscopy systems. This issue may be resolved or at least reduced via the earlier recommendations. However, if these fluctuations cannot be overcome, a method would need to be developed that factors in the count and energy variability to allow accurate quantitative analysis in applications such as X-ray fluorescence.

Lastly, it was mentioned in the literature review that comparing the results between previous studies was difficult because of the different parameters applied. Many of the studies reported the X-ray counts based off the collected energy spectra and there was little mention of the evaluation of the end-point energy. In Chapter 5, a method of correcting an X-ray energy spectrum was described but unfortunately was not applied to all the experimental results. This should be applied in the assessment of the X-ray generator performance as it is more representative of the true X-ray generator output. The end-point energy can then be evaluated using the corrected X-ray spectrum. Furthermore, the reporting of the X-ray counts should also take into account of other factors such as the solid angle coverage of the detector and duration of thermal cycle. By doing so, a more consistent means of reporting the performance of the X-ray generator can be implemented across future studies.

This page is intentionally left blank.

References

[1] P. J. Potts and M. West, "Portable X-Ray Fluorescence Spectrometry: Capabilities for *In Situ* Analysis." Cambridge, U.K.: The Royal Society of Chemistry, 2008.

[2] M. T. Cole, R. J. Parmee, and W. I. Milne, "Nanomaterial-based X-ray sources," *Nanotechnology,* vol. 27, no. 8, p. 082501, 2016.

[3] X. Hou, Y. He, and B. T. Jones, "Recent Advances in Portable X-Ray Fluorescence Spectrometry," *Applied Spectroscopy Reviews,* vol. 39, no. 1, pp. 1-25, 2004.

[4] R. Behling, *Modern diagnostic X-ray sources: Technology, Manufacturing, Reliability*. CRC Press, 2015.

[5] P. Russo, *Handbook of X-ray imaging: physics and technology*. CRC Press, 2017.

[6] A. G. Chmielewski and M. Haji-Saeid, "Radiation technologies: past, present and future," *Radiation Physics and Chemistry,* vol. 71, no. 1, pp. 17-21, 2004.

[7] M. Secchi, M. Zanatta, E. Borovin, M. Bortolotti, A. Kumar, M. Giarola, A. Sanson, B. Orberger, N. Daldosso, S. Gialanella, G. Mariotto, M. Montagna, and L. Lutterotti, "Mineralogical investigations using XRD, XRF, and Raman spectroscopy in a combined approach," *Journal of Raman Spectroscopy,* vol. 49, no. 6, pp. 1023-1030, 2018.

[8] A. Gałuszka, Z. M. Migaszewski, and J. Namieśnik, "Moving your laboratories to the field – Advantages and limitations of the use of field portable instruments in environmental sample analysis," *Environmental Research,* vol. 140, pp. 593-603, 2015.

[9] A. Górecka-Drzazga, "Miniature X-Ray Sources," *Journal of Microelectromechanical Systems,* vol. 26, no. 1, pp. 295-302, 2017.

[10] J. Schulz, "Innovation in X-ray technology," *Matéria (Rio de Janeiro),* vol. 16, no. 4, pp. 868-876, 2011.

[11] 井田博之, "X-ray fluorescence analysis with portable instruments," Doctor of Engineering Thesis, Department of Materials Science and Engineering, 京都大学 (Kyoto University), 2005.

[12] H. Kusano, N. Hasebe, H. Nagaoka, M. Naito, M. Mizone, Y. Amano, E. Shibamura, and H. Kuno, "Current Development Status of an X-ray Generator for X-ray Fluorescence Analysis on Space Mission," in *Proceedings of International Symposium on Radiation Detectors and Their Uses (ISRD2016)*, vol. 11(JPS Conference Proceedings: Journal of the Physical Society of Japan, 2016.

[13] H. Kusano, Y. Oyama, M. Naito, H. Nagaoka, H. Kuno, E. Shibamura, N. Hasebe, Y. Amano, K. J. Kim, and J. A. Matias Lopes, "Development of an X-ray generator using a pyroelectric crystal for X-ray fluorescence analysis on planetary landing missions," 2014, vol. 9213, pp. 921316-1 - 921316-11.

[14] Amptek Inc., "COOL-X Specifications," ed. Bedford, MA, U.S.A.: Amptek Inc.

[15] G. Rosenman, D. Shur, Y. E. Krasik, and A. Dunaevsky, "Electron emission from ferroelectrics," *Journal of Applied Physics,* vol. 88, no. 11, pp. 6109-6161, 2000.

[16] J. D. Brownridge and S. M. Shafroth, "Electron and Positive Ion Beams and X-rays Produced by Heated and Cooled Pyroelectric Crystals such as $LiNbO_3$ and $LiTaO_3$ in Dilute Gases: Phenomenology and Applications " in *Trends in Laser and Electro-*

Optic Research, W. T. Arkin, Ed.W. T. Arkins. 1st edition. New York, U.S.A.: Nova Science Publishers, Inc., 2006, pp. 55-95.

[17] M. Naito, N. Hasebe, H. Nagaoka, Y. Oshima, M. Mizone, E. Shibamura, H. Kuno, K. J. Kim, J. A. Matias-Lopes, and J. Martínez-Frías, "Improved pyroelectric X-ray generator for planetary active x-ray spectroscopy," in *SPIE Optical Engineering + Applications*, 2017, vol. 10392, p. 8: SPIE.

[18] R. Ghaderi and F. A. Davani, "Dynamics of pyroelectric accelerators," *Applied Physics Letters,* vol. 106, no. 4, p. 042906, 2015.

[19] E. M. Bourim, C.-W. Moon, S.-W. Lee, and I. Kyeong Yoo, "Investigation of pyroelectric electron emission from monodomain lithium niobate single crystals," *Physica B: Condensed Matter,* vol. 383, no. 2, pp. 171-182, 2006.

[20] S. M. Shafroth and J. D. Brownridge, "Modern physics lab experiments using crystal X-ray generators," in *Applications of Accelerators in Research and Industry*, 1999, vol. 475, no. 1, pp. 1100-1103.

[21] S. Fukao, Y. Nakanishi, Y. Guan, Y. Sato, Y. Ito, S. Yoshikado, and Ieee, "Radiation of X-rays using Uniaxially Polarized $LiNbO_3$ Single Crystal," in *18th IEEE International Symposium on the Applications of Ferroelectrics*New York: IEEE, 2009, pp. 427-432.

[22] J. A. Seibert, "X-ray imaging physics for nuclear medicine technologists. Part 1: Basic principles of X-ray production," *Journal of nuclear medicine technology,* vol. 32, no. 3, pp. 139-147, 2004.

[23] J. G. Webster, *Medical Instrumentation: Application and Design*, 4th ed. John Wiley & Sons, 2009.

[24] MOXTEK Inc., "MAGPRO™ Data Sheet," ed. Utah, U.S.A.

[25] Australian Synchrotron, "The synchrotron light source," ed. Melbourne, Australia, 2008.

[26] European Synchrotron Radiation Facility. 'What is a synchrotron?', 2015 [Online]. Available: http://www.esrf.eu/about/synchrotron-science/synchrotron. [Accessed: 5 Nov 2015 2015]

[27] J. D. Bourland, "Chapter 6 - Radiation Oncology Physics," in *Clinical Radiation Oncology (Fourth Edition)*, L. L. Gunderson and J. E. Tepper, L. L. Gunderson and J. E. Teppers. Philadelphia: Elsevier, 2016, pp. 93-147.

[28] H. E. Johns, *Physics of radiology*. Charles River Media, 1983.

[29] B. David, H. Barschdorf, V. Doormann, R. Eckart, G. Harding, J.-P. Schlomka, A. Thran, P. Bachmann, and P. Flisikowski, *Liquid-metal anode X-ray tube*. 2004.

[30] F. E. Zink, "X-ray tubes," *Radiographics,* vol. 17, no. 5, pp. 1259-1268, 1997.

[31] K. Tsuji, J. Injuk, and R. Van Grieken, *X-ray spectrometry: recent technological advances*. John Wiley & Sons, 2005.

[32] F. Jaundrell-Thompson and W. J. Ashworth, *X-ray physics and equipment*. Blackwell Scientific Publications, 1965.

[33] C. Kottler, R. Longtin, S. Giudice, R. Jose-James, P. Niedermann, A. Neels, R. Kaufmann, J. R. Sanchez-Valencia, H. R. Elsener, O. Gröning, C. Leinenbach, P. Gröning, and A. Dommann, "X-ray source downscaling enabled by combining

microfabricated electrodes with carbon nanotube cold electron emitters," *Microelectronic Engineering,* vol. 122, pp. 13-19, 2014.

[34] G. Harding, A. Thran, and B. David, "Liquid metal anode X-ray tubes and their potential for high continuous power operation," *Radiation Physics and Chemistry,* vol. 67, no. 1, pp. 7-14, 2003.

[35] E. Espes, T. Andersson, F. Björnsson, C. Gratorp, B. A. M. Hansson, O. Hemberg, G. Johansson, J. Kronstedt, M. Otendal, T. Tuohimaa, and P. Takman, *Liquid-metal-jet X-ray tube technology and tomography applications* (SPIE Optical Engineering + Applications). SPIE, 2014.

[36] P. P. Urone and R. Hinrichs. 'Photon Energies and Electromagnetic Spectrum', 2012 [Online]. Available: https://openstax.org/books/college-physics/pages/29-3-photon-energies-and-the-electromagnetic-spectrum. [Accessed: 13 Jan 2016 2016]

[37] C. T. Chantler, "Detailed tabulation of atomic form factors, photoelectric absorption and scattering cross section, and mass attenuation coefficients in the vicinity of absorption edges in the soft X-ray (Z= 30–36, Z= 60–89, E= 0.1 keV–10 keV), addressing convergence issues of earlier work," *Journal of Physical and Chemical Reference Data,* vol. 29, no. 4, pp. 597-1056, 2000.

[38] C. T. Chantler, "Theoretical Form Factor, Attenuation, and Scattering Tabulation for Z=1–92 from E=1–10 eV to E=0.4–1.0 MeV," *Journal of Physical and Chemical Reference Data,* vol. 24, no. 1, pp. 71-643, 1995.

[39] C. T. Chantler, K. Olsen, R. A. Dragoset, J. Chang, A. R. Kishore, S. A. Kotochigova, and D. S. Zucker. 'X-Ray Form Factor, Attenuation, and Scattering Tables (Version 2.1)', 2005 [Online]. Available: http://physics.nist.gov/ffast. [Accessed: 26 Jun 2019 2019]

[40] B. Jaffe, W. R. Cook Jr., and H. Jaffe, *Piezoelectric ceramics*. Academic Press, 1971.

[41] A. J. Moulson and J. M. Herbert, "Elementary Solid State Science," in *Electroceramics*: John Wiley & Sons, Ltd, 2003, pp. 5-93.

[42] G. H. Haertling, "Ferroelectric Ceramics: History and Technology," *Journal of the American Ceramic Society,* vol. 82, no. 4, pp. 797-818, 1999.

[43] S. B. Lang, *Sourcebook of pyroelectricity*. CRC Press, 1974.

[44] Department of Chemistry and Biochemistry Chemical Crystallography Laboratory. 'Symmetry in Crystallography', 2017 [Online]. Available: http://xrayweb.chem.ou.edu/notes/symmetry.html. [Accessed: 27 May 2019 2019]

[45] Y. Dong, M. A. McGuire, H. Yun, and F. J. Disalvo, "Synthesis, crystal structure, and properties of the rhombohedral modification of the thiospinel $CuZr_{1.86(1)}S_4$," *Journal of Solid State Chemistry,* vol. 183, no. 3, pp. 606-612, 2010.

[46] M. Niewczas, "Lattice correspondence during twinning in hexagonal close-packed crystals," *Acta Materialia,* vol. 58, no. 17, pp. 5848-5857, 2010.

[47] Y. Guo, H. Luo, D. Ling, H. Xu, T. He, and Z. Yin, "The phase transition sequence and the location of the morphotropic phase boundary region in $(1-x)[Pb(Mg_{1/3}Nb_{2/3})O_3]$–$xPbTiO_3$ single crystal," *Journal of Physics: Condensed Matter,* vol. 15, no. 2, p. L77, 2003.

[48] X. Zhao, B. Fang, H. Cao, Y. Guo, and H. Luo, "Dielectric and piezoelectric performance of PMN–PT single crystals with compositions around the MPB:

influence of composition, poling field and crystal orientation," *Materials Science and Engineering: B,* vol. 96, no. 3, pp. 254-262, 2002.

[49] A. J. Moulson and J. M. Herbert, "Piezoelectric Ceramics," in *Electroceramics*: John Wiley & Sons, Ltd, 2003, pp. 339-410.

[50] F. Jona, *Ferroelectric crystals*. Oxford: Pergamon Press Inc., 1962.

[51] A. J. Moulson and J. M. Herbert, *Electroceramics: materials, properties, applications*. John Wiley & Sons, 2003.

[52] D. M. Trucchi and N. A. Melosh, "Electron-emission materials: Advances, applications, and models," *MRS Bulletin,* vol. 42, no. 7, pp. 488-492, 2017.

[53] H. Riege, "Electron emission from ferroelectrics - a review," *Nuclear Instruments and Methods in Physics Research Section A: Accelerators, Spectrometers, Detectors and Associated Equipment,* vol. 340, no. 1, pp. 80-89, 1994.

[54] B. Rosenblum, P. Braunlic, and J. P. Carrico, "Thermally stimulated field-emission from pyroelectric $LiNbO_3$," *Applied Physics Letters,* Article vol. 25, no. 1, pp. 17-19, 1974.

[55] D. Go, "Gaseous Ionization and Ion Transport: An Introduction to Gas Discharges," *Department of Aerospace and Mechanical Engineering University of Notre Dame,* 2012.

[56] R. Gomer, *Field emission and field ionization*. Cambridge: Harvard University Press, 1961.

[57] J. D. Cobine, "Gaseous conductors: Theory and engineering applications," ed. New York: Dover Publications, 1958.

[58] A. S. Sidorkin, A. A. Sidorkin, O. V. Rogazinskaya, and S. D. Milovidova, "Electron emission of ferroelectric materials," in *IVMC 2001. Proceedings of the 14th International Vacuum Microelectronics Conference (Cat. No.01TH8586)*, 2001, pp. 227-228.

[59] K. Biedrzycki and R. Le Bihan, "Electron emission from ferroelectrics," *Ferroelectrics,* vol. 126, no. 1, pp. 253-261, 1992.

[60] G. Rosenman, V. Pechorskii, Y. L. Chepelev, E. Boikova, and L. Issakova, "Exoemission of pyroelectrics," *physica status solidi (b),* vol. 120, no. 2, pp. 667-670, 1983.

[61] F. Vurpillot, "Chapter Two - Field Ion Emission Mechanisms," in *Atom Probe Tomography*, W. Lefebvre-Ulrikson, F. Vurpillot, and X. Sauvage, W. Lefebvre-Ulrikson, F. Vurpillot, and X. Sauvages.: Academic Press, 2016, pp. 17-72.

[62] G. Rosenman and M. Urbakh, "Ion emission from ferroelectric media," *Journal of Applied Physics,* vol. 72, no. 5, pp. 1952-1954, 1992.

[63] I. Boscolo, A. Scurati, and M. Stellato, "Electron emission from ferroelectric ceramics with a special design patterned front electrode," *Journal of applied physics,* vol. 85, no. 12, pp. 8337-8342, 1999.

[64] Y. Hayashi, D. Flechtner, C. Golkowski, J. D. Ivers, and J. A. Nation, "Design of Ferroelectric Diode for High-Current Matched Electron-Beam Generation," *Japanese Journal of Applied Physics,* vol. 40, no. 1R, p. 397, 2001.

[65] Y. Hayashi, D. Flechtner, and E. Hotta, "Characteristics of electron emission from PZT ferroelectric cathode under strong accelerating field," *Journal of Physics D: Applied Physics,* vol. 35, no. 3, p. 281, 2002.

[66] Y. Hayashi and E. Hotta, "Strong Electron Emission from Ferroelectric Cathode," *Japanese Journal of Applied Physics,* vol. 45, no. 12R, p. 9185, 2006.

[67] Y. Hayashi and E. Hotta, "Material Dependence of Strong Electron Emission from Pb(Zr,Ti)O_3 Ferroelectric Cathodes," *Japanese Journal of Applied Physics,* vol. 42, no. 7R, p. 4571, 2003.

[68] M. Hockley and Z. Huang, "Strong electron emissions induced and extracted by pyroelectric crystals," *Smart Materials and Structures,* vol. 23, no. 3, p. 035010, 2014.

[69] G. A. Mesyats, "Electron emission from ferroelectric plasma cathodes," *Physics-Uspekhi,* vol. 51, no. 1, p. 79, 2008.

[70] D. Shur and G. Rosenman, "Two modes of plasma-assisted electron emission from ferroelectric ceramics," *Journal of Physics D: Applied Physics,* vol. 32, no. 6, p. L29, 1999.

[71] V. F. Puchkarev and G. A. Mesyats, "On the mechanism of emission from the ferroelectric ceramic cathode," *Journal of Applied Physics,* vol. 78, no. 9, pp. 5633-5637, 1995.

[72] J.-I. Asano, M. Okuyama, and Y. Hamakawa, "Electron emission into vacuum from lead-zirconate-titanate ferroelectric ceramics induced by polarization reversal," *Japanese journal of applied physics,* vol. 32, no. 1S, p. 396, 1993.

[73] J. Leonard. 'The development of a compact pyroelectric X-ray generator', 2015 [Online]. Available: https://slideplayer.com/slide/7060438/. [Accessed: 25 Dec 2018]

[74] B. Gall, "Investigation and Optimization of a High Voltage Piezoelectric Particle Accelerator," M.S. Thesis, Faculty of the Graduate School, University of Missouri, Columbia, MO, 2012.

[75] B. Gall, S. D. Kovaleski, J. A. VanGordon, P. Norgard, A. Benwell, B. H. Kim, J. W. Kwon, and G. E. Dale, "Investigation of the Piezoelectric Effect as a Means to Generate X-Rays," *IEEE Transactions on Plasma Science,* vol. 41, no. 1, pp. 106-111, 2013.

[76] J. D. Brownridge and S. M. Shafroth, "Self-focused electron beams produced by pyroelectric crystals on heating or cooling in dilute gases," *Applied Physics Letters,* vol. 79, no. 20, pp. 3364-3366, 2001.

[77] J. D. Brownridge and S. M. Shafroth, "Pressure dependence of energetic ($\leqslant$160 keV) focused electron beams arising from heated or cooled ($LiNbO_3$) pyroelectric crystals," *Applied Physics Letters,* vol. 83, no. 7, p. 1477, 2003.

[78] G. Rozenman, V. Bodyagin, Y. L. Chepelev, and L. Isakova, "Ferroelectric electronic emitter with controlled energy-spectrum," *Radiotekhnika I Elektronika,* vol. 32, no. 9, pp. 1997-1999, 1987.

[79] J. D. Brownridge, S. M. Shafroth, D. W. Trott, B. R. Stoner, and W. M. Hooke, "Observation of multiple nearly monoenergetic electron production by heated pyroelectric crystals in ambient gas," *Applied Physics Letters,* vol. 78, no. 8, p. 1158, 2001.

[80] J. A. Geuther and Y. Danon, "Electron and positive ion acceleration with pyroelectric crystals," *Journal of Applied Physics,* vol. 97, no. 7, p. 074109, 2005.

[81] J. D. Brownridge and S. Raboy, "Investigations of pyroelectric generation of X-rays," *Journal of Applied Physics,* vol. 86, no. 1, p. 640, 1999.

[82] J. Geuther, Y. Danon, F. Saglime, and B. Sones, "Electron acceleration for X-ray production using paired pyroelectric crystals," in *Sixth International Meeting on Nuclear Applications of Accelerator Technology, AccApp*, 2003, vol. 3, p. 124.

[83] E. Potter. 'The Incredible Shrinking X-ray', 2014 [Online]. Available: https://mizzoumag.missouri.edu/2014/05/the-incredible-shrinking-x-ray/. [Accessed: 7 Dec 2018]

[84] E. Van Cleve, B. Lucas, Z. Gamlieli, E. Wong, D. Kamkar, G. Jimenez, P. Cortes Jr, N. Mehta, J. Harper, and D. Cuadra, "Triboelectric generation of X-rays: Predictions and Results," in *Proc. ESA Annual Meeting on Electrostatics*, 2014, p. 1.

[85] C. G. Camara, S. J. Putterman, and A. Kotowski, "A novel technique to produce X-rays for XRF, medical, and scientific purposes," in *SPIE Optical Engineering+ Applications*, 2015, vol. Proc. SPIE 9590, Advances in Laboratory-based X-Ray Sources, Optics, and Applications IV, pp. 959005-0 - 959005-6: International Society for Optics and Photonics.

[86] C. G. Camara, J. V. Escobar, J. R. Hird, and S. J. Putterman, "Mechanically driven millimeter source of nanosecond X-ray pulses," *Applied Physics B,* vol. 99, no. 4, pp. 613-617, 2010.

[87] C. G. Camara, J. V. Escobar, J. R. Hird, and S. J. Putterman, "Correlation between nanosecond X-ray flashes and stick–slip friction in peeling tape," *Nature,* vol. 455, no. 7216, pp. 1089-1092, 2008.

[88] D. Krämer, D. Lützenkirchen-Hecht, B. Lühmann, K. Keite-Telgenbüscher, and R. Frahm, "New developments for the investigation of hard X-rays emitted by peeling adhesive tapes," *Review of Scientific Instruments,* vol. 84, no. 5, p. 055104, 2013.

[89] J. R. Hird, C. G. Camara, and S. J. Putterman, "A triboelectric X-ray source," *Applied Physics Letters,* vol. 98, no. 13, p. 133501, 2011.

[90] E. Van Cleve, B. Lucas, Z. Ganlieli, E. Wong, P. Cortes, N. Mehta, D. Cuadra, J. Fong, S. Hansen, and A. Kotowski, "A triboelectric closed loop band system for the generation of X-rays," in *SPIE Optical Engineering+ Applications*, 2015, pp. 95900F-95900F-7: International Society for Optics and Photonics.

[91] S. Mitroff. 'Tribogenics' incredible shrinking X-ray machines', 2012 [Online]. Available: https://www.wired.com/2012/09/tribogenics/. [Accessed: 2 May 2019]

[92] P. Frame. 'Introduction to Gas Discharge Tubes and Cold Cathode X-ray Tubes', 2008 [Online]. Available: https://www.orau.org/ptp/collection/xraytubes/introduction.htm. [Accessed: 20 May 2019]

[93] V. Filip, L. D. Filip, and F. Okuyama, "Miniature X-ray tubes: current state and future prospects," *Journal of Instrumentation,* vol. 8, no. 03, pp. T03005-T03005, 2013.

[94] A. Reyes-Mena, C. Jensen, E. Bard, D. C. Turner, K. Erdmann, Q. Qiu, B. Gao, J. Lu, and O. Zhou, "Miniature X-ray tubes utilizing carbon-nanotube-based cold cathodes," *Advances in X-Ray Analysis,* vol. 48, pp. 204-209, 2005.

[95] J. H. Ryu, J. S. Kang, and K. C. Park, "Carbon nanotube electron emitter for X-ray imaging," *Materials,* vol. 5, no. 11, pp. 2353-2359, 2012.

[96] S. H. Heo, A. Ihsan, and S. O. Cho, "Transmission-type microfocus X-ray tube using carbon nanotube field emitters," *Applied Physics Letters,* vol. 90, no. 18, p. 183109, 2007.

[97] Z. Liu, G. Yang, Y. Z. Lee, D. Bordelon, J. Lu, and O. Zhou, "Carbon nanotube based microfocus field emission X-ray source for microcomputed tomography," *Applied Physics Letters,* vol. 89, no. 10, p. 103111, 2006.

[98] Z. Liu, J. Zhang, G. Yang, Y. Cheng, O. Zhou, and J. Lu, "Development of a carbon nanotube based microfocus X-ray tube with single focusing electrode," *Review of Scientific Instruments,* vol. 77, no. 5, p. 054302, 2006.

[99] R. J. Parmee, C. M. Collins, W. I. Milne, and M. T. Cole, "X-ray generation using carbon nanotubes," *Nano Convergence,* vol. 2, no. 1, pp. 1-27, 2015.

[100] H. Sugie, M. Tanemura, V. Filip, K. Iwata, K. Takahashi, and F. Okuyama, "Carbon nanotubes as electron source in an X-ray tube," *Applied Physics Letters,* vol. 78, no. 17, pp. 2578-2580, 2001.

[101] R. Longtin, H.-R. Elsener, J. R. Sanchez-Valencia, D. Cloetta, L.-O. Nilsson, C. Leinenbach, O. Gröning, and P. Gröning, "High-temperature processable carbon–silicate nanocomposite cold electron cathodes for miniature X-ray sources," *Journal of Materials Chemistry C,* vol. 1, no. 7, pp. 1368-1374, 2013.

[102] C. Jensen, S. M. Elliott, S. D. Liddiard, A. Reyes-Mena, M. Moras, and D. C. Turner, "Improvements in low power, end-window, transmission-target X-ray tubes," *Advances in X-Ray Analysis,* vol. 47, pp. 64-69, 2004.

[103] J. D. Brownridge, "Pyroelectric X-Ray Generator," *Nature,* Letter vol. 358, no. 6384, pp. 287-288, 1992.

[104] S. Fukao, Y. Nakanishi, Y. Guan, Y. Sato, Y. Ito, S. Yoshikado, and A. Electromagnetics, *X-rays Source Using Thermal Excitation of Pyroelectric Crystal for Medical Application* (Piers 2009 Moscow Vols I and II, Proceedings). Cambridge: Electromagnetics Acad, 2009, pp. 807-815.

[105] H. Mizota, Y. Nakanishi, H. Oohashi, Y. Ito, T. Tochio, S. Yoshikado, and T. Tanaka, "X-ray emission from $LiTaO_3$ induced by thermal changes and structure analysis," *Radiation Physics and Chemistry,* vol. 75, no. 11, pp. 1626-1629, 2006.

[106] Pfeiffer Vacuum GmbH, "Introduction to vacuum technology," in *The Vacuum Technology Book*, vol. 2 Asslar, Germany: Pfeiffer Vacuum GmbH, 2013.

[107] K. Hanamoto, T. Kataoka, and K. Yamaoka, "Pressure dependence of X-rays produced by an $LiTaO_3$ single crystal at the pressures of 1–20 Pa," *Applied Radiation and Isotopes,* vol. 116, pp. 134-137, 2016.

[108] J. A. Geuther and Y. Danon, "High-energy X-ray production with pyroelectric crystals," *Journal of Applied Physics,* vol. 97, no. 10, p. 104916, 2005.

[109] T. Z. Fullem and Y. Danon, "Electrostatics of pyroelectric accelerators," *Journal of Applied Physics,* vol. 106, no. 7, p. 074101, 2009.

[110] A. Kovanen, Y. Danon, and D. Gillich, "X-ray production using stacked pyroelectric crystals," *Transactions - American Nuclear Society,* vol. 98, p. 406, 2008.

[111] Y. Guan, S. Fukao, Y. Nakanishi, Y. Sato, Y. Ito, and S. Yoshikado, "Radiation Method of X-rays using Multiple Uniaxially Polarized $LiNbO_3$ Single Crystals," in *18th IEEE International Symposium on the Applications of Ferroelectrics* New York: IEEE, 2009, pp. 412-417.

[112] Y. Guan, S. Fukao, K. Ito, Y. Nakanishi, Y. Sato, Y. Ito, and S. Yoshikado, "Improvement of Compact X-Rays Source Using Uniaxially Polarized $LiNbO_3$

R

Single Crystal," in *Key Engineering Materials*, 2010, vol. 445, pp. 43-46: Trans. Tech. Publ.

[113] H. Honda, S. Fukao, Y. Guan, Y. Nakanishi, Y. Sato, Y. Ito, S. Yoshikado, and Iop, "Continuous Emission of X-rays by Thermal Excitation of Six $LiTaO_3$ Single Crystals," in *3rd International Congress on Ceramics*, vol. 18 (IOP Conference Series - Materials Science and Engineering, Bristol: IOP Publishing Ltd, 2011.

[114] P. Sarrazin, D. Blake, L. Delzeit, M. Meyyappan, B. Boyer, S. Snyder, and B. Espinosa, "Carbon-nanotube field emission X-ray tube for space exploration XRD/XRF instrument," *Advances in X-Ray Analysis,* vol. 47, pp. 232-239, 2004.

[115] G. J. Pauley, "Studies of a pyroelectric crystal to develop a tabletop monoenergetic neutron source via nuclear fusion," Honours, Department of Physics, Indiana University, Bloomington, IN, 2010.

[116] B. Naranjo, J. K. Gimzewski, and S. Putterman, "Observation of nuclear fusion driven by a pyroelectric crystal," *Nature,* vol. 434, p. 1115, 2005.

[117] J. Geuther, Y. Danon, and F. Saglime, "Nuclear Reactions Induced by a Pyroelectric Accelerator," *Physical Review Letters,* vol. 96, no. 5, 2006.

[118] Y. Alivov, M. Klopfer, and S. Molloi, "TiO_2 nanotubes as a cold cathode for X-ray generation," *Applied Physics Letters,* vol. 96, no. 24, p. 243502, 2010.

[119] Y. Alivov, M. Klopfer, and S. Molloi, "Enhanced field emission from clustered TiO_2 nanotube arrays," *Applied Physics Letters,* vol. 99, no. 6, p. 063104, 2011.

[120] Y. Alivov, M. Klopfer, and S. Molloi, "Hybrid pyroelectric/nanotube $LiNbO_3/TiO_2$ X-ray source," *Applied Physics Letters,* vol. 102, no. 14, p. 143106, 2013.

[121] Y. Alivov and S. Molloi, "Performance of a hybrid pyroelectric $LiNbO_3$ and TiO_2 nanotubes X-ray source," *Review of Scientific Instruments,* vol. 84, no. 7, p. 073301, 2013.

[122] K. Nakahama, E. Kaga, T. Kisa, S. Abo, F. Wakaya, and M. Takai, "Electron emission from $LiTaO_3$ crystal excited by Nd:YLF laser light and its X-ray source application," in *25th International Vacuum Nanoelectronics Conference*, 2012, pp. 1-2.

[123] K. Nakahama, M. Takahashi, S. Abo, F. Wakaya, and M. Takai, "Effect of electron focusing in X-ray sources using $LiTaO_3$ crystals excited by neodymium-doped yttrium lithium fluoride laser light," *Journal of Vacuum Science & Technology B,* vol. 32, no. 2, p. 02B108, 2014.

[124] E. Arab, D. Fong, U. Lacroix, G. Travish, N. Vartanian, and R. Yoder, "Initial results on electron beam generation using pyroelectric crystals," *Proc. IPAC'10,* pp. 4384-4386, 2010.

[125] G. Travish, F. J. Rangel, M. A. Evans, B. Hollister, and K. Schmiedehausen, "Addressable flat-panel X-ray sources for medical, security, and industrial applications," in *SPIE Optical Engineering + Applications*, 2012, vol. 8502: SPIE.

[126] Adaptix Ltd. 'The Flat Panel Source', 2018 [Online]. Available: https://www.adaptiximaging.com/flat-panel-source. [Accessed: 7 Dec 2018]

[127] K. Bourzac. 'Creating a portable X-ray machine', 2010 [Online]. Available: https://www.technologyreview.com/s/418339/creating-a-portable-x-ray-machine/. [Accessed: 7 Dec 2018]

[128] Mark Allen Engineering Ltd. 'Working flat out', 2010 [Online]. Available: https://www.theengineer.co.uk/working-flat-out/. [Accessed: 25 Jun 2019]

[129] Amptek Inc., "COOL-X X-Ray Generator with Pyroelectric Crystal Operating Manual," ed. Bedford, MA, U.S.A.: Amptek Inc.

[130] K. Hanamoto, A. Kawabe, A. Sakoda, T. Kataoka, M. Okada, and K. Yamaoka, "Pressure dependence of X-rays produced by an LiTaO3 single crystal at low pressures," *Nuclear Instruments and Methods in Physics Research Section A: Accelerators, Spectrometers, Detectors and Associated Equipment,* vol. 669, pp. 66-69, 2012.

[131] J. D. Brownridge and S. M. Shafroth, "X-ray fluoresced high-Z (up to Z=82) K X-rays produced by $LiNbO_3$ and $LiTaO_3$ pyroelectric crystal electron accelerators," *Applied Physics Letters,* vol. 85, no. 7, p. 1298, 2004.

[132] S. Fukao, Y. Nakanishi, T. Mizoguchi, Y. Ito, and S. Yoshikado, "Radiation of X-rays using polarized $LiNbO_3$ single crystal in low-pressure ambient gas," *IEEE Transactions on Ultrasonics, Ferroelectrics, and Frequency Control,* vol. 56, no. 9, pp. 1850-1855, 2009.

[133] K. Nakahama, M. Takahashi, S. Abo, F. Wakaya, and M. Takai, "Effect of electron focusing in X-ray source using $LiTaO_3$ crystal excited by Nd:YLF laser light," in *26th International Vacuum Nanoelectronics Conference (IVNC)*, 2013, pp. 1-2.

[134] S. Abo, T. Uezato, F. Wakaya, and M. Takai, "Electron emission from pyroelectric crystal excited using high power infra-red laser light and its X-ray source application," in *2014 27th International Vacuum Nanoelectronics Conference (IVNC)*, 2014, pp. 106-107.

[135] M. C. Lovell, A. J. Avery, and M. W. Vernon, "Dielectrics," in *Physical Properties of Materials* Dordrecht Springer Netherlands, 1976, pp. 153-184.

[136] M. Daglish, "A dynamic method for determining the pyroelectric response of thin films," *Integrated Ferroelectrics,* vol. 22, no. 1-4, pp. 473-488, 1998.

[137] M. Davis, D. Damjanovic, and N. Setter, "Pyroelectric properties of $(1-x)Pb(Mg_{1/3}Nb_{2/3})O_3$-$xPbTiO_3$ and $(1-x)Pb(Zn_{1/3}Nb_{2/3})O_3$-$xPbTiO_3$ single crystals measured using a dynamic method," *Journal of Applied Physics,* vol. 96, no. 5, pp. 2811-2815, 2004.

[138] S. Jachalke, E. Mehner, H. Stöcker, J. Hanzig, M. Sonntag, T. Weigel, T. Leisegang, and D. Meyer, "How to measure the pyroelectric coefficient?," *Applied Physics Reviews,* vol. 4, no. 2, p. 021303, 2017.

[139] R. Jiménez and B. Jiménez, "Pyroelectricity in Polycrystalline Ferroelectrics," in *Multifunctional Polycrystalline Ferroelectric Materials: Processing and Properties* Dordrecht: Springer Netherlands, 2011, pp. 573-616.

[140] S. B. Lang and D. K. Das-Gupta, "Chapter 1 - Pyroelectricity: Fundamentals and applications A2 - Nalwa, Hari Singh," in *Handbook of Advanced Electronic and Photonic Materials and Devices*Burlington: Academic Press, 2001, pp. 1-55.

[141] A. A. Marino, "Modern bioelectricity." New York: Marcel Dekker, Inc., 1988.

[142] D. Shur and G. Rosenman, "Figures of merit for ferroelectric electron emission cathodes," *Journal of Applied Physics,* vol. 80, no. 6, pp. 3445-3450, 1996.

[143] G. Rosenman and I. Rez, "Electron emission from ferroelectric materials," *Journal of Applied Physics,* vol. 73, no. 4, pp. 1904-1908, 1993.

[144] G. Rosenman, "TrC1O: Electron emission from ferroelectrics and its applications," *Ferroelectrics,* vol. 133, no. 1, pp. 235-240, 1992.

[145] N. M. M. Nibbering, "A Historical Perspective on Field Ionization (FI) and Field Desorption (FD) Mass Spectrometry," in *The Encyclopedia of Mass Spectrometry*, M. L. Gross and R. M. Caprioli, M. L. Gross and R. M. Capriolis. Boston: Elsevier, 2016, pp. 92-100.

[146] G. Fursey, "Field Electron Emission from Metals," in *Field Emission in Vacuum Microelectronics*, I. Brodie and P. Schwoebel, I. Brodie and P. Schwoebels. Boston, MA: Springer US, 2005, pp. 1-17.

[147] C. Bowen, J. Taylor, E. LeBoulbar, D. Zabek, A. Chauhan, and R. Vaish, "Pyroelectric materials and devices for energy harvesting applications," *Energy & Environmental Science,* vol. 7, no. 12, pp. 3836-3856, 2014.

[148] S. B. Lang, "Pyroelectricity: from ancient curiosity to modern imaging tool," *Physics Today,* vol. 58, no. 8, p. 31, 2005.

[149] K.-K. Wong, "Properties of lithium niobate." London, U.K.: INSPEC, The Institute of Electrical Engineers, 2002.

[150] A. K. Batra and M. D. Aggarwal, *Pyroelectric Materials: Infrared Detectors, Particle Accelerators and Energy Harvesters*. SPIE Press Bellingham, Washington USA, 2013.

[151] S. Popescu, A. Petris, and V. Vlad, "Interferometric measurement of the pyroelectric coefficient in lithium niobate," *Journal of Applied Physics,* vol. 113, p. 043101, 2013.

[152] J. Parravicini, J. Safioui, V. Degiorgio, P. Minzioni, and M. Chauvet, "All-optical technique to measure the pyroelectric coefficient in electro-optic crystals," vol. 109, no. 3, p. 033106, 2011.

[153] Y. V. Shaldin, V. Gabriélyan, and S. J. C. R. Matyjasik, "Pyroelectric properties of real $LiNbO_3$ single crystals grown from a congruent melt," vol. 53, no. 5, pp. 847-852, 2008.

[154] G. Bergmann, "The electrical conductivity of $LiNbO_3$," *Solid State Communications,* vol. 6, no. 2, pp. 77-79, 1968.

[155] A. A. Esin, A. R. Akhmatkhanov, and V. Y. Shur, "The electronic conductivity in single crystals of lithium niobate and lithium tantalate family," *Ferroelectrics,* vol. 496, no. 1, pp. 102-109, 2016.

[156] K. Singh, "Electrical Conductivity of Non-Stoichiometric $LiNbO_3$ Single Crystals," *Ferroelectrics,* vol. 306, no. 1, pp. 79-92, 2004.

[157] Q. Wang, S. Leng, and Y. Yu, "Activation energy of small polarons and conductivity in $LiNbO_3$ and $LiTaO_3$ crystals," *physica status solidi (b),* vol. 194, no. 2, pp. 661-665, 1996.

[158] A. Dhar, N. Singh, R. K. Singh, and R. Singh, "Low temperature DC electrical conduction in reduced lithium niobate single crystals," *Journal of Physics and Chemistry of Solids,* vol. 74, no. 1, pp. 146-151, 2013.

[159] R. W. Whatmore, "Pyroelectric devices and materials," *Reports on Progress in Physics,* vol. 49, no. 12, p. 1335, 1986.

[160] A. Hossain and M. H. Rashid, "Pyroelectric detectors and their applications," *IEEE Transactions on Industry Applications,* vol. 27, no. 5, pp. 824-829, 1991.

[161] R. Skulski, P. Wawrzała, and M. Szymonik, *The electrical conductivity of PMN-PT ceramics*. 2009, pp. 935-941.

[162] S.-E. Park and T. R. Shrout, "Ultrahigh strain and piezoelectric behavior in relaxor based ferroelectric single crystals," *Journal of Applied Physics,* vol. 82, no. 4, pp. 1804-1811, 1997.

[163] B. Ploss and S. Bauer, "Characterization of materials for integrated pyroelectric sensors," *Sensors and Actuator A - Physics,* vol. 26, no. 1-3, pp. 407-411, 1991.

[164] Y. Yao, B. Ploss, C. L. Mak, and K. H. Wong, "Pyroelectric properties of $BiFeO_3$ ceramics prepared by a modified solid-state-reaction method," *Applied Physics A,* vol. 99, no. 1, pp. 211-216, 2010.

[165] J. Joshi and A. Dawar, "Pyroelectric materials, their properties and applications," *physica status solidi (a),* vol. 70, no. 2, pp. 353-369, 1982.

[166] "Piezo Material Data," Physik Instrumente (PI) GmbH & Co. KG, Ed., ed. Karlsruhe, Germany, 2011.

[167] J. J. Dih, D. R. Biswast, and R. M. Fulrath, "Effect of voids on the electrical resistivity in lead zirconate-titanate ceramics," *Journal of Materials Science,* vol. 16, no. 11, pp. 3220-3222, 1981.

[168] J. J. Dih and R. M. Fulrath, "Electrical Conductivity in Lead Zirconate - Titanate Ceramics," vol. 61, no. 9-10, pp. 448-451, 1978.

[169] T. M. Kamel and G. de With, "Pyroelectricity versus conductivity in soft lead zirconate titanate (PZT) ceramics," *Journal of Materials Research,* vol. 22, no. 12, pp. 3448-3454, 2007.

[170] R. Vaish, "Piezoelectric and Pyroelectric Materials Selection," *International Journal of Applied Ceramic Technology,* vol. 10, no. 4, pp. 682-689, 2013.

[171] S. Yao, W. Ren, H. Ji, X. Wu, P. Shi, D. Xue, X. Ren, and Z.-G. Ye, "High pyroelectricity in lead-free $0.5Ba(Zr_{0.2}Ti_{0.8})O_3$ –$0.5(Ba_{0.7}Ca_{0.3})TiO_3$ ceramics," *Journal of Physics D: Applied Physics,* vol. 45, no. 19, p. 195301, 2012.

[172] S. Kaczmarek, M. Orłowski, T. Skibiński, A. Jasik, and L. I. Ivleva, "Ferroelectric properties of relaxor type SBN single crystals pure and doped with Cr, Ni, and Ce," *Reviews on Advanced Materials Science,* vol. 23, pp. 80-87, 2010.

[173] S. M. Kaczmarek, D. Piwowarska, K. Matyjasek, M. Orłowski, and L. I. Ivleva, "Optical and dielectric properties of SBN61 single crystals doped with Co, Cr, Ni and Ce," *Optical Materials,* vol. 31, no. 12, pp. 1794-1797, 2009.

[174] H. J. Lee, S. O. Ural, L. Chen, K. Uchino, and S. Zhang, "High Power Characteristics of Lead-Free Piezoelectric Ceramics," *Journal of the American Ceramic Society,* vol. 95, no. 11, pp. 3383-3386, 2012.

[175] D. Irzhak, D. Roshchupkin, and D. Punegov, "Investigation of the piezoelectric effect in LiNbO3 and LiTaO3 crystals by X-ray diffraction," *Ferroelectrics,* Article; Proceedings Paper vol. 351, pp. 163-175, 2007.

[176] V. Shur, "Nano- and Microdomain Engineering of Lithium Niobate and Lithium Tantalate for Piezoelectric Applications," 2017, pp. 235-270.

[177] R. T. Smith and F. S. Welsh, "Temperature Dependence of the Elastic, Piezoelectric, and Dielectric Constants of Lithium Tantalate and Lithium Niobate," *Journal of Applied Physics,* vol. 42, no. 6, pp. 2219-2230, 1971.

[178] ASTM D257-14, "Standard Test Methods for DC Resistance or Conductance of Insulating Materials", ASTM International, West Conshohocken, PA,2014, www.astm.org.

[179] "Model 6487 Picoammeter/Voltage Source User's Manual," ed. Cleveland, Ohio, U.S.A.: Keithley Instruments Inc., 2011, pp. 3-9 - 3-12.

[180] "Corning Macor® Machinable Glass Ceramic," Corning SAS, Ed., ed. Avon, France: Corning Inc.

[181] W. R. Cook Jr., D. A. Berlincourt, and F. J. Scholz, "Thermal Expansion and Pyroelectricity in Lead Titanate Zirconate and Barium Titanate," vol. 34, no. 5, pp. 1392-1398, 1963.

[182] S. B. Lang, L. H. Rice, and S. A. Shaw, "Pyroelectric Effect in Barium Titanate Ceramic," vol. 40, no. 11, pp. 4335-4340, 1969.

[183] A. V. Shchagin, V. S. Miroshnik, V. I. Volkov, and A. N. Oleinik, "Ferroelectric ceramics in a pyroelectric accelerator," *Applied Physics Letters,* vol. 107, no. 23, p. 233505, 2015.

[184] K. A. Vokhmyanina, O. O. Ivashchuk, V. Y. Ionidi, A. A. Kaplii, I. A. Kishchin, A. S. Klyuev, A. S. Kubankin, M. V. Mishunin, R. M. Nazhmudinov, I. S. Nikulin, A. N. Oleinik, A. V. Sotnikov, A. S. Chepurnov, and A. V. Shchagin, "Possibility of Using the Piezoceramic PZT-19 in Pyroelectric X-ray Generators," *Glass and Ceramics,* journal article vol. 73, no. 11, pp. 415-419, 2017.

[185] S. Zhang and F. Li, "High performance ferroelectric relaxor-PbTiO3 single crystals: Status and perspective," *Journal of Applied Physics,* vol. 111, no. 3, p. 031301, 2012.

[186] P. Kumar, S. Sharma, O. P. Thakur, C. Prakash, and T. C. Goel, "Dielectric, piezoelectric and pyroelectric properties of PMN–PT (68:32) system," *Ceramics International,* vol. 30, no. 4, pp. 585-589, 2004.

[187] Y. Tang, S. Zhang, Z.-Y. Shen, W. Jiang, J. Luo, R. Sahul, and T. Shrout, "Primary and secondary pyroelectric coefficients of rhombohedral and tetragonal single-domain relaxor-PbTiO3 single crystals," *Journal of Applied Physics,* vol. 114, 2013.

[188] A. Mansingh and A. Dhar, "The AC conductivity and dielectric constant of lithium niobate single crystals," *Journal of Physics D: Applied Physics,* vol. 18, no. 10, p. 2059, 1985.

[189] A. S. Pritulenko, A. V. Yatsenko, and S. V. Yevdokimov, "Analysis of the nature of electrical conductivity in nominally undoped LiNbO3 crystals," *Crystallography Reports,* vol. 60, no. 2, pp. 267-272, 2015.

[190] W. Tornow, S. M. Lynam, and S. M. Shafroth, "Substantial increase in acceleration potential of pyroelectric crystals," *Journal of Applied Physics,* vol. 107, no. 6, p. 063302, 2010.

[191] R. Zhang, W. Jiang, B. Jiang, and W. Cao, "Elastic, Dielectric and Piezoelctric Coefficients of Domain Engineered $0.70Pb(Mg_{1/3}Nb_{2/3})O_3$ - $0.30PbTiO_3$ Single Crystal," in *Fundamental Physics of Ferroelectrics*, 2002, vol. 626, no. 1, pp. 188-197: American Institute of Physics.

[192] S. W. Ellingson, *Electromagnetics, Vol. 1*. Blacksburg, VA: VT Publishing, 2018.

[193] M. J. Matehkolaee and A. N. Asrami, "The review on the charge distribution on the conductor surface," *European Journal of Physics Education,* vol. 4, no. 3, pp. 1-6, 2017.

[194] I. W. McAllister, "Conductor curvature and surface charge density," *Journal of Physics D: Applied Physics,* vol. 23, no. 3, pp. 359-362, 1990.

[195] M. Bayssie, J. D. Brownridge, N. Kukhtarev, T. Kukhtarev, and J. C. Wang, "Generation of focused electron beam and X-rays by the doped $LiNbO_3$ crystals," *Nuclear Instruments & Methods in Physics Research Section B-Beam Interactions with Materials and Atoms,* Article; Proceedings Paper vol. 241, no. 1-4, pp. 913-916, 2005.

[196] J. D. Brownridge and S. M. Shafroth, "Using static charge on pyroelectric crystals to produce self–focusing electron and ion beams and transport through tubes," *Journal of Electrostatics,* vol. 63, no. 3-4, pp. 249-259, 2005.

[197] J. Geuther, "Radiation generation with pyroelectric crystals," PhD Thesis, Department of Mechanical Aerospace and Nuclear Engineering Rensselaer Polytechnic Institute, Troy, NY, U.S.A., 2007.

[198] V. Leus and D. Elata, "Fringing Field Effect in Electrostatic Actuators," Technion - Israel Institute of Technology, Haifa, Israel 2004.

[199] K. P. P. Pillai, "Fringing field of finite parallel-plate capacitors," *Proceedings of the Institution of Electrical Engineers,* vol. 117, no. 6, pp. 1201-1204, 1970.

[200] O. Wolf, "Arduino driver library for the MAX31865 RTD chip," ed, 2015.

[201] M. Kooijman, "SPI Master library for Arduino," 0.3 ed, 2014.

[202] S. Knight, "Fast PWM Library," ed, 2012.

[203] M. Nawrath, "Frequency Counter Library," 1.2 ed, 2012.

[204] S. Blavier, "ExtraPuTTY," 0.29 ed, 2015.

[205] D. Riseley, "PuTTY Session Manager," 0.41 ed: Sourceforge, 2010.

[206] S. Tatham, "PuTTY," 0.7 ed, 2017.

[207] H. Packard, "Fundamentals of the electronic counters," in "USA, Hewlett-Packard Company," 1997.

[208] K. Uchino, "Advanced piezoelectric materials: Science and technology." Woodhead Publishing Limited, 2010.

[209] M. Newville, T. Stensitzki, D. B. Allen, and A. Ingargiola, "LMFIT: Non-Linear Least-Square Minimization and Curve-Fitting for Python," 0.8.0 ed, 2014.

[210] B. Ganly, Y. Van Haarlem, and J. Tickner, "Measurement of relative line intensities for L-shell X-rays from selected elements between Z= 68 (Er) and Z= 79 (Au)," *X-Ray Spectrometry,* vol. 45, no. 4, pp. 233-243, 2016.

[211] J. H. Hubbell and S. M. Seltzer. 'X-Ray Mass Attenuation Coefficients', 2018 [Online]. Available: https://www.nist.gov/pml/x-ray-mass-attenuation-coefficients. [Accessed: 23 Feb 2019]

[212] M. Wilke, K. Harnisch, W. Knapp, M. Ecke, and T. Halle, "Optimization of pyroelectric electron sources for the generation of X-rays for X-ray fluorescence applications," *Journal of Vacuum Science & Technology B, Nanotechnology and Microelectronics: Materials, Processing, Measurement, and Phenomena,* vol. 36, no. 2, p. 02C101, 2018.

[213] L. Berzak, S. Dorfman, and S. Smith, "Paschen's Law in Air and Noble Gases," *Lawrence Berkeley National Laboratory,* 2006.

[214] M. Wilke, W. Knapp, M. Ecke, K. Harnisch, M. Zierau, and T. Halle, "Investigations of pyroelectric crystals for vacuum electron sources and X-ray applications," in *30th International Vacuum Nanoelectronics Conference (IVNC)*, 2017, pp. 304-305.

[215] R. Hackam and L. Altcheh, "AC (50 Hz) and DC electrical breakdown of vacuum gaps and with variation of air pressure in the range 10^{-9} - 10^{-2} Torr using OFHC copper, nickel, aluminum, and niobium parallel planar electrodes," vol. 46, no. 2, pp. 627-636, 1975.

[216] J. B. Calvert. 'Electrical Discharges', 2005 [Online]. Available: http://www.physics.csbsju.edu/370/jcalvert/dischg.htm.html. [Accessed: 23 Oct 2018]

[217] D. Faircloth, "Technological Aspects: High Voltage," CERN2014.

[218] J. L. Prince and J. M. Links, "Medical imaging signals and systems," ed. Upper Saddle River, NJ: Pearson Prentice Hall, 2006.

[219] E. B. Podgoršak, *Radiation Physics for Medical Physicists* (Biological and Medical Physics, Biomedical Engineering). Berlin Heidelberg, Germany: Springer-Verlag Berlin Heidelberg, 2010.

[220] R. E. Newnham, D. P. Skinner, and L. E. Cross, "Connectivity and piezoelectric-pyroelectric composites," *Materials Research Bulletin,* vol. 13, no. 5, pp. 525-536, 1978.

[221] E. P. Bertin, "Principles and practice of X-ray spectrometric analysis," 2nd ed. New York: New York : Plenum Press, 1975.

[222] E. M. Bourim, C.-W. Moon, S.-W. Lee, V. Sidorkin, and I. K. Yoo, "Pyroelectric electron emission from −Z face polar surface of lithium niobate monodomain single crystal," *Journal of electroceramics,* vol. 17, no. 2-4, pp. 479-485, 2006.

[223] N. Miyazaki and N. Koizumi, "Analysis of cracking of lithium tantalate ($LiTaO_3$) single crystals due to thermal stress," *Journal of Materials Science - J MATER SCI,* vol. 41, pp. 6313-6321, 2006.

[224] C. Klein and B. Dutrow, *The 23rd Edition of the Manual of Mineral Science: (after James D. Dana)*, 23 ed. John Wiley & Sons, 2008.

[225] K. W. Andrews, D. J. Dyson, and S. R. Keown, "Hexagonal and rhombohedral systems," in *Interpretation of Electron Diffraction Patterns* Boston, MA: Springer US, 1967, pp. 78-96.

[226] V. Andrianov, A. Erzinkian, L. Ivleva, and P. Lykov, "X-ray source on the basis of the piroelectric crystal $Sr_{0.61}Ba_{0.39}Nb_2O_6$," *AIP Advances,* vol. 7, no. 11, p. 115313, 2017.

[227] 大平健悟, 今宿晋, and 河合潤, "焦電結晶によるX線発生における放電現象とX線強度のエネルギー依存性," *X線分析の進歩,* no. 45, pp. 181-190, 2014.

[228] A. A. Chvyreva, "Creeping sparks: A study on surface discharge development," Technische Universiteit Eindhoven, 2016.

[229] R. Arora and W. Mosch, "High voltage and electrical insulation engineering." New Jersey, U.S.A.: John Wiley & Sons, 2011.

[230] A. S. Pillai and R. Hackam, "Surface flashover of solid dielectric in vacuum," *Journal of Applied Physics,* vol. 53, no. 4, pp. 2983-2987, 1982.

Appendix A DC conductivity

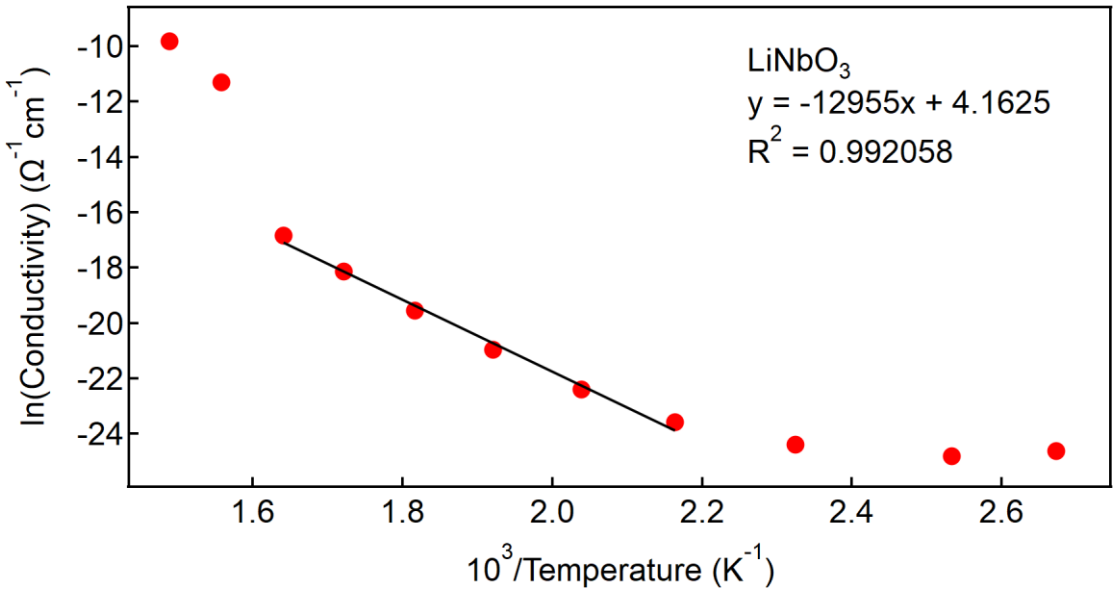

Figure A-1 Variation of the conductivity of $LiNbO_3$ with temperature.

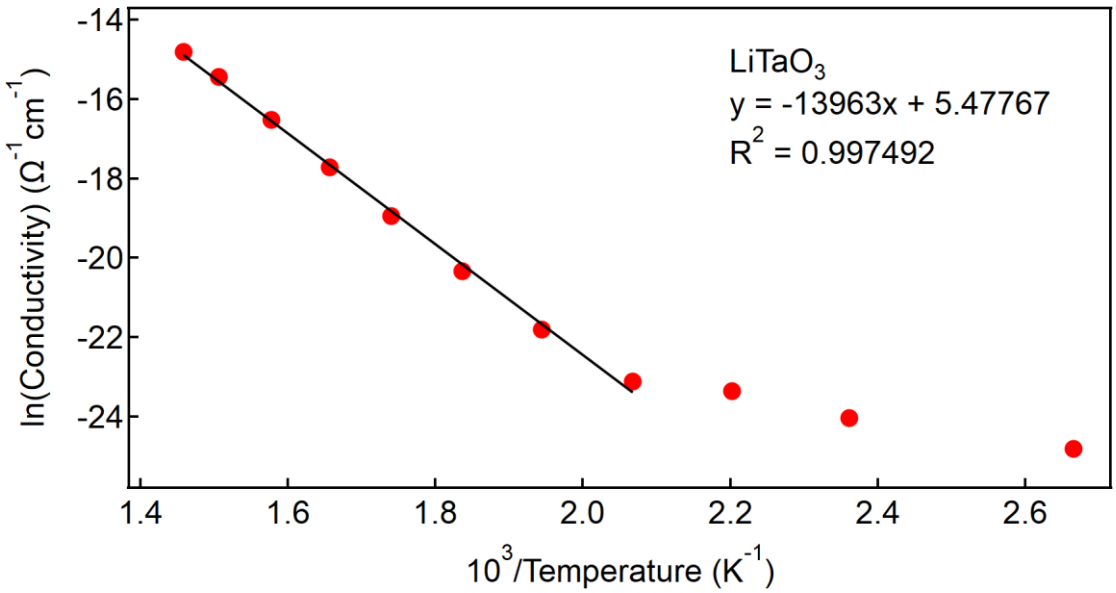

Figure A-2 Variation of conductivity of $LiTaO_3$ with temperature.

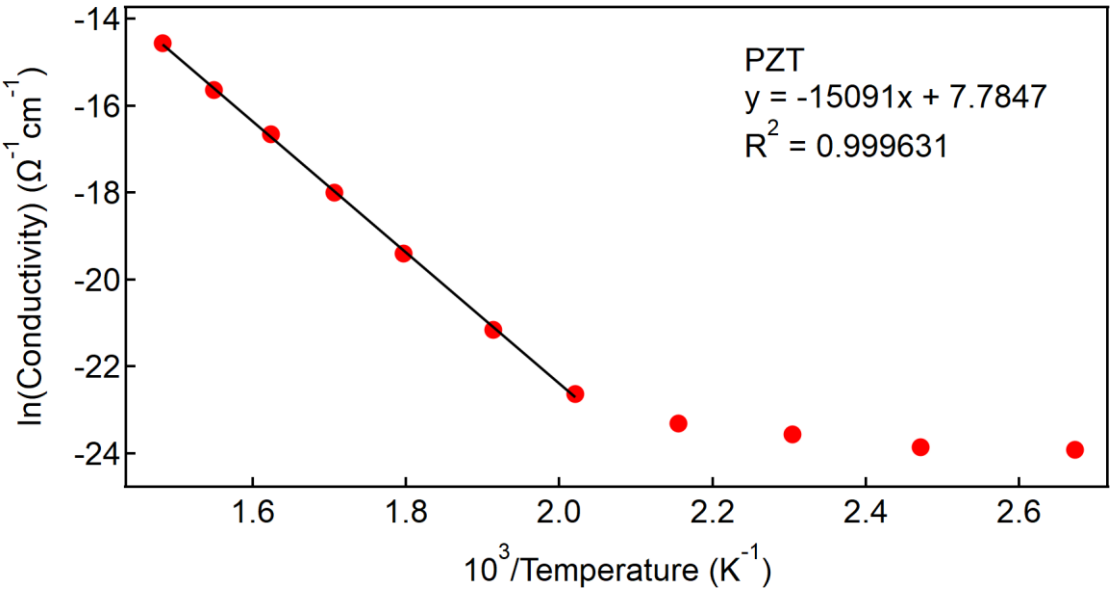

Figure A-3 Variation of conductivity of PZT with temperature.

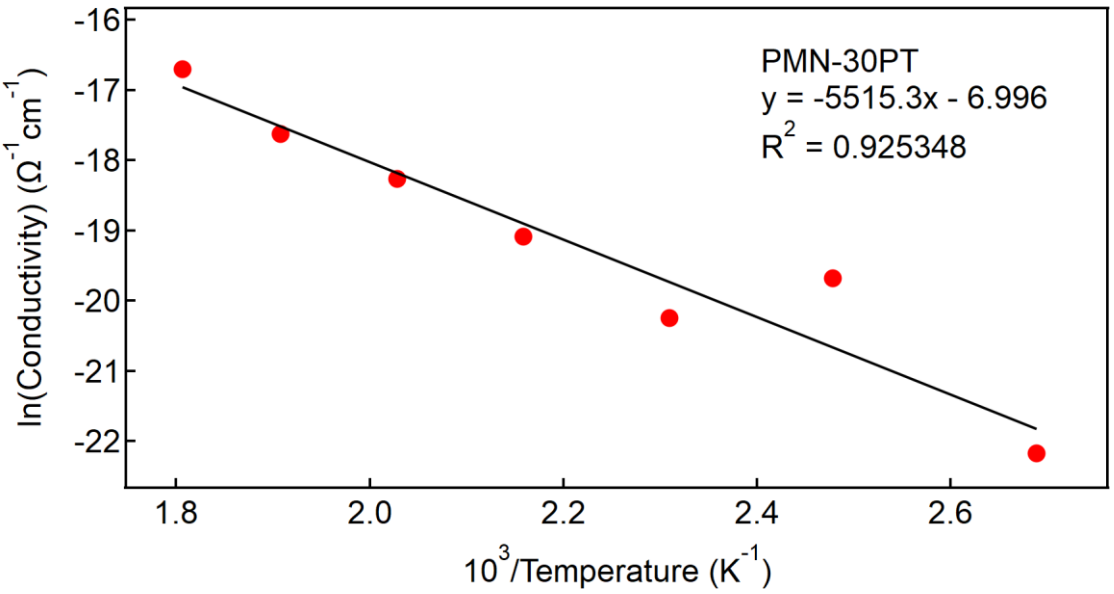

Figure A-4 Variation of conductivity of PMN-30PT with temperature.

Appendix B Electric potential distributions of $LiTaO_3$ of varying thickness

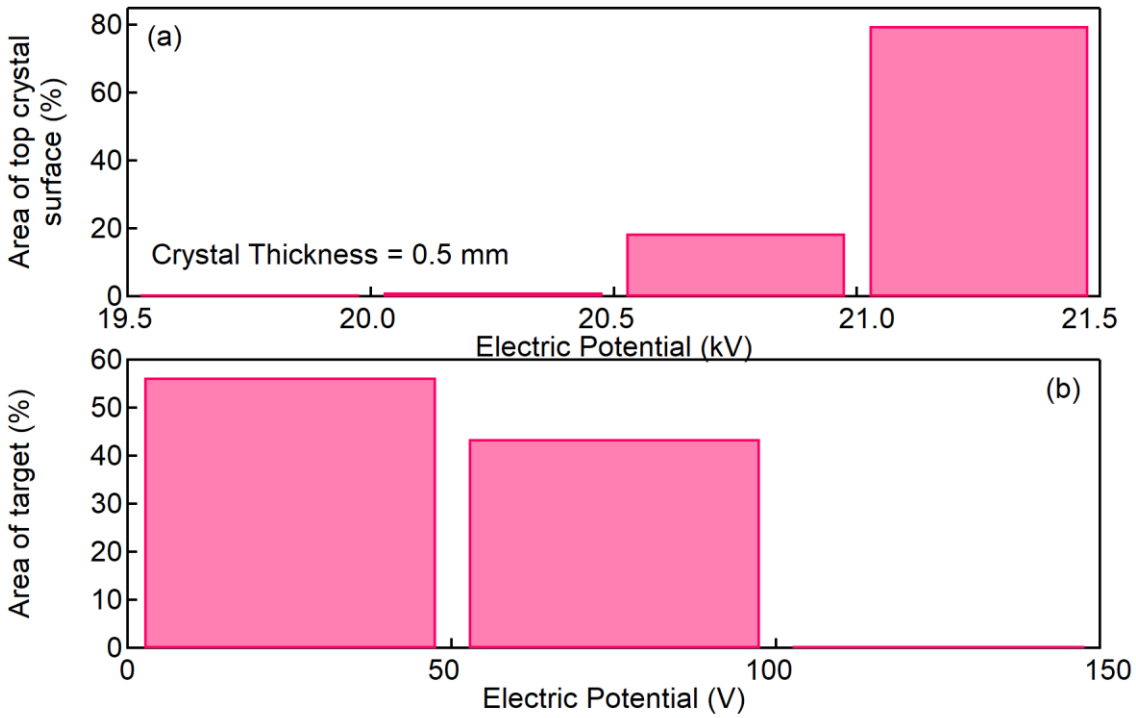

Figure B-1 Histogram of the electric potential distribution from $LiTaO_3$ with a crystal thickness of 0.5 mm at the top crystal surface (a) and target (b).

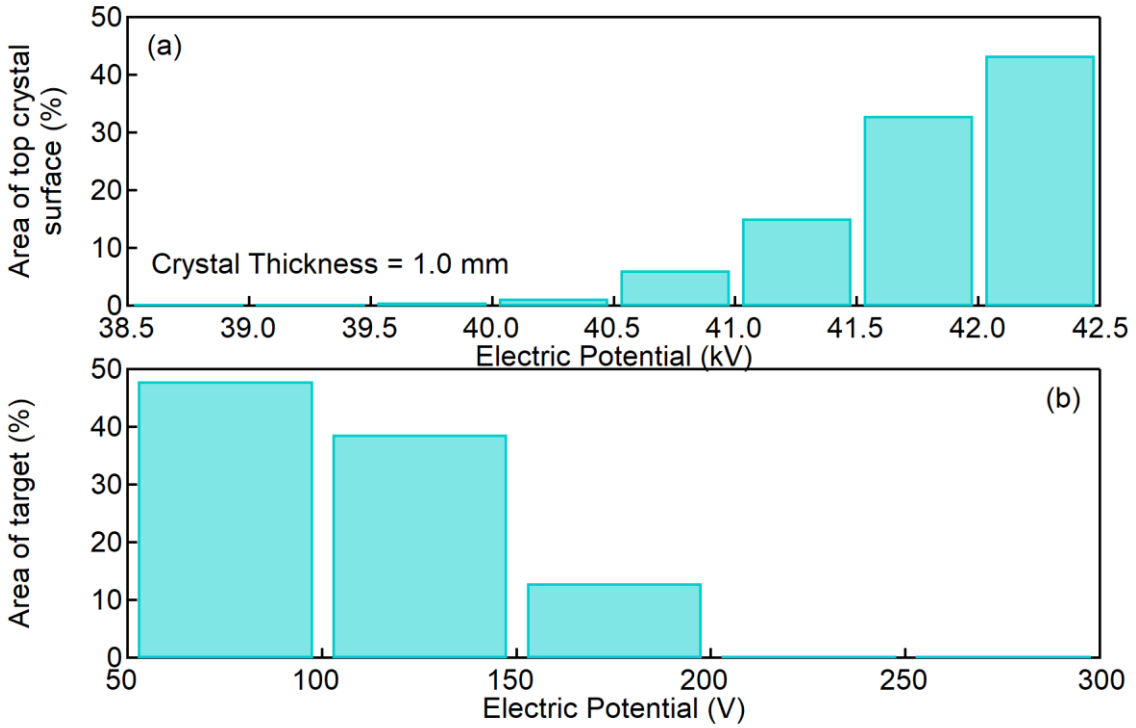

Figure B-2 Histogram of the electric potential distribution from $LiTaO_3$ with a crystal thickness of 1.0 mm at the top crystal surface (a) and target (b).

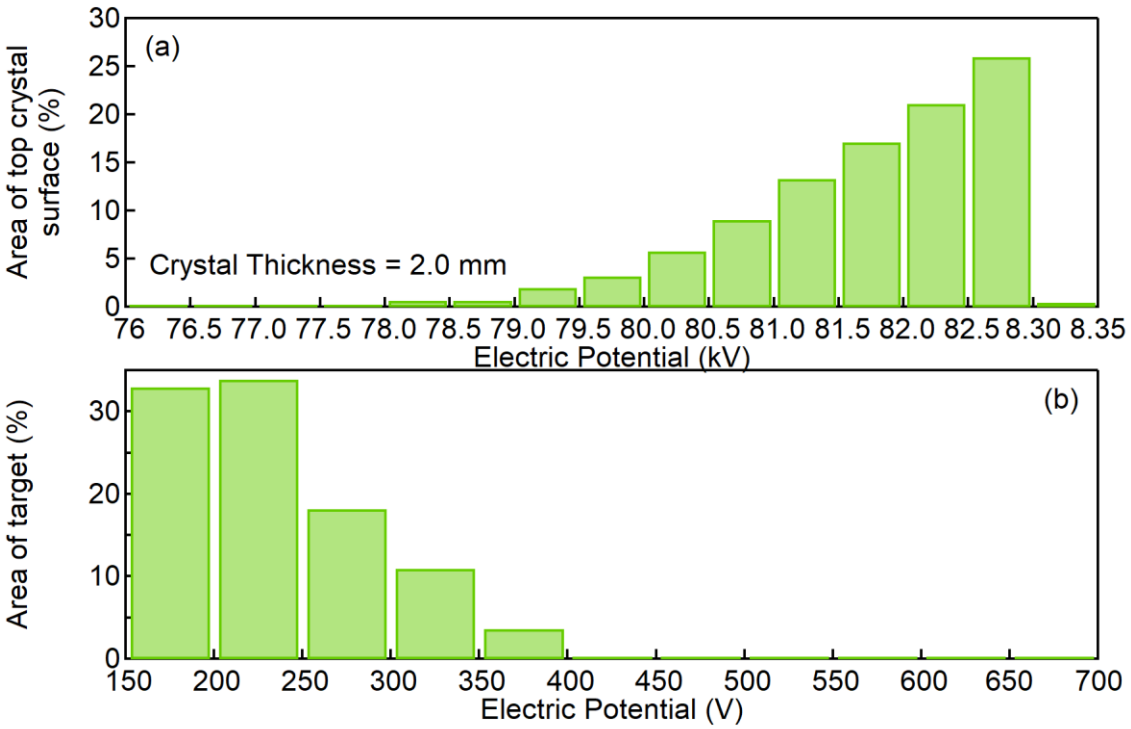

Figure B-3 Histogram of the electric potential distribution from $LiTaO_3$ with a crystal thickness of 2.0 mm at the top crystal surface (a) and the target (b).

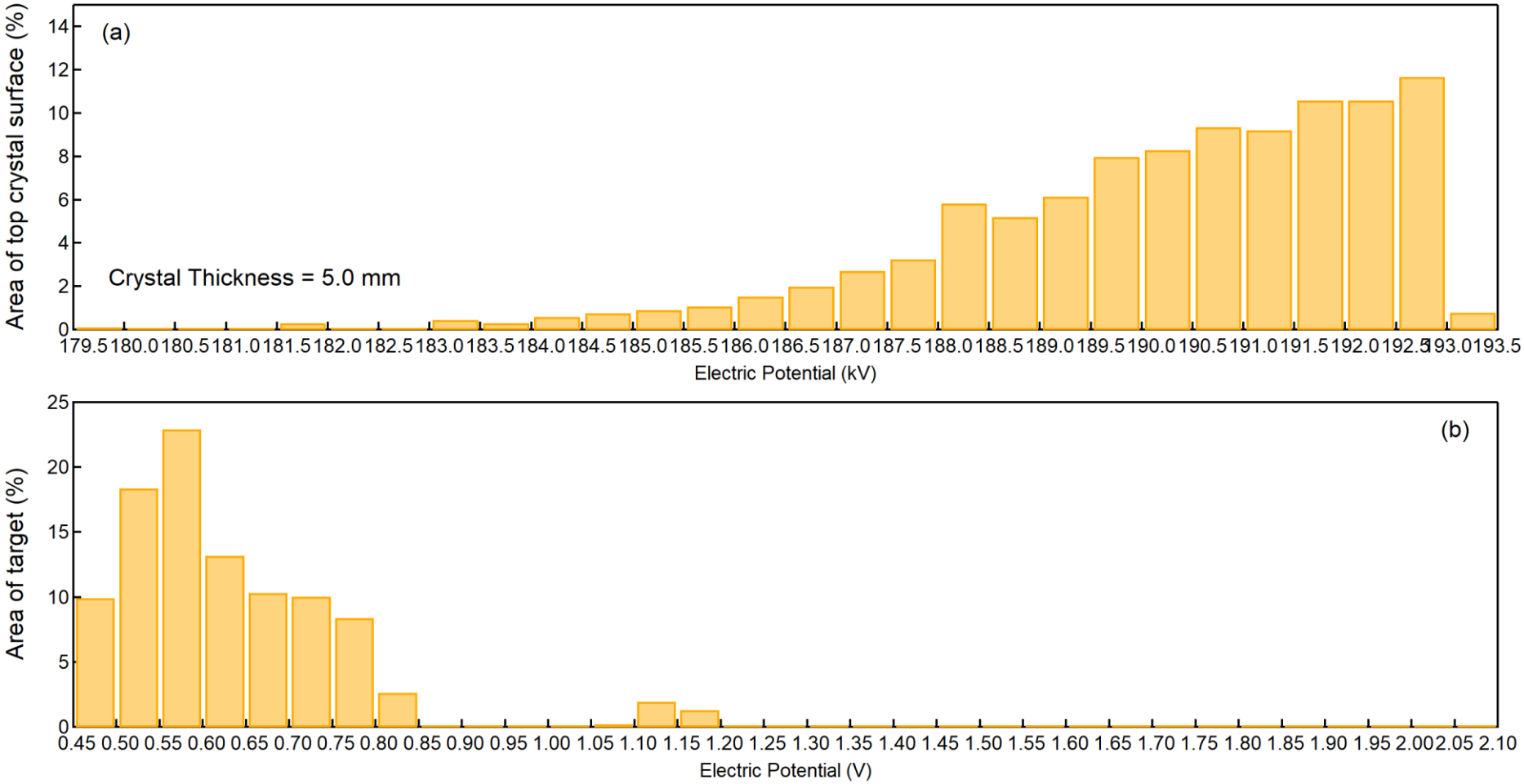

Figure B-4 Histogram of the electric potential distribution from $LiTaO_3$ with a crystal thickness of 5.0 mm at the top crystal surface (a) and the target (b). The bin width of (a) and (b) are 500 V and 50 V, respectively

Appendix C Arduino program code: Generator8

```
1.  // X-Ray Generator
2.  // Controller V8
3.  // Updated from V7 on 24 June 2018
4.  //
5.  // Controls and records the temperature and tempSensor
6.  // Records pressure readings
7.  // Uisng PWM.h library, don't use Timer 0 (Pin 5 and 6)
8.  // Instead use Timer 1 (Pin 9 and 10) or Timer 2 (Pin 3 and 11)
9.  // Uses a PID algorithm to control the set point temperature and heating/cooling rate of the Peltier
10. // Max Temperature set at 100 degrees C
11. // Included recording of pressureInput from MKS Baratron
12. // Using Peltier 03111-9L31-04CG with max 200 deg C
13.
14. #include <stdlib.h>
15. #include <stdio.h>
16. #include <PWM.h>
17. #include <PID_v1.h>
18. #include <SPI.h>
19. #include <MAX31865.h>
20.
21. #define aref_voltage 3.3
22. #define PT100
23. #define RTD_CS_PIN 10   // Chip select pin
24. #define FAULT_HIGH_THRESHOLD 0x708C   // +200C
25. #define FAULT_LOW_THRESHOLD 0x2690    // -100C
26. #define RTD_3WIRES true  // NOT using PT100 with 3 wires
27.
28. /*
29.  *  Arduino  VNH5019 (DC Motor Shield)
30.  *  12        INA
31.  *  6         INB
32.  *  3         PWM
33.  *  +5V       VDD
34.  *  GND       GND
35.  *
36.  *  Arduino         Sensor
37.  *  A0              temp
```

```
 *  A1              pressure
 *  3.3 to ArefV    tempSensorVin // more precise, less noise
 *  GND             GND (temp)
 *  GND             GND (pressure)
 *
 *  Arduino         MAX31865 (PT100 Mod board)
 *  D10             Chip Select (CS) Pin 1
 *  D11             SDI/MOSI Pin 2
 *  D12             SDO/MISO Pin 3
 *  D13             SCK Pin 4
 *  GND             GND Pin 5
 *  3v3             VCC Pin 6
 *  D2              DRDY/IRQ Pin 7 (Optional)
 */

const int pinA = 12;
const int pinB = 6;
const int PWMPin = 3;
const int voltIn = 6; // voltage input in volts

int timeRead = 100; // delay time between individual temperature and pressure readings
float polarity = 1;
float voltagePeltier;
int32_t frequency = 18500;  // Frequency in Hz
int i = 0;
int j = 0;
int arrayCount = 0;
double maxTemp = 100;  // Maximum temperature set point
double minTemp = 0;   // Minimum temperature set point
double initialTemp = 0; // Initial temperature
double maxSetPointTemp = 120; //120;
double minSetPointTemp = -10;
int heatRampRate = 10; // 15; // 5; // In degrees C/min
int coolRampRate = 10; // 15; // 5; // In degress C/min
float tempChange = 0.167; // 0.25; for 15 degrees C/min // 0.0833; for 5 degrees C/min // (timeDifference * heat/coolRampRate) in degr
ees C
int state = 0;
int heatingCycle = 0;
double holdTemp = 100;
double holdTime = 0;
```

```
77.
78. // Temperature readParameters variables
79. int tempSensor;
80. float tempSensorVolt = 0;
81. float temperature = 0;
82. float tempArray[10];
83. float tempAverage;
84. float totalT;
85. MAX31865_RTD rtd(MAX31865_RTD::RTD_PT100, RTD_CS_PIN,400);
86.
87.
88. // Pressure readParameters variables
89. int pressureSensor;
90. int pressureSensorArray[10];
91. int pressureSensorAverage;
92. int totalPSensor;
93. float pressureSensorVolt = 0;
94. float pressureVoltArray[10];
95. float pressureVoltAverage;
96. float totalPVolt;
97. float pressure = 0;
98. float pressureArray[10];
99. float pressureAverage;
100.       float totalP;
101.       float calibratePressVolt = 0.006; // Value must be updated so that pressure is calibrated
102.
103.       // PID Variables
104.       double setPointPID = 1; // Value to reach, i.e. max/min temperature
105.       double inputPID;        // Variable to control, i.e. temperature of Peltier
106.       double outputPID = 0;   // Variable to change, i.e. PWM
107.       double Kp;              // Tuning parameter proportional band
108.       double Ki;              // Tuning parameter integral
109.       double Kd;              // Tuning parameter derivative
110.       PID myPID (&inputPID, &outputPID, &setPointPID, Kp, Ki, Kd, DIRECT);  // Setting PID function
111.
112.       void setup()
113.       {
114.         Serial.begin(9600);
115.         analogReference(EXTERNAL);  // Use AREF for reference voltage (Supplying external reference voltage to the Arduino board)
116.         InitTimersSafe();           // Initialises all timers, pwmWrite needs to be used for initialised timers
```

```
117.
118.         // Setting up PID
119.         myPID.SetMode(AUTOMATIC); // Turns on PID
120.         myPID.SetOutputLimits(0, 158);  // PWM is limited between 0 and 158 so the voltagePeltier is 3.72 V max (0..255)
121.         myPID.SetControllerDirection(DIRECT);
122.         setPointPID = constrain(setPointPID, minSetPointTemp, maxSetPointTemp);
123.         state = 0;  // Begin with heating phase
124.
125.         // Setting up frequency for PWM
126.         bool success = SetPinFrequency(PWMPin, frequency);  // Sets the frequency for the specified pin, which in PWM
127.         if (success)
128.         {
129.           pinMode(PWMPin, OUTPUT);
130.           pinMode(pinA, OUTPUT);
131.           pinMode(pinB, OUTPUT);
132.         }
133.
134.         // Initialise SPI communication
135.         SPI.begin();
136.         SPI.setClockDivider(SPI_CLOCK_DIV16);
137.         SPI.setDataMode(SPI_MODE3);
138.
139.         delay(100);
140.
141.         rtd.configure(true, true, false, RTD_3WIRES, MAX31865_FAULT_DETECTION_NONE,
142.                       true, true, FAULT_LOW_THRESHOLD, FAULT_HIGH_THRESHOLD);
143.         // rtd.configure in brackets explanation
144.         /* Reconfigure this allow us to plug/unplug the module and check PT100/PT1000
145.                V_BIAS enabled
146.                No Auto-conversion
147.                1-shot disabled
148.                3-wire disabled
149.                Fault detection: we need to manual mode, set manual 1 => First stage
150.                                 because on MAX31865 beakout board, RC constant is > 100us
151.                                 see MAX31865 datasheet page 14 / Section Fault Detection Cycle (D3:D2)
152.                Fault status:  auto-clear
153.                50 Hz filter
154.                Low threshold:  FAULT_LOW_THRESHOLD = -100C
155.                High threshold:  FAULT_HIGH_THRESHOLD = +200C
156.         */
```

```
157.
158.         Serial.println("SetPointTemp (C), PWM, PeltierVoltage (V), Temperature (C), PressureAnalog, PressureVoltage (V), Pressure (m
    Torr)");
159.       }
160.
161.       void positiveVoltage() // Driving the heating phase
162.       {
163.         digitalWrite(pinA, HIGH);
164.         digitalWrite(pinB, LOW);
165.         polarity = +1;
166.         myPID.SetControllerDirection(DIRECT);
167.       }
168.
169.       void negativeVoltage() // Driving the cooling phase
170.       {
171.         digitalWrite(pinA, LOW);
172.         digitalWrite(pinB, HIGH);
173.         polarity = -1;
174.         myPID.SetControllerDirection(REVERSE);
175.       }
176.
177.       void readParameters()
178.       {
179.         // Initialising total variables
180.         totalT = 0;
181.         totalP = 0;
182.         totalPVolt = 0;
183.         totalPSensor = 0;
184.
185.         for (arrayCount = 0; arrayCount <= 9; arrayCount++)
186.         {
187.           // Reading in temperature
188.           rtd.read_all();
189.           double temperature = rtd.temperature();
190.           tempArray[arrayCount] = temperature;
191.           totalT = tempArray[arrayCount] + totalT;
192.
193.           // Reading in pressure
194.           pressureSensor = analogRead(A1);  // A1 is the pressure sensor pin
195.           pressureSensorVolt = float(pressureSensor)*aref_voltage/1024; // Converts 0-1023 to 0-3.3 V
```

```
196.           pressure = (pressureSensorVolt - calibratePressVolt)*1000/aref_voltage; // 1000 mTorr = 3.3 V DC = 1023 w/ voltage offset
197.           pressureSensorArray[arrayCount] = pressureSensor;
198.           pressureVoltArray[arrayCount] = pressureSensorVolt;
199.           pressureArray[arrayCount] = pressure;
200.
201.           totalPSensor = pressureSensorArray[arrayCount] + totalPSensor;
202.           totalP = pressureArray[arrayCount] + totalP;
203.           totalPVolt = pressureVoltArray[arrayCount] + totalPVolt;
204.           delay(timeRead);
205.         }
206.
207.         // Calculating averages
208.         tempAverage = totalT/arrayCount;
209.         pressureSensorAverage = totalPSensor/arrayCount;
210.         pressureAverage = totalP/arrayCount;
211.         pressureVoltAverage = totalPVolt/arrayCount;
212.
213.         voltagePeltier = (float(outputPID)/255)*voltIn*polarity;
214.         inputPID = tempAverage;
215.       }
216.
217.       void printParameters(double setPointPID, double outputPID, float voltagePeltier, float inputPID, int pressureSensorAverage, fl
    oat pressureVoltAverage, float pressureAverage)
218.       {
219.         Serial.print(setPointPID, 3);         Serial.print(", ");
220.         Serial.print(outputPID, 3);           Serial.print(", ");
221.         Serial.print(voltagePeltier, 3);      Serial.print(", ");
222.         Serial.print(inputPID, 3);            Serial.print(", ");
223.         Serial.print(pressureSensorAverage);  Serial.print(", ");
224.         Serial.print(pressureVoltAverage, 3); Serial.print(", ");
225.         Serial.println(pressureAverage, 3);
226.       }
227.
228.       void runPID(double Kp, double Ki, double Kd)
229.       {
230.         myPID.SetTunings(Kp, Ki, Kd);
231.         myPID.Compute();
232.         pwmWrite(PWMPin, outputPID);
233.       }
```

```
234.
235.       void holdPWM(double Kp, double Ki, double Kd, double PWM)
236.       {
237.         myPID.SetTunings(Kp, Ki, Kd);
238.         pwmWrite(PWMPin, PWM);
239.       }
240.
241.       void runCycleTime(void)
242.       {
243.         if (state == 0)
244.         {
245.           // The temperature in the heating direction increases with increasing PWM
246.           readParameters();
247.           initialTemp = inputPID;
248.           setPointPID = initialTemp;
249.           while (inputPID <= (maxTemp - 0.5)) // REMEMBER: inputPID = actual temperature reading!
250.           {
251.             readParameters();
252.             if (setPointPID < maxSetPointTemp)
253.             {
254.               setPointPID = tempChange + setPointPID; // setPoint temperature increases every 1 s
255.               if (setPointPID <= 20 && heatingCycle >= 1)
256.               {
257.                 negativeVoltage();
258.               }
259.               else
260.               {
261.                 positiveVoltage();
262.               }
263.             }
264.             else if (setPointPID >= holdTemp)
265.             {
266.               do
267.               {
268.                 setPointPID == holdTemp;
269.               }
270.               while (holdTime <60000);
271.             }
272.             else if (setPointPID >= maxSetPointTemp)
273.             {
```

```
274.                 setPointPID = maxSetPointTemp;  // hold the setPoint temperature at max if the tempAverage has not reached max tempe
    rature
275.               }
276.               printParameters(setPointPID, outputPID, voltagePeltier, inputPID, pressureSensorAverage, pressureVoltAverage, pressureAv
    erage);
277.               runPID(2, 4, 1); // runPID(2, 5, 1);
278.             }
279.           }
280.           else if (state == 1)
281.           {
282.             // The temperature in cooling direction decreases with increasing PWM
283.             readParameters();
284.             setPointPID = maxTemp;
285.             while (inputPID >= (minTemp + 1.0))
286.             {
287.               readParameters();
288.               if (setPointPID > minTemp)
289.               {
290.                 setPointPID = setPointPID - tempChange;
291.                 if (setPointPID >= 40)
292.                 {
293.                   positiveVoltage();
294.                   runPID(2, 3, 0.5);  //runPID(2, 2, 0.5);
295.                 }
296.                 else if (setPointPID < 35) // (setPointPID < 40)
297.                 {
298.                   if (inputPID <= (setPointPID - (0.1*setPointPID)))
299.                   {
300.                     positiveVoltage();
301.                     runPID(2, 3, 0.5);
302.                   }
303.                   else
304.                   {
305.                     negativeVoltage();
306.                     runPID(2, 2, 1);
307.                   }
308.                 }
309.               }
310.               else if (setPointPID <= minTemp && inputPID >= minTemp)
311.               // if the setPoint temperature has gone below 0 degrees C but the input temperature has not reached it
```

```
312.             {
313.               setPointPID = setPointPID - tempChange;
314.               negativeVoltage();
315.               runPID(2, 3, 0.5);
316.             }
317.             printParameters(setPointPID, outputPID, voltagePeltier, inputPID, pressureSensorAverage, pressureVoltAverage, pressureAv
    erage);
318.           }
319.         }
320.       }
321.
322.       void loop()
323.       {
324.         switch (state)
325.         {
326.           case 0:
327.             runCycleTime();
328.             state = state + 1;
329.             heatingCycle = heatingCycle + 1;
330.             break;
331.           case 1:
332.             runCycleTime();
333.             state = state - 1;
334.             break;
335.         }
336.       }
```

Appendix D End-point energy evaluation for various parametric variations

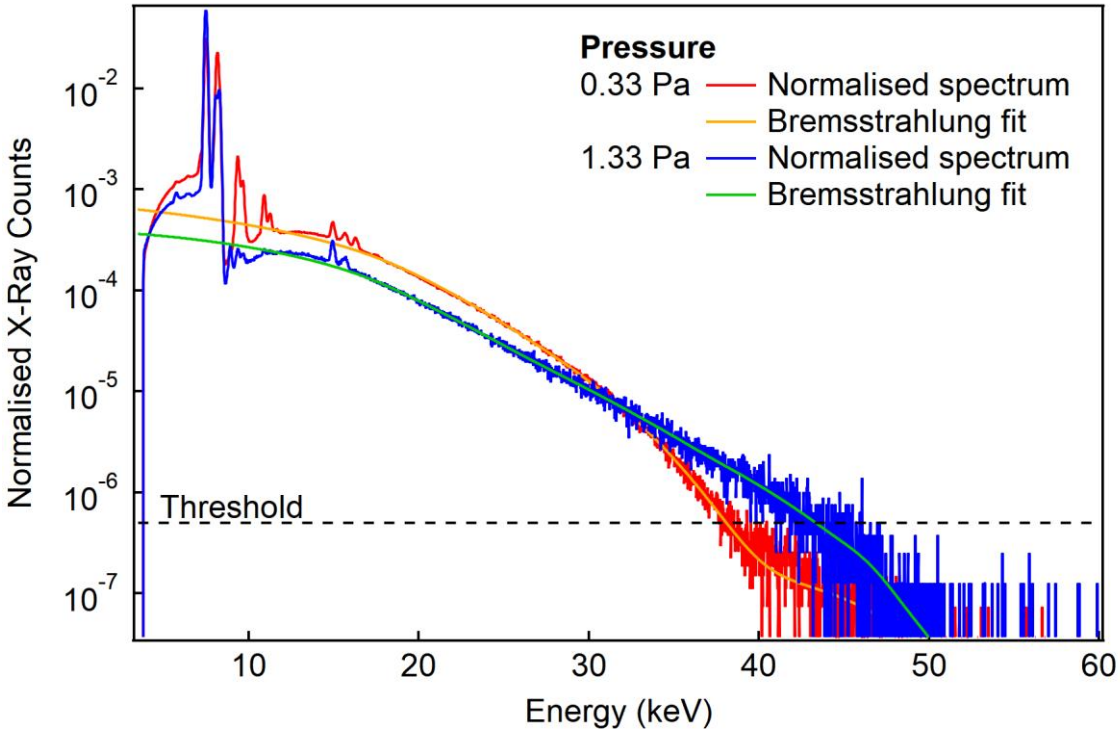

Figure D-1 Comparison of the end-point energies from normalised spectra belonging to $LiTaO_3$ with a crystal thickness of 2.0 mm and performed at a gap distance of 5.0 mm.

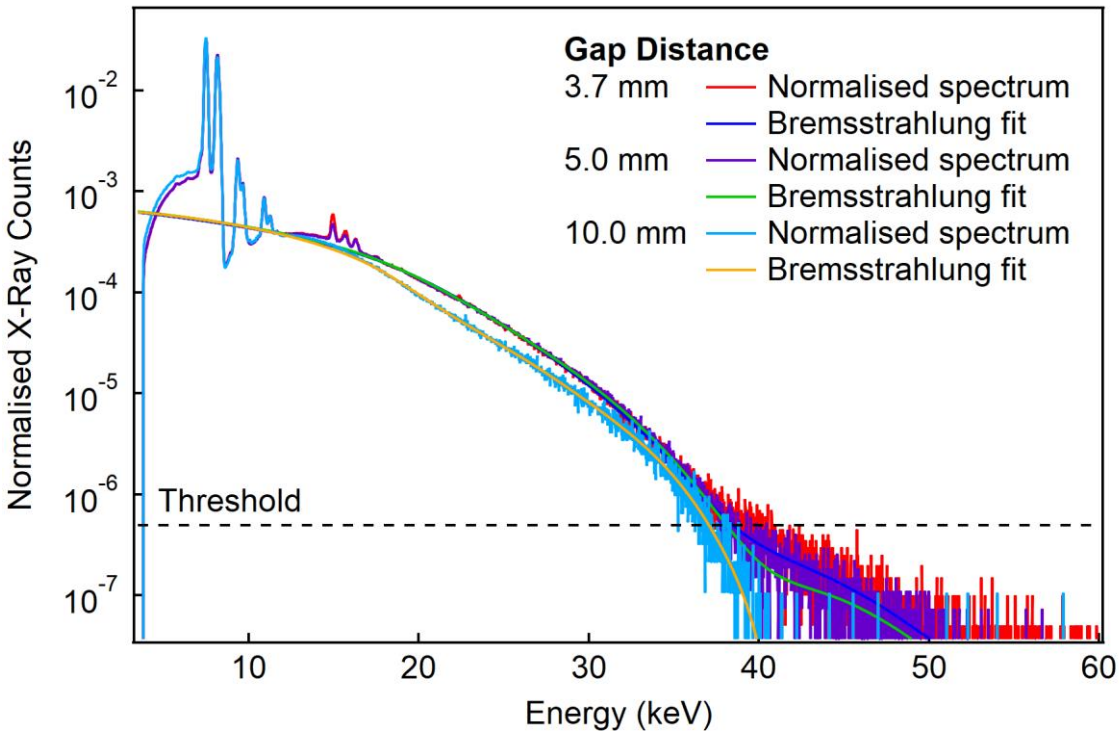

Figure D-2 Comparison of the end-point energies from normalised spectra belonging to $LiTaO_3$ with a crystal thickness of 2.0 mm and performed at a pressure of 0.33 Pa.

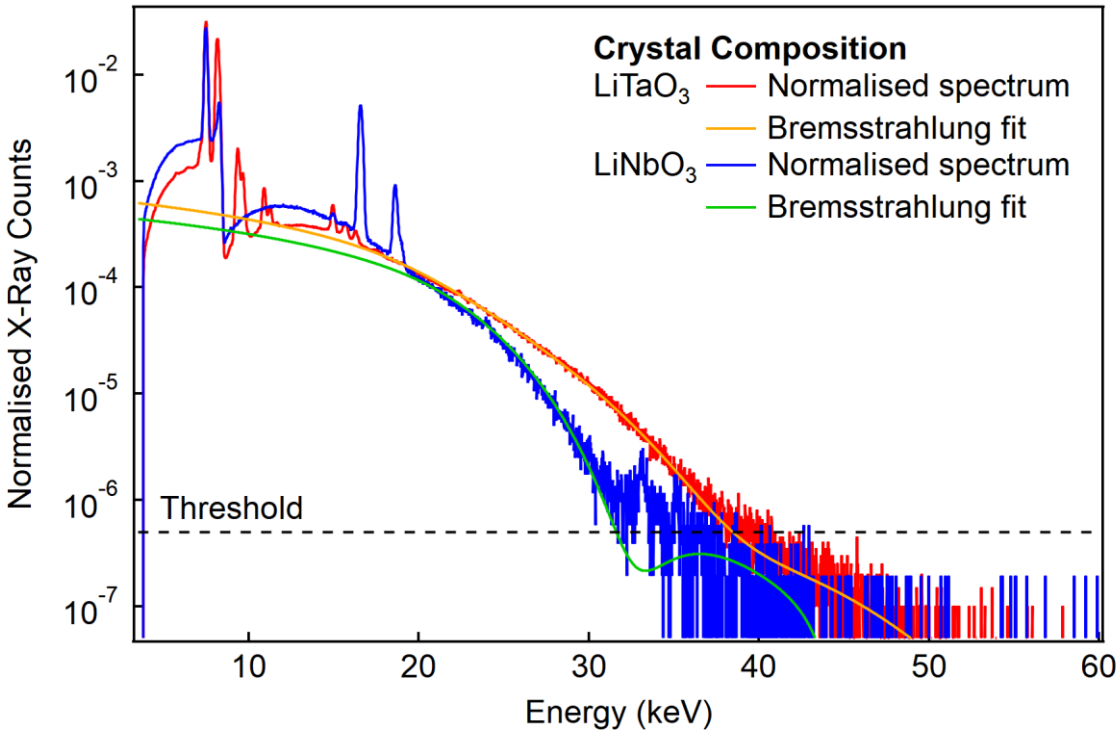

Figure D-3 Comparison of the end-point energies from the normalised spectra of $LiTaO_3$ and $LiNbO_3$. The measurements were performed at a pressure of 0.33 Pa and a gap distance of 3.7 mm.

Appendix E Electric potential distribution of $LiTaO_3$ with insulated edges

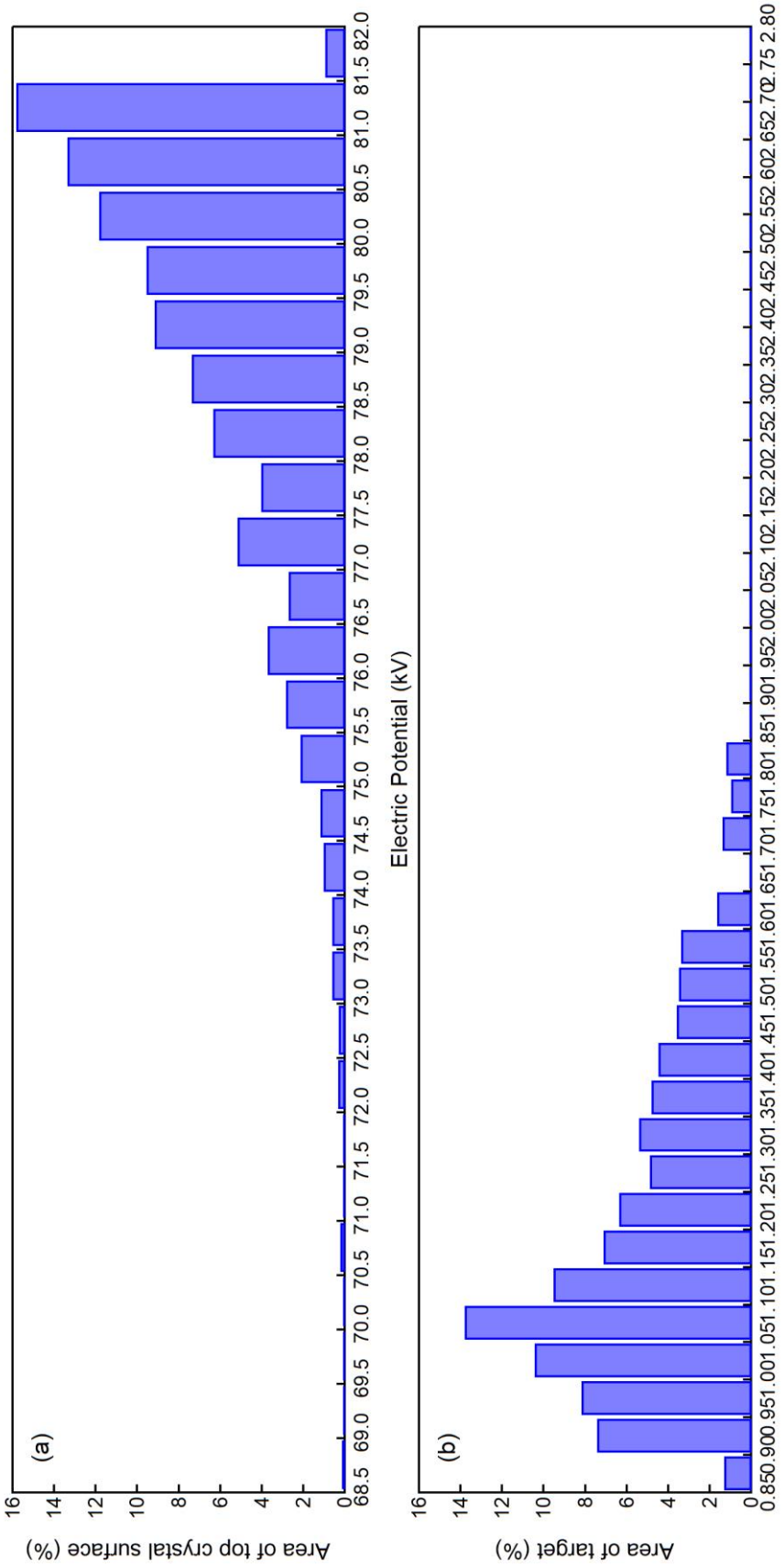

Figure E-1 Histogram of the electric potential distribution at the top crystal surface (a) and target (b) from $LiTaO_3$ with silicone insulated edges. The bin width of (a) and (b) are 500 V and 50 V, respectively. 11.9

Appendix F Updated Arduino program code: Generator12

```
// X-Ray Generator
// Controller V12 for Fatigue measurements
// Updated from V11 on 18 September 2018
//
// Controls and records the temperature and tempSensor
// Records pressure readings
// Uisng PWM.h library, don't use Timer 0 (Pin 5 and 6)
// Instead use Timer 1 (Pin 9 and 10) or Timer 2 (Pin 3 and 11)
// Uses a PID algorithm to control the set point temperature and heating/cooling rate of the Peltier
// Max Temperature set at 100 degrees C
// Included recording of pressureInput from MKS Baratron
// Using Peltier 03111-9L31-04CG with max 200 deg C
// Includes communication to Igor Pro 7 VDT2
//
// Author: Emily Wern Jien Yap

#include <stdlib.h>
#include <stdio.h>
#include <PWM.h>
#include <PID_v1.h>
#include <SPI.h>
#include <MAX31865.h>
#include <Time.h>
#include <TimeLib.h>

#define aref_voltage 3.3
#define PT100
#define RTD_CS_PIN 10   // Chip select pin
#define FAULT_HIGH_THRESHOLD 0x708C   // +200C
#define FAULT_LOW_THRESHOLD 0x2690    // -100C
#define RTD_3WIRES true  // NOT using PT100 with 3 wires

/*
 *  Arduino  VNH5019 (DC Motor Shield)
 *  12        INA
 *  6         INB
 *  3         PWM
```

```
 *  +5V       VDD
 *  GND       GND
 *
 *  Arduino         Sensor
 *  A0              temp
 *  A1              pressure
 *  3.3 to ArefV    tempSensorVin // more precise, less noise
 *  GND             GND (temp)
 *  GND             GND (pressure)
 *
 *  Arduino         MAX31865 (PT100 Mod board)
 *  D10             Chip Select (CS) Pin 1
 *  D11             SDI/MOSI Pin 2
 *  D12             SDO/MISO Pin 3
 *  D13             SCK Pin 4
 *  GND             GND Pin 5
 *  3v3             VCC Pin 6
 *  D2              DRDY/IRQ Pin 7 (Optional)
 */

const int pinA = 12;
const int pinB = 6;
const int PWMPin = 3;
const int voltIn = 6; // voltage input in volts

int timeRead = 100; // delay time between individual temperature and pressure readings (Unit: millisecond)
float polarity = 1;
float voltagePeltier;
int32_t frequency = 18500;  // Frequency in Hz
int i = 0;
int j = 0;
int arrayCount = 0;
double maxTemp = 105; //80; for PMN-30PT  //100; for LT, LN     // Maximum temperature set point
double minTemp = 20;//  0;       // Minimum temperature set point
double initialTemp = 0;   // Initial temperature
double maxSetPointTemp = 120; //85; below PMN-PT R-T temp //120; for LT, LN
double minSetPointTemp = -10;
int heatRampRate = 15;    // 12; // 15; //10;  // 5; // In degrees C/min
int coolRampRate = 15;    // 12; // 15; //10;  // 5; // In degress C/min
```

```
77. float tempChange = 0.25;   // 0.167; // 0.25; for 15 degrees C/min // 0.0833; for 5 degrees C/min // (timeDifference * heat/coolRampRa
    te) in degrees C/second
78. int state = 0;            // start at prepSystem
79. String cycle = "";
80.
81. // Temperature readParameters variables
82. int tempSensor;
83. float tempSensorVolt = 0;
84. float temperature = 0;
85. float tempArray[10];
86. float tempAverage;
87. float totalT;
88. MAX31865_RTD rtd(MAX31865_RTD::RTD_PT100, RTD_CS_PIN,400);
89.
90. // PID Variables
91. double setPointPID = 1; // Value to reach, i.e. max/min temperature
92. double inputPID;        // Variable to control, i.e. temperature of Peltier
93. double outputPID = 0;   // Variable to change, i.e. PWM
94. double Kp;              // Tuning parameter proportional band
95. double Ki;              // Tuning parameter integral
96. double Kd;              // Tuning parameter derivative
97. PID myPID (&inputPID, &outputPID, &setPointPID, Kp, Ki, Kd, DIRECT);  // Setting PID function
98.
99. // Variables for fatigue tests
100.       double holdSetPointTemp = 18; //21;   // Temperature to hold at
101.
102.       // Variables for IGOR Pro VDT2 serial communication
103.       char acqStatus[2];         // g = go, s = stop
104.
105.       void setup()
106.       {
107.         Serial.begin(9600);
108.         analogReference(EXTERNAL);  // Use AREF for reference voltage (Supplying external reference voltage to the Arduino board)
109.         InitTimersSafe();           // Initialises all timers, pwmWrite needs to be used for initialised timers
110.
111.         // Setting up PID
112.         myPID.SetMode(AUTOMATIC); // Turns on PID
113.         myPID.SetOutputLimits(0, 158);  // PWM is limited between 0 and 158 so the voltagePeltier is 3.72 V max (0..255)
114.         myPID.SetControllerDirection(DIRECT);
115.         setPointPID = constrain(setPointPID, minSetPointTemp, maxSetPointTemp);
```

```
116.          state = 0;  // Begin with prepSystem phase
117.
118.          // Setting up frequency for PWM
119.          bool success = SetPinFrequency(PWMPin, frequency);  // Sets the frequency for the specified pin, which in PWM
120.          if (success)
121.          {
122.            pinMode(PWMPin, OUTPUT);
123.            pinMode(pinA, OUTPUT);
124.            pinMode(pinB, OUTPUT);
125.          }
126.
127.          // Initialise SPI communication for the PT100 board
128.          SPI.begin();
129.          SPI.setClockDivider(SPI_CLOCK_DIV16);
130.          SPI.setDataMode(SPI_MODE3);
131.
132.          delay(100);
133.
134.          rtd.configure(true, true, false, RTD_3WIRES, MAX31865_FAULT_DETECTION_NONE,
135.                        true, true, FAULT_LOW_THRESHOLD, FAULT_HIGH_THRESHOLD);
136.          // rtd.configure in brackets explanation
137.          /* Reconfigure this allow us to plug/unplug the module and check PT100/PT1000
138.                V_BIAS enabled
139.                No Auto-conversion
140.                1-shot disabled
141.                3-wire enabled
142.                Fault detection: we need to manual mode, set manual 1 => First stage
143.                                 because on MAX31865 beakout board, RC constant is > 100us
144.                                 see MAX31865 datasheet page 14 / Section Fault Detection Cycle (D3:D2)
145.                Fault status:  auto-clear
146.                50 Hz filter
147.                Low threshold:  FAULT_LOW_THRESHOLD = -100C
148.                High threshold:  FAULT_HIGH_THRESHOLD = +200C
149.          */
150.
151.          cycle = "heating";
152.          readParameters();
153.          initialTemp = inputPID;
154.          setPointPID = initialTemp;
155.        }
```

```
156.
157.      void positiveVoltage() // Driving the heating phase
158.      {
159.        digitalWrite(pinA, HIGH);
160.        digitalWrite(pinB, LOW);
161.        polarity = +1;
162.        myPID.SetControllerDirection(DIRECT);
163.      }
164.
165.      void negativeVoltage() // Driving the cooling phase
166.      {
167.        digitalWrite(pinA, LOW);
168.        digitalWrite(pinB, HIGH);
169.        polarity = -1;
170.        myPID.SetControllerDirection(REVERSE);
171.      }
172.
173.      void runPID(double Kp, double Ki, double Kd)
174.      {
175.        myPID.SetTunings(Kp, Ki, Kd);
176.        myPID.Compute();
177.        pwmWrite(PWMPin, outputPID);
178.      }
179.
180.      void holdPWM(double Kp, double Ki, double Kd, double PWM)
181.      {
182.        myPID.SetTunings(Kp, Ki, Kd);
183.        pwmWrite(PWMPin, PWM);
184.      }
185.
186.      void readParameters()
187.      {
188.        // Initialising total variables
189.        totalT = 0;
190.
191.        for (arrayCount = 0; arrayCount <= 9; arrayCount++)
192.        {
193.          // Reading in temperature
194.          rtd.read_all();
195.          double temperature = rtd.temperature();
```

```
196.          tempArray[arrayCount] = temperature;
197.          totalT = tempArray[arrayCount] + totalT;
198.          delay(timeRead);
199.        }
200.
201.        // Calculating averages
202.        tempAverage = totalT/arrayCount;
203.        voltagePeltier = (float(outputPID)/255)*voltIn*polarity;
204.        inputPID = tempAverage; // REMEMBER: inputPID = actual temperature reading!
205.      }
206.
207.      void printParameters(double setPointPID, double outputPID, float voltagePeltier, float inputPID)
208.      {
209.        Serial.print(setPointPID, 3);         Serial.print(", ");
210.        Serial.print(outputPID, 3);           Serial.print(", ");
211.        Serial.print(voltagePeltier, 3);      Serial.print(", ");
212.        Serial.println(inputPID, 3);
213.      }
214.
215.      void heatingCycle(void)
216.      {
217.        readParameters();
218.        if (setPointPID < maxSetPointTemp)
219.        {
220.          setPointPID = tempChange + setPointPID; // setPoint temperature increases every 1 s
221.          if (setPointPID <=  25)  // For 15-105degC range //30) Adjusting  //20) For 0-100degC range
222.          // If the thermal cycle is not the initial cycle, let the cooling drive force reduce then switch to heating driving force
223.          {
224.            negativeVoltage();
225.          }
226.          else if (inputPID >= (setPointPID - (0.2*setPointPID)))
227.          {
228.            positiveVoltage();
229.          }
230.        }
231.        else if (setPointPID >= maxSetPointTemp)
232.        {
233.          setPointPID = maxSetPointTemp;  // hold the setPoint temperature at max if the tempAverage has not reached max temperature
234.        }
235.
```

```
236.          printParameters(setPointPID, outputPID, voltagePeltier, inputPID);
237.          runPID(2, 5, 1); // runPID(2, 4, 1);
238.
239.          if (inputPID >= (maxTemp -  1.0))  // 0.5))  // if measured temp is at 95 degC
240.          {
241.            cycle = "cooling";
242.            setPointPID = inputPID;
243.          }
244.        }
245.
246.        void coolingCycle(void)   // The temperature in cooling direction decreases with increasing PWM
247.        {
248.          readParameters();
249.          if (setPointPID > minTemp)
250.          {
251.            setPointPID = setPointPID - tempChange; // setpoint temperature decreases at specified rate
252.            if (setPointPID >= 60)  // For 10-120degC range //45) Adjusting //40) For 0-100degC range
253.            // when setpoint temperature is still above 40, let the heating drive force reduce to slow down cooling rate
254.            {
255.              if (inputPID >= (setPointPID - (0.5*setPointPID)))
256.              {
257.                negativeVoltage();
258.                runPID(2,3,0.5);
259.              }
260.              else
261.              {
262.                positiveVoltage();
263.                runPID(2, 3, 0.5);
264.              }
265.            }
266.            else if (setPointPID < 45)  //35) // if the crystal cools too fast, heat up again
267.            {
268.              if (inputPID <= (setPointPID - (0.1*setPointPID)))
269.              {
270.                positiveVoltage();
271.                runPID(2,3,1);  //runPID(2, 3, 0.5);  //runPID(2, 2, 0.5);
272.              }
273.              else  // if cooling speed is still within range
274.              {
275.                negativeVoltage();
```

```
276.               runPID(2,5,2);  //runPID(2, 2, 1);
277.             }
278.           }
279.         }
280.         else if (setPointPID <= minTemp && inputPID >= minTemp)
281.         // if the setPoint temperature has gone below 0 degrees C but the input temperature has not reached it
282.         {
283.           if (setPointPID <= minSetPointTemp)
284.           {
285.             setPointPID = minSetPointTemp;
286.           }
287.           else
288.           {
289.             setPointPID = setPointPID - tempChange;
290.           }
291.           negativeVoltage();
292.           runPID(2, 3, 0.5);
293.         }
294.         printParameters(setPointPID, outputPID, voltagePeltier, inputPID);
295.
296.         if (inputPID <= (minTemp + 1.0))  // if the measured temp is below 1 degC
297.         {
298.           cycle = "heating";
299.           initialTemp = inputPID;
300.           setPointPID = initialTemp;
301.         }
302.       }
303.
304.       void holdCycle(void)
305.       {
306.         readParameters();
307.       //  if (inputPID > (holdSetPointTemp+2.0))
308.       //  {
309.       //    negativeVoltage();
310.       //    runPID(2, 3, 0.5);
311.       //  }
312.       //  else if (inputPID <= (holdSetPointTemp+2.0))
313.       //  {
314.       //      holdPWM(0,0,0,0);
315.       ////    runPID(0,0,0);
```

```
316.        ////    positiveVoltage();
317.        //  }
318.          outputPID = 0;
319.          holdPWM(2,3,0.5,0);
320.          printParameters(setPointPID, outputPID, voltagePeltier, inputPID);
321.        }
322.
323.        void loop()
324.        {
325.          if (Serial.available() > 0)
326.          {
327.            Serial.setTimeout(5000);
328.            Serial.readBytes(acqStatus, 1);
329.            if (acqStatus[0] == 'g') // if cycle running as usual
330.            {
331.              if (cycle.compareTo("heating") == 0)
332.              {
333.                state = 0;
334.              }
335.              else if (cycle.compareTo("cooling") == 0)
336.              {
337.                state = 1;
338.              }
339.            }
340.            else if (acqStatus[0] == 's')  // holding the cycle
341.            {
342.              setPointPID = holdSetPointTemp;
343.              state = 2;
344.            }
345.          }
346.
347.          switch (state)
348.          {
349.            case 0:
350.              heatingCycle();
351.              break;
352.            case 1:
353.              coolingCycle();
354.              break;
355.            case 2:
```

```
356.             holdCycle();
357.             break;
358.           }
359.       }
```

Appendix G IGOR Pro operation program code

```
Function arduino_Generator()

    // *** Procedure Description *** //
    // Procedure written as an in-between to read in data from the Arduino and
    // to scan PC folders if an X-ray spectra file exists
    // Includes parameter to determine if Serial has been disconnected
    // (primitive solution)
    //
    // Updated on: 3 October 2018

    // UPDATE FOLDER PATH
    string path = "C:Users:z3375169:Documents:Spectra:196 18 March 2019:"
    NewPath /Z /Q /O spectraFolder path
    // UPDATE TEST NUMBER
    string testNumber = "160_"
    variable testRun = 1    // current run number
    string fileName
    variable numRun = 4 // total number of runs

    string year, month, day, hour, minute, second, millis
    string exprDate = "([[:digit:]]+)-([[:digit:]]+)-([[:digit:]]+)"
    string exprTime = "([[:digit:]]+):([[:digit:]]+):([[:digit:]]+).([[:digit:]]+)"
    string timeStamp

    // Port settings
    VDT2  /P = COM3 baud = 9600, databits = 8, parity = 0, stopbits = 1, in = 2, out = 2

    // Values for sending signals to Arduino
    string status = ""      // g = go, s = stop
    string check
    string stringCheck
    string readCheck
    string data
    string experimentDone = "done\n"
    variable fileExists = 0
    variable error = 0

```

```
38.     variable holdStart
39.     variable holdCurrent
40.     variable holdTime = 1800    // 60   // in seconds
41.     variable stopTime = 120 // in seconds
42.     variable acqStart = dateTime
43.     variable acqCurrent = dateTime
44.
45.     splitString /E=(exprDate) secs2date(DateTime, -2), year, month, day
46.     splitString /E=(exprTime) secs2time(DateTime, 3, 3), hour, minute, second, millis
47.     string nb
48.     string generatorLog = year + month + day + "-" + hour + minute + second + "_Generator"
49.     NewNotebook /F=0 /K=0 /N=nb as generatorLog
50.
51.     Variable keys
52.
53.     VDTOpenPort2 COM3
54.     VDTOperationsPort2 COM3
55.     VDT2 killio
56.
57.     do
58.         splitString /E=(exprDate) secs2date(DateTime, -2), year, month, day
59.         splitString /E=(exprTime) secs2time(DateTime, 3, 3), hour, minute, second, millis
60.         sprintf timeStamp, "[%s/%s/%s - %s:%s:%s:%s]", day, month, year, hour, minute, second, millis
61.         Notebook nb text = timeStamp + "\r"
62.         print timeStamp
63.
64.         // for individual test runs
65.         fileName = "generatorSpectrum_" + testNumber +  num2str(testRun) + ".mca"
66.
67.         // for multiple test runs above 10
68. //      if (testRun < 10)
69. //          fileName = "generatorSpectrum_" + testNumber + "0" + num2str(testRun) + ".mca"
70. //      else
71. //          fileName = "generatorSpectrum_" + testNumber + num2str(testRun) + ".mca"
72. //      endif
73.
74.         // Constantly check if a new spectra file exists
75.         GetFileFolderInfo /Z=1 /Q /P=spectraFolder fileName
76.         if (V_Flag == 0)
77.             fileExists = 1
```

```
78.             holdStart = dateTime
79.             testRun += 1
80.             print "File exists"
81.             Print testRun
82.         endif
83.
84.         if (fileExists == 0)    // if new spectra has not been found
85.             status = "g"
86.             VDTWrite2 /O=5 status
87.             VDTRead2 /O=5 /T="\n" data
88.             Notebook nb text = data
89.
90.             // To detect if there is an error where no new spectra is collected over acquisition time
91.             acqCurrent = dateTime
92.             if (acqCurrent - acqStart >= 3700)   // time has passed beyond spectra acquisition time
93.                 status = "s"                     // tell the arduino to hold the temperature first
94.                 VDTWrite2 /O=5 status
95.                 VDTRead2/O=2 /T="\n" data
96.                 Notebook nb text = data
97.                 if (V_Flag != 0)                 // let the program know there is an error
98.                     error = 1
99.                 endif
100.                endif
101.
102.            elseif (fileExists == 1 && testRun <= numRun)    // if a new spectra has been found
103.                status = "s"
104.                VDTWrite2 /O=5 status
105.                VDTRead2/O=2 /T="\n" data
106.                Notebook nb text = data
107.
108.                if (holdStart > 0)   // control the hold phase for holdTime
109.                    holdCurrent = dateTime
110.                    if ((holdCurrent - holdStart) >= holdTime)
111.                        fileExists = 0
112.                        holdStart = 0
113.                        acqStart = dateTime
114.                        Print "Start new run"
115.                    endif
116.                endif
117.
```

```
118.                elseif (fileExists == 1 && testRun > numRun)
119.                    status = "s"
120.                    VDTWrite2 /O=5 status
121.                    VDTRead2/O=2 /T="\n" data
122.                    Notebook nb text = data
123.
124.                    if (holdStart > 0)       // control the stop phase for stopTime
125.                        holdCurrent = dateTime
126.                        if ((holdCurrent - holdStart) >= stopTime)
127.                            Print "Finish run"
128.                        endif
129.                    endif
130.
131.                endif
132.
133.                // Escape function to abort if experiment goes wrong
134.                keys = GetKeyState(0)
135.                if ((keys & 32) != 0)   // If user presses the Escape key
136.                    Print "Aborting program"
137.                    break
138.                endif
139.
140.            while (testRun < numRun || error != 1)   // repeat if num of test runs has not reached 24 and no error has been received
141.
142.        End
```